Mechano-regulation of Intraocular Pressure through eNOS

JASON (YIN-HAO) CHANG

SUPERVISORS: DR. DARRYL R OVERBY
PROF. W DANIEL STAMER
PROF. C ROSS ETHIER

IMPERIAL COLLEGE OF SCIENCE, TECHNOLOGY AND MEDICINE
DEPARTMENT OF BIOENGINEERING

Thesis submitted in fulfillment of the requirements for the award of Doctor of Philosophy and the Diploma of the Imperial College.

Abstract

Glaucoma is the leading cause of irreversible blindness worldwide, and is characterized by elevated intraocular pressure (IOP) caused by increased resistance to aqueous humor outflow. The majority of outflow resistance is generated near the inner wall endothelium of Schlemm's canal (SC). The inner wall experiences a basal-to-apical directed flow as aqueous humor crosses the outflow pathway. As IOP increases, the outflow pathway responds in a pressure-dependent manner, resulting in the expansion of the trabecular meshwork (TM) and the collapse of SC. This effectively reduces the cross-sectional area of the SC lumen and increases the shear stress experienced by SC cells, reaching levels known to activate endothelial nitric oxide synthase (eNOS) in vascular endothelia.

Our central hypothesis examines the role of eNOS as part of a dynamic mechano-regulatory feedback system to regulate the outflow resistance sites through nitric oxide (NO) production to maintain IOP homeostasis. We firstly demonstrated the physiological role of NO and eNOS in regulating aqueous humor outflow through the use of NO-donor and NOS-inhibitors. We also demonstrated that spatial variations in eNOS expression in the SC correlates with regions of greater outflow in the TM. Furthermore, we developed NO-sensitive biosensors to detect changes in NO production in response to elevated IOP, showing that NO production was pressure-dependent. Finally, we demonstrated that targeted delivery of NO to the outflow resistance sites in the TM results in a $\sim$3-fold increase in outflow facility.

Taken together, these studies reveal that eNOS plays a crucial regulatory role in conventional outflow physiology by modulating outflow resistance through NO production. This mechano-regulatory feedback mechanism appears to be altered in glaucoma, and thus leads to ocular hypertension and pathogenesis of the disease. Therefore, targeting the NO-regulatory machinery within the outflow pathway may provide a promising therapeutic target for treating glaucoma.

To my parents,
for supporting me throughout my pursuit of education

To my grandfather,
who inspired and fueled my curiosity about medicine

To my grandmother,
who left us too soon, but personified kindness, patience and humility

Acknowledgements

I would firstly like to express my sincere gratitude towards my supervisor Dr. Darryl Overby, for all the support and invaluable guidance throughout the past four years, constantly pushing me to ask the right questions through constructive and critical comments. Additionally, he has mentored me and supported my pursuit in research and development as a researcher from my days as a MSc student all the way to the end of my PhD studies. My co-supervisors, Prof. Dan Stamer and Prof. Ross Ethier, have both been very supportive and committed towards my research projects, providing helpful comments, insightful suggestions and sometimes questions that I just do not know how to answer. I would like to thank them for their input into the work presented in this thesis.

I would also like to thank the departmental support staff: Allan Nyunt, Kate Hobson, Kenneth Keating, Reva Vaze, Gary Jones, Edit Toth, Laura McKay and Britta Ross for their help throughout the years.

I would like to also thank all the members of the Stamer lab at Duke University, which I was a honorary member of from during 2013/2014. I'd especially like to thank Ms. Kristin Perkumas for her help and support whilst I was conducting research there and also for transporting me back and forth from Target on the weekends; and to Dr. Mike Dismuke for his helpful discussions and technical assistance in the lab.

I would also like to thank the members of the Stevens group at Imperial College, which I seem to have gravitated towards over the past four years. I'd like give special thanks to the following people for their scientific contributions towards my research projects and my time here at Imperial: (Prof.) Lesley Chow for her help on peptide synthesis and polymer chemistry which has resulted in an interesting, highly entertaining and successful collaboration. I'd like to thank (Prof.) Rona Chandrawati for always being encouraging throughout my PhD, and providing insight into how to tackle different aspects of my research projects, which has resulted in another successful collaboration. Also for being an awesome house mate. Last but not least, Dr. Eugene Thomas Pashuck III, thank you for always helping me with random polymer chemistry questions, finding reagents, and being the "GO-TO-GUY" in the lab whenever I have other questions. Also for being an awesome friend, Imperial is not the same without you around (we will always have Taza). Other members I'd like to thank include: Yiyang, Coline, Astrid, Paresh, JP, Mark, (tall) Mike, Chris (spicy), Phil, Geraldine and Jenny for making the casual friday union nights memorable.

I'd like to express my utmost gratitude towards the Overby lab members, both former and present for making my time here at Imperial unforgettable. Former members include: Dr. Ryan Pedrigi, for showing me the "ropes" in the lab during my time as a Master's student and also for the moral support you have given me over the years during our climbing sessions. Dr. Alexandra Boussommier-Calleja for always being supportive and teaching me how to use the mouse eye per-

fusion system... and also for being a great friend. Dr. Sietse Braakman for always providing great technical assistance in the lab and also providing a good laugh. To the current members of the Overby lab: Ester Reina Torres for always being positive and care-free in the lab, always willing to help and being so understanding when a perfusion does not go well. Also you should be submitting as well. Jacques Bertrand for taking care of all the orders and keeping the lab running, and also being a good laugh whenever we hang out. Alice Spenlehauer (the baby of the group) for being so bubbly and energetic in the lab making perfusion days that more "exciting". (Also I had to look up how to spell your last name as its too hard to write.) Anabela Cepa Arieas for being a great friend and joyful all the time, for sharing music and general good vibes its been great getting to know you. Dr. Cristoforo Silvestri, even though you have only joined our lab for one year, your presence has made the lab better. Also thank you for proof reading my chapters, it has been very helpful. I'd also like to thank Michael, Kathy and Dr. Joseph Sherwood for making the group dynamic more interesting.

I'd also like to thank all the following people I have encountered over the years whether it be in the lab, office, or the climbing gym for making my time at Imperial unforgettable: Jose Rivera-Rubio, Yean Chooi, Hinesh Patel, Ethan Rowland, Ani Setchi, Joe Prinold, Eugene Chang, Lucas Hadjilucas, Olga Korolkova, Gaëlle Chapuis and Mehrdad Kiani.

Finally, I am forever grateful to my parents for their continued support, advice and perspectives on everything, reminding me that there is more than just science. I'd especially like to thank my mom for always believing in me, even when I did not believe in myself.

Contribution Statement

Several researchers have contributed to the work presented in this thesis. Their contributions have been acknowledged below.

Chapter 2: The calibration and characterization of the NO-donors release kinetics with the WPI nitric oxide probe was carried out by Jason Chang and Catherine Marando. The genotyping and maintenance of the eNOS-GFPtg mice colony were carried out by Jack Bertrand. All the perfusion studies and analysis were carried out by Jason Chang and Jack Bertrand. The confocal imaging were performed by Dr. Thomas Read.

Chapter 3: Peptide design and synthesis was performed by Jason Chang and Dr. Lesley Chow. All UV-VIS peptide nitration data, *in vitro* peptide-NP immunoassay development and data analysis, *in situ* peptide-NP immunoassay and shear stress experiments were carried out by Jason Chang.

Chapter 4: All *ex vivo* perfusion experiments, whole mount immunostaining, confocal imaging, were carried out by Jason Chang. The genotyping and maintenance of the eNOS-GFP (reporter) mice colony were carried out by Jack Bertrand. Colocalisation analysis and image processing were carried out by Jason Chang and Jose Rubio-Rivera.

Chapter 5: All *ex vivo* perfusion experiments and dissections were carried out by Jason Chang. The development of PDMS casting protocol were carried out by Jason Chang and Marco Ravot Licheri. *In vivo* two-tracer C57BL/6 wild-type mice injections were carried out by Ester Reina-Torres and Jason Chang. Design and development of experiments were carried out by Jason Chang, Ester Reina-Torres, Marco Ravot Licheri and Dr. Darryl Overby. Casting, image acquisition and image processing of *ex vivo* mouse eyes were carried out by Marco Ravot Licheri, under the supervision of Jason Chang and Dr. Darryl Overby.

Chapter 6: Design and development of β-galactosidase containing PMA capsules and β-gal-NONOate containing liposomes were carried out by Dr. Rona Chandrawati. The design of the experimental study was carried out by Jason Chang and Dr. Rona Chandrawati. The calibration and characterization of the β-gal-NONOate release kinetics with the WPI nitric oxide probe was carried out by Jason Chang and Dr. Rona Chandrawati. *In vivo* PMA capsule injections in C57BL/6 wild-type mice were carried out by Ester Reina-Torres and Jason Chang. All *ex vivo* perfusion experiments were carried out by Jason Chang.

Copyright ad Financial Disclosure

I hereby declare that the studies presented in this thesis are my own work, performed in Dr. Overby's laboratory between October 2011 and October 2015. All data, results and figures from third party works have been duly referenced. Contributions by other researchers are specified in the Contribution Statement. I certify that this thesis complies with copyright laws and does not contain any instance of plagiarism.

This study was supported by a PhD scholarship (UK/EU portion of funds) from the Department of Bioengineering at Imperial College London obtained by Dr. Overby, in addition to financial support provided by my parents (International student portion of fees). From June 2013 to July 2014, I received the opportunity to conduct research at Department of Ophthalmology at Duke University as an *"Visiting Graduate Scholar"*, funded by Prof. Stamer.

The Academic Regulations 2014/15 from Imperial College London state:
The copyright of this thesis rests with the author and is made available under a Creative Commons Attribution-Non Commercial-No Derivatives licence. Researchers are free to copy, distribute or transmit the thesis on the condition that they attribute it, that they do not use it for commercial purposes and that they do not alter, transform or build upon it. For any reuse or distribution, researchers must make clear to others the license terms of this work.

Associated Publications

Refereed Journal Publications:

- **Chang JYH***, Folz SJ*, Laryea SN, Overby DR. "Multi-Scale Analysis of Segmental Outflow Patterns in Human Trabecular Meshwork with Changing Intraocular Pressure." *Journal of Ocular Pharmacology and Therapeutics*, **2014**, doi:10.1089/jop.2013.0182.
- **Chang JYH**, Stamer WD, Bertrand J, Read AT, Marando CM, Ethier CR, Overby DR. "The Role of Nitric Oxide in Murine Conventional Outflow Physiology." *AJP: Cell Physiology*, **2015**, doi:10.1152/ajpcell.00347.2014.
- **Chang JYH**, Chow LW, Dismuke WD, Stevens MM, Ethier CR, Stamer WD, Overby DR. "Peptide-Functionalized Nanoparticles for Localized Detection of Nitric Oxide: A Peroxynitrite Mediated Nitration." *In preparation*, to be submitted to *ACS Nano*.
- **Chang JYH**, Rivera-Rubio J, Bertrand J, Mohri Z, Weinberg PD, Bharath AA, Ethier CR, Stamer WD, Overby DR. "Preferential Outflow in Relation to Endogenous eNOS Activity in Murine Conventional Outflow Pathway." *In preparation*, to be submitted to *PLoS Biology*.
- Ravot Licheri M*, **Chang JYH***, Reina-Torres E, Boussommier-Calleja A, Bertrand J, Chandaria V, Martin S, Sharpe J, Nowlan NC, Overby DR. "Imaging of Segmental Outflow in *Ex Vivo* Mouse Eyes by OPT." *In preparation*, to be submitted to *Experimental Eye Research*.
- Chandrawati R*, **Chang JYH***, Reina-Torres E, Jumeaux C, Stamer WD, Stevens MM, Overby DR. "Targeted Delivery of Nitric Oxide to the Trabecular Outflow Pathway via Enzyme Loaded Nanoparticles." *In preparation*, to be submitted to *Proceedings of the National Academy of Science*.

  ** denotes co-first authors.*

Conference Presentations:

- **Chang JYH**, Braakman ST, Mohri Z, Weinberg PD, Ethier CR, Stamer WD, Overby DR **(2015)**. "Colocalization of Segmental Outflow and Endogenous eNOS Activity in the Conventional Outflow Pathway of Mice." *The Association of Research in Vision and Ophthalmology Conference*, Denver, USA
- **Chang JYH**, Dismuke WM, Overby DR, Stamer WD **(2014)**. "Investigation of Enucleated Mouse Eyes in Organ Culture", at *International Society of Eye Research Conference*, San Francisco, USA
- **Chang JYH**, Ethier CR, Stamer WD, Overby DR **(2014)**. "Differential Effects of Nitric Oxide Synthase Inhibitors on Conventional Outflow Facility in Mice", at *The Association of Research in Vision and Ophthalmology Conference*, Orlando, USA
- **Chang JYH**, Marando CM, Ethier CR, Stamer WD, Overby DR **(2013)**. "Effects of Nitric Oxide Donor on Outflow Facility in Mice", at *The Association of Research in Vision and Ophthalmology Conference*, Seattle, USA
- **Chang JYH**, Overby DR **(2012)**. "Eye-on-a-chip: Reconstituting the Conventional Outflow Pathway of the Eye on a Microfluidics Platform", at *Bioengineering 2012 Conference*, Oxford, United Kingdom. **Podium Presentation**.
- **Chang JYH**, McKay B, Stamer WD **(2012)**. "Plate Assay for Glaucoma Drugs", at *The Association of Research in Vision and Ophthalmology Conference*, Fort Lauderdale, USA

List of Abbreviations

3-NT	3-Nitrotyrosine
AH	Aqueous humour
C	Outflow facility
DMSO	Dimethyl sulfoxide
ECM	Extracelluar matrix
IOP	Intraocular pressure
JCT	Juxtacanalicular connective tissue
NO	Nitric Oxide
NP	Nanoparticles
OHT	Ocular hypertension
ONOO–	Peroxynitrite anion
PDMS	Polydimethylsiloxane
PMA	Poly(methacrylic acid)
POAG	Primary open-angle glaucoma
Q	Flow rate
R	Outflow resistance
ROI	Region of interest
SC	Schlemm's canal
TM	Trabecular Meshwork

Contents

Abstract i

1 Introduction and Background 1

1.1 Introduction . . . 2

1.2 Background . . . 4

1.2.1 Anatomy of the Aqueous Humour Outflow Pathway . . . 4

1.2.2 Glaucoma . . . 12

1.2.3 Aqueous Humour Dynamics . . . 12

1.2.4 Outflow Resistance Generation . . . 13

1.2.5 Outflow Resistance: Synergistic Model . . . 14

1.2.6 Segmental Flow of the Outflow Pathway . . . 16

1.2.7 Role of Nitric Oxide in Outflow Physiology . . . 20

1.3 Motivation of Thesis . . . 28

1.4 Specific Aims . . . 29

2 Role of Nitric Oxide in Murine Conventional Outflow Physiology 31

2.1 Introduction . . . 32

2.2 Materials and Methods . . . 33
2.2.1 Experimental Design . . . 33
2.2.2 Calibration of NO-donor . . . 34
2.2.3 Animal Husbandry . . . 35
2.2.4 *Ex Vivo* Mouse Eye Perfusion . . . 36
2.2.5 Immunofluorescence Microscopy . . . 39
2.2.6 Statistical Analysis . . . 40
2.3 Results . . . 40
2.3.1 Effects of Light on NO-Donors . . . 40
2.3.2 Effect of NO-Donors on Conventional Outflow Facility . . . 41
2.3.3 Effect of NOS-Inhibitors on Conventional Outflow Facility . . . 41
2.3.4 Localization of eNOS Transgene Expression within the Conventional Outflow Pathway . . . 43
2.4 Discussion . . . 45
2.5 Appendix A: Effects of NO-Donor on the Inner Wall Endothelium of Schlemm's Canal 51
2.5.1 Methods: Histology and Ultramicroscopy . . . 51
2.5.2 Results and Discussion . . . 52

3 Peptide-Functionalized Nanoparticles for *in Situ* Detection of Nitric Oxide *via* Peroxynitrite-Mediated Nitration 55

3.1 Introduction . . . 56
3.2 Materials and Reagents . . . 58
3.3 Methods . . . 59

3.3.1 Peptide Synthesis . . . 59
3.3.2 Detection of Nitrated Peptides in Solution . . . 60
3.3.3 Peptide-Nanoparticle Conjugates . . . 60
3.3.4 3-Nitrotyrosine Detection on Nanoparticle Complex . . . 61
3.3.5 Cell Culture . . . 62
3.3.6 Shear Stress Experiments . . . 62
3.3.7 Immunofluorescence Microscopy . . . 63
3.3.8 Statistical Analysis . . . 63
3.4 Results and Discussion . . . 64
3.4.1 Characterization of Unbound Peptides to Nitration . . . 64
3.4.2 Characterization of Peptide-NPs to Nitration . . . 66
3.4.3 Detection of Shear-Mediated Nitric Oxide Produced by HUVECs . . . 67
3.5 Conclusions . . . 70
3.6 Supplementary Information . . . 73
3.7 Appendix A: Solid-phase peptide synthesis – (Fmoc) . . . 76

4 Preferential Outflow in Relation to Endogenous eNOS Activity in the Murine Conventional Outflow Pathway 79

4.1 Introduction . . . 80
4.2 Materials and Methods . . . 82
4.2.1 Experimental Design . . . 82
4.2.2 Animal Husbandry . . . 82

4.2.3 Peptide-Nanoparticle Synthesis and Conjugation . . . 83
4.2.4 Fabrication of Microfluidic Chip . . . 84
4.2.5 *Ex Vivo* Mouse Eye Perfusion . . . 84
4.2.6 Anterior Eye Cup Flat Mounting . . . 86
4.2.7 Immunofluorescence and Confocal Microscopy . . . 87
4.2.8 Colocalisation Analysis . . . 89
4.2.9 Image Processing . . . 90
4.2.10 Statistical Analyses . . . 92
4.3 Results . . . 94
4.3.1 Visualization of eNOS transgene expression within the conventional outflow pathway . . . 94
4.3.2 Relationship between eNOS-GFP expression and tracer intensity . . . 96
4.3.3 Effect of elevated IOP on NO production *in situ* . . . 99
4.4 Discussion . . . 102
4.5 Supplementary Information . . . 106

5 Imaging of Segmental Outflow in *Ex Vivo* Mouse Eyes by Optical Projection Tomography 107

5.1 Introduction . . . 108
5.2 Materials and Supplies . . . 109
5.2.1 Animal Husbandry . . . 109
5.2.2 eNOS-GFP transgenic mice . . . 110
5.2.3 Fluorescent Tracers for *Ex Vivo* Perfusions and *In Vivo* Injections . . . 110

5.2.4 Anesthesia . . . 111
5.2.5 Embedding of Mouse Eyes for OPT Imaging . . . 111
5.2.6 Glass Needles for *In Vivo* Injections . . . 111
5.3 Detailed Methods . . . 112
5.3.1 Experimental Design . . . 112
5.3.2 *Ex Vivo* Tracer Perfusions . . . 112
5.3.3 *In Vivo* Tracer Injections . . . 113
5.3.4 Embedding Protocol of Enucleated Mouse Eyes . . . 114
5.3.5 Image Acquisition with OPT . . . 116
5.3.6 Segmental Tracer Distribution Analysis . . . 117
5.3.7 Image Processing of Limbal Vasculature . . . 118
5.4 Results . . . 118
5.4.1 Comparison of PDMS Protocol vs. Standard BABB Protocol . . . 118
5.4.2 Visualization of the Limbal Vasculature in eNOS-GFP Mice . . . 119
5.4.3 360° View of Tracer Distribution . . . 120
5.4.4 Image Processed Limbal Vasculature . . . 123
5.5 Potential Pitfalls and Trouble Shooting . . . 124
5.5.1 *In Vivo* Tracer Injections . . . 124
5.5.2 PDMS Embedding and Positioning of Eyes . . . 125
5.6 Conclusion and Potential Applications . . . 126

6 Targeted Delivery of Nitric Oxide to the Trabecular Outflow Pathway via Enzyme Loaded

Nanoparticles **128**

6.1 Introduction . . . 129

6.2 Materials and Methods . . . 130

6.2.1 Materials . . . 130

6.2.2 Experimental Design . . . 131

6.2.3 PMA Capsule Assembly . . . 131

6.2.4 Preparation of Alexa Fluor 488-labeled β-galactosidase . . . 132

6.2.5 Liposome Formation . . . 132

6.2.6 Characterization of β-galactosidase Mediated Release of NO . . . 132

6.2.7 Animal Husbandry . . . 133

6.2.8 *In Vivo* Delivery of β-galactosidase Encapsulated PMA Capsules . . . 133

6.2.9 *Ex Vivo* Delivery of β-gal-NONOate Encapsulated Liposomes via Mouse Eye Perfusions . . . 134

6.3 Results . . . 136

6.3.1 *In Vitro* Release of NO via Enzymatic Catalysis . . . 136

6.3.2 Enzyme-Mediated NO Release from Encapsulated β-gal-NONOate *In Vitro* . . . 136

6.3.3 Targeted Delivery of NO Synthesis to the Trabecular Meshwork . . . 138

6.4 Discussion . . . 140

7 Conclusions **142**

7.1 Future Work . . . 147

7.1.1 Effect of Selective-Inhibition of eNOS on Segmental Outflow Distribution . . . 147

7.1.2 Targeted NO Synthesis within the Conventional Outflow Pathway 147

A Permission Documents for Reprint **149**

Bibliography **154**

List of Figures

1.1 Schematic representation of endogenous NO regulatory feedback mechanism for aqueous humour outflow. . . . 4

1.2 Overview of conventional outflow pathway in the human eye. . . . 5

1.3 Light micrograph of a meridional section through the trabecular meshwork. . . . 8

1.4 Electron micrograph images of the inner wall endothelium of Schlemm's canal . . . 10

1.5 Post-trabecular aqueous humour outflow pathway. . . . 11

1.6 Schematic representation of IOP induced Schlemm's canal collapse. . . . 16

1.7 Macro-scale segmental outflow patterns in enucleated human eyes. . . . 17

1.8 Micro-scale segmental outflow patterns in enucleated human eyes. . . . 18

1.9 Schematic of eNOS regulatory feedback in the conventional outflow tract. . . . 28

2.1 Perfusion system to measure outflow facility in enucleated ex vivo mouse eyes. . . . 38

2.2 Characterization of NO concentration following release by SNAP or NAP under varying lighting conditions. . . . 42

2.3 The effects of NO-donor on conventional outflow facility in eyes from wild-type (WT) and eNOS-GFPtg mice. . . . 43

2.4 Effect of NOS-inhibitors on conventional outflow facility in enucleated eyes from wild-type (WT) and eNOS-GFPtg mice. . . . 44

2.5 Localization of transgene expression in the conventional outflow pathway of eNOS-GFPtg mice. 45

2.6 Light micrograph of the conventional outflow pathway of a WT mouse eye perfused with SNAP and NAP. . . . 53

2.7 Transmission electron micrograph of the inner wall endothelium of SC in WT mice treated with SNAP and NAP. . . . 53

2.8 Scanning electron micrograph of the inner wall endothelium of SC in WT mice treated with SNAP and NAP. . . . 54

3.1 Schematic representation of peroxynitrite-induced nitration. . . . 61

3.2 3-Nitrotyrosine detection with UV-Vis spectrophotometry. . . . 65

3.3 Nitration detection with peptide-nanoparticle immunoassay. . . . 68

3.4 HUVECs exposed to different levels of shear stress . . . 69

3.5 3-Nitrotyrosine detection at the cellular level under shear stress. . . . 71

3.6 Chemical structures, MALDI and analytical HPLC trace of purified peptide sensors . . . 73

3.7 Nitration sensitivity of synthetic tyrosine-containing peptides with UV-Vis spectrophotometry . . 74

3.8 Representative peptide-nanoparticle complex dot blot sensitivity immunoassay . . . 75

3.9 Schematic diagram of peptide synthesis. . . . 78

4.1 Schematic representation of controlled delivery of perfusates via a microfluidic chip. . . . 86

4.2 Schematic representation of flat mount procedure to visualize segmental tracer distribution in the outflow tract. . . . 87

4.3 eNOS-GFP expression throughout the conventional outflow pathway visualized using flat-mount mouse eyes . . . 89

4.4 Colocalisation analysis between tracer intensity and eNOS-GFP expression. . . . 91

4.5 Localization of eNOS-GFP expression in the conventional outflow pathway of eNOS-GFP mice. 94

4.6 Schlemm's canal visualized via flat-mount imaging. . . . 95

4.7 Representative whole mount confocal imaging to visualize the relationship between segmental tracer distribution in the TM and spatial variation of eNOS-GFP expression in the SC. . . . 97

4.8 Relationship between eNOS-GFP expression and tracer intensity. 99

4.9 Localized detection of NO-mediated nitration in the conventional outflow pathway. 100

4.10 Comparison of 3-nitrotyrosine detection in the conventional outflow pathway as a function of IOP.101

4.11 Relationship between eNOS-GFP expression and tracer intensity. 106

5.1 Schematic representation of tissue embedding protocol for OPT imaging. 116

5.2 Schematic of the fluorescence OPT imaging setup. 117

5.3 Comparison of sample preparation protocols used for fluorescence OPT imaging of eNOS-GFP mouse eyes. 119

5.4 Visualization of the limbal vascular network of eNOS-GFP mouse eyes imaged with fluorescence OPT. 121

5.5 360° view of tracer distribution in *ex vivo* mouse eyes. 122

5.6 Segmental outflow patterns of living WT mice. 123

5.7 Enhancement of fluorescence OPT acquired images of the limbal vasculature. 124

6.1 Schematic representation of targeted delivery of NO via enzymatic biocatalysis. 130

6.2 Characterization of NO synthesis resulting from β-galactosidase-mediated hydrolysis of β-gal-NONOate. 137

6.3 NO synthesis from β-galactosidase encapsulated PMA capsules and β-gal-NONOate encapsulated liposomes. 138

6.4 Cyclic NO synthesis from β-galactosidase encapsulated PMA capsules and β-gal-NONOate encapsulated liposomes. 139

6.5 Effects of targeted delivery of NO synthesis on conventional outflow facility in eyes obtained from wild-type (WT) mice. 140

7.1 Mechano-regulatory feedback system via shear-induced eNOS activity and NO production. . . 146

A.1 Permission for reprint of Figure 1.3 150

A.2 Permission for reprint of Figure 1.4a 151

A.3 Permission for reprint of Figure 1.4b 152

A.4 Permission for reprint of Figure 1.5b 153

List of Tables

4.1 Summary of the correlations between GFP intensity and tracer intensity. 98

4.2 Outflow facility data for *ex vivo* mouse eyes 106

Chapter 1

Introduction and Background

1.1 Introduction

Glaucoma is a group of ocular diseases characterized by the irreversible damage caused to the optic nerve head, commonly referred as "glaucomatous optic neuropathy", affecting more than 60 million people worldwide, of which 8.4 million are bilaterally blind[176]. The primary risk factor associated with the development of glaucoma is elevated intraocular pressure (IOP); this increase in IOP leads to the compression of the optic nerve head, which damages the retinal ganglion cells responsible for transmitting visual information from the eye to the brain. Current glaucoma treatments aim to lower IOP, through either surgical or drug interventions to slow the progression of vision loss. However, these therapies are often unable to achieve a sustained IOP reduction, largely because the treatments do not target the underlying root cause of elevated IOP; increased hydraulic resistance of the outflow pathway. Thus, identifying the physiological mechanisms responsible for the increased outflow resistance in the conventional outflow tract would provide more targeted and efficacious glaucoma therapies.

The intraocular pressure is determined by the balance between the production of aqueous humour (AH) by the ciliary processes and the drainage through the conventional outflow pathway of the eye. Elevated IOP is associated with the increased hydraulic resistance of the conventional outflow pathway (responsible for $\sim$80% of AH drainage[92,118]), which consists of the trabecular meshwork (TM), juxtacanalicular tissue (JCT) and the inner wall endothelium of Schlemm's canal (SC). The majority of the outflow resistance is generated proximal to or within close vicinity of the endothelium of Schlemm's canal; however, the mechanisms involved in outflow regulation are still not well understood[116,118,147]. Recent data have suggested that nitric oxide (NO), a key signaling molecule responsible for mediating various physiological functions, including modulating vascular tone[154,155,232], neuronal signaling[31] and immunological processes[74], may also play an important role in aqueous humour outflow regulation. NO is a diatomic free radical produced by the family of enzymes, nitric oxide synthase (NOS), through the conversion of L-arginine to L-citrulline. In the vascular and lymphatics system, NO is known to mediate endothelial permeability through targeting cellular mechanisms such as soluble guanylate cyclase (sGC)[55,56] and junctional complexes[57,175]; as the SC is derived from vascular endothelia[99,185] and expresses both vascular and lymphatic markers[12,126,169,185], we hypothesize that SC cells possesses the same NO-regulatory

machinery and that this mechanism may contribute to the physiological regulation of conventional outflow. Recent studies have demonstrated that SC cells in culture are shear-sensitive, and secrete NO in response to increasing shear stress through the activation of endothelial NOS[11,135], similar to vascular endothelial cells[44,45]. Interestingly, at elevated IOP the SC lumen collapses and in turn increases the shear stress acting on the SC cells *in vivo*, and is predicted to approach levels of shear experienced by endothelial cells in arteries[73]. We hypothesize that SC cells function as "stress-sensors" within this endogenous feedback loop that detects changes in IOP and regulates AH outflow by modulating the outflow resistance sites, in part through NO signaling. Within this regulatory feedback system, NO acts as an autocrine or paracrine signaling molecule[210] that can freely diffuse either upstream to relax the TM/JCT cells[61,236,237] and/or along the circumference of the canal to increase the permeability of the inner wall endothelium of SC by disrupting the adherens junctions[44,57]. This leads to decreased outflow resistance and increased aqueous humour outflow, which in turn restores IOP back to normal physiological levels (Figure 1.1).

Furthermore, the presence of NADPH-diaphorase[1] labeling in the conventional outflow pathway of human donor eyes, suggests endogenous NO production and NOS activity, whilst decreased NADPH-diaphorase labeling has been reported in glaucomatous eyes[158]. Additionally, genome-wide association studies[121,141,174] have linked polymorphisms in the *NOS3* gene that encodes eNOS to the pathogenesis of glaucoma, and overexpression of eNOS in a mouse model leads to decreased outflow resistance and lower IOP[117,211]. Taken together, these data suggest that endogenous NO signaling within the conventional outflow pathway by NOS enzymes contributes to outflow regulation and that alterations in NO signaling in part mediates outflow dysfunction in glaucoma. In this thesis, we examine the central hypothesis that the conventional outflow pathway functions as a "dynamic mechano-regulatory system" that modulates the outflow resistance sites through NO production to help maintain IOP homeostasis.

[1] NOS isozyme independent marker used to locate sites of NO synthesis.

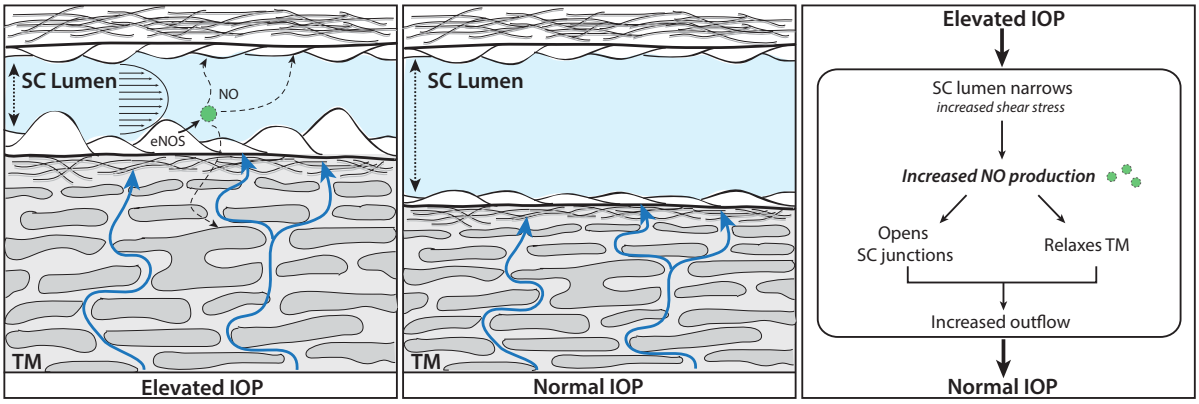


Figure 1.1: Schematic representation of endogenous NO regulatory feedback mechanism for aqueous humour outflow. (*Left*) At elevated IOP, the inner wall endothelium of SC distends into the lumen resulting in a collapsed canal. This increases the theoretical hydrodynamic shear stress[73] acting on the shear-sensitive SC endothelial cells[11,135] and results in increased NO production (green circle). NO can travel by retrograde diffusion upstream to relax the TM/JCT cells and/or advection along the canal to disrupt SC cell-cell junctions to increase outflow. (*Middle*) NO mediates the outflow resistance sites in the conventional outflow pathway to help increase outflow and restore IOP, resulting in a more open SC lumen. (*Right*) NO mediated regulatory feedback mechanism to restore normal IOP. *TM = Trabecular meshwork, JCT = Juxtacanalicular connective tissue, Solid blue lines: transendothelial flow.*

1.2 Background

In order to fully appreciate and understand the significance of the work presented in this thesis, the reader will be provided with an background of the anatomy of the eye, the role of nitric oxide in outflow physiology and how it is involved in aqueous outflow regulation.

1.2.1 Anatomy of the Aqueous Humour Outflow Pathway

The human eye is pressurised by a transparent fluid, called aqueous humour (AH), which provides nutrients to the avascular tissues in the anterior chamber of the eye. This fluid is secreted by the ciliary processes in the posterior chamber of the eye, and flows through the pupil and circulates the anterior chamber before exiting the eye through either the conventional outflow pathway or the unconventional outflow pathway. The majority of the fluid drains through the 'pressure-dependent' conventional outflow pathway (also commonly referred to as the trabecular outflow pathway), which consists of the trabecular meshwork, juxtacanalicular connective tissue and Schlemm's canal (Figure.1.2A). The unconventional or uveoscleral outflow pathway only accounts for a small portion (approximately 10%) of the bulk aqueous outflow, and is considered as the 'pressure-insensitive' pathway[22,92].

Once the majority of the fluid has entered the conventional outflow pathway, it filters through the trabecular meshwork then crosses the inner wall endothelium of Schlemm's canal into its lumen, and flows circumferentially to its downstream collector channels that connect with the intra- and episcleral venous system (Figure.1.2B)[90]. As the AH is secreted at a near constant rate ($\sim$2.5μl/min) and the eye is considered as a closed system, it is the resistance of outflow system that determines the IOP in the eye. It should be recognized that in healthy individuals, IOP is maintained within a narrow range of pressures throughout their lifetime[50,127] despite IOP fluctuations caused by choroidal blood flow[124], and diurnal oscillations[138,139], in addition to other environmental factors. As previously mentioned, when the outflow resistance increases, the balance between AH production and AH outflow is compromised which leads to elevated IOP, the primary risk factor for developing primary open angle glaucoma (POAG). Thus, by identifying the mechanisms involved in maintaining IOP homeostasis, this would lead to more effective therapies for ocular hypertension and glaucoma.

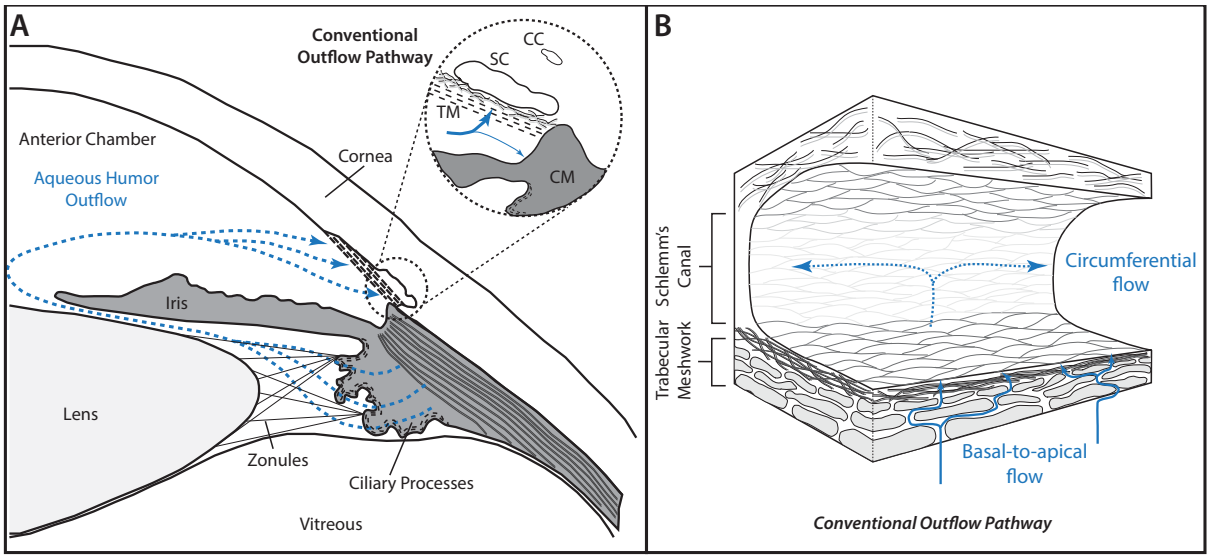


Figure 1.2: Schematic representation of the conventional outflow pathway in the human eye. **(A)** Aqueous humour (AH) is produced in the posterior chamber by the ciliary processes, which flows into the anterior chamber though the pupil and exits the eye by the iridocorneal angle (*dotted blue lines*). *(Inset)* The majority of AH leaves through the conventional outflow pathway that consists of the trabecular meshwork (TM) and inner wall of Schlemm's canal (SC), and into the downstream collector channels (CC); whilst a small portion of the fluid leaves through the iris root between the muscle fibers of the ciliary muscle (CM), commonly referred to as the unconventional outflow pathway (*narrow blue arrow*). **(B)** The conventional outflow pathway experiences a basal-to-apical directed flow, where the AH filters through the different layers of TM before crossing the inner wall endothelium of SC through transendothelial pores and drains circumferentially to the downstream episcleral venous system.

Unconventional Outflow Pathway

The unconventional or uveoscleral outflow pathway is considered as a major target for current anti-glaucoma therapies, although interestingly only contributes to a small portion of the bulk aqueous outflow ($\sim$ 10%). The uveoscleral pathway originally discovered in the mid-1960s by Bill[21], showed that the AH leaves the eye through the iris root by passing through the connective tissues and in between the muscle fibers of the ciliary muscle to the suprachoroidal spaces, from which it is drained through the sclera and lymphatic vessels[6,160,244]. Early works conducted by Bill and colleagues[21,22] have shown that the uveoscleral outflow is relatively insensitive towards elevations in IOP when compared to the trabecular pathway, hence why this route is often referred to as an "pressure-independent" pathway. This pressure insensitivity could be caused by the compression of the supraciliary and suprachoroidal space, which results in suppressed uveoscleral outflow[160].

Conventional Outflow Pathway

The conventional or trabecular outflow pathway consists of the trabecular meshwork (TM), the inner wall endothelium of Schlemm's canal (SC), and the downstream post-trabecular outflow pathway located in the iridocorneal angle (angle formed by the iris and cornea) that encircles the eye. It is within this network of tissue structures that provides the resistance to AH outflow, and helps maintain the IOP and structure of the eye.

Trabecular Meshwork

The trabecular meshwork consists of a network of connective tissue beams that encircles the anterior chamber, bridging the iridocorneal angle of the eye and terminates as it blends in with the stroma of the iris, ciliary body and scleral spur. The meshwork itself consists of three differentiated layers: (i) the uveal meshwork (UTM), (ii) corneoscleral meshwork (CTM) and (iii) juxtacanalicular meshwork (JCT; shown in Figure 1.3). The uveal and corneoscleral meshworks are porous structures composed of a series of trabecular beams or lamellae, which are made up of various collagen sub-types (mostly type I and III), elastic fibers and proteoglycans. The lamellae are lined with a

continuous monolayer of TM cells, that resides on a continuous basement membrane of extracellular matrix (ECM) consisting of collagen type IV, laminin and fibronectin[2,90]. The flow within the trabecular meshwork converges, as the intracellular spaces from the uveal meshwork (20 – 75 μm) towards the corneoscleral meshwork (5 – 20μm)[32] become progressively smaller, hence the meshwork acts like a 'filtration system' before the flow continues downstream to the Schlemm's canal and its collector channels.

Additionally, the trabecular cells have been documented to be phagocytic; this property allows them to ingest both endogenous and exogenous materials, which helps keep the trabecular outflow channels clear of potentially obstructive debris.[90,220] Because of the relatively high porosity of the uveal and corneoscleral meshworks, this portion of the TM does not contribute significantly towards outflow resistance. In contrast, the juxtacanalicular tissue (JCT, also called the cribriform meshwork) situated adjacent to the inner wall of SC is considered as a primary site(s) of resistance to AH in the eye. The JCT cells, unlike the TM cells from the uveal and corneoscleral meshwork, are arranged in an irregular network of ECM, which form a loose connective tissue consisting of a variety of macromolecules such as collagen IV, fibronectin, laminin, proteoglycans and glycosaminoglycans (GAGs)[2,220]. Underlying the JCT is a network of elastic fibers (cribriform plexus) arranged tangentially to the SC endothelium, which provide structural characteristics similar to those of the trabecular beams. These elastic-like collagen fibers extend from the ciliary muscle into the scleral spur, which attaches to the JCT and are closely connected to the inner wall of SC through the sheath material surrounding the fibers[186,222]. The cribriform plexus allows for the translation of mechanical forces from the ciliary muscle to the JCT and inner wall of SC. This is commonly experienced during accommodation of the lens or after treatment with cholinergic agents such as pilocarpine, which has been shown to affect the contractility of the ciliary muscle and effectively opens up the meshwork to increase aqueous humour outflow through the tethering of the cribriform plexus[14,136,145]. Interestingly, a small portion of TM cells have been shown to stain positive for α-smooth muscle actin, mainly residing in the scleral spur insertion site suggesting that the TM cells possess contractile properties similar to vascular smooth muscle cells[61,220]. Furthermore, the elastic fibers from the scleral spur are continuous and extends into the TM beams and cribriform plexus in the JCT, changes in the scleral spur cell tone would likely modulate the contractility function of the TM, and thus alter the trabecular outflow resistance[140,220].

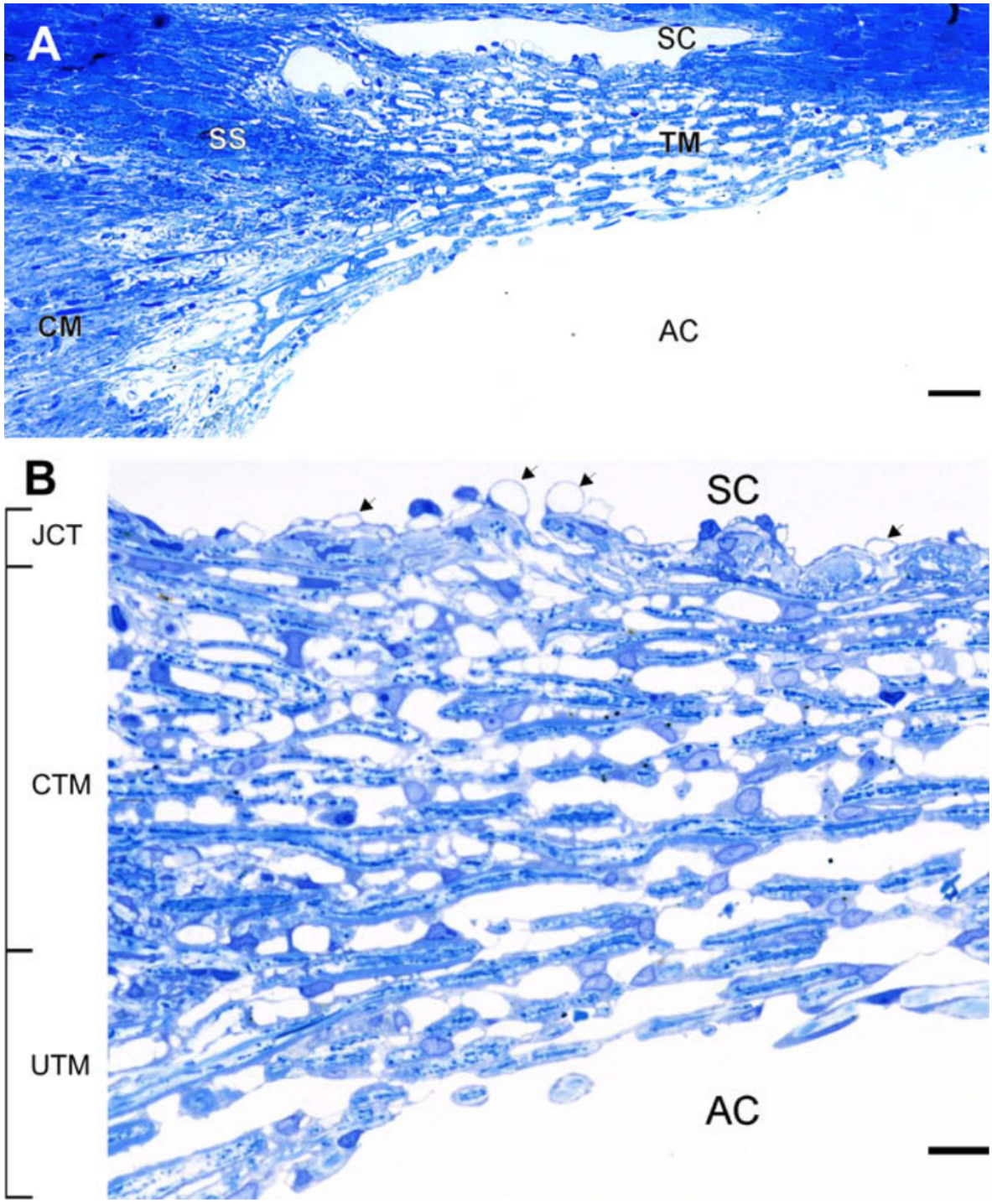


Figure 1.3: Light micrograph of a meridional section through the trabecular meshwork. (B) is a magnification of (A). In the plane of this section, Schlemm's canal (SC) has two lumens that are separated by a septum. TM: Trabecular meshwork; SS: Scleral spur; CM: Ciliary muscle; AC: Anterior chamber; JCT: Juxtacanalicular tissue; CTM: Corneoscleral trabecular meshwork; UTM: Uveal trabecular meshwork. Arrows in B point to giant vacuoles in the inner wall endothelium of SC. Magnification bars: 20 μm (A), 5 μm (B). Reproduced with permission from: Tamm, ER. The trabecular meshwork outflow pathway: Structural and functional aspects. *Experimental Eye Research* **2009**, 88: 648-655.[220]

Schlemm's Canal Endothelium

The Schlemm's canal is a elliptical vessel that runs circumferentially around the eye, located within the iridocorneal angle adjacent to the JCT, and is considered as the final barrier to the drainage of AH in the conventional outflow pathway. The SC lumen directly connects to the downstream collector channels and fuses with the downstream venous system of the eye[90]. Interestingly, the inner wall of SC is lined with vascular-derived endothelial cells joined together by tight junctions to form a continuous monolayer along the longitudinal axis of the canal, and is supported by a discontinuous basement membrane.[69,90] Even though SC is a vascular-derived vessel, the inner wall endothelia possess several unique features unlike most other endothelia. Firstly, the SC endothelial cells experience a pressure gradient across the inner wall in the basal-to-apical direction which pushes the cells off their basal lamina. As a result, the endothelium forms cellular outpouchings (known as giant vacuoles; GVs) which distends into the lumen of SC and effectively narrows the canal[120,225] (Figure 1.4). These so-called giant vacuoles are highly pressure-dependent, and act as 'smart one-way' valves to AH flow. Giant vacuole formation are highly dynamic and undergoes large cellular strains due to the direction of AH and pressure drop across the inner wall[28,69,166,170]. This leads to the formation of micron-sized pores in the endothelial monolayer to allow for the drainage of AH.

Secondly, the SC endothelia possesses unusually high hydraulic conductivity, in other words, low flow resistance, similar to that of the renal glomerulus[69]. It is theorized that the dynamic behavior of these SC endothelial cells are responsible for regulating the hydraulic conductivity of the conventional outflow pathway, mainly through the formation of transendothelial pores in the SC endothelium. These pores can form through two main pathways: (i) transcellularly through individual cells (known as "I-pores"), through the fusion of the apical and basal cell membranes[28] or the disruption of fusogenic proteins involved in the formation of "mini-pores"[108], and (ii) paracellularly through the disassembly of junctional complexes between neighboring cells (known as "B-pores")[68,71]. Once the AH has crossed the JCT/SC barrier, the fluid drains circumferentially towards the collector channels (CC) and aqueous veins, which pools together the AH at the site of the deep intrascleral venous plexus (DIVP) and enters the vascular circulation, or connects directly to the episcleral veins[32,90,227].

Finally, the developmental origin of the SC endothelia has been a long-standing subject of debate. The SC endothelial cells (SCECs) have drawn comparisons from both blood endothelial cells (BECs) and lymphatic endothelial cells (LECs), and thus may explain the unique properties of the SC vessel[185]. Recent studies have identified the molecular phenotypes involved in the development of SC, indicating that transcription factor prospero-related homeobox1 (PROX1) and vascular endothelial growth factor receptor 3 (VEGFR-3) are expressed in both developing and mature SC in mice, both of which are key regulators of lymphatic fate[12,126,226]. In addition to lymphatic markers, the SC also expresses vascular endothelial markers CD31[2] and vascular endothelial cadherin (VECAD)[73,106]. Taken together, the SC is considered to have characteristic traits of both BECs and LECs, thus the SC endothelium may modulate AH flow through similar mechanosensory signaling pathways to maintain IOP homeostasis in the eye.

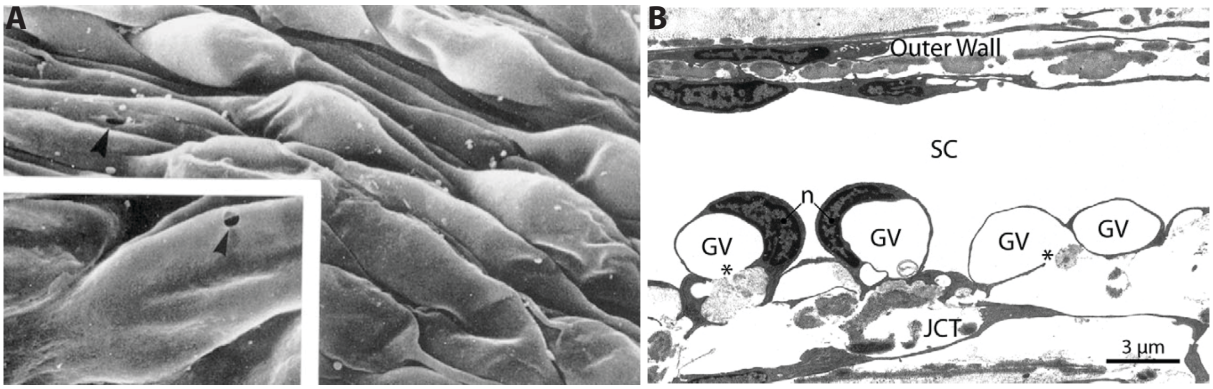


Figure 1.4: (A) Scanning electron micrograph of the inner wall of Schlemm's canal as seen from the canal lumen. *Arrowhead* shows a pore and inset shows high magnification image of pore. **(B)** A transmission electron micrograph showing giant vacuoles (GVs) along the inner wall endothelium of Schlemm's canal (SC). The classic "signet ring" appearance is particularly well exhibited by the second giant vacuole from the left where the cell appears as a thin, continuous lining around the giant vacuole cavity with the nucleus (n) bulging to one side. The first and third giant vacuoles from the left have basal openings or "meshwork pores" (asterisks) where, presumably, aqueous humour enters the giant vacuole cavity from the underlying juxtacanalicular tissue (JCT). Note that the endothelial cells on the outer wall of Schlemm's canal, which is not typically involved in aqueous humour filtration, are flat. Reproduced with permission from: Overby, DR et al. The changing paradigm of outflow resistance generation: Towards synergistic models of the JCT and inner wall endothelium. *Experimental Eye Research* **2009**, 88: 656-670.[166]; Pedrigi, RM et al. A model of giant vacuole dynamics in human Schlemm's canal endothelial cells. *Experimental Eye Research* **2011**, 92: 57-66.[170]

Post-Trabecular Pathway: Limbal Vasculature

The post-trabecular outflow pathway consists of a complex network of micro-vessels that connect the outer wall of SC to the downstream episcleral veins and conjunctival vessels. This network of limbal vessels help transport the AH back towards the venous circulation[227]. Once AH

[2] Also commonly referred to as platelet endothelial cell adhesion molecule-1 (PECAM-1)

has crossed the inner wall endothelium of SC into its lumen, the fluid flows circumferentially towards the downstream collector channels and aqueous veins, where it reconnects with the venous system (Figure 1.5). In the human eye, there are approximately 20–30 collector channels or aqueous veins present, which are non-uniformly distributed around the circumference of the eye[101,103]. Collector channels drains AH from the SC lumen into the deep intrascleral venous plexus, where it can then either directly join the venous circulation or continue to flow towards the deeper venous plexi (mid and deep venous plexus), where it eventually connects with the perilimbal vessels or episcleral veins[90,227]. In contrast, the aqueous veins connect the SC directly to the episcleral veins, bypassing the intermediary venous plexi. Interestingly, these collector channels also possess similar contractile properties to TM cells, as the vessels are surrounded by smooth muscle cells[54] that may control the intrascleral vessel dimensions to influence the post-trabecular or distal outflow resistance downstream of SC[188]. Additionally, the post-trabecular pathway has been shown to account for approximately 25% of the outflow resistance in human eyes[93,116], suggesting that the distal outflow resistance may also play a regulatory role in aqueous humour outflow.

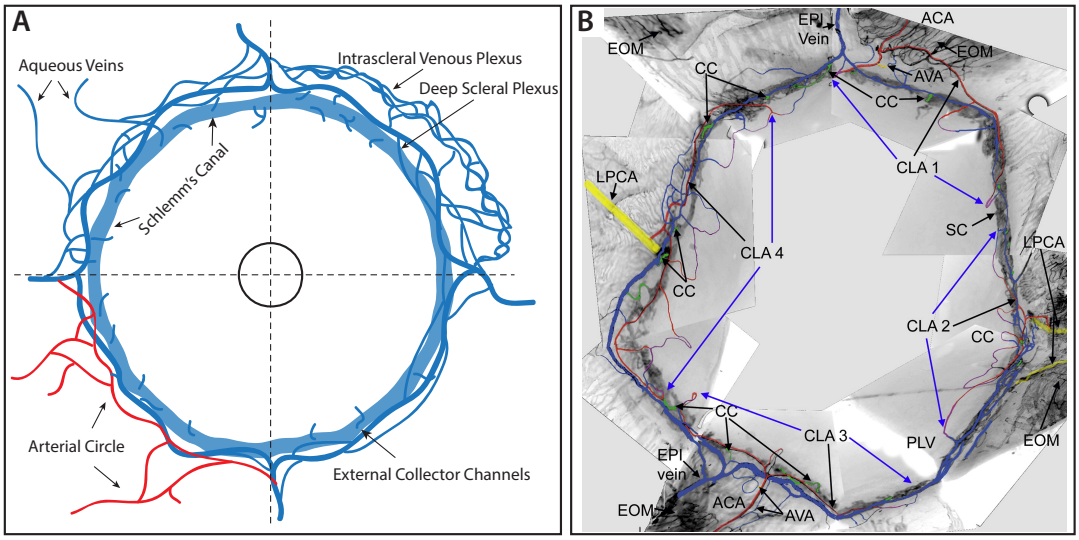


Figure 1.5: Post-trabecular aqueous humour outflow pathway. **(A)** Schematic representation of the post-trabecular outflow pathway. **(B)** Three-dimensional reconstruction of the limbal vessels of a normal mouse eye. All limbal aqueous and blood vessels are detected in this reconstructed image of PECAM-1 immunostained corneoscleral wholemount from an ICR WT mouse. The lateral boundaries of each image segment have been digitally transformed to show the continuity of vessels around the limbus. Each of the vessel phenotypes were traced and colour-washed to show their anatomical relationship with one another. The anterior ciliary (ACA) and circular limbal arteries (CLA) are indicated in red. The veins of the perilimbal plexus (PLV) and those associated with the episclera (EPI veins) are indicated in blue. Corneal arcades arising off the CLA are in red and become blue where they anastomose with veins of the PLV. Schlemm's canal (SC) is in grey and collector channels/aqueous veins (CC) are indicated in green. The long posterior ciliary artery (LPCA) is indicated in yellow and arterial branches that feed the CLA segments are clearly seen. Arteriovenous anastomoses (AVA) are indicated in the superficial limbus. Reproduced with permission from: van der Merwe, EL et al. The three-dimensional organisation of the post-trabecular aqueous outflow pathway and limbal vasculature in the mouse. *Experimental Eye Research* **2014**, 125: 226-235.[228]

1.2.2 Glaucoma

Glaucoma is a group of progressive optic neuropathies characterized by the irreversible damages caused to the retinal ganglion cells (RGCs) and their axons at the site of the optic nerve head. The loss of RGCs leads to progressive loss of vision and onset of irreversible blindness[176,235]. Elevated intraocular pressure (IOP) is commonly associated with the development of glaucoma, where increases in IOP causes mechanical insult to the RGCs through the deformation of the lamina cribrosa resulting in cell death[202]. Glaucoma is the world's leading cause of irreversible blindness, affecting more than 60 million people worldwide, of which 8.4 million are bilaterally blind[176]. Two of the most prevalent forms of glaucoma are primary open angle glaucoma (POAG) and angle-closure glaucoma (ACG).[177] POAG is the variant of glaucoma that poses the most interesting biological question – what are the mechanism(s) responsible for the increase in outflow resistance in the eye?

The elevation of IOP is the primary risk factor for POAG, but the mechanism(s) responsible for ocular hypertension remains unclear. Current treatments of ocular hypertension aim to lower IOP, through either surgical or drug interventions to postpone the progression of vision loss. Majority of pharmacological agents used to lower IOP target the uveoscleral pathway, with either muscarinic agonists (pilocarpine) or prostaglandin analogues (latanoprost)[6], both treatments affect the ciliary muscle tone to increase AH outflow. Alternatively, beta-blockers (timolol) and carbonic anhydrase inhibitors[234,235] have also been used to reduce AH production to help lower IOP. However, these therapies are often unable to achieve a sustained IOP reduction, largely because the treatments do not target the underlying root cause of elevated IOP; increased outflow resistance of the conventional outflow pathway. Thus, identifying the physiological mechanism(s) responsible for the increased outflow resistance in the conventional outflow tract would provide more targeted and efficacious glaucoma therapies.

1.2.3 Aqueous Humour Dynamics

The eye is considered as an closed system, where IOP is determined by the balance between aqueous humour production (F_p) and drainage (F_d), such that at steady state $F_p = F_d$. AH outflow (F_d) is more accurately represented by the 'pressure-dependent' conventional outflow (F_c)

and the 'pressure-independent' unconventional outflow (F_u). Additionally, the AH outflow is determined by the difference in pressure between the anterior chamber (IOP) and the downstream episcleral venous pressure (EVP), and the rate at which the fluid drains the eye is determined by the resistance of the conventional outflow pathway (R_c). Therefore, the governing equation is defined by the following relationship, known as the Goldmann's Equation is shown below[33]:

$$F_{\mathrm{p}} = \frac{(IOP - EVP)}{R_{\mathrm{c}}} + F_{\mathrm{u}} \tag{1.1}$$

This relationship could also be expressed as a function of outflow facility of the conventional pathway (C), which is defined as the inverse measure of outflow resistance, as shown below:

$$F_{\mathrm{p}} = C \times (IOP - EVP) + F_{\mathrm{u}} \tag{1.2}$$

The Goldmann's equation can also be re-arranged as a function of IOP, as shown below:

$$IOP = \frac{(F_{\mathrm{p}} - F_{\mathrm{u}})}{C} + EVP \tag{1.3}$$

1.2.4 Outflow Resistance Generation

Elevated intraocular pressure has been identified as the primary risk of factor for the development of POAG for over a century now. Yet the underlying mechanism(s) responsible for regulating the outflow resistance in the conventional outflow pathway are still inconclusive. It is widely accepted that the majority of the outflow resistance lies within the vicinity of the JCT and inner wall region of Schlemm's canal, even though numerous pharmacological and morphometric studies have been unable to attribute the bulk resistance to any one of these tissues[23,97,98,166]. The outflow resistance generated by the uveal and corneoscleral meshworks are considered negligible due to its

highly porous structures[32,90,116]. Grant and colleagues[93,188] have shown that by surgically removing the uveal and corenoscleral meshworks did not significantly affect the outflow resistance in enucleated human eyes. In contrast, when the entire JCT and inner wall of SC were removed, the overall outflow resistance was reduced by approximately 75%, suggesting that the majority of the outflow resistance was generated by the JCT and inner wall region[93]. Mäepea and Bill[146] also showed that 50% or more of the outflow resistance lies within close vicinity of the JCT and inner wall. Furthermore, the presence of giant vacuoles and pores in the SC endothelium cell layer only accounts for 10% of the outflow resistance[72]. The distal resistances generated by the collector channels and aqueous veins are also unlikely to generate significant resistance due to their large vessel diameters (50 μm)[227]. Taken together, this suggests that the resistance generated in the outflow pathway is not as straightforward as adding the resistances of each tissue layer together; thus suggesting that there must be some form of interaction or "hydrodynamic coupling" between the tissue structures, in particular, the JCT, basement membrane and inner wall of SC to account for the bulk of outflow resistance. This hydrodynamic coupling between the different tissue layers is supported by the *"funneling model"*[116,166].

1.2.5 Outflow Resistance: Synergistic Model

Hydrodynamic Coupling

The funneling model, originally theorized by Johnson and colleagues[118], is considered as the primary synergistic model of outflow resistance generation in the eye. It is believed that pores in the inner wall endothelium ($\sim$micron sized) are separated by an average distance of 20 – 30 μm[166], which implies that flow towards the inner wall are preferentially directed towards the regions in the JCT close to a pore. In addition, Ethier *et al.*[72] has suggested that the JCT by itself does not generate significant outflow resistance, unless the openings are filled with glycosaminogylcans (GAGs) a major ECM component found in the TM. This suggests that GAGs and other ECM components may control the spacing between the trabecular lamellae, and thus the outflow resistance of the JCT. Therefore, by factoring in the JCT filled with extracellular matrix gel and the presence of downstream pores, it is likely that the flow distribution in the JCT becomes non-uniform as AH funnels toward the pores[166]. Furthermore, in human organ cultured eyes perfused with purified matrix

metalloproteinases (MMPs), enzymes that digest ECM molecules, resulted in an increase in outflow facility. Whilst the inhibition of endogenous MMP activity reduced outflow facility, thus supporting the role of ECM in outflow resistance generation in the TM[30].

Mechanical Coupling

As previously mentioned, the hydrodynamic coupling between each tissue strata may account for the outflow resistance, but unfortunately does not take into consideration the mechanical forces experienced by these tissue structures. The JCT and inner wall endothelium experiences a basal-to-apical pressure drop as AH crosses the outflow pathway. This imposes a mechanical load on the tissues, which causes morphological changes to the JCT and inner wall. In order for these tissues to withstand these forces induced by changes in IOP, structural attachments must exist to hold the subsequent tissues in place. Johnstone and Grant[120] first described the concept of mechanical tethering between the JCT and inner wall by examining their morphological changes in response to increasing IOP in human and monkey eyes. At low IOP, the inner wall endothelium is relatively flat and the lumen is open allowing AH to flow through (Figure 1.6A). As IOP increases, the JCT expands and pushes the inner wall endothelium into the lumen, and results in the formation of GVs. This leads to the narrowing and partial collapse of the SC, reducing the cross-sectional area of the lumen, which in turn increases the outflow resistance in the meshwork (Figure 1.6B). These results show that the JCT and inner wall responds to elevations in IOP in a pressure-dependent manner, and that changes in SC lumen dimensions are highly dependent on IOP.

The mechanical coupling of the JCT and inner wall exists through multiple mechanisms. Johnstone[119] showed that cell-cell tethering exists between the two subsequent tissue layers, whereby cytoplasmic processes from the SC cells anchors itself to the processes from the JCT cells. Additionally, studies have shown that adherens junctions, in particular VE-cadherin and CD31 are abundantly expressed in the SC cells at the inner and outer wall[106,172,230]. Thus, suggesting cell-cell tethering and junctional proteins may also be involved in the regulation of outflow facility. Consistent with this notion, Lu *et al.*[143] showed in bovine eyes perfused with a rho kinase inhibitor (Y27632), increased outflow facility by promoting cell relaxation through disassembly of actin stress fibers and focal adhesions. In the same study, the Y-27 also caused an increase in separation length

along the inner wall of the aqueous plexus (AP; analogous to human SC) from its underlying substratum. This disassociation in cell-cell or cell-ECM tethering introduces intercellular space between the two resistance sites, thus reducing the resistance and allowing more uniform flow to occur. Thus, suggesting that the aqueous outflow resistance is governed by this synergistic model, and that the hydrodynamic and mechanical interactions between the different tissues (SC endothelium, basement membrane and JCT) are crucial for regulating outflow.

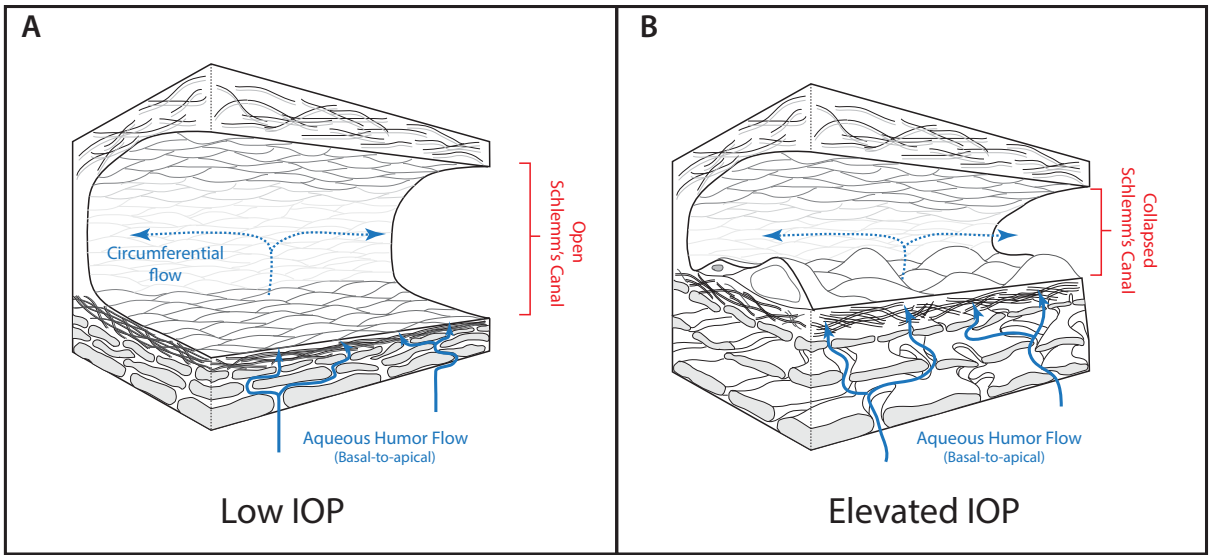


Figure 1.6: Schematic representation of the collapse of the Schlemm's canal in the human eye. The conventional outflow pathway experiences a basal-to-apical directed flow, where the AH filters through the different layers of TM before crossing the inner wall endothelium of SC through transendothelial pores and drains circumferentially to the downstream episcleral venous system. **(A)** At low IOP, the SC lumen is relatively flat and open. **(B)** At elevated IOP, the pressure-dependent giant vacuoles form and distend into the SC lumen resulting in a collapsed canal. *Solid blue lines: transendothelial flow, Dashed blue lines: circumferential flow.*

1.2.6 Segmental Flow of the Outflow Pathway

Aqueous humour filtration has long been recognized as non-uniform or "segmental" around the circumference of the outflow pathway, such that only a fraction of the total area of the JCT and inner wall of SC are actively involved with the drainage of AH at any given time. The mechanism(s) responsible for this segmental flow behavior are still not well understood. Previous studies have used tracers such as cationic ferritin[53,70,100] and fluorescent microspheres[102,123,143,231] to decorate and identify preferential drainage routes in the trabecular outflow tract, which are separated into "high flow" and "low flow" regions (as shown in Figure 1.7)[42]. These regions of preferential flow in the TM are commonly referred to as the "effective filtration area" (EFA), which are active portions of the meshwork involved in the filtration of AH. Studies have suggested that segmental filtration patterns

are likely associated with regional variations in ECM proteins residing in the JCT. Previous studies have shown that tracer patterns in the TM tend to correlate with the distribution of ECM proteins in the trabecular outflow tract, in particular, versican[2,123,231] and SPARC (secreted protein acidic and rich in cysteine)[218]. Interestingly, in human organ cultured eyes perfused with fluorescent tracers, the flow patterns were inversely correlated with the distribution of versican in the TM[123]. Whilst in a separate study, researchers found that in SPARC-null mice, the tracer patterns in the TM were more uniformly distributed when compared against wild-type littermate controls[218]. Furthermore, the inhibition of GAG biosynthesis in both porcine and human organ cultured eyes dramatically increased outflow facility by 3-fold and 1.5-fold, respectively[122]. Taken together, these studies suggest that ECM proteins and GAGs play a crucial role in regulating the local hydraulic conductivity of the JCT/inner wall, and areas of higher ECM deposits tend to correlate with regions of lower tracer labeling.

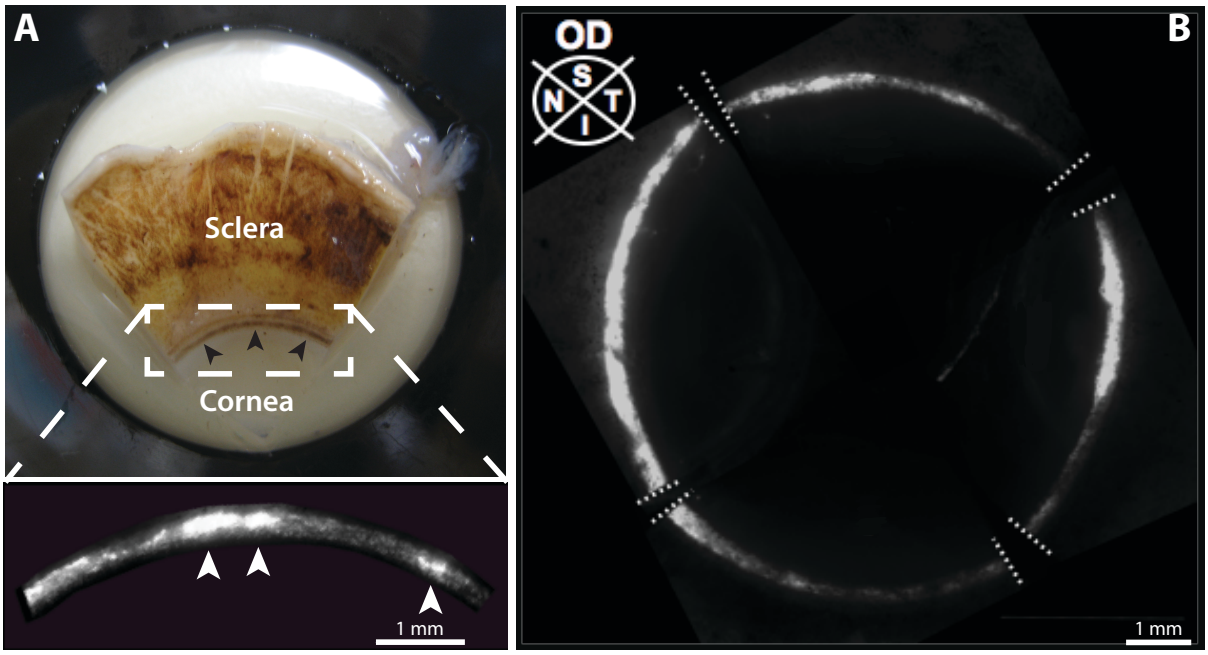


Figure 1.7: (A) Macro-scale tracer image shown segmental filtration patterns (arrowheads) in the trabecular meshwork of an enucleated human eye perfused with fluorescent microspheres. **(B)** Four images, each containing one quadrant, were pieced together and displayed on the same intensity scale. Dotted lines indicate where quadrants were cut. *S, superior; T, temporal; I, inferior; N, nasal; OD, right eye.* Reproduced with permission of the authors and the publisher[42].

Alternatively, segmental flow patterns could also be attributed to variable mechanical tethering between the inner wall endothelium and the basement membrane or JCT, which could lead regional variations in flow distribution (as previously mentioned in Chapter 1.2.5). Morphological changes in the outflow tract have been associated with the segmental outflow patterns in

bovine[17,143], monkey[144], and human[102,242] eyes, where regions of higher tracer accumulation coincided with areas of greater separation between the SC endothelia and the underlying JCT. The increased separation between the subsequent tissue layers effectively uncouples the hydrodynamic influence of the inner wall, which has been described to eliminate the funneling effect and decrease outflow resistance, leading to a more uniform flow distribution though the JCT[166]. Other factors such as the non-uniform distribution of collector channels along the circumference of the eye[101,103], and possible variable distal resistances of the episcleral venous system may also contribute towards the segmental flow patterns in the JCT. Prior reports have shown that in both bovine[17] and human[42,102] eyes, tracer patterns tend to coincide with the distribution of collector channel ostia, accumulating in regions of lower downstream resistance (as shown in Figure 1.8)[42].

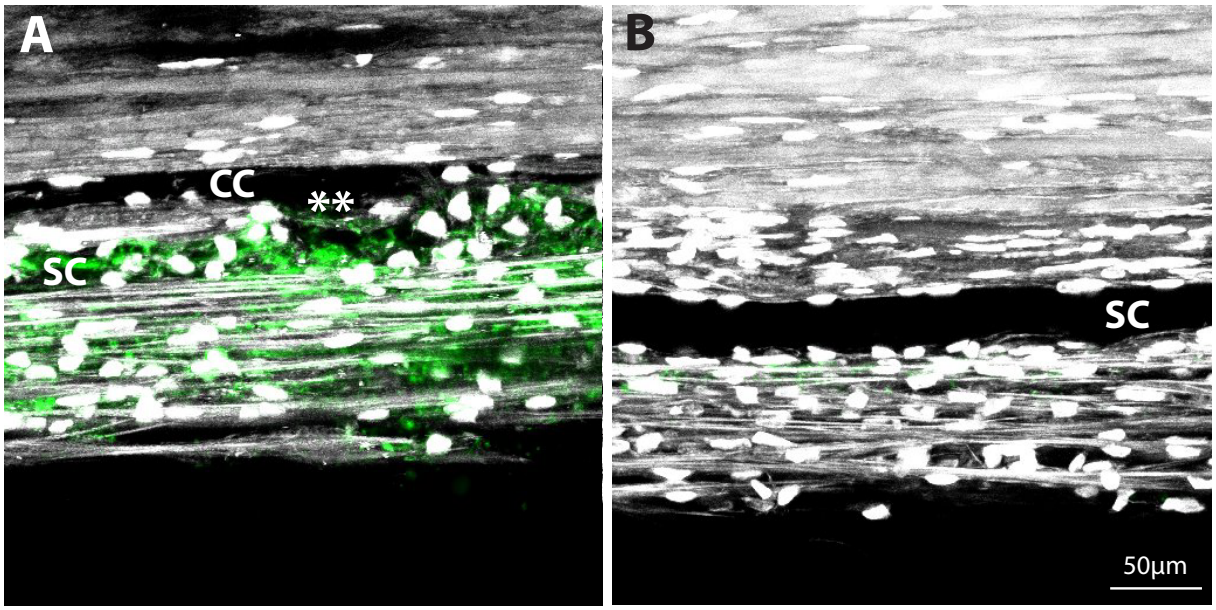


Figure 1.8: Micro-scale tracer images showing segmental filtration patterns in the JCT and inner wall (IW) endothelium of SC of an enucleated human eye perfused with fluorescent microspheres. **(A)** High flow region of the JCT/IW with the presence of collector channel ostia (*). **(B)** Low flow region of the JCT/IW with no observed presence of collector channels. *SC, Schlemm's canal; CC, collector channel.* Reproduced with permission of the authors and the publisher[42].

Taken together, these data suggests that segmental flow in the TM occurs over two different length scales: (i) the macro scale (order of mm), and (ii) the micro scale (order of several μm). At the macro-scale, the bulk flow preferentially drains towards regions of lower downstream resistance, which are influenced by the distribution of collector channel ostias along the SC. Whilst at the micro-scale, the ECM accumulation and morphology of the inner wall of SC influences the local filtration function of the outflow pathway, which results in segmental distribution of AH. Currently, it remains to be determined whether segmental distribution at the macro- and micro-scales are coupled, and whether segmental flow patterns is considered as a static or dynamic process[42].

One plausible hypothesis is the presence of an endogenous feedback loop that detects changes in IOP and regulates the local hydraulic conductivity of the outflow pathway, partly through NO signaling to help restore IOP homeostasis, analogous to the vascular system. Stamer *et al.*[211] originally hypothesized that the conventional outflow pathway acts as a mechano-regulatory system, whereby changes in IOP expands the JCT and pushes the inner wall of SC into the lumen, which effectively narrows the canal lumen. This in turn increases the shear stress acting on the SC endothelial cells, increasing NO production which feeds back into the outflow pathway as an autocrine/paracrine signaling molecule to modulate the local resistance sites. Interestingly, in a prior study conducted by Ethier *et al.*[73] showed that the calculated theoretical wall shear stresses in the SC are comparable to those experienced by the arterial system. Recent studies have also demonstrated that SC cells secrete NO in response to elevated shear stress[11,135], similar to vascular endothelial cells[44,45]. Therefore, in this scenario, increased shear stress in the SC up-regulates the NO production, which is then convected downstream towards the collector channel ostias. This predicted elevation in NO concentration near the collector channel ostias may affect the local hydraulic conductivity, and thus explain the segmental outflow patterns that tends to coincide with these regions. In contrast, if large areas of the TM/JCT are starved of flow, this would result in decreased shear stress and NO levels, which would further exacerbate the local outflow resistance contributing to increased IOP and ocular hypertension[211].

This proposes several interesting questions: **(i)** what is the role of NO signaling in the conventional outflow pathway? **(ii)** Does NO signaling contribute towards the spatial distribution of segmental outflow in the eye? **(iii)** Can NO be utilized as a potential therapeutic for treating ocular hypertension and glaucoma? In order to effectively address these questions, we need to first gain an understanding of how NO is synthesized and how it functions as a signaling molecule and its effects on biological systems, as described in the following section.

1.2.7 Role of Nitric Oxide in Outflow Physiology

Nitric Oxide as a Signaling Molecule

Nitric oxide (NO) is a diatomic free radical and an important signaling molecule, that is responsible for mediating various physiological functions across multiple biological systems; these include the modulation of vascular tone[153–155,232], neuronal signaling[31,52] and immunological processes[74]. NO is synthesized by a family of enzymes, called nitric oxide synthases (NOS), which catalytically convert the amino acid L-arginine to NO and L-citrulline through a two-step oxidation process[80]. NOS enzymes are differentiated into three main types, endothelial NOS (eNOS), neuronal NOS (nNOS) and inducible NOS (iNOS), all of which are expressed in mammalian tissues. The active form of these enzymes are composed of heme-bound homodimers that transfer electrons from nicotinamide-adenine-dinucleotide phosphate (NADPH) to its co-factors (flavin adenine dinucleotide (FAD) and flavin mononucleotide (FMN)) and the heme moieties, where the substrate L-arginine is oxidized to L-citrulline and NO[5,80].

The activity of all isoforms of NOS are mediated through calmodulin-binding. Thus, constitutively expressed eNOS and nNOS activity are regulated by intracellular calcium (Ca^{2+}) levels. Typically between 200 nM – 400 nM of Ca^{2+} is required to initiate calmodulin-binding to the enzyme[80]. Both eNOS and nNOS produce low basal levels of NO which are regulated by receptor-mediated signaling pathways to maintain physiological functions (described in more detail below). In contrast, iNOS expression is considered calcium-insensitive, as calmodulin binds to iNOS with extremely high affinity even at low intracellular Ca^{2+} levels (<40 nM)[80]. iNOS is typically expressed in response to inflammatory stimuli such as endotoxins and cytokines, producing NO as a important defense mechanism against pathogens[56,81,154,167].

NO is produced and released by many cell types in the body, where it can act as an autocrine or paracrine signaling molecule to target a number of enzymes and proteins[81]. The biochemical reactions of NO under physiologically relevant conditions can be simplified to three main categories: the activation of guanylate cyclase, responsible for signal transduction; the conversion to peroxynitrite ($ONOO^-$) after reacting with superoxide (O_2^-), responsible for post-translational modifications of

proteins such as S-nitrosothiols and 3-nitrotyrosines; and the scavenging of NO by oxyhemoglobin (Hb-O_2) to form nitrates[19,167,182]. The most physiologically relevant signaling pathway stimulated by NO is the activation of soluble guanylate cyclase (sGC) and the generation of cyclic guanosine 3'-5' monophosphate (cGMP)[19,56,80,81]. Nanomolar levels of NO binds to the heme moiety on the β-subunit of sGC to activate the enzyme. This activation of sGC results in the conversion of guanosine 5'-triphosphate (GTP) to cGMP, increasing the levels of intracellular cGMP, which interacts with various cyclic-nucleotide gated ion channels, protein kinase G (PKGs) and phosphodiesterases (PDEs) to elicit physiological effects[55,56,81].

NO can also elicit other biological effects through cGMP-independent pathways such as post-translational modification of proteins via S-nitrosylation, in which the NO moiety is coupled to a reactive cysteine thiol to form S-nitrosothiols. This has been shown to play a role in cellular signal transduction and provides a mechanism for redox-based physiological regulation[109,148]. In addition, strong oxidants such as superoxide can react with NO to form peroxynitrite, resulting in the nitration of the phenol moiety of tyrosine residues and the formation of 3-nitrotyrosine[19,184,219]. The processes of S-nitrosylation and nitration have been shown to affect the function of various proteins under both physiological and pathophysiological conditions[19,148,208]. Therefore, it is crucial to gain an understanding of how NO regulates vascular tone and potentially how endothelial dysfunction may contribute towards the pathogenesis of glaucoma[121,141,174,191,192].

The vascular endothelium is regulated by various signaling molecules and hormones, which includes NO and endothelin-1 (ET-1), which act as opposing vascular modulators that help maintain the vascular tone, endothelial permeability and general physiological function of the vascular system.[153–155,232] NO, as previously mentioned, activates sGC to increase intracellular cGMP which interacts with various downstream cellular targets to elicit physiological effects, including the most common vasodilatory effect on blood vessels. In contrast, ET-1, is a potent vasoconstrictor secreted by vascular endothelium and acts as an inhibitor of endothelial permeability[162,241]; together NO and ET-1 help maintain vascular homeostasis. Interestingly, previous studies have shown that patients with normal tensive glaucoma (NTG) have impaired blood flow in their forearms when compared to age-matched controls.[35,107,214,215] Furthermore, increased plasma and aqueous levels of ET-1 have been detected in patients with primary open-angle glaucoma[67,161], which would induce vasoconstriction of the blood vessels and decrease endothelial permeability. These results suggest that

the pathogenesis of glaucoma may be associated with a systemic vascular endothelial dysfunction, which could cause an imbalance between NO and ET-1 levels resulting in the lack of vasodilation in the vessels.

In the context of outflow physiology, previous studies have also used NADPH-diaphorase as an indicator of NOS activity, to label and identify NO production sites in the conventional outflow pathway of human donor eyes[157,158]. Interestingly, the NADPH-diaphorase labeling was enriched in the major outflow resistance sites, which included the trabecular meshwork, inner wall of Schlemm's canal endothelium and the downstream collector channels; whilst decreased NADPH-diaphorase labeling has been reported in glaucomatous eyes[157]. Additionally, genome-wide association studies have linked polymorphisms in the *NOS3* gene that encodes eNOS to the pathogenesis of glaucoma[121,141,174]. Taken together, these data suggests that endogenous NO production within the conventional outflow pathway by NOS enzymes may play a regulatory role in maintaining IOP homeostasis, and impaired NO signaling may in part lead to outflow dysfunction in glaucoma.

NO Production and Cellular Response

To fully appreciate how endogenous NO signaling may influence outflow facility and IOP regulation, an understanding of how NOS enzymes are activated and regulated under physiological conditions is required. Here we will be focussing on eNOS in particular, as it has been previously reported to be the primary isoform expressed in the human outflow pathway[158] and polymorphisms in the *NOS3* gene have been linked to the pathogenesis of glaucoma[121,141,174]. Therefore, eNOS may play a regulatory role in aqueous humour dynamics. As previously mentioned, constitutively expressed eNOS is activated by an increase in intracellular Ca^{2+} that leads to enhanced binding of calmodulin to the enzyme. This facilitates the flow of electrons from NADPH in the reductase domain to the heme moiety in the oxygenase domain of the homodimers. However, eNOS can also interact with several other proteins such as heat shock protein 90 (hsp90)[85], G protein-coupled receptors (GPCRs)[91] and caveolin-1[209], resulting in either the inhibition or stimulation of NOS activity. The location of eNOS within the cell can also determine its activity. When the enzyme is located within the caveolae it can readily bind to caveolin-1, which has been shown to function as a negative regulator or inhibitor of eNOS activity[80,94,196,209]. Whilst calmodulin and hsp90 binding to

eNOS dissociates caveolin-1 from eNOS and activates the enzyme[94].

Mechanical stimuli such as fluid shear stress has also been shown to activate and mediate eNOS activity[58,91,201], by activating various receptor-mediated pathways including the activation of the phosphatidylinositol-3-OH kinase (PI(3)K) and downstream effector serine/threonine kinase Akt/PKB[3] pathway. Shear stress acting on endothelial cells results in the phosphorylation of eNOS by PI(3)K/Akt-dependent pathway at serine 1177, which stimulates the flux of electrons to the reductase domain, resulting in increased sensitivity to Ca^{2+} and enzyme activity[59,82]. eNOS can also be phosphorylated at theronine 495, which functions as a negative regulatory site to decrease the electron flux whilst also interfering with calmodulin-binding domain to decrease the enzyme's activity[78,80]. Hence, eNOS activity *in vivo* is mediated in part by shear stress induced phosphorylation of the enzyme. As previously mentioned, we theorise that the conventional outflow pathway functions as a mechano-regulatory system, whereby changes in IOP expands the JCT and pushes the inner wall of SC into the lumen effectively narrowing the canal lumen. This narrowing of the SC lumen would lead to an increase in shear stress experienced by the SC endothelial cells, hence up-regulates eNOS expression and leads to increased NO production. NO being a free radical gas can rapidly diffuse across cell membranes to affect the biological activity of several proteins and enzymes, to elicit an physiological response by mediating the outflow resistance sites to enhance outflow facility and lowering IOP.

The precise mechanisms of how NO affects outflow facility and IOP remains unclear, but likely involves mechanisms related to cellular contractility and endothelial permeability. NO is considered as the "messenger" or signaling molecule that initiates the sGC/cGMP/PKG signaling pathway. One of the most important physiological responses to the activation of this signaling cascade, is the vasodilatory effects on smooth muscle cells in the cardiovascular system mediated through its cellular contractile properties; crucial for maintaining vascular tone[81]. It has been well established that NO elicits smooth muscle relaxation by regulating intracellular Ca^{2+} levels, myosin light chain phosphorylation and BK_{Ca} channels[81]. Interestingly, in the conventional outflow pathway, the ciliary muscle, trabecular meshwork and downstream collector channels all possess similar contractile properties to vascular smooth muscle cells, expressing common contractile proteins such as α-smooth muscle actin and smooth muscle myosin[54,79,236].

[3] PKB = Protein kinase B

Previous studies have shown that in isolated bovine TM strips, pre-contracted with carbachol, when treated with NO donors and cGMP analog (8-br-cGMP; 8-bromoguanosine 3'5'-cyclic monophosphate sodium salt) it reversed the effect of carbachol-induced contraction of the TM strips and relaxed the TM cells[236,237]. In human TM cells, NO has also been shown to not only induce relaxation of TM cells[61], but also decrease TM cell volume through the activation of BK_{Ca} channel[60]. Furthermore, a reduction in phosphorylated myosin light chain was detected in TM cells treated with NO donors when compared against vehicle-controls[61]. Consistent with this notion, downstream collector channels are also surrounded by smooth muscle cells[54]. Therefore, NO production in the SC and downstream collector channels, could potentially control the intrascleral vessel dimensions and induce the relaxation of these vessels to influence the post-trabecular or distal outflow resistance downstream of SC[188]; although the relationship between NO production and distal outflow resistance has not been studied yet. These results suggest that NO can mediate the cellular contractility of TM cells, which in part regulate outflow resistance and facilitate aqueous humour outflow through the conventional outflow pathway.

NO has also been shown to induce relaxation of the ciliary muscle[18,84,89,236]. However, the relaxation of ciliary muscle tends to oppose the effects of TM relaxation, as these two tissues are connected through the extensive tendinous connections[165,186,187,222]. Therefore, the contraction/relaxation of one tissue will affect the response in the other, functioning as an antagonist pair to regulate aqueous humour outflow[237]. Although it has been shown that the activation of NO/sGC/cGMP pathway favors the relaxation of TM cells, and thus results in the increase of aqueous humour outflow[236].

Alternatively, NO could also mediate endothelial permeability of the inner wall of SC by disrupting the adherens junctions[44,57] or by altering the SC cell volume by activating the BK_{Ca} channel[65]; both mechanisms could potentially affect the porosity of the inner wall endothelium by modulating the dimensions of pores or flow pathways to increase outflow facility. In contrast, earlier studies carried out by Kubes *et al.*[132] showed the inhibition of NO production with L-NAME led to increased endothelial permeability in the microvasculature, therefore it remains to be determined whether NO increases or decreases permeability of the inner wall endothelium of SC. Interestingly, the SC endothelium expresses key vascular endothelial markers such as CD31 and VE-cadherin[106], which serves to maintain the endothelial barrier function to regulate aqueous humour outflow. The phos-

phorylation state of VE-cadherin has been associated with the regulation of vascular permeability both *in vitro* and *in vivo*[163]. NO production has been shown to be crucial for regulating VE-cadherin phosphorylation in addition to stress fiber formation in endothelial cells by controlling the balance between Rho and Rac activation[57]. The loss of eNOS activity, and subsequent lack of NO, results in the remodeling of the actin cytoskeleton by redistributing F-actin towards the cell periphery, enhancing cortical actin assembly and strengthened cell-to-cell adhesion in a TIAM1 (activator of Rac) and Rac-dependent manner. The recruitment of TIAM1 to adherens junctions and VE-cadherin leads to a reduction in VE-cadherin phosphorylation[57], thus in turn alters the endothelial permeability[163].

NO may also affect other aspects of aqueous humour dynamics; for example, NO donors may decrease aqueous humour inflow[197], increase episcleral venous pressure[245], and affect choroidal blood volume[125]. Therefore, it is possible that NO could target multiple potential mechanisms to affect aqueous humour dynamics, and, depending on the site of NO activity and the species being examined, NO may either increase or decrease IOP. While the cellular mechanisms by which NO regulates IOP are certainly important, but to gain therapeutic effect in the context of physiological regulation of outflow facility, we need to investigate the effects of NO on conventional outflow physiology at the organ level.

Effects of NO on Conventional Outflow Physiology

Exogenously delivered NO typically decreases IOP and increases outflow facility, by reducing the outflow resistance situated in the conventional outflow pathway. The reduction of outflow resistance is likely mediated through the activation of sGC-dependent signaling cascades, as previously described. The IOP-lowering effects of various NO donors has long been established in various animal models, including in living monkeys[24,111,130,193], in living rabbits[20,24,41,129], and in eyes obtained postmortem from pigs[62,65] and humans[191]. Recent efforts have resulted in the development of several NO-donating compounds[24,113,130], including latanoprostene bunod (LBN), a NO-donating prostaglandin F2α receptor agonist that has been shown to be more efficacious than latanoprost at reducing elevated IOP in ocular hypertensive patients[233]. This improved IOP reduction is likely attributed to the effects of the NO-donating moiety targeting the TM/SC cells to enhance aqueous humour outflow. Even with the recent success of the LBN compound and other exogenous

NO-donating compounds on increasing outflow facility, it is still important to understand the physiological role of endogenous NOS within the conventional outflow pathway, as this would lead to better development of potential therapeutics to treat glaucoma. As previously mentioned, all three NOS isoforms have been identified throughout the trabecular, post-trabecular, and ciliary muscle regions, suggesting that endogenous NOS activity and NO production may influence outflow physiology.

Despite the potential role of other NOS isoforms, eNOS appears to be particularly important for the physiological regulation of outflow facility. Stamer *et al.*[211] have shown that in enucleated mouse eye perfusions, that elevated eNOS expression in eNOS-GFPtg mice leads to a reduction in IOP and increases outflow facility when compared to litter-mate wild-type mice. Additionally, when the eNOS-GFPtg mice were treated with N^G-nitro-L-arginine methyl ester (L-NAME; non-selective NOS inhibitor) the pressure-flow relationship of the transgenic mice returned to levels that were comparable to those of wild-type mice. These results suggest that the endogenous NO regulation may play a important role in regulating aqueous humour outflow. Interestingly, in a recent study conducted in sGCα_1 deficient mice, the lack of α_1-subunit of the protein has been shown to contribute to ocular hypertension and glaucomatous optic neuropathy[37]. This is consistent with the hypothesis that NO production and its subsequent physiological responses through the sGC/cGMP/PKG signaling pathway may therefore play an important role in regulating aqueous humour dynamics.

Although, currently the mechanism by which eNOS is activated within the conventional outflow pathway remains to be determined. Recent data suggests that human SC endothelial cells[11] and porcine angular aqueous plexus cells (the porcine equivalent of SC cells)[135] are both capable of shear-induced NO production. This presents the possibility that eNOS may be activated through shear stress acting on the inner wall through circumferential flow within the SC lumen. Stamer *et al.*[211] originally outlined the hypothesis that with IOP elevation, SC lumen collapses, which in turn increases the shear stress acting on the inner wall as the same volumetric flow rate of the aqueous humour must now flow through a smaller SC lumen. Shear-induced NO release by SC cells then increases outflow facility to oppose the IOP elevation to restore IOP homeostasis. This homeostatic mechanism functions as a mechano-regulatory feedback loop, whereas in glaucomatous eyes this homeostatic mechanism may become impaired as reflected by the reduced NOS activity in the conventional outflow pathway[158]. Alternatively, TM in normal eyes have been shown to increase in stiffness with age, whilst in glaucomatous eyes the TM stiffness is increased further[39,40,133].

Increased TM stiffness could effectively desensitise the mechano-regulatory feedback loop by becoming less compliant and thus reduces the amount of SC collapse with increasing IOP. This would lead to decreased shear stress and lower NO levels that feeds back into the system. Furthermore, decreased cellularity in the TM as observed in older patients[8,40], can also contribute towards elevations in IOP, due to less TM cells responding to the shear-induced NO release by SC cells to help regulate aqueous humour outflow.

Taken together, NO-based therapeutics proves to be a potential viable option to make an impact on glaucoma patients, by reducing IOP through the above mentioned mechanisms. Although, depending on where NO is released in the anterior chamber and conventional outflow pathway, that would dictate the physiological effects. Therefore, NO must be released in close proximity to the juxtacanalicular region and inner wall of SC, where endogenous eNOS regulation of outflow normally occurs. Additionally, targeting the NO-regulatory machinery within the conventional outflow pathway may also provide a promising therapeutic target for treating glaucoma.

1.3 Motivation of Thesis

The central hypothesis of this thesis focusses on the concept of a dynamic endogenous regulatory system or a "feedback loop" that regulates the conventional outflow resistance to maintain IOP homeostasis. The majority of the outflow resistance is generated by the JCT, basement membrane and inner wall of SC, which are considered as the main "controller(s)" of the feedback circuit (as shown in Figure 1.9). Alternatively, increased episcleral venous pressure and resistance generated by downstream aqueous/episcleral veins could also contribute to the outflow resistance to AH drainage[203]. As the outflow resistance of the conventional outflow tract increases, this leads to elevations in IOP. It is known that elevations in IOP leads to the collapse of SC[73,120], which reduces the cross-sectional area of the SC lumen. This effectively increases the shear stress experienced by the SC endothelial cells, as the same volumetric flow rate of AH must flow through a smaller SC lumen. The SC cells functions as a "barostat" or "sensor" within this endogenous feedback loop by detecting IOP-induced changes in shear stress. Elevated shear stress has been shown to up-regulate eNOS activity in vascular-derived endothelial cells and increase NO production[11]. Therefore, we hypothesize that NO produced by the SC cells act as a "local mediator", which feeds back into the circuit to help modulate the outflow resistance and restore IOP homeostasis. In the context of the endogenous regulatory system, NO acts in a similar fashion as other autocrine or paracrine signaling molecules[210], by either retrograde diffusing upstream to relax the TM/JCT cells and/or advection along the circumference of the canal to increase the permeability of the inner wall endothelium, and possibly affecting the distal resistance of episcleral veins further downstream.

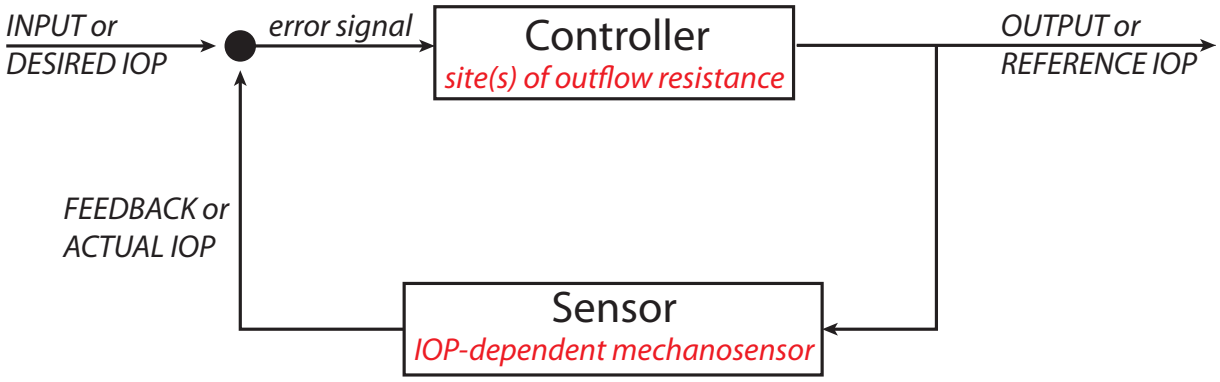


Figure 1.9: Schematic of eNOS regulatory feedback in the conventional outflow tract.

The goals of this thesis are: **(1)** to investigate the role of NO and endogenous NOS activity

in the conventional outflow pathway, and its effects on aqueous humour outflow regulation, **(2)** to develop new methods of detecting NO production levels *in vivo*, and **(3)** to investigate whether up-regulation of eNOS expression and activity at the inner wall of SC influences the segmental outflow patterns in the TM by modulating the local outflow resistance. In order to achieve these goals, five specific aims were formulated, which are addressed in separate chapters of this thesis.

1.4 Specific Aims

Specific Aim 1: To investigate the role of NO and endogenous NOS activity in the conventional outflow pathway of mice. Our study utilizes *ex vivo* mouse eyes from both wild-type (C57BL/6) mice and transgenic mice with elevated eNOS expression tagged with GFP (eNOS-GFPtg), to determine how exogenous NO-donors (S-nitroso-N-acteylpenicillamine; SNAP) and NOS-inhibitors (N^G-nitro-L-arginine methyl ester; L-NAME, and Cavtratin) may influence conventional outflow regulation. We hypothesize that exogenous NO delivered to mouse eyes will decrease outflow resistance and increase outflow[62,65,111,211], whilst the use of NOS-inhibitors would investigate whether the endogenous NOS activity in mice contributes to outflow regulation, and if altered NO signaling contributes to decreased outflow and potentially outflow dysfunction in glaucoma. *This specific aim is addressed in Chapter 2: Role of Nitric Oxide in Murine Conventional Outflow Physiology.*

Specific Aim 2: To develop a NO-sensitive biosensor that can detect local changes in NO production in both *in vitro* and *in situ* models. NO is highly reactive, with a extremely short half life (<1 to 30 seconds[167]), thus the detection of this elusive signaling molecule can be highly challenging. Our NO-sensitive biosensor consists of tyrosine-containing peptides derived from proteins that are prone to nitration, a selective oxidative process that results in the post-translational modification of tyrosine residues to form 3-nitrotyrosine[19,184]. The conversion of tyrosine into 3-nitrotyrosine serves as a biological footprint for local changes in NO levels. *This specific aim is addressed in Chapter 3: Peptide-Functionalized Nanoparticles for Localized Detection of Nitric Oxide via Peroxynitrite-Mediated Nitration.*

Specific Aim 3: To investigate whether local eNOS activity in the SC correlates with segmental

outflow patterns in the conventional outflow pathway. Aqueous humour filtration through the conventional outflow pathway is non-uniform or "segmental", but it remains unclear what regulates segmental outflow patterns[42,70,102,143]. We hypothesize that spatial variations in the expression of eNOS within the SC cells may effect the segmental distribution of outflow in the TM. Fluorescent tracers are perfused into *ex vivo* mouse eyes from transgenic mice expressing GFP driven by the human eNOS promoter superimposed on the C57BL/6 background expression of eNOS (eNOS-GFP; reporter mice), to determine whether regions of high eNOS expression coincides with regions of high tracer intensity. *This specific aim is addressed in Chapter 4: Preferential Outflow in Relation to Endogenous eNOS Activity in Murine Conventional Outflow Pathway.*

Specific Aim 4: To investigate the relationship between SC morphology and segmental outflow patterns. Aqueous humour filtration patterns are considered segmental, but it remains unclear whether the segmental outflow patterns are governed by the ECM accumulation at the micro-scale, or if the bulk flow preferentially drains towards regions of lower resistance at the macro-scale[42,70,102,143]. We hypothesize that aqueous humour filtration is a "multi-scale" problem, that multiple factors influence the segmental outflow patterns, including the post-trabecular drainage pathways and distal resistance sites. To determine the relationship between downstream episcleral vessels and the tracer distribution, we aim to develop an imaging technique that will enable the visualization of the downstream limbal vasculature in relation to the tracer distribution over the entire circumference of the eye. *This specific aim is addressed in Chapter 5: Imaging of Segmental Outflow in Ex Vivo Mouse Eyes by Optical Projection Tomography.*

Specific Aim 5: To develop a localized NO-drug delivery that directly targets the conventional outflow pathway. Current NO-donating drug therapies have shown varied success in decreasing IOP and enhancing outflow facility[62,66,193,197,233,236,245], caused by off target effects of NO release within the anterior chamber of the eye. Therefore, to achieve full therapeutic effect, NO must be released in close proximity to the JCT and inner wall of SC where the main sites of outflow resistance are situated. *This specific aim is addressed in Chapter 6: Targeted Delivery of Nitric Oxide to the Trabecular Outflow Pathway via Enzyme Loaded Nanoparticles.*

Chapter 2

Role of Nitric Oxide in Murine Conventional Outflow Physiology

This chapter consists of a paper published in AJP:Cell Physiology, reproduced with permission from American Physiological Society.

2.1 Introduction

Elevated intraocular pressure (IOP) is a primary risk factor for glaucoma. All current glaucoma therapies aim to lower IOP, but no current treatments directly target the conventional outflow pathway that serves as the primary drainage route for aqueous humor. Because decreased outflow facility is the root cause of elevated IOP in primary open-angle glaucoma[210], identifying drugs that enhance conventional outflow may lead to new, more effective therapies for ocular hypertension and primary open-angle glaucoma.

Experimental evidence supports the idea that the bulk of aqueous humor outflow resistance is generated proximal to or at the endothelium of Schlemm's canal (SC)[117]; however, the mechanisms responsible for outflow regulation are not well understood. Recent data suggest that exogenous nitric oxide (NO) delivered via NO donors decreases outflow resistance and IOP in several species[24,62,65,111,158,191,211], but it is unclear whether endogenous NO production by NO synthase (NOS) enzymes has a physiological role in regulation of aqueous humor outflow. NO is well known to mediate various physiological functions, including vasodilation, junctional complex assembly, and permeability, in vascular and lymphatic endothelial cells[57,175], and because SC is derived from vascular endothelia[99,185] and expresses both vascular and lymphatic markers[12,126,169,185], we hypothesize that NO release from SC cells contributes to physiological regulation of conventional outflow. Consistent with this notion, the presence of NADPH-diaphorase, an indicator of NOS activity, has been identified in the conventional outflow pathway of human donor eyes and suggests endogenous NO production by NOS enzymes[158], and decreased NADPH-diaphorase labeling has been reported in glaucomatous eyes[158]. Recent studies have demonstrated that SC cells in culture secrete NO in response to increasing shear stress[11,135], similar to vascular endothelial cells[44,45], and the shear stress acting on SC cells *in vivo* during SC narrowing is predicted to approach the shear experienced by endothelial cells in arteries[73]. Genome-wide association studies[121,141,174] have linked polymorphisms in the *NOS3* gene encoding the endothelial-specific isoform of NOS (eNOS), in addition to mutations in the caveolin genes (*CAV1* and *CAV2*)[223,238] to the pathogenesis of glaucoma, whilst the overexpression of eNOS in a mouse model leads to decreased outflow resistance and lower IOP[211]. Taken together, these data suggest that endogenous NO signaling within the conventional outflow pathway by NOS enzymes contributes to outflow regulation and that alterations

in NO signaling in part mediate outflow dysfunction in glaucoma.

In this work, we test the hypothesis that endogenous NO production by eNOS influences conventional outflow facility in mice. Our studies use *ex vivo* mouse eyes, because the conventional outflow pathway in mice is anatomically and functionally similar to that in humans[165,204] and pharmacological modulation of outflow facility in mice resembles the responses previously reported in human eyes[25]. To investigate the role of NO and NOS activity, we measured the effect of NO donors and NOS inhibitors on outflow facility. Studies were performed in eyes from wild-type (WT) mice and from transgenic mice with elevated eNOS expression.

2.2 Materials and Methods

All experiments were conducted in compliance with the Association for Research in Vision and Ophthalmology Statement for the Use of Animals in Ophthalmic and Vision Research under UK Home Office Project License approval for research at Imperial College London and under Institutional Animal Care and Use Committee approval for research at Duke University.

2.2.1 Experimental Design

This study investigated the influence of exogenous NO and endogenous NOS activity on conventional outflow facility in enucleated mouse eyes. Eyes were obtained from C57BL/6 WT or transgenic mice that express the human variant of eNOS fused to GFP (eNOS-GFPtg) superimposed on the C57BL/6 background expression of eNOS[211,229]. To examine whether exogenous NO influences outflow facility, eyes were perfused with the NO donor S-nitroso-N-acetylpenicillamine (SNAP) or its inactive analog N-acetyl-D-penicillamine (NAP). Because SNAP is light-sensitive, the NO release kinetics of SNAP and NAP were first characterized to identify an optimal lighting condition, which was controlled for all SNAP/NAP perfusion experiments. To examine whether endogenous NOS activity contributes to regulation of outflow facility, eyes were perfused with or without a broad-spectrum NOS inhibitor [N^{G}-nitro-L-arginine methyl ester (L-NAME)] or an eNOS-selective in-

hibitor (cavtratin, caveolin-1 scaffolding domain peptide). All experiments were performed using both WT and eNOS-GFPtg eyes, with the exception of L-NAME perfusions, since we previously reported that L-NAME decreases outflow facility in eNOS-GFPtg eyes to levels consistent with WT eyes[211].

2.2.2 Calibration of NO-donor

Because SNAP and NAP are light sensitive, NO release from SNAP and NAP was first characterized using a NO-sensitive electrode (ISO-NOS II, WPI, Hertfordshire, UK), calibrated following the manufacturer's instructions. Briefly, the NO probe was placed in a solution containing 0.1M H_2SO_4 and 0.1 M KI to polarize the sensor and obtain a baseline current. To determine the standard curve, changes in current were measured in response to incremental volumes of 50 μM KNO_2 added to the H_2SO_4/KI solution within a glass vial. Conversion of KNO_2 to NO occurs rapidly and follows 1:1 stoichiometry, such that the NO concentration is dictated by the added concentration of KNO_2.

Once the standard curve was generated, we examined NO release from SNAP and NAP. Preliminary data indicated that NO release from SNAP depended on the intensity and duration of light exposure. Thus we tested NO release under two lighting conditions that could be controlled during the perfusion: 1) initial high-intensity light (700 – 1,000 lumens/m^2) exposure of the stock solution (113 mM) for 10 min (measured with a luminometer; Mastech, GuangDong, China) followed by low-light (100 – 200 lumens/m^2) conditions, where the NO donor was diluted to the working concentration (0.1 – 1 mM) and protected from surrounding laboratory light with aluminum foil, and 2) initial high-intensity light (700 – 1,000 lumens/m^2) exposure of the stock solution for 10 min followed by continuous light exposure of the working solution at the same level (700 – 1,000 lumens/m^2). NO release was measured over 60 min starting immediately after the initial 10-min light exposure for both conditions. Condition 1 was used for subsequent SNAP/NAP perfusions. Because conversion of SNAP to NO is catalyzed by metal ions and is temperature-sensitive, all NO measurements were performed in perfusion solution (containing divalent cations) at 37℃. The probe tip was immersed in 10 ml of solution within a glass vial during continuous mixing with a magnetic stir bar.

2.2.3 Animal Husbandry

This study used transgenic mice of the same C57BL/6 background strain as the WT controls. Perfusions were performed with enucleated (*ex vivo*) eyes from mice of either sex. eNOS-GFPtg mice were 8 – 13 wk of age (for SNAP/NAP and cavtratin perfusions). WT mice were 6 – 12 wk of age (for SNAP/NAP perfusions) or 25 – 30 wk of age (for L-NAME and cavtratin perfusions). Mice were housed in individually ventilated cages, fed ad libitum, and maintained at 21℃ with a 12:12-h light-dark cycle, with lights on from 6 AM to 6 PM.

Transgenic mice express the human gene variant of eNOS fused to green fluorescent protein (GFP) on a C57BL/6 background. The transgene contains the full-length human eNOS promoter, such that transgene expression is regulated by endogenous transcriptional activity and is superimposed on the background expression of murine eNOS[229]. In these animals, eNOS-GFP expression has been shown to be specific to endothelial tissues, to lead to a twofold increase in plasma NO concentrations in large arteries[229], and to cause decreased aqueous humor outflow resistance and reduced IOP compared with age-matched controls[211]. eNOS-GFPtg mice also have reduced mean aortic pressure, reduced heart rate, and lower systemic vascular resistance[229]. Transgenic mice were a kind gift from Prof. Rob Krams (Imperial College London, UK) and Prof. Rini de Crom (Erasmus MC, Rotterdam, The Netherlands).

Genotyping of transgenic mice was performed to detect sequences of GFP and the human variant of eNOS present in the genome of eNOS-GFPtg mice but absent from the genome of WT mice. Genotyping was performed using ear tissue samples obtained at weaning, with tissue lysis and DNA purification performed according to the manufacturer's instructions (DNeasy Blood & Tissue Kit, Qiagen, Hilden, Germany). Separate PCRs were performed using a hot-start mix (KAPA2G Robust HotStart ReadyMix, Kapa Biosystems, Cambridge, MA). For human eNOS, 29 cycles were performed with an annealing temperature of 63℃ using sense primer AGGGCGCAATGGTAACCTGAAGAT and antisense primer AAAGCTCTGGGTGCGTATGCGG to yield a predicted product of 699 bp. These sequences are specific for the human eNOS and are not predicted to react with C57BL/6 murine eNOS. For GFP, 29 cycles were performed with an annealing temperature of 59.9℃ using sense primer AGCTGACCCTGAAGTTCATCTG and antisense primer GACGTTGTGGCTGTTGTAGTTG to yield a predicted product of 327 bp. PCR products were resolved by gel

electrophoresis (1% agarose) in the presence of DNA gel stain (SYBR Safe, Invitrogen, Carlsbad, CA). Bands were visualized on an imaging station (Biospectrum 500, UVP, Upland, CA).

2.2.4 *Ex Vivo* Mouse Eye Perfusion

The first set of experiments examined the effect of the NO donor (SNAP; Calbiochem) compared with its inactive analog (NAP; Sigma) on outflow facility. Treated eyes were perfused with 100 μM SNAP in Dulbecco's phosphate-buffered saline (PBS) including divalent cations and 5.5 mM D-glucose (DBG) passed through a 0.2 μm filter. Contralateral control eyes were perfused with 100 μM NAP in DBG. Stock solutions of SNAP or NAP at 113 mM in dimethyl sulfoxide (DMSO) were divided into aliquots and stored at – 20° C, with care taken to protect the solutions from light at all times. Working solutions were prepared immediately prior to each experiment, with high-intensity light exposure of the stock solution for 10 min followed by low ambient light exposure of the working solution (see above) immediately prior to initiation of the perfusion. Eyes were perfused at sequential pressure steps of 8, 15, 20, and 25 mmHg to determine outflow facility (see below).

In the second and third sets of experiments, we used a nonselective NOS inhibitor (L-NAME; second set) or an eNOS-selective inhibitor (cavtratin; third set) to examine the effect of NOS inhibitors on conventional outflow facility. For L-NAME experiments, the treated eye was perfused with 10 or 100 μM L-NAME in DBG, while the contralateral control eye was perfused with DBG alone. L-NAME perfusions were performed only in WT mice, because we previously reported the effects of L-NAME in eNOS-GFPtg mice[211]. L-NAME solution was prepared from powder immediately prior to each experiment. For cavtratin experiments, the treated eye was perfused with 50 μM cavtratin in DBG containing 0.6% DMSO, while the contralateral vehicle control eye was perfused with DBG containing 0.6% DMSO without cavtratin. Cavtratin is a chimeric peptide that contains a cellular internalization sequence antennapedia (AP) domain fused to the caveolin-1 scaffolding domain, which binds to and inhibits eNOS. Cavtratin has been shown to enter murine vascular endothelial cells and inhibit eNOS activity and NO production for up to 20 h *in vivo* and *in vitro*[34,95,190,196]. Based on these data, we expect that cavtratin should inhibit eNOS within the trabecular outflow pathway of the murine eye. Cavtratin experiments were performed in WT and eNOS-GFPtg mice, with the contralateral control eye perfused with DBG alone. In a second set of cavtratin experiments, the contralateral

eye was perfused with a scrambled cavtratin domain but an intact AP domain (cavtratin-X) at the same concentration (50 μM). Cavtratin was stored as a stock solution (8 mM in DMSO) at – 20℃ and diluted to a working concentration immediately prior to each experiment, with care taken to protect the solutions from light at all times. Eyes were perfused at sequential pressure steps of 4, 8, 15, and 20 mmHg. These pressure steps differ from those used in the first experimental set: because, in the first set of experiments, we observed nonlinear pressure-flow behavior at the highest (25 mmHg) pressure step, we therefore decreased the pressure range in the second and third sets of experiments to minimize this nonlinearity.

The eyes were enucleated within 10 min of death by cervical dislocation and stored in PBS (Invitrogen) at 4℃ until perfusion, typically within 1 – 3h. Experiments used paired contralateral eyes, except in the cases where data from one eye were rejected on the basis of the stability criterion described below. Paired eyes were perfused sequentially (one eye immediately after enucleation, the second eye 2 – 3 h after enucleation), with the treatment assigned randomly to the first or second eye to control for any time-dependent postmortem changes. No differences in outflow facility were observed between untreated controls perfused immediately and those perfused 2 – 3 h later (not shown).

Our perfusion method follows previously described techniques[25,27,134,211]. The eye was affixed to a support using cyanoacrylate glue to stabilize the eye for cannulation by a 33-gauge beveled needle (NanoFil, World Precision Instruments, Hitchin, UK), with the tip positioned in the anterior chamber using a micromanipulator (Figure 2.1A). Before cannulation, each needle was backfilled from the tip with 200 μL of the perfusate, a volume sufficient to last several hours during perfusion. The needle was connected via pressure tubing to a glass syringe (25 μL; Hamilton GasTight, Reno, NV) mounted on a motorized syringe pump (PHD Ultra, Harvard Apparatus, Cambridge, MA). Custom-written LabVIEW software (National Instruments, Austin, TX) was used to control the syringe pump flow rate to maintain the eye at a user-defined perfusion pressure[164], which was monitored by a pressure transducer (model 142PC01G, Honeywell, Columbus, OH) located upstream of the cannulation needle. Eye temperature was maintained at 34 – 37℃, with the eye kept hydrated by submersion to the limbus in PBS and the cornea covered with moist tissue paper. Both the experimental and control eyes were pressurized from a reservoir at 8 mmHg for 45 min before initiation of the perfusion to allow sufficient time for the pressure to stabilize within the eye.

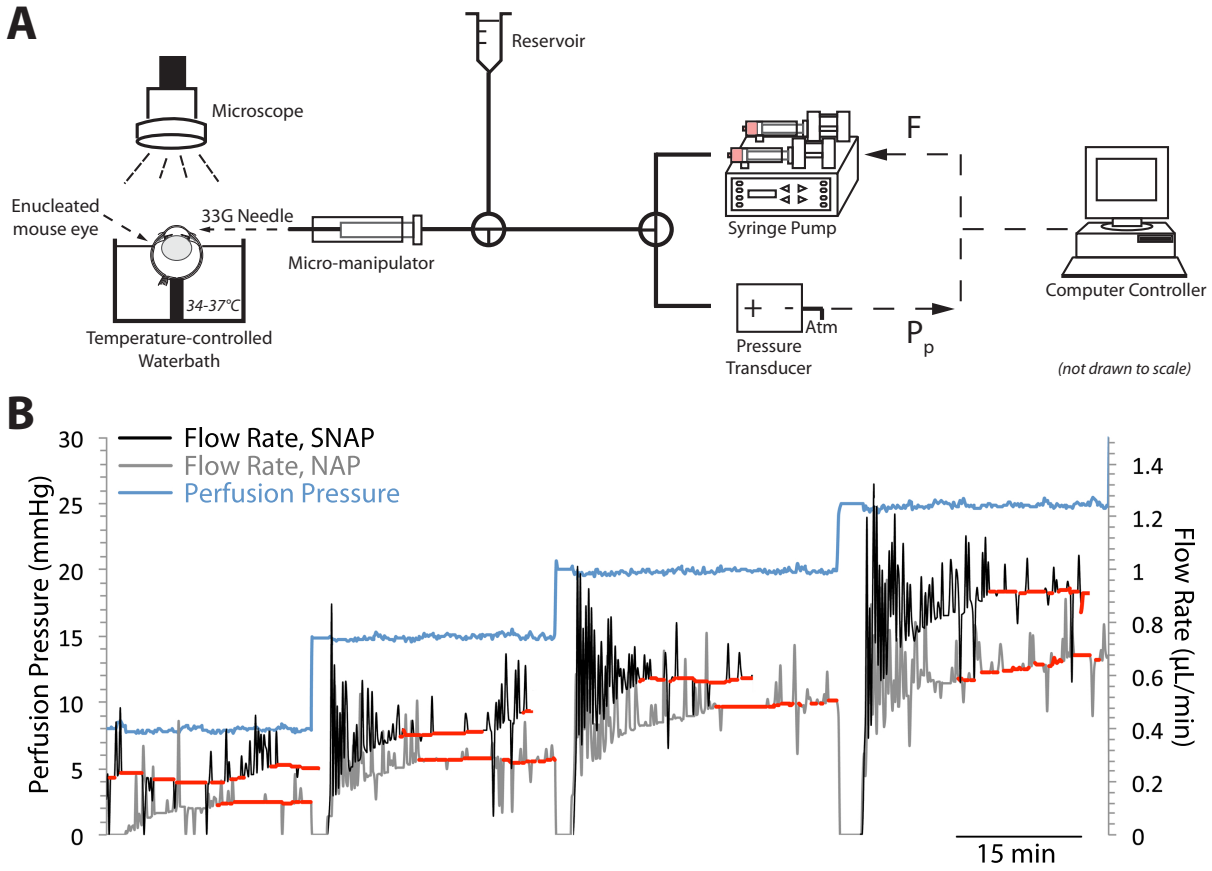


Figure 2.1: Perfusion system to measure outflow facility in enucleated *ex vivo* mouse eyes. **(A)** Computer-controlled syringe pump controls the perfusion flow rate *(F)* into the mouse eye to maintain a user-defined perfusion pressure (P_p), which is measured by a pressure transducer (see Equation 2.1). Mouse eye is held within an isotonic bath at 34-37℃ and cannulated by a 33 gauge needle that is positioned into the anterior chamber using a micromanipulator while the preparation is viewed under a stereomicroscope. Perfusion is open to a reservoir set to 8 mmHg above the eye during needle insertion and during the initial pressurization period, but the reservoir is closed during the perfusion. **(B)** Representative perfusion tracings showing the perfusion pressure (blue line) and flow rate data from paired eyes perfused with 100 μM N-acetyl-D-penicillamine (NAP; grey line) or 100 μM S-Nitroso-N-acetylpenicillamine (SNAP; black line). Red highlighted regions represent data used to calculate the average flow rate at each corresponding pressure step. Spikes represent rapid increases in flow rate to maintain the user-defined perfusion pressure. Only one perfusion pressure tracing is shown, but pressure tracings are generally similar for both eyes.

Each pressure step during perfusion was maintained for 20 – 30 min, and the average stable flow rate was calculated over 10 min near the end of each pressure step (Figure 2.1B). Data were considered acceptable if a stable flow rate was achieved in at least three of the four pressure steps. Conventional outflow facility (C) was estimated by fitting our pressure-flow rate data to the modified Goldmann equation[134]:

$$F = C * P_{\mathrm{p}} + F_{\mathrm{u}} \tag{2.1}$$

where F represents the average stable flow rate at each perfusion pressure (P_p) and F_u represents the apparent flow rate at zero pressure. Equation 2.1 is only valid when aqueous humor production and episcleral venous pressure are zero (appropriate for enucleated eyes), when F reaches equilibrium at each value of P_p, and when C and F_u are independent of P_p. The value of C is estimated as the slope of the best-fit linear regression to the measured F vs. P_p data. At the end of the perfusion, eyes were fixed by immersion in 4% paraformaldehyde for 1 h followed by long-term storage in 0.1% paraformaldehyde.

2.2.5 Immunofluorescence Microscopy

The expression and localization of eNOS-GFP in the conventional outflow pathway were examined by immunofluorescence microscopy of eyes from eNOS-GFPtg and WT mice ($n = 2$ each). After immersion fixation, eyes were opened at the cornea and infiltrated with 30% sucrose in PBS and then with a 1:1 mixture of 30% sucrose solution and cryostat embedding compound (Tissue-Tek OCT, Sakura-Finetek, Torrance, CA). The eyes were embedded in cryomolds (Sakura-Finetek), frozen on dry ice, mounted in a cryostat (Microm HM 525, ThermoFisher Scientific, Waltham, MA), and sagittally sectioned in steps of 16 μm. Cryosections were dried for 1 h at room temperature, rehydrated in PBS, permeabilized in 0.2% Triton X-100 in PBS for 5 min, and blocked in 10% normal goat serum in PBS for 30 min. The sections were incubated with antibodies raised in rabbit against GFP[212] at a dilution of 1:500 in PBS for 2 h at room temperature and then with rat anti-mouse CD31 antibodies (clone mec13.3, BD Pharmingen, Mississauga, ON, Canada) at a dilution of 1:100 for 2 h at room temperature to label the endothelium of SC. The sections were then incubated with Alexa 555 goat anti-rat and Alexa 647 goat anti-rabbit secondary antibodies (Life Technologies, Burlington, ON, Canada) diluted 1:200 in PBS at room temperature for 2 h. The sections were incubated with 5 μM SYTOX (Life Technologies) for 10 min at room temperature to label nuclei, mounted in Prolong Gold fluorescent mounting medium (Life Technologies), and examined with a confocal microscope (LSM 510, Zeiss, Jena, Germany).

2.2.6 Statistical Analysis

Differences in outflow facility between treated and untreated eyes were examined with the linear mixed model using commercial statistical software (SPSS, IBM) following previous methods[27]. The linear mixed model accounts for correlated errors between paired eyes from individual mice, while allowing for unpaired eyes that arise when the contralateral eye fails to meet the stability criteria. Differences were considered statistically significant when the P value (estimating the probability that the null hypothesis was true) was <0.05.

2.3 Results

2.3.1 Effects of Light on NO-Donors

The initial 10-min exposure of the stock solution at 700 – 1000 lumens/m^2 triggered NO release from SNAP that increased over 1 h under ambient light conditions (Figure 2.2A). Continuous light exposure at 700 – 1000 lumens/m^2, however, led to an initial rise in NO followed by a decline to zero within 1 h (Figure 2.2A). These data reveal that NO release by SNAP is light-dependent, whereby the irradiation of the NO donor with light leads to the release of NO (typically between the UV and visible light range)[75], but that prolonged light exposure can disrupt NO release kinetics. Importantly, this suggests that lighting conditions must be carefully controlled during SNAP perfusion experiments. Therefore, for all subsequent SNAP/NAP experiments, the SNAP-containing solutions were exposed to 700 – 1000 lumens/m^2 for 10 min prior to the perfusion, which was performed under low ambient light. After this protocol, the concentration of NO released from 100 μM SNAP reached 140 $\pm$ 20 nM (mean $\pm$ SD; N = 3) at 1 h (Figure 2.2B). The NO concentration released from 100 μM SNAP far exceeds the Michaelis concentration (K_M = 23 nM)[46] for the reaction between NO and soluble guanylate cyclase (sGC) and, thus, likely yields a saturating dose of NO. In contrast, 100 μM NAP released no detectable NO (0 $\pm$ 4 nM; N = 3) under otherwise identical conditions (Figure 2.2B). We also examined an alternative NO donor (100 μM diethylenetriamine-NO; DETA-NO), but we found that NO release by DETA-NO was nearly threefold less than NO release by the same concentration of SNAP (140 $\pm$ 20 nM vs. 49 $\pm$ 9 nM; data not shown) over 60 min.

2.3.2 Effect of NO-Donors on Conventional Outflow Facility

To determine whether NO donors affect conventional outflow facility, we perfused paired eyes from WT or eNOS-GFPtg mice with 100 μM SNAP or 100 μM NAP. In WT mice, SNAP increased the flow rate at each perfusion pressure and increased conventional outflow facility by 62 $\pm$ 28% compared with NAP (0.051 $\pm$ 0.015 vs. 0.031 $\pm$ 0.010 μL/min/mmHg; N = 6 vs. 5; P=0.016; Figure 2.3A). In eNOS-GFPtg mice, SNAP had no detectable effect on the flow rate (Figure 2.3B) and there was no difference in conventional outflow facility between SNAP- and NAP-treated eyes (0.019 $\pm$ 0.006 vs. 0.021 $\pm$ 0.005 μL/min/mmHg; N = 5 vs. 4; P = 0.40). Taken together, these data reveal that a NO donor increases outflow facility in WT mice but has no detectable effect in eNOS-GFPtg mice.

2.3.3 Effect of NOS-Inhibitors on Conventional Outflow Facility

To determine whether endogenous NOS activity contributes to the regulation of conventional outflow facility, we perfused WT mice with L-NAME, a nonselective inhibitor of all NOS isoforms. At 10 μM, L-NAME reduced the flow rate at each perfusion pressure relative to vehicle-treated eyes (Figure 2.4A) and decreased conventional outflow facility by 36 $\pm$ 13% (0.014 $\pm$ 0.002 vs. 0.021 $\pm$ 0.007 μL/min/mmHg; N = 5 each, P=0.012). However, 100 μM L-NAME had no apparent effect on the flow rate or conventional outflow facility (0.028 $\pm$ 0.007 vs. 0.024 $\pm$ 0.005 μL/min/mmHg; N = 9 vs. 8; P=0.22; Figure 2.4B). These data reveal that L-NAME has a biphasic effect on outflow facility in WT mice: a decrease in conventional outflow facility at lower concentrations but little effect on conventional outflow facility at higher concentrations.

To investigate specifically the influence of eNOS, as opposed to other NOS isoforms, we perfused eyes with cavtratin, an eNOS-selective inhibitor. Cavtratin at 50 μM decreased conventional outflow facility in WT eyes by 19 $\pm$ 12% relative to vehicle-treated contralateral eyes (0.021 $\pm$

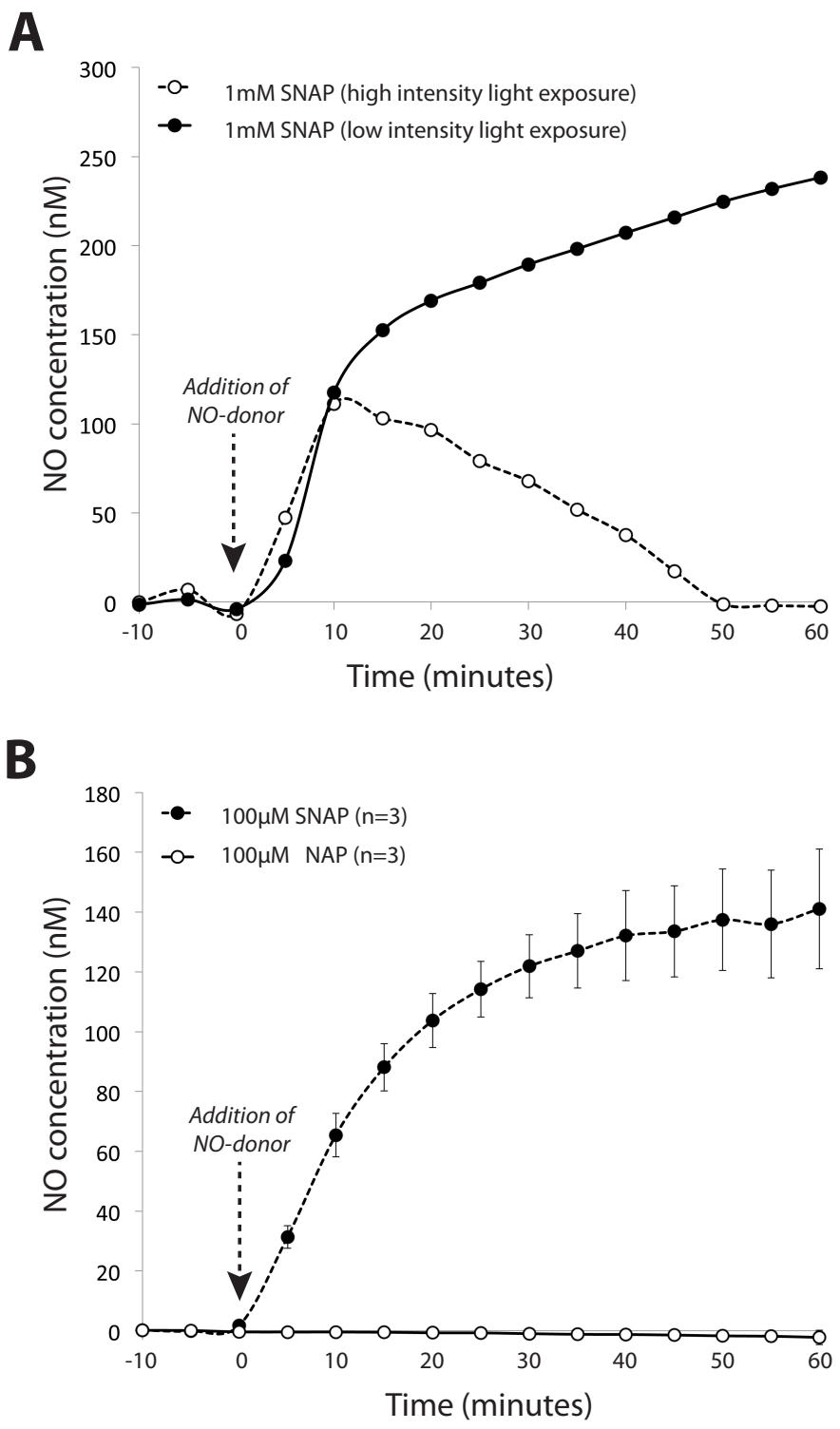


Figure 2.2: Characterization of NO concentration following release by SNAP or NAP under varying lighting conditions. **(A)**: NO release following initial high-intensity light (700 – 1000 lumens/m^2) exposure of stock solution (113 mM) for 10 min followed by dilution to the working solution [1 mM in Dulbecco's PBS including divalent cations and 5.5 mM D-glucose (DBG)] and either low-intensity (100 – 200 lumens/m^2 or prolonged high-intensity (700 – 1000 lumens/m^2) light. Data are from 1 experiment but are representative of 3 individual experiments. *Time 0* corresponds to the end of the initial 10-min period, during which SNAP stock solution was exposed to high-intensity light and after which NO release was measured in the working solution by the probe. **(B)**: NO release from 100 μM SNAP or 100 μM NAP in DBG (N = 3 each; bars are SD). Each stock solution was treated with an initial 10-min exposure to high-intensity light (700-1000 lumens/m^2) followed by low-intensity light (100-200 lumens/m^2) starting at *time 0*. NO was measured using an NO – sensitive probe (ISO-NOS II). Data in B are representative of NO release during 100 μM SNAP/NAP perfusions.

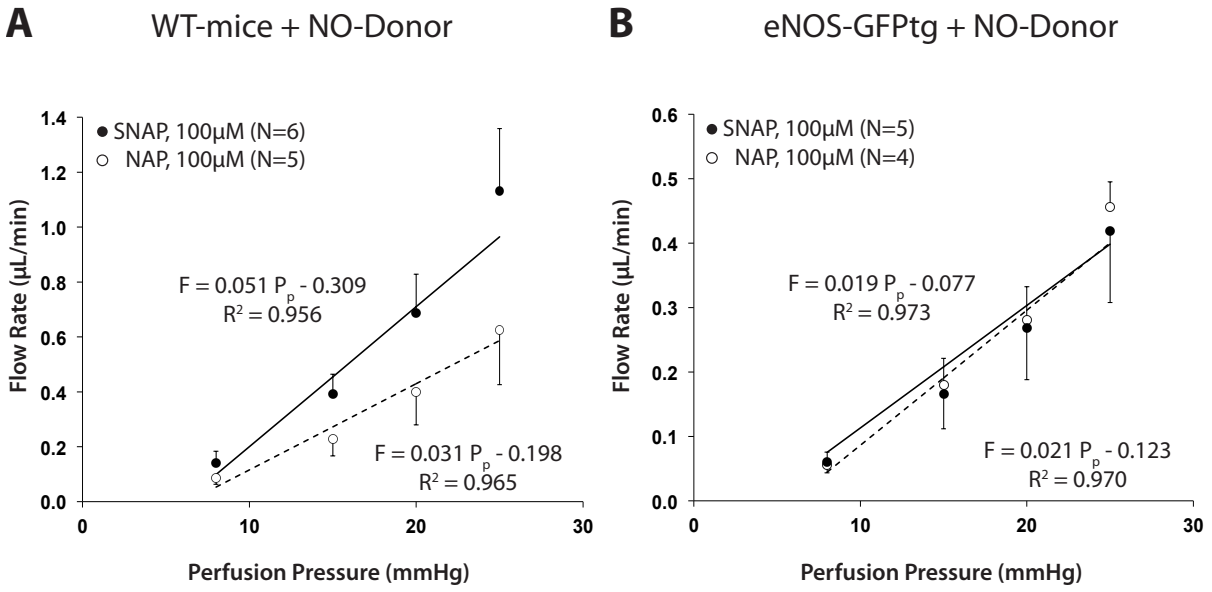


Figure 2.3: The effects of NO-donor on conventional outflow facility in eyes from wild-type (WT) and eNOS-GFPtg mice. **(A)** Perfusion flow rate measured as a function of pressure in enucleated eyes from WT mice perfused with 100 μM SNAP (NO-donor; filled circles) or 100 μM NAP (inactive analog; open circles). Outflow facility was estimated based on the slope on the linear regression through the data points, as described by Equation 2.1. **(B)** Perfusion flow rate measured as a function of pressure in enucleated eyes from eNOS-GFPtg mice perfused with 100 μM SNAP (filled circles) or 100 μM NAP (open circles). Bars represent SD. Note different vertical axis scales in panels A and B.

0.009 vs. 0.025 $\pm$ 0.012 μL/min/mmHg; N = 7 vs. 8; P=0.011; Figure 2.4C). In a separate set of experiments, we compared the effects of cavtratin with the effects of a control peptide with a scrambled cavtratin domain and an intact AP domain (cavtratin-X) and found a similar 25 $\pm$ 17% reduction in conventional outflow facility (0.019 $\pm$ 0.008 vs. 0.014 $\pm$ 0.007 μL/min/mmHg; N = 9 each; P=0.026; not shown). However, in eNOS-GFPtg mice, 50 μM cavtratin decreased conventional outflow facility by 39 $\pm$ 25% relative to vehicle-treated contralateral eyes (0.008 $\pm$ 0.004 vs. 0.014 $\pm$ 0.006 μL/min/mmHg; N = 7 vs. 5 each; P=0.014; Figure 2.4D). These data suggest that eNOS may be the predominant isoform involved in aqueous humor outflow regulation, decreasing conventional outflow facility in both WT and eNOS-GFPtg mice.

2.3.4 Localization of eNOS Transgene Expression within the Conventional Outflow Pathway

To confirm and localize expression of the eNOS transgene within the conventional outflow pathway, eyes from eNOS-GFPtg mice were enucleated and processed for immunofluorescence microscopy. The immunofluorescence signal from antibody complexes against GFP in eNOS-GFPtg

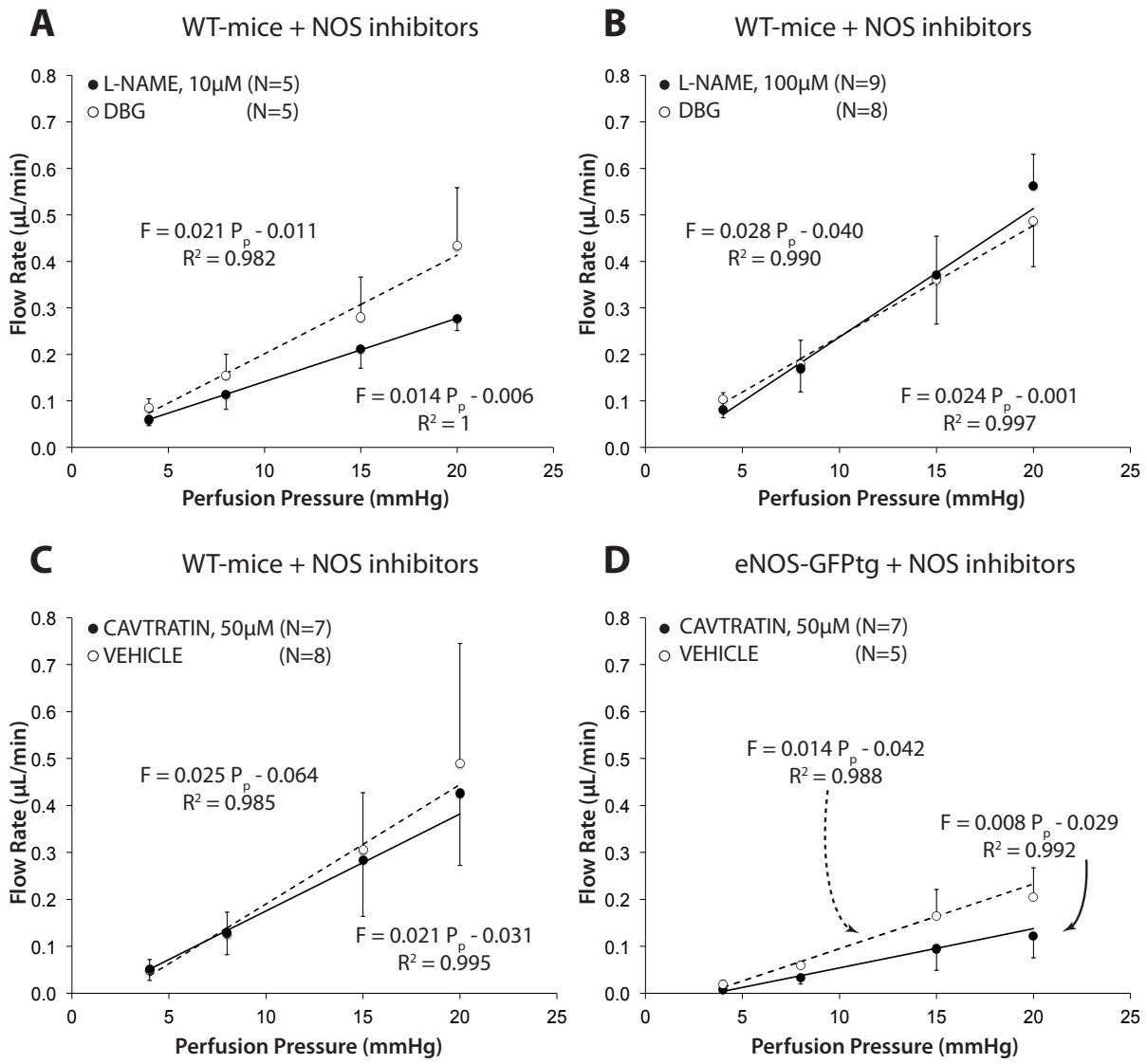


Figure 2.4: (A,B) Perfusion flow rate measured as a function of pressure in WT eyes perfused with L-NAME (non-selective NOS inhibitor; filled circles) at 10 μM (A) or 100 μM (B) in DBG versus DBG vehicle alone (open circles). **(C,D)** Perfusion flow rate measured as a function of pressure in eyes perfused with 50 μM cavtratin (eNOS-selective inhibitor; filled circles) versus vehicle control (DBG + 0.6% DMSO; open circles) from WT (C) or eNOS-GFPtg (D) mice. Outflow facility is estimated based on the slope on the linear regression through the data points, as described by Equation 2.1. Error bars represent SD.

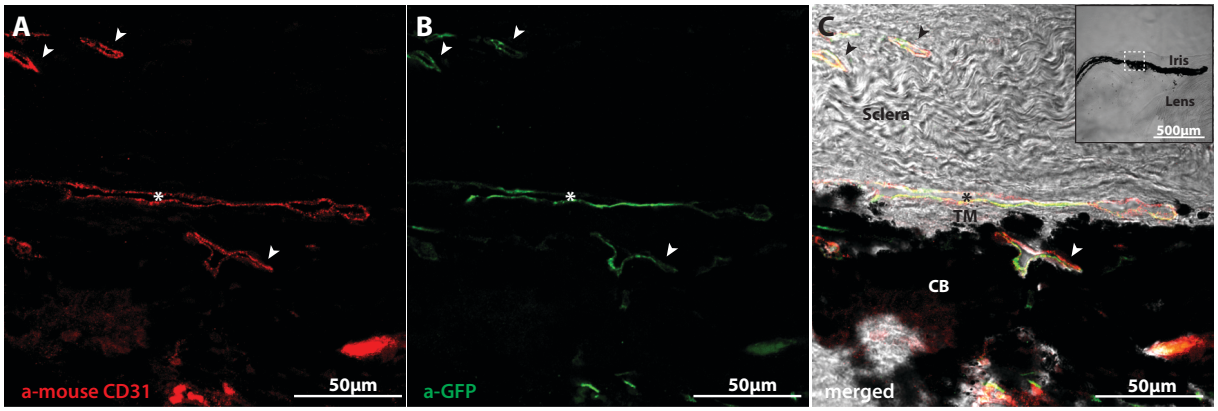


Figure 2.5: Localization of transgene expression in the conventional outflow pathway of eNOS-GFPtg mice. **(A)** Sagittal section through the trabecular meshwork (TM) and Schlemm's canal (asterisk) labeled with the endothelial marker CD31, showing labeling of SC endothelium as well as blood vessels (arrowheads) in the ciliary body (CB) and sclera. **(B)** Indirect immunofluorescence against GFP from the same section shown in panel A, revealing co-localization of the eNOS-GFP transgene along the endothelium of SC and along blood vessels in the CB. **(C)** Merged color image showing labeling for CD31 and GFP superimposed on the brightfield image to show the location of SC and TM with respect to the CB, iris and sclera. *Inset*: lower magnification of the brightfield sagittal section showing the location of the outflow pathway with respect to the iris and lens. Data are representative images from two eNOS-GFPtg mouse eyes.

mice colocalized with the endothelial marker CD31 within blood vessels of the iris and ciliary body, confirming the endothelial-specific expression of the eNOS-GFP transgene and its promoter[229]. In the conventional outflow pathway (Figure 2.5), GFP immunofluoresence was restricted to the endothelium of SC, collector channels, and episcleral vessels, which also expressed CD31[106]. Interestingly, there was no apparent GFP staining of the trabecular meshwork (TM), and GFP labeling was entirely absent from WT mice, which lacked the eNOS-GFP transgene. No obvious differences were observed in the morphology of SC and TM between eNOS-GFPtg and WT mice.

2.4 Discussion

Exogenously delivered NO typically decreases IOP by increasing outflow facility. The outflow facility-increasing effect of various NO donors was first demonstrated in living monkeys[111,193] and, subsequently, in living rabbits[129] and in eyes obtained postmortem from pigs[62,65] and humans[191]. The current study demonstrates that exogenous NO, delivered via SNAP, also increases outflow facility in enucleated eyes from C57BL/6 mice. This suggests a common outflow facility response to exogenous NO across several species that can be examined in mice as a model system that resembles the functional anatomy[165] and pharmacology[25] of the human outflow pathway.

Precisely how NO affects outflow facility and IOP remains unclear but likely involves mechanisms related to cellular contractility or endothelial permeability. NO is a free radical gas that can rapidly diffuse across cell membranes to affect the biological activity of several proteins and enzymes. For instance, sGC mediates the vasodilatory effect of NO on smooth muscle cells in the cardiovascular system, and sGC is necessary for the increase in outflow facility following exogenous NO in *ex vivo* pig eyes[65]. Deficiencies in sGC signaling contribute to ocular hypertension and glaucomatous optic neuropathy in mice[37]. Similarly, NO induces relaxation of TM cells[61] and decreases TM[60] and SC[66] cell volume to potentially affect the dimensions of inner wall pores or flow pathways in the juxtacanalicular tissue. Alternatively, NO mediates the disruption of adherens junctions to increase permeability of vascular endothelia[44,57] and, thereby, may disrupt the adherens junctions along the inner wall of SC[106] to increase outflow facility. Downstream of SC, NO may induce relaxation of smooth muscle cells that surround the collector channels[54] to increase intrascleral vessel diameter and, therefore, may influence post-trabecular or distal outflow resistance downstream of SC[188].

NO also induces relaxation of the ciliary muscle[18,84,89,236]. However, as pointed out previously[193,236], ciliary muscle relaxation tends to decrease outflow facility and oppose the increase in outflow facility putatively caused by TM/SC relaxation. This effect should be more pronounced in primates[186,187,222] and mice[165], which have a ciliary muscle with more extensive tendinous connections to the juxtacanalicular tissue and inner wall endothelium of SC than other species such as pigs[13,150]. NO may also affect other aspects of aqueous humor dynamics; for example, NO donors may decrease aqueous humor inflow[197], increase episcleral venous pressure[245], and affect choroidal blood volume[125]. Thus there are numerous potential mechanisms by which NO may affect aqueous humor dynamics, and, depending on the site of NO activity and the species being examined, NO may either increase or decrease IOP. While the downstream mechanisms by which NO regulates IOP are certainly important, the current study focused upstream on the role of NOS enzymes and how production of endogenous NO may be involved in the physiological regulation of outflow facility.

Endogenous NO is produced *in vivo* by a family of NOS enzymes encoded by three genes and their splice variants, including the calcium-dependent eNOS and nNOS, which are constitutively expressed in endothelial cells and nitrergic neurons, respectively, and the calcium-independent

iNOS, which is expressed predominantly in macrophages. While Nathanson and McKee[158] argue, based on immunohistochemistry, that eNOS is the primary NOS isoform in the human outflow pathway, the TM is innervated by nitrergic nerve fibers, which contain nNOS in primate and porcine eyes[149,195]. Macrophages are commonly found within the TM, particularly after laser trabeculoplasty[7], and express iNOS[239], which, when activated, yields greater quantities of NO than either eNOS or nNOS[158,191,192]. Within the TM, the NOS expression profile, particularly for iNOS, changes in response to IOP[192]. Downstream of the TM, nNOS-labeled nerve fibers and terminals surround episcleral veins in mice[165] and arteriovenous anastomoses within the intrascleral vessel network in primates[83]. eNOS itself, while expressed by SC inner wall cells, is also expressed by the endothelium of the intrascleral collector channels and aqueous humor veins[211]. In primates, the longitudinal ciliary muscle fibers are enriched in eNOS[158] and insert directly into the juxtacanalicular region[186,187]. Thus all three NOS isoforms, and likely their splice variants, are present throughout the trabecular, post-trabecular, and ciliary muscle regions, suggesting multiple locations where NOS activity may influence outflow physiology.

To examine the physiological role of endogenous NO in aqueous humor dynamics, we perfused enucleated mouse eyes with inhibitors of NOS enzymes and measured conventional outflow facility. By examining enucleated eyes, one can measure outflow facility independently of NO-mediated effects on inflow, episcleral venous pressure, or unconventional outflow, since such effects are very likely eliminated in enucleated eyes and would otherwise confound measurements *in vivo*. This assumes that the outflow facility is unaffected by postmortem changes and that the NO signaling pathways are preserved *ex vivo*. In support of the *ex vivo* model, Millar and colleagues[151] showed that the outflow facility measured *in vivo* is not significantly different from that measured immediately after death in the same mice prior to enucleation. Furthermore, the pharmacological outflow facility response measured in enucleated mouse eyes mimics the response previously observed in enucleated human eyes to several receptor-mediated compounds, including sphingosine 1-phosphate[25,216], prostaglandin EP4 agonist[25,152], and pilocarpine[14,165].

In WT mice, nonselective inhibition of NOS enzymes by 10 μM L-NAME decreased outflow facility, suggesting that there is a basal tone of endogenous NO involved in regulation of outflow facility. However, no detectable facility decrease was observed in response to 100 μM L-NAME. It is puzzling why higher concentrations of L-NAME had no detectable effect on outflow facility; one

possibility is that differential NOS inhibition between different tissues of the outflow pathway may, in some cases, exert opposing effects on outflow facility. For example, one may speculate that the higher concentration of L-NAME is more available to the ciliary muscle, where NO-mediated ciliary muscle relaxation may tend to oppose the increase in outflow facility caused by NO action within the TM (see above). Alternatively, the data may reflect differences in the inhibition of different NOS isoforms by L-NAME, which tends to be more selective for nNOS (IC_{50} = 0.15 μM) than eNOS (IC_{50} = 2.7 μM) or iNOS (IC_{50} = 14 μM)[224], and perhaps the locations or actions of the different isoforms have opposing effects on outflow facility. L-NAME must also be converted to a free acid to become bioactive[173], and the kinetics of this reaction may vary between the TM and ciliary muscle, which exert opposing effects on outflow facility. Alternatively, L-NAME may act as a muscarinic antagonist[36], affecting the M2 and M3 receptors within the ciliary body and iris sphincter of humans[87,111]. If a similar receptor profile is present in mice, then L-NAME could presumably act directly on muscarinic receptors to modulate ciliary muscle contractility, which affects outflow facility in mice[136,165]. Apart from NOS, NO itself exhibits a biphasic effect on TM cell contractility[61] and IOP[131,156]; thus the response to L-NAME that we observed may reflect the underlying biphasic nature of the effect of NO on outflow facility. Regardless of the underlying mechanism, the literature is inconsistent on how L-NAME affects aqueous humor dynamics. For example, in living monkeys, L-NAME does not appear to affect IOP[111]; yet in monkey anterior segment organ culture perfusion, L-NAME lowers IOP by increasing outflow facility[191]. More studies are necessary to better understand how NOS inhibition by L-NAME influences aqueous humor dynamics and, in particular, outflow facility.

Despite the potential role of other NOS isoforms, eNOS appears to be particularly important for the physiological regulation of outflow facility. Stamer *et al.*[211] showed that elevated eNOS expression in eNOS-GFPtg mice leads to reduced IOP and increased outflow facility. However, our data suggest that exogenous NO does not increase outflow facility in eNOS-GFPtg mice, although it significantly increases outflow facility in WT mice. This demonstrates that the outflow facility-increasing effect of NO becomes saturated under conditions of elevated eNOS expression. When eNOS expression was selectively inhibited by cavtratin, outflow facility was reduced in WT and eNOS-GFPtg mice, with a twofold greater reduction in the transgenic mice, which have elevated eNOS activity. Similarly, Stamer *et al.* reported a similar reduction in outflow facility in the eNOS-GFPtg mice in response to L-NAME. This is consistent with the hypothesis that NO production by eNOS contributes to the normal physiological regulation of outflow facility in mice. Disruption of nor-

mal eNOS activity, as may occur in some cases of glaucoma[121,141,174], may therefore contribute to the pathogenesis of ocular hypertension associated with the disease.

One limitation of this study was that the baseline outflow facility was consistently larger in WT than eNOS-GFPtg mice. In contrast, Stamer *et al.*[211] reported a twofold-larger outflow facility in eNOS-GFPtg mice than in their WT littermates. Two important differences may contribute to this discrepancy between the present study and that of Stamer *et al.* 1) Perfusions in the current study were done at physiological temperature, with the eyes submerged under isotonic saline, whereas perfusions in the prior study were conducted with the eyes at room temperature and exposed to room air. Environmental factors such as temperature and hydration likely influence the measurement of outflow facility[27] and, thus, may have contributed to differences in baseline outflow facility between the current study and prior studies. 2) The current study did not directly compare transgenic and WT mice from the same litter. Instead, WT mice used in the current study, despite being from the same background strain, were obtained from a separate colony, which may have exhibited a baseline outflow facility different from that of the transgenic colony. For these reasons, the current experiments were not designed to detect differences in baseline outflow facility between WT and eNOS-GFPtg mice but, rather, to examine the effect of NO donors or NOS inhibitors between paired eyes of a given cohort.

The mechanism by which eNOS regulates outflow facility remains to be determined. However, expression of the eNOS- GFP transgene in the conventional outflow pathway was localized to the endothelium of SC and the intrascleral vessels, with no apparent expression within the TM. This strongly suggests that NO release by endothelial cells within SC or intrascleral vessels influences outflow facility. Furthermore, because NO production by eNOS is shear-sensitive[44,45] and because the shear stress acting on the inner wall reaches levels known to activate eNOS in vascular endothelia[73], it is possible that SC cells produce NO in response to circumferential flow within SC. In fact, recent studies have demonstrated shear-induced NO production by human SC cells[11] and porcine angular aqueous plexus cells (the porcine equivalent of SC cells)[135]. This presents the possibility that eNOS may act as part of an endogenous feedback loop to regulate IOP and offset any potential changes in outflow resistance within the TM. According to this hypothesis, originally outlined by Stamer *et al.*[211], IOP elevation causes collapse of SC, which increases the shear stress acting on the inner wall, because the same volumetric flow rate of the aqueous humor must then flow through

a smaller SC lumen. Shear-induced NO release by SC cells then increases outflow facility to oppose the IOP elevation. One should note that this scenario requires that both the original outflow obstruction and the action of NO on outflow facility occur within the TM, and not downstream of the inner wall of SC. The same mechanism could respond to reductions in IOP, reducing basal NO production, which would tend to increase IOP. Such a mechanism may underlie IOP homeostasis and contribute to the relative consistency of IOP, which lies within a surprisingly narrow range, despite decades of life, in healthy individuals[50,127]. This homeostatic mechanism may become impaired in glaucomatous eyes, in which NOS activity in the conventional outflow pathway appears to be reduced[158]. Our findings predict that, in order for NO-based therapeutics to achieve optimal IOP reduction, NO must be released in close proximity to the juxtacanalicular region and inner wall of SC, where endogenous eNOS regulation of outflow normally occurs. NO donors that release NO in the anterior chamber, for instance, may not achieve full therapeutic benefit, and NO release in other tissues, such as the ciliary muscle or episcleral veins, may be counterproductive and potentially lead to elevations in IOP. Thus, targeting the NO-regulatory machinery within the conventional outflow pathway may provide a promising therapeutic target for treating glaucoma.

2.5 Appendix A: Effects of NO-Donor on the Inner Wall Endothelium of Schlemm's Canal

To examine the effects of NO-donor on the hydraulic conductivity of SC endothelium, we processed WT mouse eyes perfused with SNAP and NAP for electron microscopy to determine whether exogenous NO affects the hydraulic condctivity of the inner wall by changing its morphology, predominately through the disassembly of cell-cell junctions[44,57,175] and potentially through increased pore formation.

2.5.1 Methods: Histology and Ultramicroscopy

To visualize the morphology of the TM and SC, immersion-fixed, whole globes from NAP and SNAP perfused WT mouse eyes (N=2 each) were hemisected proximal to the equator and cut into quadrants. The samples were prepared for standard light microscopy and transmission electron microscopy (TEM). Briefly, the globes were immersed in 2.5% paraformaldehyde, 2.5% glutaraldehyde in Sörensen's buffer, post-fixed in 1% osmium tetroxide, dehydrated, infiltrated, and embedded in Epon-Araldite (EMS, Hatfield, PA). Half-micron thick sagittal sections were cut across the outflow region, mounted on glass slides, and stained with toluidine blue. Sections were examined and photographed using a Zeiss Axiovert microscope. Ultra-thin sagittal sections (70–90 nm) were cut with a diamond knife, mounted on formvar-coated single-slot or copper mesh grids, stained with uranyl acetate and lead citrate, examined and photographed with a Hitachi H-7000 transmission electron microscope (Hitachi, Clarksburg, MD).

Additionally, specimens from NAP and SNAP perfused WT mouse eyes (N=2 each) were also processed for scanning electron microscopy (SEM), following previously established protocols[73]. Briefly, eyes were hemisected proximal to the equator and cut into quadrants, where each quadrant was cut into wedges for microdissection to expose the inner wall endothelium of the SC. The SC was incised along its posterior margin and opened such that the TM and adherent inner wall of SC could be imaged. The samples were incubated in 2% (w/v) tannic acid, 2% (w/v) guanidine hydrochloride in PBS for two hours, followed by one hour in 1% (w/v) osmium tetroxide in PBS.

Between each solution change, the tissue was rinsed thoroughly in PBS. The tissue specimen was then dehydrated through a graded ethanol series, followed by two changes in hexamethyldisilazane, air-dried, mounted on stubs with carbon cement, and sputter-coated with gold. An overview montage, composed of several contiguous smaller image tiles, was acquired to show the entire inner wall surface within the wedge at x1000 magnification by SEM (Hitachi S-3400N VP; Hitachi, USA).

2.5.2 Results and Discussion

We firstly examined the gross morphology of the inner wall endothelium of SC and TM with light microscopy, where we found no obvious differences in morphology between the SNAP- and NAP-treated WT mouse eyes (Figure 2.6). We then examined the sagittal sections with electron microscopy to get a closer look at the JCT and inner wall section of the outflow pathway. From the electron micrographs of SNAP- and NAP-treated eyes, we found that in the NAP-treated eyes there were less giant vacuole formations observed when compared to SNAP-treated eyes (Figure 2.7). Additionally, in the SNAP-treated eyes the giant vacuoles appeared to be larger in size. Interestingly, when examining the inner wall endothelium of SC with scanning electron microscopy, we observed regions of greater porosity in the SNAP-treated eyes compared to NAP-treated eyes (Figure 2.8). These results suggest that exogenously delivered NO to the conventional outflow pathway not only affects the contractility of TM cells[61,236,237], but may also affect the hydraulic conductivity of the inner wall endothelium by regulating pore formation in SC cells.

Although we did not observe this increased porosity in all our samples, this could possibly be attributed to segmental outflow that occurs within the conventional outflow pathway. For instance, depending on where the NO donor gets delivered along the circumference of the SC, we may or may not observe regions of increased porosity. Therefore, it still remains to be determined whether NO is involved in the regulation of pore formation along the inner wall endothelium of SC. One possibility is to use NO-donors in addition to fluorescent tracers to identify regions of high and low flow, which has previously been shown to correlate with increased pore density in the SC endothelium[29] and examine those regions to see whether NO has affected the morphology of the inner wall.

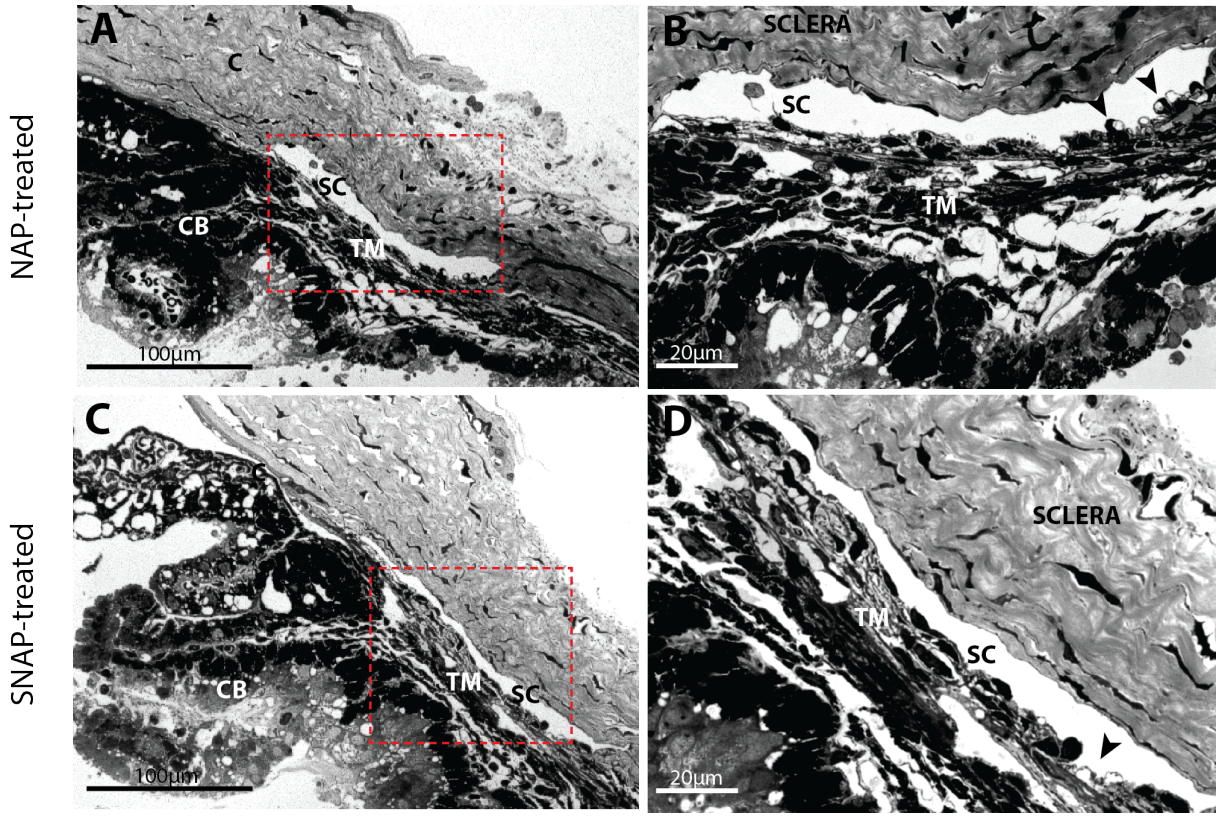


Figure 2.6: Light micrograph of the conventional outflow pathway of a WT mouse eye perfused with SNAP and NAP.. **(A-B)** Representative image of WT mouse eyes perfused with NAP (N=2). **(C-D)** Representative image of WT mouse eyes perfused with SNAP (N=2). *Arrowheads = Giant vacuoles.*

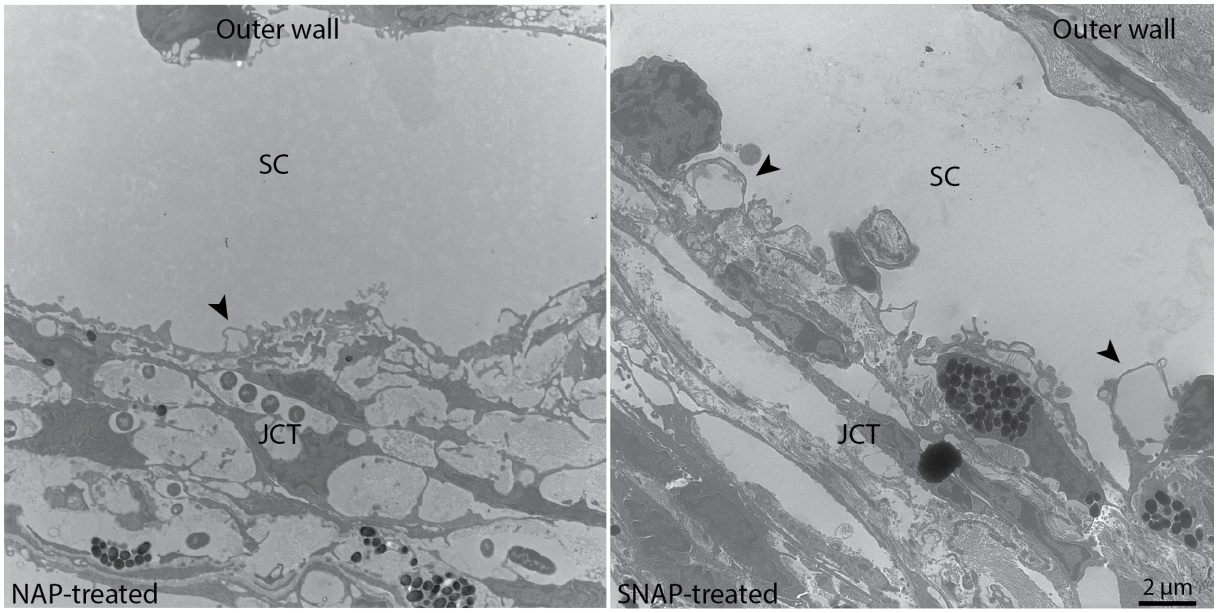


Figure 2.7: Transmission electron micrograph of the inner wall endothelium of SC in WT mice treated with SNAP and NAP (x5000 magnification). **(Left)** Representative image of WT mouse eyes perfused with NAP (N=2). **(Right)** Representative image of WT mouse eyes perfused with SNAP (N=2). *Arrowheads = Giant vacuoles.*

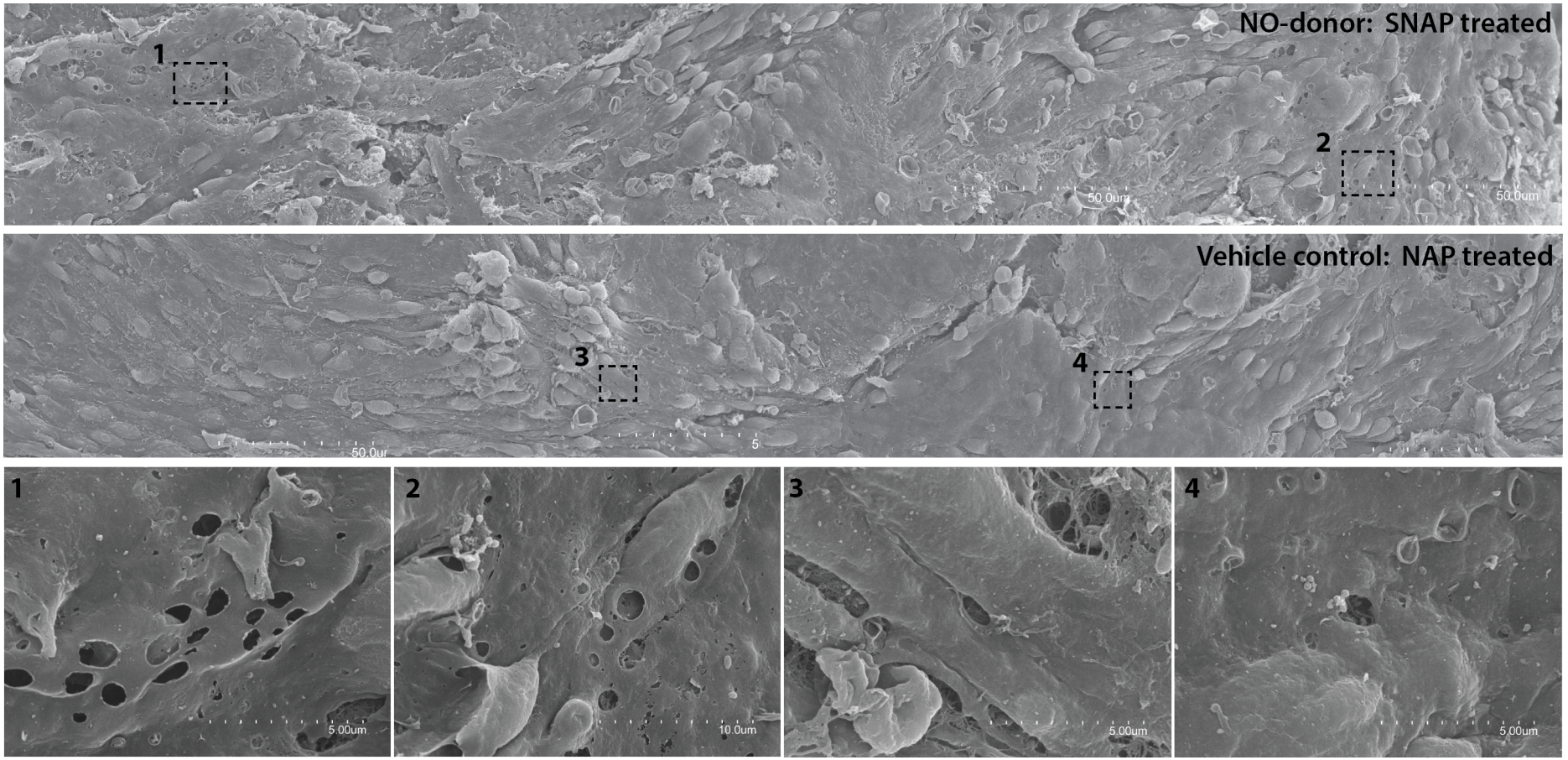


Figure 2.8: Scanning electron micrograph of the inner wall endothelium of SC in WT mice treated with SNAP and NAP (x1000 magnification). **(Top)** Representative image of WT mouse eyes perfused with SNAP (N=2). **(Middle)** Representative image of WT mouse eyes perfused with NAP (N=2). **(1–2)** Eyes perfused with SNAP has more regions of the inner wall with increased pore formation compared to NAP perfused eyes **(3–4)**.

Chapter 3

Peptide-Functionalized Nanoparticles for *in Situ* Detection of Nitric Oxide *via* Peroxynitrite-Mediated Nitration

This chapter consists of a paper in preparation for submission to ACS Nano.

3.1 Introduction

Nitric oxide (NO) is a diatomic free radical with important physiological roles across multiple biological systems. NO is capable of rapidly diffusing across cell membranes and between cells, where it may act as a signaling molecule to modulate vascular homeostasis,[153–155,232] neuronal activity[31,52] and immunological processes.[74] NO dysregulation has been linked to the pathogenesis of Parkinson's and Alzheimer's disease,[10,86,207] cardiovascular disease,[38,96,171,240] glaucoma,[43,174,191,192] and cancer.[95,137] The detection and quantification of NO is therefore important for physiology and pathophysiology, but the reactive nature of NO and its typically short half-life (order of seconds[31,74,154,155,167,232]), makes the measurement of NO challenging.

To measure NO within biological systems, researchers generally rely on indirect detection methods to assess NO-derived products, such as nitrates, nitrites or post-translational modifications of proteins that form nitrosothiols or 3-nitrotyrosines. The Griess assay is one of the most widely used NO detection techniques, which measures the concentration of nitrite (NO_2–) produced in biological fluids after the oxidation of NO. Although the Griess assay provides a useful indication for NO production with a detection limit of $\sim 0.5 \mu$M,[19,110,167,217] the assay is unable to resolve nanomolar concentrations typical of NO-mediated signal transduction. For instance, the activation of soluble guanylate cyclase (sGC) that produces cyclic guanosine monophosphate (cGMP) responsible for maintaining vascular tone, requires a minimum NO concentration of 5 – 10 nM, with typical physiological NO concentrations on the order of hundreds of nanomoles (100 – 500 nM).[56,86,167,207,213] Other factors such as the type of buffer or presence of amino acids[47,112] can interfere with the Griess reaction. Furthermore, measurement of NO within native tissues is technically challenging due to limitations with accessibility and extraction of sample volumes. Hence, there is a need for a NO biosensor that can resolve nanomolar concentrations of NO within biological systems *in situ*.

3-Nitrotyrosine has been identified as a "footprint" of NO-dependent nitroxidative stress.[19,182,208] The process of tyrosine nitration is an oxidative post-translational modification, driven by NO-derived oxidants, such as peroxynitrite (ONOO–; ONOOH) and nitrogen dioxide radical ($^{\bullet}NO_2$), that yield 3-nitrotyrosine. Under normal physiological conditions, low levels of 3-nitrotyrosine can be detected in healthy tissues, which reflect basal steady state levels of nitration and oxidation that occur *in vivo*. However, nitration end products increase several-fold once the formation of oxidants and NO are

augmented (e.g. during inflammation).[174,182,191,192] This results in elevated levels of 3-nitrotyrosine, which is commonly associated with multiple disease progressions in both human and animal models.[16,86,95,137,171,181]

Nitration of tyrosine residues is predominately mediated through the peroxynitrite-dependent pathway, which incorporates a nitro (–NO^2) group to the aromatic ring to form 3-nitrotyrosine.[184] The formation of peroxynitrite is generated through a diffusion-limited reaction between NO and superoxide ($O_2^{\bullet}$–) radicals. Under physiological conditions, both peroxynitrite anion (ONOO–) and its protonated form peroxynitrous acid (ONOOH) are present in biological systems, and can participate in the oxidation of biomolecules. Peroxynitrite is a short-lived oxidant species that readily reacts with carbon dioxide (CO_2) that yields an intermediate adduct, nitroso-peroxocarboxylate ($ONOOCO_2^{\bullet}$–), which quickly homolyses into carbonate ($CO_3^{\bullet}$–), and $^{\bullet}NO_2$ radicals. Alternatively, peroxynitrous acid (ONOOH) can undergo a similar homolytic fission to generate hydroxyl ($^{\bullet}OH$) and $^{\bullet}NO_2$ radicals. These one-electron oxidants promote the formation of a tyrosyl radical intermediate ($Tyr^{\bullet}$), which then combines at diffusion-limited rates with $^{\bullet}NO_2$ to yield 3-nitrotyrosine.[1,19,76,114,167,182–184,208,219] Nitration of tyrosine residues can therefore serve as an indirect indicator for local NO levels. However, conversion of tyrosine to 3-nitrotyrosine under nitroxidative conditions is sensitive to local amino acid sequence and selective for specific proteins *in vivo*.[9,15,115,171,189]

Several site-specific tyrosine residues from native proteins have been identified as preferential targets for nitration *in vivo*.[167,181] Multiple mechanistic studies have shown that the local primary structure of peptides play a crucial role in determining site-specific nitration of tyrosine residues, whereby proximal charged residues increase nitration yield whilst hydrophobic residues tend to yield lower nitration through possible steric hindrance of bulky side groups.[1,63,64,128,178,194,240,243] Therefore, by mimicking the amino acid sequence of nitration-prone sites within native proteins, we have the opportunity to design and synthesize peptide-based biosensors that are sensitive to local changes in NO production. In this study, we synthesized four tyrosine-containing peptides (P1-4) and compared their relative sensitivity towards NO-derived oxidants. Three of the peptides were derived from nitration-prone proteins, with two of these peptides (P1-2) from prostacyclin synthase (PGI_2 synthase)[63,159,171,189,206] and one peptide (P3) from manganese superoxide dismutase (Mn-SOD).[1,15,219,240] Additionally, we designed a fourth peptide (P4) with multiple tyrosines flanked by charged amino acids with the aim to amplify nitration. Incorporating adjacent charged amino acids

such as glutamate (E) and arginine (R) has been shown to enhance the selective nitration of tyrosine residues in proteins.[1,63,64,115] As illustrated in Figure 3.1, each of the synthetic peptides were covalently bound to fluorescent nanoparticles (NPs) such that the nitration reaction is confined to the NP surface. In the presence of NO-derived oxidants, the tyrosine residues within the peptide become nitrated resulting in the formation of 3-nitrotyrosine. The detection of 3-nitrotyrosine residues were carried out by incubating the peptide-NPs with a commercially available monoclonal antibody that is selective for 3-nitrotyrosine, followed by incubation with a secondary fluorescently-labeled antibody. 3-Nitrotyrosine yields were assessed based on its immunofluorescence signal intensity relative to fluorescence signal intensity of the NPs themselves. By combining the specificity of immunochemical techniques and exploiting the selective nitration process of tyrosine residues, we have the opportunity to develop bio-inspired peptide-based NO sensors that can monitor local changes in NO production whilst overcoming the limitations of the standard Griess assay. The goal of this study was to demonstrate proof-of-concept that our peptide-NP biosensors are capable of detecting peroxynitrite-mediated nitration *in vitro* as well as NO released from endothelial cells in response to physiological levels of shear stress.

3.2 Materials and Reagents

FluoSpheres$_{580/605}$ (carboxylated-nanoparticles, 500nm in diameter) were purchased from Molecular Probes (Invitrogen). 9-Fluorenylmethoxycarbonyl (Fmoc)-protected amino acids, Rink amide 4-Methylbenzhydrylamine (MBHA) resin, N,N-diisopropylethylamine (DIEA), 2-(1Hbenzotriazol-1-yl)-1,1,3,3-tetramethyluronium hexafluorophosphate (HBTU), dichloromethane (DCM), dimethylformamide (DMF), 80:20 dimethylformamide/ piperidine pre-mix, and spectroscopic grade acetonitrile (ACN) were purchased from AGTC Bioproducts, UK. Peroxynitrite and 3-nitrotyrosine were both purchased from Cayman Chemical and stored at – 80℃ and at room temperature, respectively. 1-Ethyl-3-(3-dimethylaminopropyl) carbodiimide hydrochloride (EDC), N-hydroxysuccinimide (NHS) and 2-(N-morpholino)ethanesulfonic acid (MES) were all obtained from ThermoFisher Scientific. Mouse monoclonal anti-nitrotyrosine (clone 2A8.2; MAB5404) antibody was obtained from Merck Millipore; goat anti-rabbit VE-Cadherin (XP® monoclonal #2500) antibody was obtained from Cell Signaling; Alexa Fluor 488 goat anti-rabbit IgG secondary antibody was obtained from Life Tech-

nologies Inc., and goat anti-mouse IgG secondary antibody (IRDye® 800CW) was obtained from LI-COR Biosciences.

3.3 Methods

3.3.1 Peptide Synthesis

Four synthetic peptides (P1: EKKDFY$_{421}$KDGKRL-CONH$_2$; P2: GKRLKNY$_{430}$SLP-CONH$_2$; P3: LHHSKHHAAY$_{34}$VNNLNV-CONH$_2$; and P4: GGREYYY-CONH$_2$; Figure 3.6) were prepared either by manual solid phase peptide synthesis (SPPS) or on a PTI Quartet peptide synthesizer using standard Fmoc solid phase peptide synthesis chemistry[142] on a Rink-amide MBHA resin. Briefly, Fmoc deprotection was performed with 20% piperidine in dimethylformamide (DMF) for 10 min, repeated twice. Amino acid couplings were carried out with (4 equivalents) Fmoc protected amino acids, (3.75 equivalents) HBTU, and (6 equivalents) of DIEA in DMF for 1 to 2 h. The peptides were cleaved from the resin and deprotected with 95% trifluoroacetic acid (TFA), 2.5% triisopropylsilane (TIS), and 2.5% distilled water (dH$_2$O) for 4 hours. The TFA was removed using rotary evaporation, and the peptide was precipitated and washed with cold diethyl ether. For purification, the peptide was dissolved in a solution of 4.9% ACN in ultrapure water with either 0.1% TFA or NH_4OH and purified using reverse-phase preparative high performance liquid chromatography (HPLC; Shimadzu) running a mobile phase gradient of ultrapure water with 5% ACN to 100% ACN with 0.1% TFA or NH_4OH. The phenomenex C_{18} Gemini column was 150 x 21.2 mm and had a 5 μm pore size and 100 Å particle size. The HPLC fractions were checked for the correct mass using matrix-assisted laser desorption spectroscopy (MALDI; Waters), and the pure peptide solution was rotary evaporated to remove ACN and lyophilized on a freeze dryer (Labconco). After lyophilization, the purified peptides were confirmed with analytical HPLC and MALDI (Supplemental Figure 3.6) then stored at – 20℃ until needed.

3.3.2 Detection of Nitrated Peptides in Solution

Peptides were dissolved in phosphate buffered saline (PBS, pH 7.4) supplemented with 10% dimethyl sulfoxide (DMSO) at stock concentration of (1 mM) then diluted to a working concentration of 0.1 mM for the nitration experiments. For nitration experiments, each peptide were incubated with peroxynitrite (0.5mM) for 1 hr at 37℃ followed by UV-Vis spectrophotometry (Beckman Coulter DU 800). Peroxynitrite was used as an intermediate NO-derived oxidant to simulate peroxynitrite-mediated nitration. Peroxynitrite concentration was measured spectrophotometrically using $\epsilon 302$ = 1670 M^{-1} cm^{-1} before each experiment. Sodium hydroxide (0.01M NaOH) was used as a vehicle control, as peroxynitrite is supplied in NaOH to maintain its stability. Peroxynitrite and vehicle treated peptides were both measured under basic conditions by raising the pH with NaOH to better distinguish the 3-nitrotyrosine peaks. 3-Nitrotyrosine has a characteristic spectral shift upon alkanization, which is reflected by the secondary maximum shifting from 357nm to 430nm.[48,49]

3.3.3 Peptide-Nanoparticle Conjugates

The peptides were covalently bound to the carboxyl-functionalized nanoparticles (NPs) using standard EDC/NHS chemistry, as illustrated in Figure 3.1. The nanoparticles were initially washed with 0.1 M MES buffer (pH 4.7), followed by activation of surface carboxylic acids with EDC ($\sim$20 mM) and NHS ($\sim$50 mM) for 15 min before conjugation in MES buffer. Once the carboxyl groups have been activated, the pH of the buffer was then raised from 4.7 to 7.4 using PBS to improve coupling efficiency. Tyrosine-containing peptides (P1-4) were then conjugated to the NPs, each peptide was conjugated to the NPs at 1mM final concentration in PBS and incubated overnight on a temperature-controlled shaker at 1,000 rpm and 4℃ (Thermomixer; Eppendorf). After incubation, the peptide-NP complex was washed with PBS three times; the unbound peptides were removed after each centrifugation step (10 min at 14,000 rpm). Finally, the peptide-NP complex was re-suspended in PBS at 1% (v/v) stock solution.

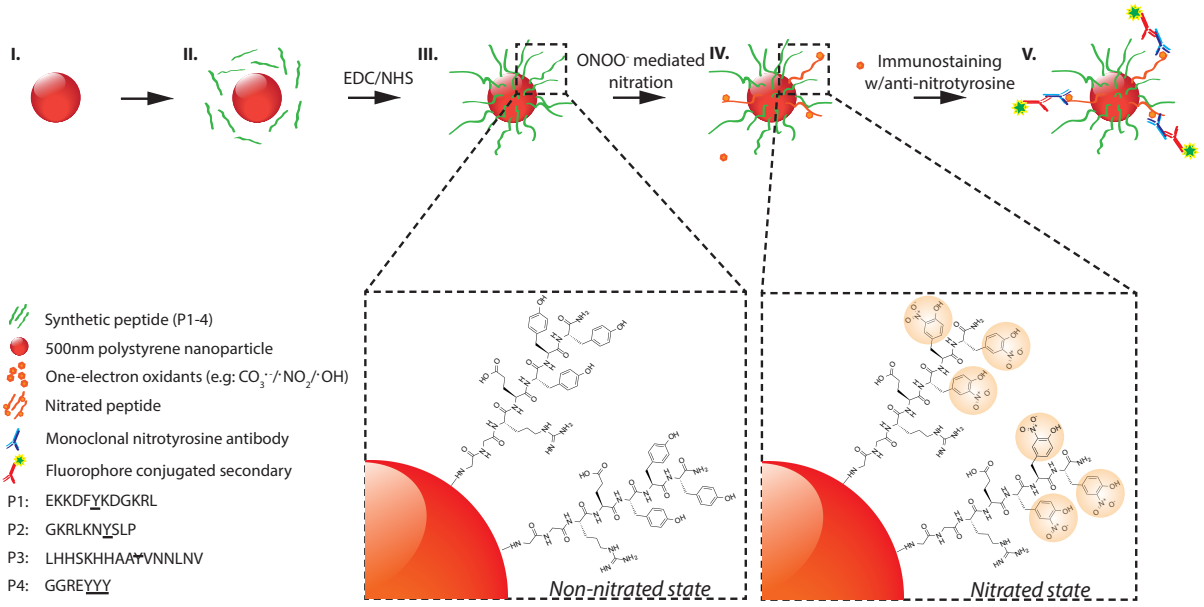


Figure 3.1: Schematic representation of peroxynitrite-induced nitration. **(I)** The fluorescent nanoparticle, **(II)** conjugation of peptides with EDC/NHS cross-linker (P1-4), **(III)** non-nitrated peptides conjugated to surface of nanoparticles, **(IV)** nitration of tyrosine through peroxynitrite-mediated pathway, **(V)** immunostaining of nitrated peptides with anti-nitrotyrosine IgGs and fluorescent secondary IgGs. **(Step I-III)**: Carboxyl-functionalized red fluorescent polystyrene nanoparticles ($\sim$ 500nm in size) are coated with tyrosine-containing peptides (P1-P4, green strands). **Step IV**: Peroxynitrite-mediated nitration of tyrosine residues resulting in the formation of 3-nitrotyrosine. **Step V**: Immunostaining of nitrated peptides with monoclonal anti-nitrotyrosine IgGs (MAB5404; Millipore) and fluorophore conjugated secondary IgGs.

3.3.4 3-Nitrotyrosine Detection on Nanoparticle Complex

To induce nitration, each peptide-NP complex was incubated with varying concentrations of peroxynitrite in a 96-well plate and incubated for 1 hr at 37℃, then followed by 3-nitrotyrosine detection. Nanoparticles conjugated with 3-nitrotyrosine amino acids served as a positive control for all immunoassay studies whilst NaOH (0.01M) treated peptide-NP complex were used as negative vehicle controls. To determine the sensitivity of 3-nitrotyrosine conversion, peptide-NP complexes were loaded on a nitrocellulose membrane with a Bio-Dot® microfiltration system using gravity flow (Bio-Rad Laboratories, Inc.). After loading, the membranes were incubated in 5% nonfat dry milk in Tris buffered saline containing 0.2% Tween-20 (TBS-T) which served as a blocking buffer. Nitrated NPs were detected with a mouse monoclonal anti-nitrotyrosine antibody (1:500) diluted in blocking buffer and incubated with membranes overnight at 4℃. Membranes were then washed with TBS-T (4 times; 10 min each) and incubated for 1 hr at room temperature in a goat anti-mouse IgG secondary antibody (1:5,000) diluted in blocking buffer. This was followed by TBS-T wash (4 times; 10 min each) prior to visualization. Immunoreactivity was visualized using an infrared imaging system (Odyssey® CLx, LI-COR), where the 3-nitrotyrosine signals were detected at $778_{ex}/794_{em}$, whereas the NPs

were detected at $580_{ex}/605_{em}$. 3-Nitrotyrosine antibody signal (G_i) was corrected for background binding signal (G_b) obtained from the vehicle-treated peptide-NPs and then divided by the nanoparticle fluorescence of each peptide-NP complex (R_i), this allowed for normalization of 3-nitrotyrosine signal to concentration of NPs loading on the nitrocellulose membrane. The background fluorescence from the nanoparticles were negligible, and thus was not included in the correction for the fluorescence signals. Each experimental reading was carried out in triplicates to minimize dot-to-dot variations in loading, thus we obtain a normalized 3-nitrotyrosine antibody signal (G^*) as represented in Equation 3.1.

$$G^* = \frac{G_{\mathrm{i}} - G_{\mathrm{b}}}{R_{\mathrm{i}}} \tag{3.1}$$

3.3.5 Cell Culture

Human umbilical vein endothelial cells (HUVEC-2; BD Biosciences, MA) were cultured in Medium 199 (Invitrogen) supplemented with 15% fetal bovine serum (Premium select; Atlanta Biologics), heparin sodium salt (90 μg/ml), endothelial mitogen (0.1 mg/ml; Biomedical Technologies, MA), penicillin (100 U/ml), streptomycin (0.1 mg/ml), and glutamine (0.29 mg/ml) at 37℃ and 5% CO_2. Cells from passages 3-7 were used for the shear stress experiments.

3.3.6 Shear Stress Experiments

HUVECs were seeded at confluence (1 x 10^5 cells/cm^2) into μ-slides I$^{0.6}$ (Ibidi, Munich, Germany) and cultured overnight ($\sim$18-20 hours) in an incubator at 37℃ with 5% CO_2 to allow for cell attachment. The μ-slides were then connected to the Ibidi pump system (Ibidi) and exposed to either low (1.5 dynes/cm^2) or high (15 dynes/cm^2) shear stress for 24 hours. Low and high levels of shear stress were chosen to help better distinguish shear-dependent NO release from the endothelial cells. Cells exposed to the high shear were subjected to a gradual increase in shear stress levels over the first hour (1.5, 5 to 15 dynes/cm^2) to allow for adaptation to continuous laminar flow (following the manufacturer's protocol). Each μ-slide was loaded with 0.01% (v/v) of peptide-NP complexes in the

media at the start of the shear experiment. After 24 hours of shear stress, the media was collected and the peptide-NPs were pelleted (30 mins at 14,000 rpm). The supernatant was frozen at – 20℃ and used for quantifying nitrite concentration using the Griess assay. The peptide-NPs (in the pellet) were washed and centrifuged in PBS for 10 mins at 14,000 rpm; this process was repeated three times. The peptide-NPs were re-suspended in PBS for immunodetection of 3-nitrotyrosine by dot blot.

3.3.7 Immunofluorescence Microscopy

Following each shear stress experiment cells were fixed with 4% paraformaldehyde (PFA) in PBS at 4℃ for 30 min. Cells were washed in PBS (3 times; 5 min each) then permeabilized with 0.2% Triton X-100 in PBS for 15 min at room temperature and blocked with 10% goat serum in PBS for 1 hr or overnight at 4℃. The cells were then incubated with an antibody raised in rabbit against VE-cadherin at a dilution of 1:400 in blocking solution for 3 hours at room temperature, followed by Alexa Fluor 488 goat anti-rabbit secondary antibody diluted 1:1000 in PBS for 1 hr. Finally, nuclei were labeled by incubating the cells for 5 min at RT in 2 μg/mL DAPI in PBS and mounted in ProLong® Diamond anti-fade reagent. Images were acquired using a Leica SP5 confocal microscope with a 20x objective.

3.3.8 Statistical Analysis

To analyze our data, we performed a two-tailed Student's *t*-test analysis to determine the statistical differences between treatment groups. The statistical significance threshold was taken to be a P value of 0.05. Results are expressed as mean $\pm$ 1-standard deviation (SD).

3.4 Results and Discussion

3.4.1 Characterization of Unbound Peptides to Nitration

To characterize the sensitivity of unbound peptides to nitration, each peptide was solubilized and treated with saturating levels of peroxynitrite (0.5 mM) in PBS for 1 hour at 37℃. 3-Nitrotyrosine yields were measured at 430 nm using UV-Vis spectrophotometry (Figure 3.2). P1 (EKKDFYKDGKRL; derived from PGI_2 synthase) was the most susceptible to peroxynitrite-mediated nitration, exhibiting a 69-fold increase in 3-nitrotyrosine signal compared to vehicle-treated control (0.231 $\pm$ 0.018 vs. 0.003 $\pm$ 0.001; N = 3; p = 0.002). P2 (GKRLKNYSLP; also derived from PGI_2 synthase) showed a 52-fold increase in 3-nitrotyrosine signal compared to vehicle-treated control (0.163 $\pm$ 0.006 vs. 0.003 $\pm$ 0.001; N = 3; p = 0.0006). P3 (LHHSKHHAAYVNNLNV; derived from MnSOD) displayed a high background signal (see Supplementary Figure 3.7) and exhibited only a 5-fold increase in 3-nitrotyrosine signal compared to vehicle-treated control (0.104 $\pm$ 0.045 vs. 0.022 $\pm$ 0.012; N = 3; p = 0.07). P4 (GGREYYY) containing three tyrosines yielded a 39-fold increase in 3-nitrotyrosine signal compared to vehicle-treated control (0.117 $\pm$ 0.003 vs. 0.003 $\pm$ 0.002; N = 3; p = 0.0004). Additionally, we also examined the dose-dependent response of each peptide over a range of peroxynitrite concentrations (10 – 500 μM) to determine their relative detection limits (Supplementary Figure 3.7). Each peptide produced different levels of 3-nitrotyrosine signal in response to peroxynitrite-mediated nitration, suggesting that nitration is a selective process that is sensitive towards the local amino acid sequence.

Peptides P1 and P2, derived from PGI_2 synthase, were the most susceptible towards peroxynitrite-mediated nitration. The amino acid sequence of P1 consists of alternating acidic (E and D) and basic (R and K) residues in close proximity to the hydrophobic residues (F and Y), whilst P2 consists of mainly basic (R and K) and polar (N and S) residues adjacent to the target tyrosine. This may have created a local hydrophilic environment around the tyrosine residue, increasing the exposure and susceptibility of tyrosine residues to peroxynitrite-meditated nitration. In contrast, P3 derived from MnSOD, consists of several hydrophobic residues (H, A and V) that may limit the accessibility of peroxynitrite to the target tyrosine residue, thus resulting in lower 3-nitrotyrosine yield. P4 was designed with an acidic and basic residue proximal to three tyrosine residues to potentially amplify the tyro-

sine nitration signal. Interestingly, this peptide was outperformed by P1 and P2 suggesting that the nitration process is highly selective and sensitive towards the amino acid sequence, whilst the presence of additional tyrosines does not necessarily yield greater nitration. Additionally, the nitration of tyrosine residues within native proteins are not only influenced by the local amino acid sequence, but also the existence of secondary and tertiary structures. Most notably, the interaction between peroxynitrite and metal- or heme prosthetic group binding sites,[181] which promote the formation of secondary radicals that enhances peroxynitrite-mediated nitration. Therefore, the lack of secondary and tertiary structures in our peptide biosensors could exhibit lower nitration yields, which may reflect our results shown in P3. Furthermore, the detection limit for peroxynitrite-mediated nitration with UV-Vis was approximately 10 μM, which is not sensitive enough to measure basal physiological concentrations around 100 nM.[19,167] Therefore, to overcome this detection limit we incorporated immunochemical techniques specific towards 3-nitrotyrosine with our peptide-sensors to amplify the detection of nitrated peptides.

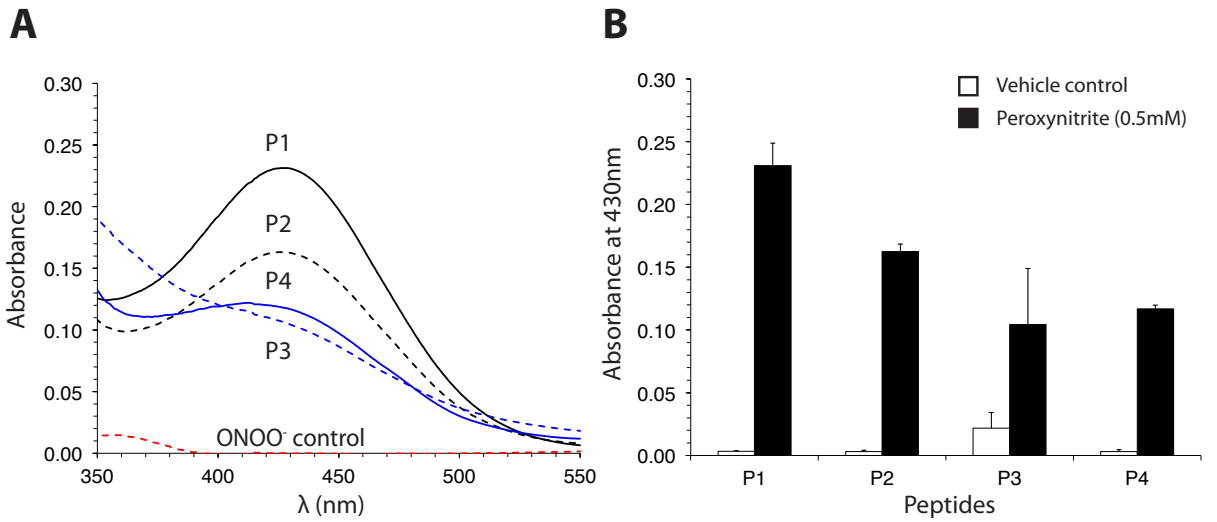


Figure 3.2: 3-Nitrotyrosine detection with UV-Vis spectrophotometry. **(A)** Representative spectra of 3-nitrotyrosine detection for each peptide. Peptides (P1-4; 0.1mM) were exposed to peroxynitrite (0.5mM) in phosphate buffer (pH 7.4) for 1 hr at 37℃; nitration yields were determined with UV-Vis. The presence of 3-nitrotyrosine in P1 (solid black line), P2 (dashed black line), P3 (dashed blue line) and P4 (solid blue line) was shown as an increase in absorbance at 430nm, where it was compared to peroxynitrite alone (dashed red line). **(B)** Average 3-nitrotyrosine detection shown (black bars) compared to vehicle controls (white bars). Error bars represent SD.

3.4.2 Characterization of Peptide-NPs to Nitration

We conjugated the peptides to nanoparticles to confine and concentrate the peptide-sensors for immunochemical detection (Figure 3.3A). 3-Nitrotyrosine signal was detected by immunofluorescence using fluorescently-labeled antibody in a dot blot immunoassay. The sensitivity of each peptide-NP complex towards peroxynitrite-mediated nitration was determined by generating dose-response curves utilizing 0.01% (v/v) peptide-NP solutions treated with increasing concentrations of peroxynitrite (500nM – 500μM; Figure3.3B). P2-NPs was found to be the most sensitive towards nitration with an EC_{50} value of 8.4μM while P1, P3 and P4-NPs had EC_{50} values of 16, 35 and 91μM, respectively. We went on to determine whether the sensitivity of each peptide-NP complex towards peroxynitrite changes with respect to peptide-NP concentration (0.0015% v/v – 0.025% v/v; y-axis) over a greater range of peroxynitrite concentration (100 nM – 1 mM; x-axis), as shown in Figure 3.3C.

To better illustrate the relative sensitivities of each peptide-NP complex, the averaged 3-nitrotyrosine signal was presented in a pseudo-color-heatmap (N=3 per peptide-NP complex), as shown in Figure 3.3D. From the heatmap generated, P2-NPs exhibited the most consistent dose-dependent response with increasing peroxynitrite treatment that was independent of peptide-NP concentrations, whilst the other peptide-NPs showed more variability in fluorescence signal as a function of peptide-NP concentrations. When comparing the detection limits of these peptide-NP complexes, P2-NPs had the greatest sensitivity towards the lower ranges of peroxynitrite treatment achieving detection limits of $\sim$100 nM, whilst P1-NPs showed more variability in its detection of sub-micromolar levels of peroxynitrite. P3 and P4-NPs were both less sensitive towards peroxynitrite-mediated nitration, especially at the micromolar range of peroxynitrite. Moreover, both P3 and P4-NPs showed greater variability in its immunofluorescence signals compared to P1 and P2-NPs. These results are consistent with the UV-Vis data, showing a similar trend in peptide sensitivity towards peroxynitrite-mediated nitration, but with further enhanced detection sensitivity by 2-orders of magnitude (from 10 μM down to 100 nM) for P1 and P2-NPs. Taken together, this suggests that P1 and P2-NPs may be the better candidates for detecting low levels of NO-derived oxidants, affirming the use of immunochemical detection methods to amplify the signal and detection limit of our peptide-sensors platform.

One limitation of the peptide-bound NPs is the potential loading differences on the surface of the nanoparticles, which could be attributed to the individual peptide sequences. These potential loading differences could reflect differences in detection sensitivity between peptide-NP complexes. Hence, our platform focuses on the relative change in 3-nitrotyrosine signal of each peptide-NP complex and it's ability to detect different levels of peroxynitrite-mediated nitration.

3.4.3 Detection of Shear-Mediated Nitric Oxide Produced by HUVECs

To determine whether our peptide-NPs can detect NO production by living cells, we introduced the peptide-NPs into the circulating media of an *in vitro* shear stress model lined with human umbilical vein endothelial cells (HUVECs) whilst under different levels of shear stress over 24 hours (Figure 3.4A). Endothelial cells are shear responsive,[88,221] exhibiting changes in cell morphology, and increased NO production in response to shear stress. HUVECs were exposed to either low (1.5 dynes/cm^2) or high (15 dynes/cm^2) physiological levels of shear stress. Cells exposed to low shear did not align in the direction of flow or exhibit any obvious changes in cell morphology (Figure 3.4B). In contrast, cells exposed to high shear aligned in the direction of fluid flow after 24 hours, changing their morphology from cobblestone-like to elongated spindle-shaped, as demonstrated by immunolabeling for the endothelial cell-cell junctional protein VE-cadherin (Figure 3.4C).

To determine the level of NO produced by the cells, the flow-through media collected from each individual experiment was centrifuged and separated into the following: (i) the supernatant, which was used for the traditional Griess reaction assay and (ii) the peptide-NPs, which was used for the 3-nitrotyrosine immunoassay (as shown in Figure 3.5A). The Griess assay served as a positive control for NO detection, and a basis for comparison against our NO-detection platform. Results showed that cells exposed to higher levels of shear stress (15 dynes/cm^2) resulted in increased levels of nitrite in the media when compared to the low shear condition (1.5 dynes/cm^2) (1.82 $\pm$ 0.62 μM vs. 0.98 $\pm$ 0.33 μM; N = 24 vs. 22; P < 0.001) after 24 hours exhibiting a $\sim$2-fold increase in NO production (Figure 3.5C; left panel), consistent with previous findings.[11]

To compare the relative nitration yields for each peptide-NP complexes, the pelleted peptide-NPs were dot-blotted and analyzed for 3-nitrotyrosine signals after 24 hours of low and high shear

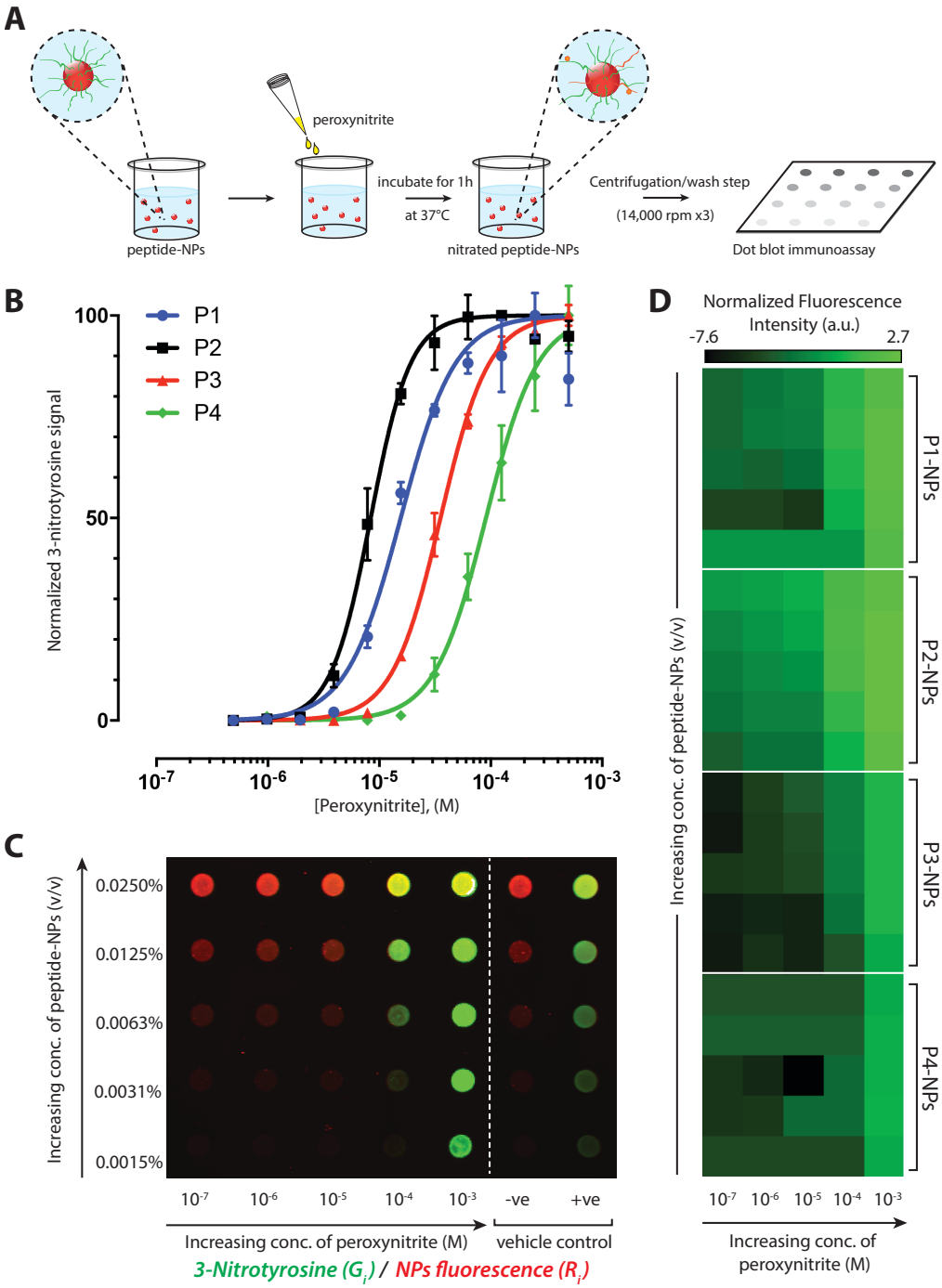


Figure 3.3: Representative immunoassay of peroxynitrite-induced nitration of nanoparticle-complex. **(A)** Schematic representation of peptide-nanoparticle complex treated with peroxynitrite in a 96-well plate and incubated at 37°C for 1 hr, followed by centrifugation/wash step (at 14,000 rpm for 10 min – x3) and dot blotted onto a nitrocellulose membrane. **(B)** Dose-response curves of each peptide-nanoparticle complex as a function of increasing concentration of peroxynitrite (500nM – 500μM). Peptide-nanoparticles were loaded at 0.01% v/v concentration (N=2). **(C)** Representative immunoarray of 3-nitrotyrosine detection sensitivity as a function of concentration of peptide-nanoparticles or peroxynitrite. Nanoparticle auto-fluorescence is shown in red; anti-nitrotyrosine immunofluorescence signal is shown in green; vehicle treated controls: [sodium hydroxide (0.3 M NaOH; -ve); 3-nitrotyrosine-conjugated nanoparticles (+ve)]. Fluorescence was detected with an two-channel infra-red scanner (Odyssey; Licor). **(D)** Averaged fluorescence intensity of 3-nitrotyrosine detection as a function of peptide-nanoparticles concentration (y-axis; same concentrations as panel C) or peroxynitrite concentration (x-axis) presented in a heat map (N=3). Each dot blot fluorescence signal was normalized against the nanoparticles auto-fluorescence to account for variations nanoparticle concentration. Normalized fluorescence intensity (G*) is shown on a log-scale to show the sensitivity of the 3-nitrotyrosine antibody signal.

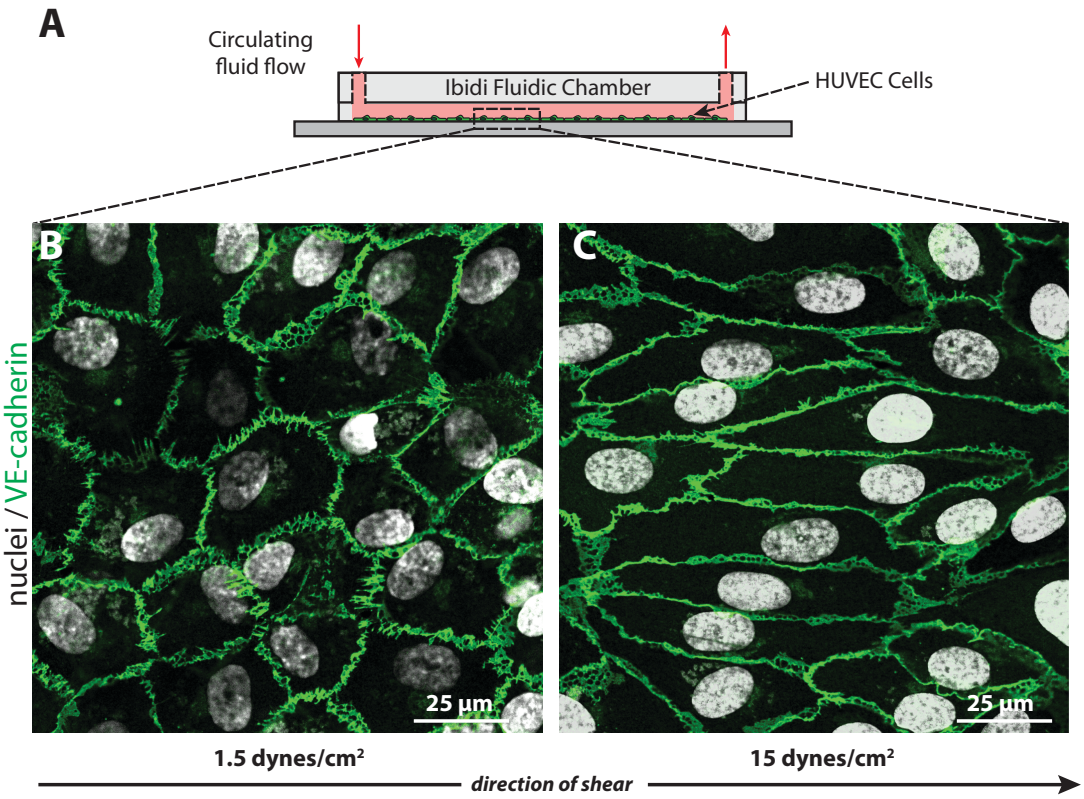


Figure 3.4: HUVECs exposed to different levels of shear stress. HUVECs were sheared under low and high shear stress for 24 hours with peptide-nanoparticles circulating in the culture media. HUVECs at low shear (1.5 dynes/cm^2; left panel) exhibited the characteristic cobblestone morphology, whilst HUVECs exposed to high shear (15 dynes/cm^2; right panel) showed elongated cell shapes aligned with the direction of flow. Cells were stained for nuclei (white) and junctional proteins as an indication of cell monolayer confluency (VE-cadherin; green), which localized to cell borders. The arrow indicates the direction of laminar flow applied to the cells.

stress (Figure 3.5B). Each of the peptide-NP complexes were able to detect NO production at both low and high levels of shear stress. When comparing the averaged 3-nitrotyrosine signals (Figure 3.5C; right panel), P1-NPs had the highest fluorescence signals but also exhibited greater variability in fluorescence signal between experimental samples, which resulted in a $\sim$3-fold increase in shear-induced nitration when comparing the high shear to low shear condition (N=6 and N=5, respectively; $P<0.05$). P2-NPs had the second highest fluorescence signals whilst exhibiting less variability between experimental samples, which resulted in the best signal-to-noise ratio with a $\sim$5-fold increase in 3-nitrotyrosine signal when comparing the high shear to low shear condition (N=6 and N=5, respectively; $P<10^{-5}$). These results are consistent with the nitration immunoassay previously shown in Figure 3.3. P3 and P4-NPs had lower fluorescence signals but was still able to detect changes in NO production when exposed to low and high shear stress. For the high shear condition, the average fluorescence intensities increased by $\sim$4-fold for both P3 and P4-NPs (N=6 for each condition, $P<10^{-5}$ and $P<0.05$, respectively) when compared to low shear. Interestingly, from these results the

novel peptide (P4) designed with features that enhance nitration did not outperform the bio-inspired peptides (P1, P2 and P3) in detecting NO-induced peroxynitrite nitration, suggesting that the nitration process is highly selective and sensitive towards the amino acid sequence and the presence of additional tyrosines does not necessarily yield greater nitration.

The nitration of these peptide-NP complexes are governed by the peroxynitrite-mediated pathway, which is generated through a diffusion-limited reaction between NO and $O_2^{\bullet}-$. Elevated shear stress is known to increase NO production by endothelial cells[88,221], but simultaneously, increased shear stress could also lead to an increase in $O_2^{\bullet}-$ production in blood vessels with an impaired endothelium[96]. Therefore, these peptides could potentially be detecting an increased production of $O_2^{\bullet}-$ in addition to NO, although uncoupling the interaction between NO and $O_2^{\bullet}-$ remains to be determined. Additionally, when comparing between high and low levels of shear stress, increased flow rates at the high shear condition could also promote better mixing and detection of NO compared to low shear conditions, which could potentially bias the detection of NO production. In spite of these potential limitations, we demonstrated that our peptide-NP platform could detect shear-induced NO production by HUVECs in culture, through the highly selective and specific nitration process, whilst also achieving greater dynamic range and sensitivity towards NO detection than the traditional Griess assay.

3.5 Conclusions

In summary, we have demonstrated that our bio-inspired peptides can be utilized as potential biosensors to detect low levels of NO *in vitro* by exploiting the highly selective nitration process. Each of the peptide-sensors consists of specific amino acid sequences that promote nitration when exposed to NO-derived oxidants, which result in the detection of a stable by-product – 3-nitrotyrosine. The relative sensitivities of each peptide-sensor was charaterized with UV–Vis, achieving a detection limit of 10 μM for peroxynitrite-mediated nitration. This detection limit was further enhanced by 2-orders of magnitude (from 10 μM to 100 nM) by conjugating the peptide-sensors to fluorescent nanoparticles to concentrate the 3-nitrotyrosine signals for immunoassay detection. Finally, we demonstrated that our peptide-NP complexes can successfully detect NO release from

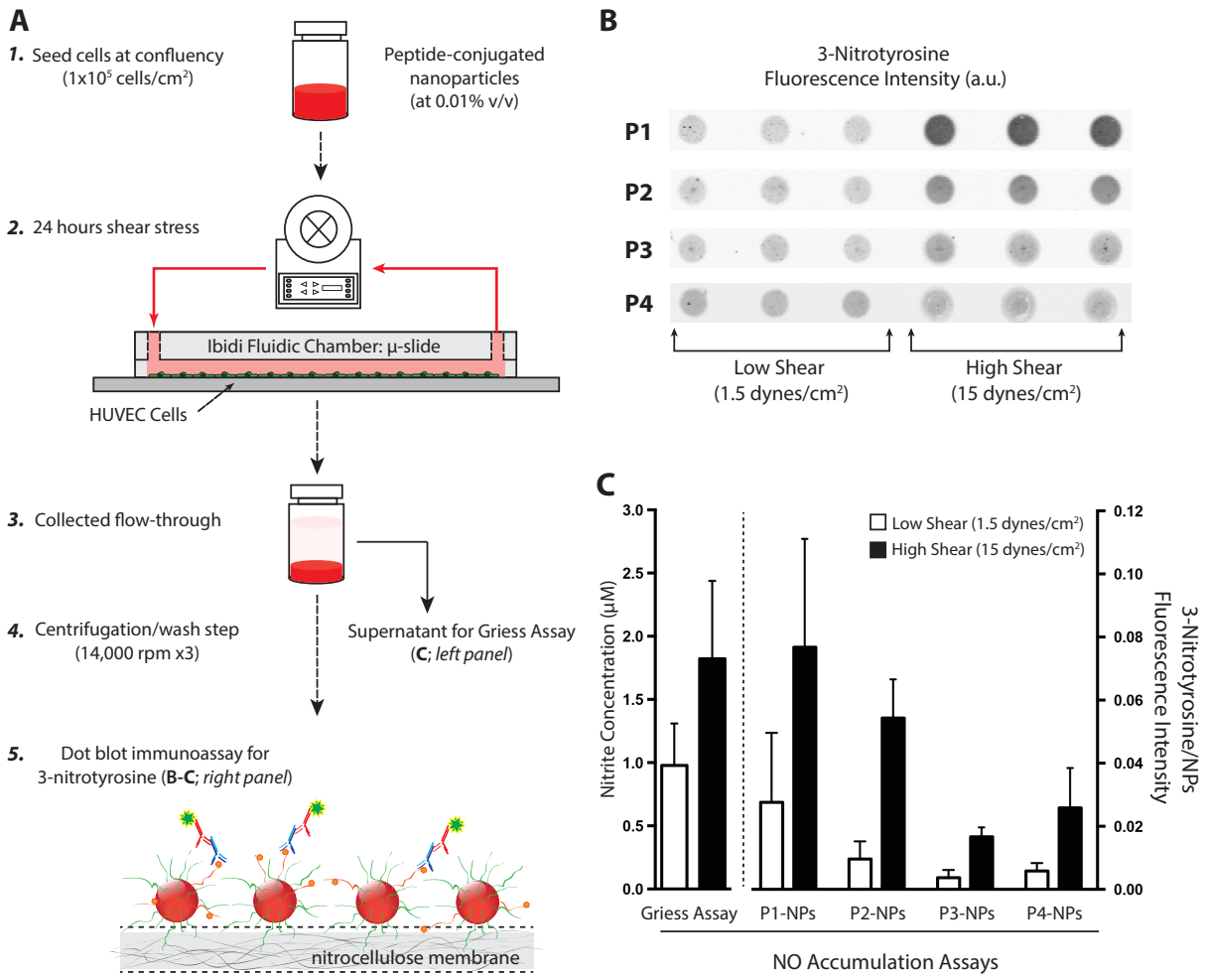


Figure 3.5: 3-Nitrotyrosine detection of cells under shear stress. **(A)** Schematic representation of HUVECs cultured under low and high shear with the presence of circulating peptide-nanoparticle complex to detect NO production. Step 1: Cells were seeded at confluency ($1x10^5$ cells/cm^2) and allowed to acclimate overnight (18-24 hours). Step 2: Each μ-slide was loaded with peptide-nanoparticle complex (at 0.01% v/v) at the start of the shear experiments. Step 3-4: After 24 hours of shear stress, both media and nanoparticles were collected and pelleted. Step 5: Peptide-nanoparticles were washed and analyzed for 3-nitrotyrosine formation (panel B). The collected media was stored for nitrite detection (by Griess assay). **(B)** Representative dot blot immunoassay comparing the amount of 3-nitrotyrosine binding for each peptide-nanoparticle complex (P1-4) under either low or high shear stress. For each peptide-nanoparticle complex six individual experiments were conducted, each with triplicate measures per experimental condition. **(C)** Comparison of NO accumulation assays. *(Left)* Griess reagent assay detection for nitrite concentration. Nitrite release (24 hours – accumulation) was assayed from the supernatant of each sheared experiment. Data shows the averaged nitrite release from HUVECs between low vs. high shear (N = 22 vs. 24; $p<0.01$). *(Right)* Averaged 3-nitrotyrosine signal for each peptide-nanoparticle complex normalized against nanoparticles auto-fluorescence to account for loading differences. Data are expressed as mean$\pm$SD for all shear experiments (N=6) except for P1 and P2-NPs at low shear with only N=5 each. Error bars represent SD.

endothelial cells in response to different levels of shear stress, exhibiting an increased sensitivity towards changes in NO production ($\sim$5-fold increase in 3-nitrotyrosine signal; P2-NPs) over the traditional Griess assay ($\sim$2-fold increase in nitrite signal), where both detection assays provide an integrated NO signal over the time course of the experiment. The development of this NO detection platform lends itself to a multitude of potential applications; for example, the NO-sensors may

be introduced into the circulation to access specific tissues of interest to monitor NO activity in situ (e.g. the progression of neurodegenerative diseases caused by NO dysregulation[86,114,207,243]); the NPs may be functionalized to target specific tissues to detect "localized" NO production (e.g. the localized detection of pressure-induced NO production in the trabecular outflow pathway in the eye[42,100,102,211]); and potential cell-based/therapeutic screening of basal peroxynitrite levels to monitor pro-nitroxidative stress in biological samples.

3.6 Supplementary Information

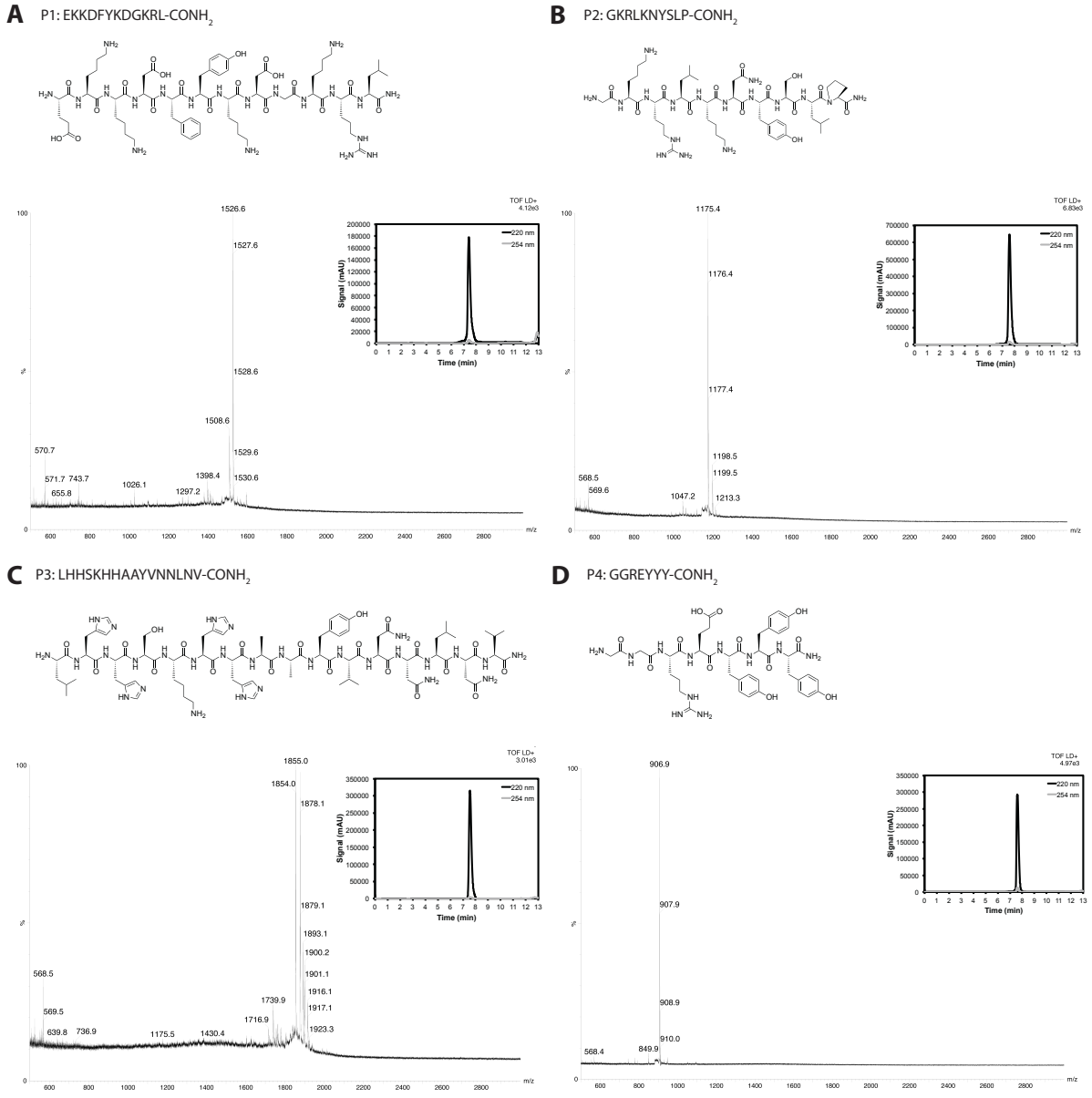


Figure 3.6: Chemical structures, MALDI and analytical HPLC trace of the purified peptide sensors. (A) P1: EKKD-FYKDGKRL (MW 1526). (B) P2: GKRLKNYSLP (MW 1175). (C) P3: LHHSKHHAAYVNNLNV (MW 1854). (D) P4: GGREYYY (MW 906).

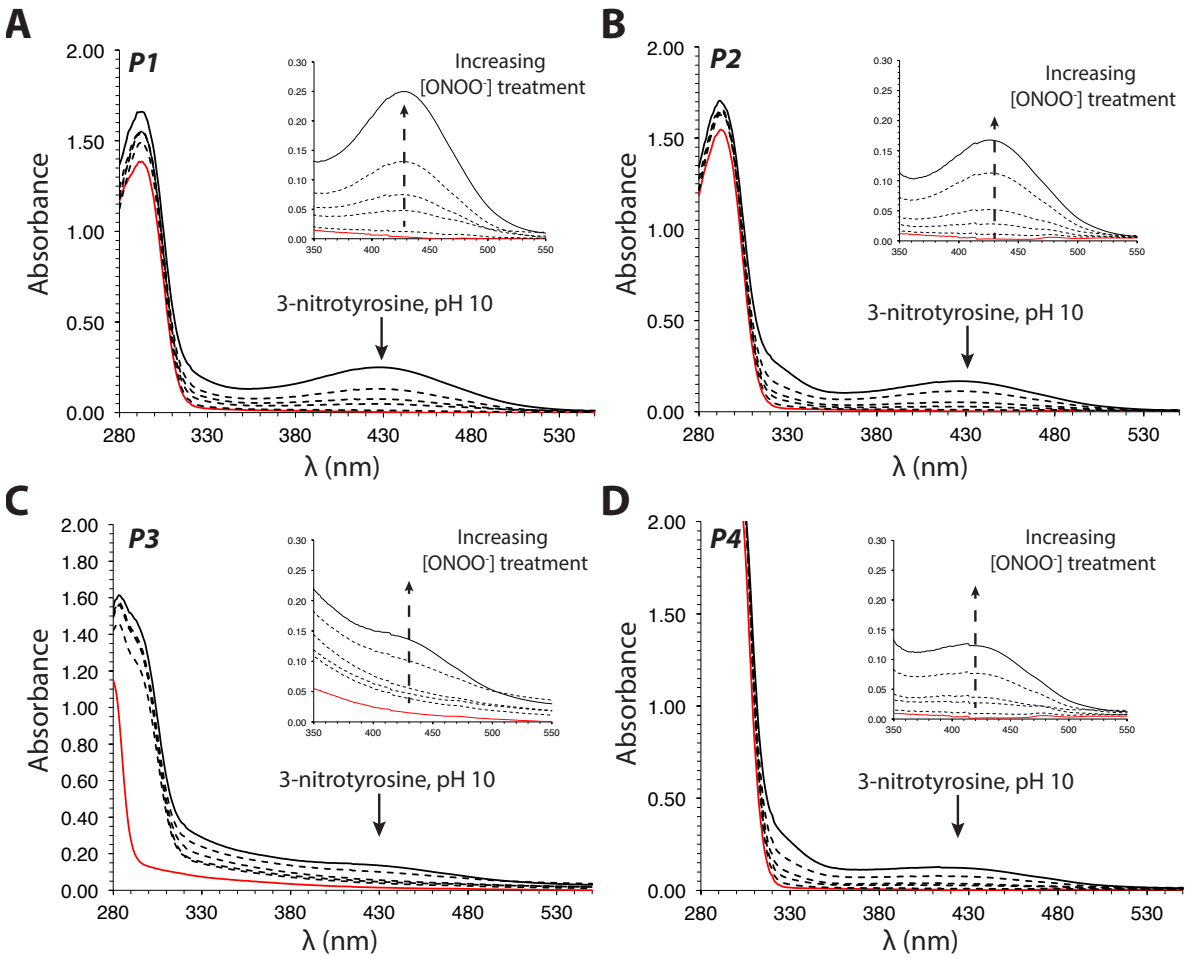


Figure 3.7: Nitration sensitivity of synthetic tyrosine-containing peptides with UV-VIS spectrophotometry. **(A-D)** Peptides (P1-4) sensitivity towards nitration as a function of increasing concentration of peroxynitrite treatment (10μM – 500μM; black lines). 3-Nitrotyrosine absorbance is measured at 430nm under basic conditions (~pH 10). *Red lines = vehicle treated controls.*

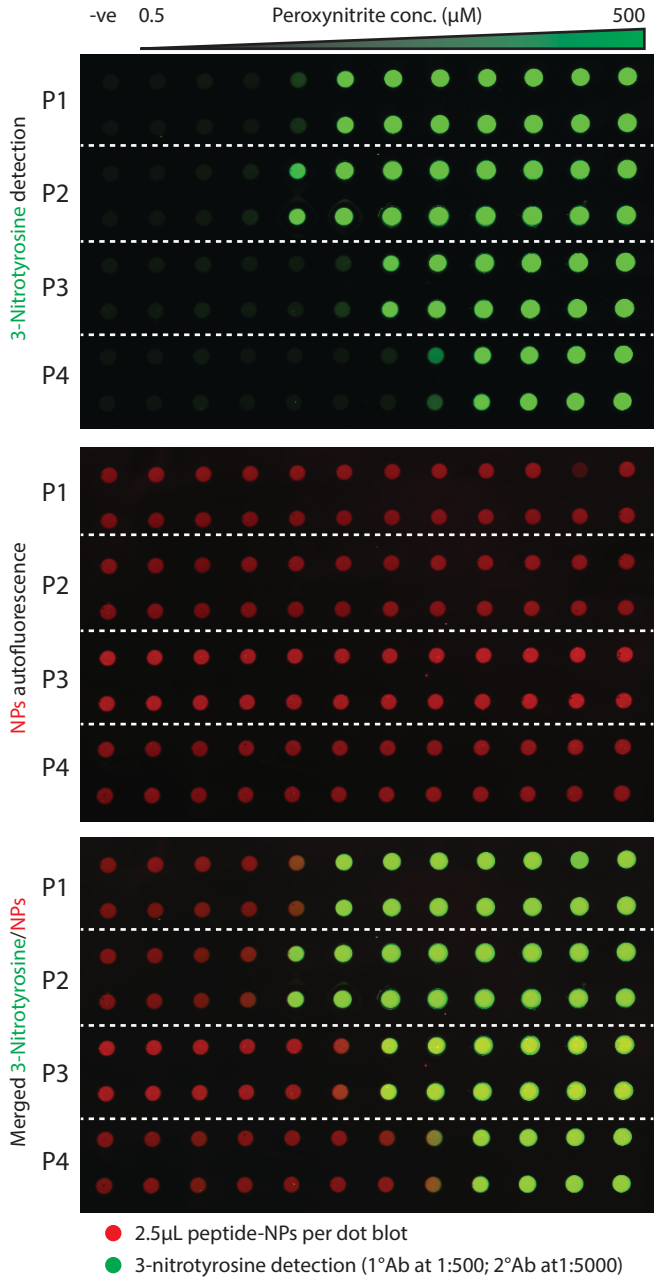


Figure 3.8: Representative peptide-nanoparticle complex dot blot sensitivity immunoassay. **(Top)** 3-Nitrotyrosine detection for each of the synthetic peptide-nanoparticle complexes with decreasing concentration of peroxynitrite treatment (green). **(Middle)** Auto-fluorescence of nanoparticles to quantify the loading concentration per sample (red). **(Bottom)** Overlay of 3-nitrotyrosine and nanoparticle auto-fluorescence.

3.7 Appendix A: Solid-phase peptide synthesis – (Fmoc)

The methods detailed in this section utilizes established protocols in solid-phase peptide synthesis, we will be using an automated peptide synthesizer (Symphony Quartet, Protein Technologies, Inc) to create our desired peptide sequence by following the subsequent steps (illustrated in Figure 3.9).

i. **Preparing resin for amine-terminated peptides**

Firstly, we start with a Rink amide MBHA resin (AGTC, UK) which has been functionalized with a protected amine supported by a insoluble polystyrene bead via an acid-labile linker; the amine group are protected by a temporarily base labile α-amino protecting group, Fmoc. In order to obtain maximum binding between the desired amino acid and resin, we need to "swell" the resin in dichloromethane (DCM) which exposes the amine binding sites on the resin by 3-5 fold. The resin will then be agitated on a shaker for at least 30 minutes, before filtering off the DCM from the peptide synthesis vessel leaving only the resin behind.

ii. **Fmoc deprotection**

In order to prepare for the amino acids (AA) to couple to the resin, we need to deprotect the amine group attached to the resin, with 20% piperidine in dimethylformamide (DFM) solution. This solution was added to the reaction vessel and left on the shaker for 5-10 minutes and then drained; this Fmoc deprotection step was carried out twice to ensure all the protecting groups are off and the amine group are exposed. Wash steps follow after, in the order of DMF wash (2x), then DCM (2x).

iii. **Amino acid coupling**

Once the resin has been washed, we can then measure out 4x molar excess Fmoc amino acid (in our case - tyrosine (Y)). Add **4: 3.95: 6** ratio of **AA: HCTU**[1]**: DIPEA**[2], all of which are relative to resin. For example, for 0.25 mmol resin, measure out 1 mmol of amino acid, 0.95 mmol of HCTU, 1.5 mmol of DIPEA; hence we always want more amino acid than HCTU. Now we add 20mL of DMF to the amino acid coupling cocktail and vortexes throughly to completely mix and dissolve all components. Leaving this mixture to incubate at room temperature for $\sim$2-3 minutes

[1] HCTU=(2-(6-Chloro-1H-benzotriazole-1-yl)-1,1,3,3-tetramethylaminium hexafluorophosphate)
[2] DIPEA = N,N-Diisopropylethylamine

to allow for the activation of the -COOH group. *Note: The HCTU was used to activate the carboxyl group of the Fmoc amino acid under basic conditions (hence the addition of DIPEA) to react with the free amine on resin.* Now the amino acid coupling cocktail are ready to be added to the peptide reaction vessel, and placed on the shaker for ∼1-2 hours or even left reacting overnight. This was then followed by draining the synthesis vessel and wash steps were carried out; DMF (3x) whilst agitating the resin followed by wash with DCM (2x).

iv. **Cleaving the peptide from the resin**

When cleaving the peptide off the resin, we need to make sure that we have removed the final Fmoc on the last amino acid before cleaving. The cleaving solution consists of 95% Trifluoroacetic acid (TFA), 2.5% TIS, and 2.5% water by volume[3]. Now we fill the vessel ∼ 1/2 full of the cleavage solution, and place on the shaker for at least 2 hours but no more than 5 hours. Once the cleavage is complete, we drain the vessel into a round bottom flask, whilst using DCM to wash the resin and drain DCM into the flask. Now we can use the rotary evaporator (rotavap) to remove the DCM and TFA off the sample leaving the peptide. This was then followed by precipitating the peptide in cold diethyl ether and washed with ether, which helps recover the peptide and also purifies out the protecting groups (which are soluble in ether). For ether washes, we centrifuge the solution at 6500rpm at 4℃ for 10 mins, wash steps were repeated two extra times (with fresh cold ether). Once the peptide precipitate was washed, it was then put in a vacuum desiccator overnight to remove the residual ether. This was then followed by dissolving the peptide in milliQ water, freezer at -80℃ and lyophilized on the freeze dryer and stored at 20℃ before purification.

v. **Peptide evaluation**

To evaluate the composition of our peptide synthesis, a preliminary (crude) mass spectral analysis was conducted to determine the molecular weight of the sample. This was then followed by high-performance liquid chromatography (HPLC) to determine the purity of the sample, and preparative HPLC were used to fragments of the desired peptide, filtering out the fragments that are a by-product of the peptide synthesis. HPLC was done on a water/acetonitrile gradient under acidic conditions (0.1% TFA). The collected fragments can then be pooled together and sent for further mass spectral analysis and analytical HPLC to determine the final purity of the peptide.

[3]Note: this cleavage solution is designed for peptides without cysteine or tryptophan amino acids

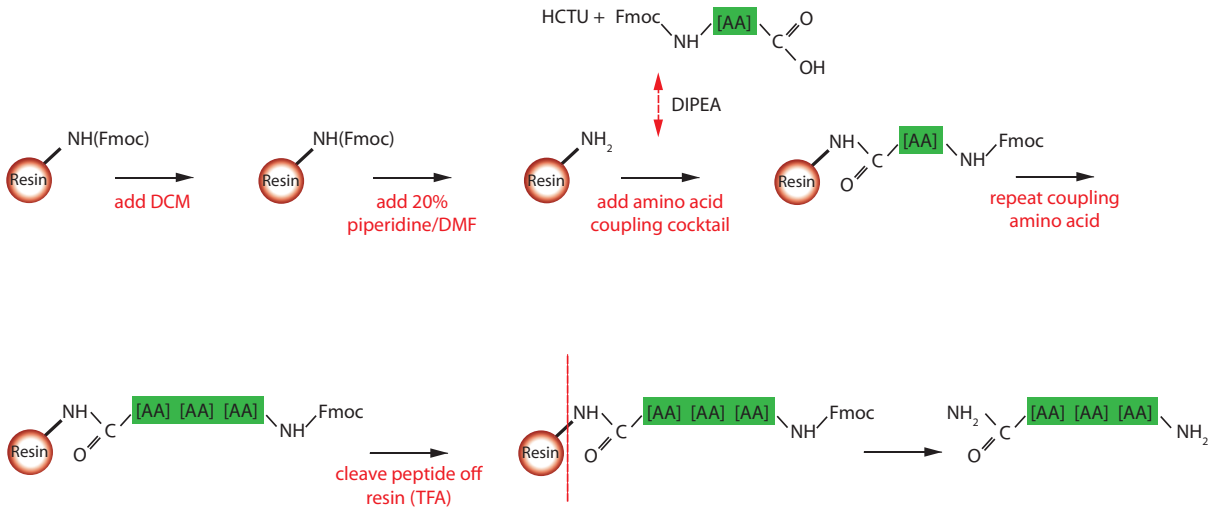


Figure 3.9: Schematic diagram of peptide synthesis.

Chapter 4

Preferential Outflow in Relation to Endogenous eNOS Activity in the Murine Conventional Outflow Pathway

This chapter consists of a paper in preparation for submission to PLoS Biology.

4.1 Introduction

Aqueous humor outflow regulation plays a central role in maintaining normal ocular function and physiology. The balance between aqueous humor production and outflow determines intraocular pressure (IOP). Increased outflow resistance results in elevated IOP, a key contributor to the pathogenesis of glaucoma.[210] The majority of outflow resistance is generated within close vicinity of the inner wall endothelium of Schlemm's canal (SC), its underlying basement membrane and juxtacanalicular connective tissue (JCT) of the trabecular meshwork (TM)[117,166]. These resistance sites are located in the iridocorneal angle, which encircles the anterior portion of the eye and serves as regulators of aqueous humor drainage in the conventional outflow pathway. However, the mechanism(s) responsible for modulating these resistance sites are not well understood.

Aqueous humor filtration is non-uniform or "segmental" around the circumference of the outflow pathway, such that only a fraction of the trabecular meshwork is considered filtration-active at any given instant. Previous studies have used tracers such as cationic ferritin[53,70,100] and fluorescent nanoparticles[42,102,123,143,231], to decorate and identify preferential drainage routes in the outflow pathway. These segmental filtration patterns are presumably associated with regional variations in local hydraulic conductivity[1] and have been linked to variations in the extracellular matrix (ECM) composition[122,123,218,231], pores in the SC[29] and/or the local architecture of the outflow tissues[17,102,143,144,242]. It should be recognized that despite segmental outflow in healthy individuals, IOP is maintained within a narrow range of pressures throughout their lifetime[50,127], suggesting that a regulatory mechanism must be involved in maintaining IOP homeostasis. In contrast, in glaucomatous eyes, the filtration-active regions of the meshwork appear to be further reduced in comparison to normal human eyes[53], which further exacerbates the local hydraulic conductivity of the outflow pathway contributing to elevated IOP[211]. Hence, understanding the mechanism(s) controlling segmental outflow could contribute towards the development of more efficacious treatments for glaucoma.

Recent studies have shown that nitric oxide (NO) increases aqueous humor outflow by decreasing outflow resistance and subsequently IOP in several species[24,62,65,111,158,191,211]. In partic-

[1]The hydraulic conductivity L_p is defined as the ratio of flow rate (Q) to the pressure drop (ΔP) across the resistive barrier, normalised by the area (A) of the barrier. Hence, $L_p = Q/\Delta P * A$.

ular, our previous study[43] showed that exogenous delivery of NO leads to increased outflow facility in wild-type mice, whilst the pharmacological inhibition of endothelial NO synthase (eNOS) leads to a decrease in outflow facility. Moreover, data indicates that in both human SC cells[11] and porcine angular aqueous plexus cells (the porcine equivalent of SC cells)[135] are shear-sensitive, producing NO in response to increasing shear stress, similar to vascular endothelial cells[44,45]. Interestingly, the lumen of SC narrows as IOP increases, which effectively reduces the cross-sectional area of the lumen[120] and increases the shear stress experienced by the SC cells, reaching levels known to activate eNOS in vascular endothelia[58,73,91,201]. We hypothesize that eNOS plays a crucial regulatory role in maintaining IOP homeostasis, by modulating the local outflow resistance sites within the TM in part through NO. Furthermore, genome-wide association studies[121,141,174] have linked polymorphisms in the *NOS3* gene that encodes eNOS to the pathogenesis of glaucoma. Consistent with this notion, this homeostatic mechanism may become impaired in glaucomatous eyes, in which NOS activity in the conventional outflow pathway appears to be reduced[157]. Taken together, these data suggest that endogenous NO signaling within the conventional outflow pathway by eNOS may be involved in physiological regulation of aqueous humor outflow. We therefore hypothesize that NO release from SC cells contributes to the regulation of local hydraulic conductivity in the TM, and thus may contribute towards changes in segmental outflow.

In this study, we investigate two hypotheses: 1) that spatial variations in eNOS expression within the SC lumen correlates with the segmental filtration patterns in the TM, and 2) increases in IOP results in the up-regulation of eNOS promoter expression and activity leading to increased NO production in the conventional outflow pathway. To test these hypotheses, fluorescent nanoparticles (tracers; NPs) functionalized with a NO-sensitive peptide sequence were perfused into enucleated eNOS-GFP transgenic mouse eyes to label the outflow pathway. The spatial expression of eNOS-GFP, tracer distribution and NO-detection with the biosensor in relation to perfusion pressure were all visualized with flat-mount *en face* confocal microscopy.

4.2 Materials and Methods

4.2.1 Experimental Design

This study investigated the relationship between endogenous eNOS expression within the SC endothelium and the segmental outflow patterns in the TM, to determine whether these flow patterns change in response to pressure in enucleated mouse eyes. Our studies use *ex vivo* mouse eyes, because the conventional outflow pathway in mice is anatomically and functionally similar to that in humans[26,165,204,205] and pharmacological modulation of outflow facility in mice resembles the responses previously reported in human eyes[25]. Eyes were obtained from transgenic mice expressing GFP driven by the human eNOS promoter (eNOS-GFP) superimposed on the C57BL/6 background expression of endogenous eNOS. This study is divided into three parts: (1) to examine whether the spatial variations in eNOS expression in the SC relates to segmental outflow patterns in the TM; (2) to investigate whether the spatial variations in eNOS expression are sensitive to changes in pressure; and (3) to examine whether elevated IOP correlates to higher production of NO *in situ*. To investigate these goals, mouse eyes were perfused with fluorescent NPs, which served as tracers to decorate the flow patterns. Additionally, the nanoparticles were functionalised with a peptide sequence sensitive towards NO-derived oxidants that drives the nitration process of tyrosine residues, resulting in the formation of 3-nitrotyrosine (3-NT), which serves as an *in situ* sensor for detecting local changes in NO production through immunochemical detection (ref. Chapter 3).

4.2.2 Animal Husbandry

All experiments were conducted in compliance with the ARVO Statement for the Use of Animals in Ophthalmic and Vision Research under UK Home Office Project License approval for research at Imperial College London. Perfusions were performed with enucleated *(ex vivo)* eyes from mice of either gender. eNOS-GFP mice were aged 10 to 15 weeks. Mice were housed in individually ventilated cages, fed ad libitum and maintained at 21℃ with a 12-hour light (6 AM to 6 PM) and 12-hour dark cycle.

Mouse Genotyping

Transgenic mice express the human gene variant of the eNOS promoter fused to green fluorescent protein (GFP; as a reporter) on a C57BL/6 background. The transgene contains the human eNOS promoter region only, such that transgene expression is regulated by endogenous transcriptional activity but there is no over-production of nitric oxide. In these animals, GFP expression has been shown to be specific to endothelial tissues, with no increase in endogenous NO-production. Transgenic mice were a kind gift from Prof. Rob Krams (Imperial College London, UK) and Prof. Rini de Crom (Erasmus MC, Rotterdam, The Netherlands). Genotyping of transgenic mice was performed to detect sequences of GFP and the human variant of eNOS promoter present in the genome of eNOS-GFP mice but are absent from the genome of WT mice. Genotyping was performed using ear tissue samples obtained at weaning, with tissue lysis and DNA purification performed according to manufacturer's instructions (Kapa Express Extract; Kapa- Biosystems, Cambridge, MA). Separate PCR reactions were performed using a hot-start mix (KAPA2G Robust HotStartReadyMix; Kapa- Biosystems, Cambridge, MA). For human eNOS promoter, 29 cycles were performed with an annealing temperature of 59.3℃ using the sense primer ACCAGGGCATCAAGCTCTTC and the antisense primer TCTGTGATGTGGCACCAGAC to yield a predicted product of 500 bp. These sequences are specific for the human eNOS promoter and are not predicted to react with C57BL/6 murine eNOS. For GFP, 29 cycles were performed with an annealing temperature of 59.9℃ using the sense primer AGCTGACCCTGAAGTTCATCTG and the antisense primer GACGTTGTGGCTGTTGTAGTTG to yield a predicted product of 327 bp. PCR products were resolved by gel electrophoresis (1% agarose) in the presence of DNA gel stain (SYBR Safe; Invitrogen, Carlsbad, CA). Bands were visualized on an imaging station (Biospectrum 500; UVP, Upland, CA).

4.2.3 Peptide-Nanoparticle Synthesis and Conjugation

The peptide (GKRLKNYSLP) was synthesized using standard Fmoc solid phase peptide synthesis chemistry on a Rink-amide MBHA resin, purified and confirmed with analytical HPLC and MALDI, as previously described (ref. Chapter 3). The purified peptide was then conjugated to the carboxyl-functionalised fluorescent NPs (200 nm) using standard EDC/NHS chemistry. Briefly, the nanoparticles were washed with 0.1M 2-(N-morpholino) ethanesulfonic acid (MES, pH 4.7) buffer,

followed by activating the surface carboxylic acids with 1-Ethyl-3-(3-dimethylaminopropyl) carbodiimide hydrochloride (EDC, ∼20mM) and N-hydroxysuccinimide (NHS, ∼50mM) for 15 min before conjugation. Once the carboxyl groups have been activated, the pH of the buffer was raised from 4.7 to 7.4 with phosphate buffered saline (PBS, Invitrogen) to improve the coupling efficiency. The peptide (at 1mM concentration) was then coupled to the NPs and incubated overnight on a temperature-controlled shaker at 4℃ (Thermomixer; Eppendorf). After incubation, the peptide-NP complex was washed with PBS three times; the unbound peptides were removed after each centrifugation step (10 min at 14,000 rpm). Finally, the peptide-NPs were re-suspended in PBS at 1% (v/v) stock solution. Prior to all perfusion experiments the peptide-NP containing solutions were sonicated to break up aggregates.

4.2.4 Fabrication of Microfluidic Chip

The microfluidic chips were constructed from polydimethylsiloxane (PDMS) using standard soft lithographic techniques. PDMS base and curing agent (Sylgard 184; Dow Corning, Wiesbaden, Germany) were mixed in a 10:1 w/w ratio. This mixture was then degassed and poured over a SU8 master and cured overnight at 65℃. The PDMS layer was peeled off and inlet and outlet holes were punched through. The device was treated with oxygen plasma for 30 seconds before sealing to a glass microscope slide and cured overnight at 65℃.

4.2.5 *Ex Vivo* Mouse Eye Perfusion

To examine the relationship between the spatial distribution of eNOS expression in the SC and the segmental outflow patterns in the TM, paired eyes were obtained from eNOS-GFP mice and perfused with a fixed volume of peptide-NPs (6.5 μL; $\sim$1x10^5 particles) to decorate the flow patterns. Additionally, to determine whether changes in IOP will affect the spatial distribution of eNOS expression, and thus in turn the segmental outflow patterns, the enucleated eyes were subjected to either 8 or 16 mmHg of applied pressure. In enucleated mouse eyes both episcleral venous pressure and aqueous humour production are reduced to zero, where typically episcleral venous pressure is between 6–9 mmHg *in vivo*[26,203]. Therefore, we used 8 and 16 mmHg of applied pressure for our

perfusions to simulate the pressure drop across the conventional outflow pathway resulting in a physiological and elevated IOP of 16 and 24 mmHg, respectively. Hence, treated eyes were perfused at elevated IOP (16 mmHg), while the contralateral control eyes were perfused at normal physiological IOP (8 mmHg). The perfusate used for all mouse eye perfusions consisted of PBS including divalent cations and 5.5mM D-glucose passed through 0.2 μm filter (referred to as "DBG"). The eyes were enucleated within 10 minutes of death by cervical dislocation and stored in PBS at 4℃ until perfusion, typically within 15 min. Experiments used paired contralateral eyes, which were perfused simultaneously on two identical iPerfusion systems[200], with the treatment assigned randomly to the either the left or right eye.

Our perfusion method follows previously described techniques[25,27,43,134,211]. Briefly, eyes were affixed to a support using cyanoacrylate glue to stabilize the eye and submerged in PBS in a thermo-regulated bath at 35℃. A 33-gauge beveled needle (Nanofil; World Precision Instruments, Europe; Hitchin, UK) was connected to a two-channel microfluidic chip, one channel filled with peptide-NPs (NPs line; *red*) and the other channel filled with DBG perfusate (DBG line; *black*). The microfluidic chip allowed for the careful control and delivery of small volumes of perfusate (DBG and peptide-NPs) to the eye. The eye was then cannulated with the tip of the needle positioned in the anterior chamber using a micro-manipulator (Figure 4.1A). The pressure and flow rate inside the eye were measured using a wet-wet differential pressure transducer (PX409, Omegadyne, US) and a flow sensor (SLG64-0075, Sensirion, Switzerland), respectively. The flow sensor was also used to monitor the volumes of each perfusate delivered to the eye. Each eye received three boluses of perfusate (6.5 μL each), consisting of (i) DBG, followed by (ii) peptide-NPs suspended in DBG and (iii) DBG (shown in Figure 4.1B). The initial DBG bolus served as an acclimatisation step that allowed the eye to stabilize at the applied pressure. The second bolus was the peptide-NPs, which served as both a tracer and a biosensor for *in situ* NO-detection. The final DBG bolus was used to flush the peptide-NPs circulating in the anterior chamber towards the meshwork. After each perfusion the eyes were fixed in 4% paraformaldehyde (PFA) overnight at 4℃.

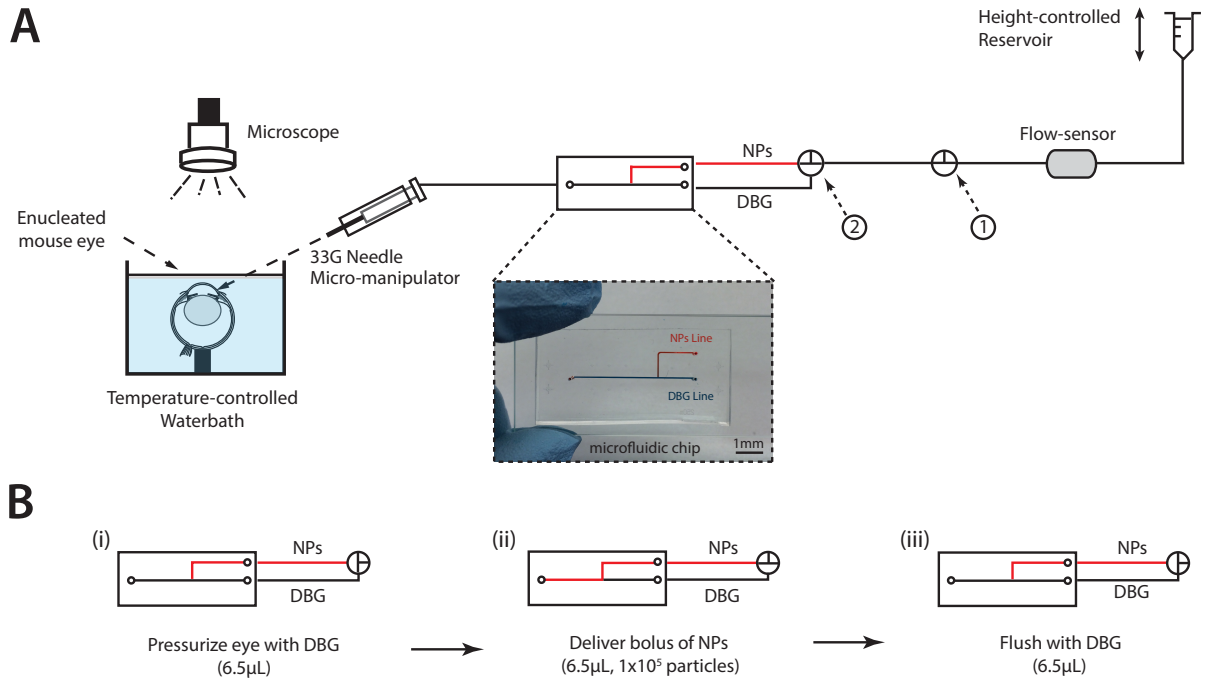


Figure 4.1: Schematic representation of controlled delivery of perfusates via a microfluidic chip. **(A)** The mouse eye is submerged in an isotonic bath at 35°C and is cannulated by a 33-gauge needle positioned into the anterior chamber using a micromanipulator while viewing under a stereomicroscope. The needle is connected to an upstream microfluidic chip with two-channels; (i) filled with DBG and (ii) filled with NPs. The three-way valves (1) and (2) controls which perfusate is delivered to the eye. The flow rate (F) and perfusion pressure (P_p) are measured by a flow sensor and pressure transducer upstream of the cannulated eye. **(B)** Schematic representation of the protocol for delivering a bolus of known concentrations of NPs to the eye. (i) The eye is pressurised from the reservoir at 8 or 16 mmHg with DBG, followed by (ii) delivering a bolus of tracers (6.5μL at a concentration of $\sim$1x10^5 nanoparticles), then (iii) flushing the eye with DBG to allow the tracers to reach the meshwork.

4.2.6 Anterior Eye Cup Flat Mounting

After immersion fixation, the eyes went through a series of PBS washes then hemisected just posterior to the limbus (see Figure 4.2). The lens and remaining retina were carefully removed to obtain the anterior eye-cups. The iris and ciliary body were left in place due to its close tethering to the trabecular outflow pathway[119,145,165], which if removed could damage and alter the segmental outflow patterns. Once the anterior eye-cups were obtained, four centripetal cuts were made to relax the eye-cup and facilitate flat mounting onto the slide. The anterior eye-cups were stored in 0.1%PFA until GFP-imaging and immunofluorescence was carried out.

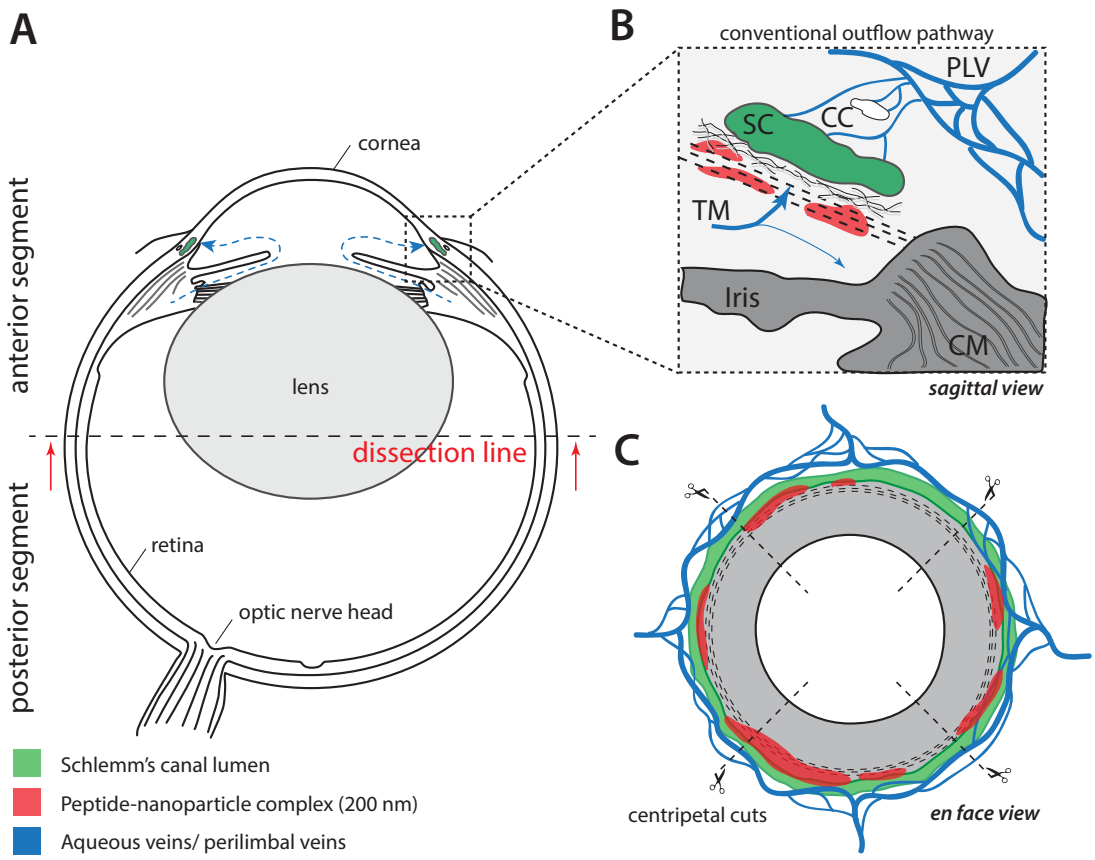


Figure 4.2: Schematic representation of flat-mount procedure to visualize segmental tracer distribution in the outflow tract.(**A**) The eye is enucleated and the anterior eye cup is dissected away along the equator of the eye (*red line*). Next, the lens are removed from the eye-cup leaving the iris and ciliary body intact. (**B**) Schematic representation of segmental tracer distribution viewed sagittally, as presented in cyrosections. (**C**) For flat-mount confocal imaging, four centripetal cuts were made to the anterior eye cups to relax the cup to facilitate mounting and image acquisition.

4.2.7 Immunofluorescence and Confocal Microscopy

Flat Mount Imaging

Anterior eye-cups were washed with 1x PBS multiple times after storage in 0.1% PFA. Each eye was first imaged with confocal microscopy (to visualize the eNOS-GFP signal and the segmental outflow patterns of the peptide-NPs) then followed by immunofluorescence staining (to visualize the 3-nitrotyrosine staining on the peptide-NPs) and re-imaged with confocal microscopy. The immunofluorescence staining was carried out after the first set of image acquisitions to account for possible loss of tracers during antibody incubation and PBS washes. For the immunofluorescence staining of 3-nitrotyrosine, the eye-cups were incubated in blocking buffer (10% goat serum and 1% Triton X-100 in 1x PBS) overnight at 4℃ to block nonspecific binding of antibody and permeabilize the tissue. This was followed by an additional blocking step with unconjugated Fab fragment goat

anti-mouse IgG (20 μg/mL; Stratech, UK) in 1% Triton X-100 and 1x PBS overnight at 4℃. Once the blocking steps were completed, the eye-cups were then incubated with goat anti-mouse monoclonal 3-nitrotyrosine antibody (1:100; MAB5404, Calbiochem) diluted in 200 μL of blocking buffer for 2 days, with rocking at 4℃. The eye-cups were washed three times over a 3-hour period with 1x PBS containing 0.1% Tween-20. The antigen was then detected with Alexa 546 goat anti-mouse IgG2b secondary antibody (1:500, Life Technologies) diluted in blocking buffer. The immunostained eye-cups were washed three times over a 3-hour period with 1x PBS. Eye-cups were then flat-mounted on slides in ProLong® Diamond anti-fade mounting media (Molecular Probes).

For confocal imaging, each eye was mounted with the cornea side down (facing the objective). The eNOS-GFP (Ex: 505 nm/ Em: 520 nm), 3-nitrotyrosine (560/575) and tracers (580/605) were imaged *en face* using a Leica SP5 confocal microscope with a 10x/0.4 NA dry objective. Images were acquired with the sequential scan mode to minimize potential bleed over between the 3-nitrotyrosine and tracer channels. The 'Tile Scan' mode was also used to automate collection of images and stitched together to create a montage encompassing the entire eye. Images were obtained as a z-stack starting from the external ocular surface of the corneoscleral shell (imaging the perilimbal vessels; PLV) and stretching 50–80 μm deep into the TM (Figure 4.3). During the acquisition of confocal images, each pair of eyes were imaged under the same confocal settings allowing for paired image analysis.

Cryosection Imaging

The expression and localization of eNOS-GFP in the conventional outflow pathway was examined by immunofluorescence microscopy of non-perfused eyes (N=2). Additionally, to confirm the specificity of the anti-nitrotyrosine antibody to the surface of peptide-NPs, perfused eyes (N=2) were also processed for sagittal cryosection imaging. Both set of eyes were immersion fixed in 4% PFA for 20 mins, followed by series of PBS washes then incubated in 20% sucrose in PBS overnight at 4℃. This was followed by a 1:1 mixture of 20% sucrose solution and cryostat embedding compound (Tissue-Tek OCT; Sakura-Finetek, Torrance, CA). The eyes were embedded in cryomolds (Sakura-Finetek), frozen on dry ice, mounted in a cryostat (Cryostat OTF/AS; Bright Instrument Co Ltd, Cambridgeshire, UK), and sagittally sectioned in steps of 7 μm. Cryosections were dried for

1 hour at room temperature, rehydrated in PBS, permeabilized in 0.2% Triton X-100 in PBS for 5 minutes and blocked in 10% goat serum in PBS for 30 min in a humidifying chamber at 37℃. The sections were incubated with goat anti-mouse 3-nitrotyrosine (1:100) or rat anti-mouse CD31 (1:100; Clone MEC 13.3, BD Pharmingen) IgGs in blocking buffer for 1 hour in a humidifying chamber at 37℃. The sections were then detected with the appropriate species-specific secondary antibody (either Alexa 546, or 594 at 1:500 dilution) in blocking buffer for 30 mins in a humidifying chamber at 37℃. PBS washes were carried out after each incubation step. The sections were then mounted in anti-fade media and imaged with a 20x/0.7 NA multi-immersion objective.

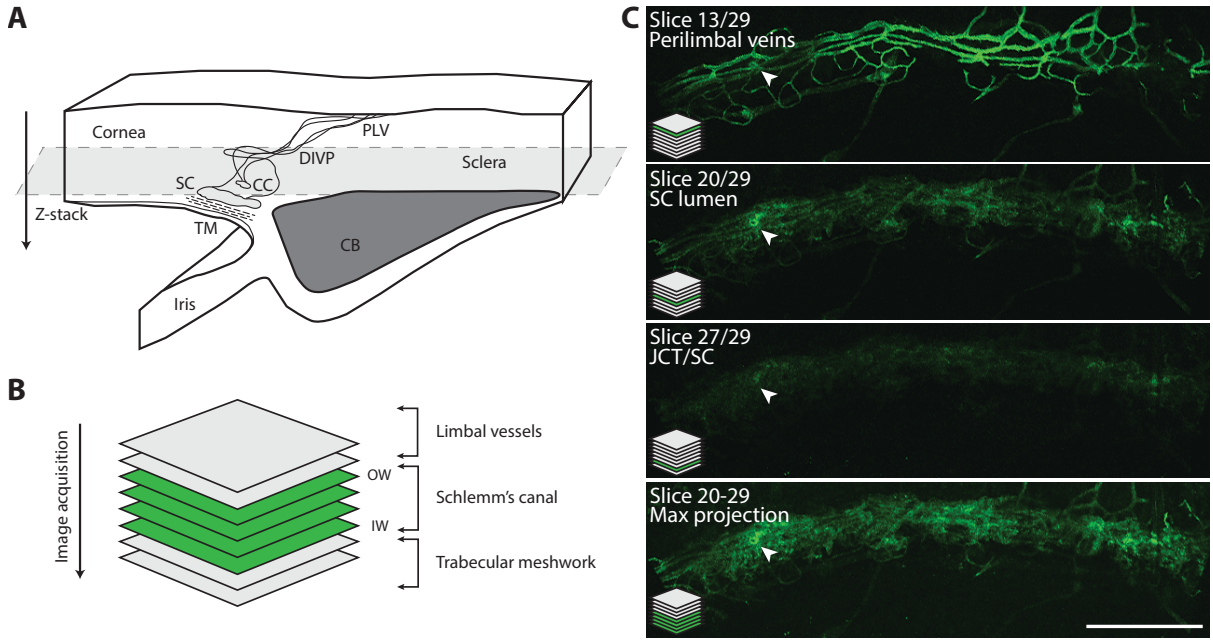


Figure 4.3: eNOS-GFP expression throughout the conventional outflow pathway visualized using flat-mount mouse eyes. **(A)** Schematic drawing of conventional outflow pathway as imaged in the transverse plane. **(B)** Representative Z-stack images identifying the eNOS-GFP expression is localized to the SC. **(C)** Individual confocal scans of eNOS-GFP expression imaged en face from the outer surface of the corneoscleral shell through to the TM. *TM: trabecular meshwork, JCT: juxtacanalicular connective tissue, SC: Schlemm's canal, CC: collector channels, CB: ciliary body, DIVP: deep intrascleral venous plexus, PLV: perilimbal veins.* Scale bars, 500μm.

4.2.8 Colocalisation Analysis

For the colocalisation analysis, the confocal z-stacks were restricted to only include images from the outer wall of SC inward towards the TM. This range encompasses both the spatial eNOS-GFP expression throughout the SC lumen and the fluorescent NPs enmeshed in the outer layers of the TM. Additionally, downstream perilimbal and aqueous veins were excluded from the confocal z-stacks, as the fluorescence signals from the vessels may influence the fluorescence intensity

values. Maximum projection images were then created from the confocal z-stacks and used for the analysis (Figure 4.3C). To examine the spatial relationship between endogenous eNOS expression in the SC and the tracer distribution in the TM, fluorescence intensities from the confocal z-stack images were measured. Each eye was assigned 16 regions of interest (ROIs), with 160 ROIs per treatment condition (eyes perfused at either 8 mmHg or 16 mmHg), and data from each ROI yielded a single data-point for the colocalisation analysis between eNOS-GFP intensity and tracer intensity (Figure 4.4). The ROI aspect ratio (200 μm x 200 μm) was chosen to allow for spatial variations in tracer distribution in the TM whilst still capturing the eNOS-GFP expression in the SC lumen. To maximize the range and provide sufficient leverage for the colocalisation analysis, ROIs were typically chosen from regions with high or low eNOS-GFP intensity. Within each ROI both the eNOS-GFP and tracer intensities were measured as the average pixel intensity over the entire ROI, as outputted by FIJI (NIH, MD, USA). A linear regression analysis was then applied to the dataset using MATLAB (v2014b, MathWorks, MA, USA) to determine whether there is any relationship between eNOS-GFP expression in the SC lumen and tracer labeling enmeshed in the TM as a function of IOP.

4.2.9 Image Processing

3-Nitrotyrosine Signal Analysis

The confocal z-stack images were separated into individual fluorescent channels; the 3-nitrotyrosine and tracers channel. From this we created a maximum intensity projection of the tracers channel for each individual eye, to identify regions of the outflow pathway occupied by tracers. This maximum intensity projection image was then imported into a custom-built MATLAB graphical user interface (GUI) script, that allows for the manual segmentation of the regions of interest. Each eye was assigned 4 ROIs, where each ROI corresponds to an individual quadrant of the eye. The selected ROIs were used as a 'mask' for all subsequent image analysis to clearly separate the background signal from the signal of interest. Masks were generated for each individual eye and then applied to the raw confocal z-stack images for both tracer and 3-nitrotyrosine channels.

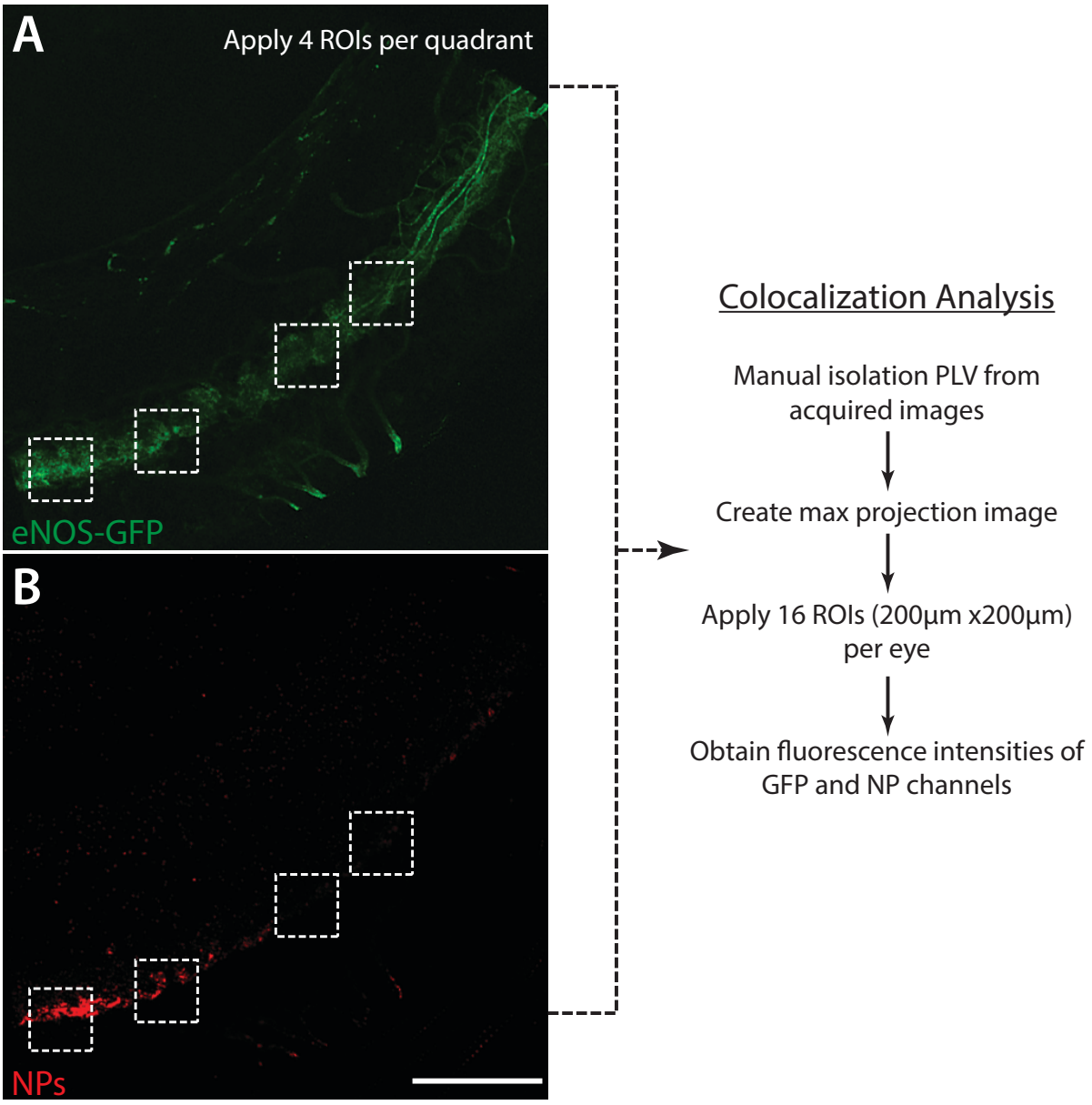


Figure 4.4: Colocalisation analysis between tracer intensity and eNOS-GFP expression. **(A)** Maximum intensity projection image of eNOS-GFP expression in the SC after isolating the perilimabl and aqueous veins. **(B)** Maximum intensity projection image of tracers (NPs) throughout the TM and SC of the same stack of confocal images. Four 200μm x 200μm ROI's were applied to the image to determine the average fluorescence intensities of the eNOS-GFP and tracer channels (*white dashed boxes)*. Scale bar, 500μm.

Once the selected ROIs were applied to all the images in the z-stack, the fluorescence signals were subjected to an 'Otsu-like' thresholding algorithm to optimize the signal-to-noise ratio. The 'Otsu-like' thresholding algorithm calculates the pixel intensity threshold which minimizes within-class variance and maximizes the between-class variance to eliminate the background signal from the true signals of interest. This thresholding algorithm was applied to each layer of the z-stack images, and based upon the distribution of pixel intensities from the 3-nitrotyrosine and tracer channels, a quantitative threshold value was generated for each individual eye. Fluorescence signals

above the determined quantitative threshold values were then used for further signal analysis.

To account for potential variability in tracers delivered to each individual eyes, the fluorescence intensity of the 3-nitrotyrosine channel was normalized by the fluorescence intensity of the tracer channel on a pixel-by-pixel basis, generating an array of fluorescence intensity ratios for each layer of the z-stack images. Once all the layers have been processed, an integrated matrix for each image was obtained by summing across the layers to produce an aggregated ratio of fluorescence intensity for the i^{th} pixel of the j^{th} layer. All non-valid numbers (NaNs) and 0/0 divisions were discarded from the normalization step. By processing the images layer-by-layer it eliminates the possibility of over-saturation of fluorescence signal for a given *x,y* location that may mask the signal of the same location in subsequent layers. The aggregated ratios were then averaged and normalized by the number of elements of that ROI, giving a mean value of the normalized signal. This normalization takes into account of the fluorescence intensity and ROI sampling variations between eyes, resulting in a non-parametric fluorescence intensity ratio for each eye that allow for comparisons between eyes and treatment conditions. Once all the dataset has been analyzed and processed into non-parametric fluorescence intensity ratios, we performed a paired eye analysis to compare the fluorescence signals based upon treatment group, eyes perfused at 8 and 16 mmHg.

4.2.10 Statistical Analyses

In order to perform statistical analysis on the data acquired, we needed to first determine the underlying probability distribution of the dataset. The Shapiro-Wilk test was used to determine the normality of the dataset, where small *p*-values reject the null hypothesis that the data is normally distributed. Both the eNOS-GFP and tracer intensities were better represented by a lognormal distribution than a normal distribution ($p=0.029$ vs. $p<10^{-6}$ and $p=0.005$ vs. $p<10^{-6}$, respectively, with the significance level defined at $p < 0.01$), therefore, in order to use standard statistical tools such as paired Student's *t*-test the data was log-transformed into the normal domain.

To determine whether there was a relationship between eNOS-GFP expression and tracer intensity, a linear regression was applied to the dataset, whereby each ROI contributes to a single data point in the regression analysis. However, due to possible variability in fluorescence intensity

values that may arise from the dataset, the GFP and tracer intensity values were normalized to eliminate the inter-pair variability, whilst preserving the intra-pair variability, as each pair of eyes were imaged under the same confocal settings. This allows for all the ROI data points to be compared on a single linear regression. For each pair of eyes, the raw fluorescence intensity values were normalized according to $F^*_{i,k} = [F_{i,k} - \hat{\mu}(F_k)]/\hat{\sigma}(F_k)$, where F represents the raw fluorescence value of either the GFP or tracer channel, the asterisks represent normalized values, the subscript i and k refer to the i^{th} ROI of the k^{th} pair of eyes, and $\hat{\mu}$ and $\hat{\sigma}$ represent the estimated mean and standard deviation of fluorescence values for all the i ROIs within the k^{th} pair of eyes. Note that the normalization of the raw fluorescence intensities expresses both GFP and tracer intensity in terms of units of standard deviation. The linear regression analysis applied to the aggregate data assumes that all the data points (160 ROIs per pressure condition) are from a single dataset, therefore leads to an inflated statistically significant p-value. A two-tailed Student's *t*-test was used to determine whether the slope of the linear regression was significantly different from the null hypothesis of zero slope, with significance defined at $p < 0.05$.

To overcome this, we computed the Spearman's rank correlation coefficient (ρ) for the relationship between GFP and tracer intensity for each individual eye at each pressure condition (N=10 for eyes perfused at 8 and 16 mmHg). This assumes a monotonic relationship between the variables and avoids the assumption of linearity. To find the average "individual-level" correlation, the Fisher *r* to *z* transform[77], was applied to each individual correlation (this is required because the coefficient is not normally distributed). The average *z* value was computed and the inverse transform was applied to get the average correlation coefficient. A two-tailed Student's *t*-test was used to determine statistical significance ($p < 0.05$).

Additionally, to quantify whether elevated IOP correlates with higher production of NO *in situ*, we isolated the fluorescence intensities obtained from the 3-nitrotyrosine and tracer channels, and normalized the signals to obtain a non-parametric fluorescence intensity ratio for each eye (as previously described in "3-Nitrotyrosine Signal Analysis"). From the non-parametric fluorescence intensity ratios we can then perform paired eye analyses to determine whether elevated IOP leads to greater NO production when compared to physiological IOP. Student's *t*-test was used to determine statistical significance between treatment conditions, with significance defined at $p < 0.05$. All statistical analyses was performed using MATLAB.

4.3 Results

4.3.1 Visualization of eNOS transgene expression within the conventional outflow pathway

To confirm the localization of the eNOS transgene within the conventional outflow pathway, eyes from eNOS-GFP mice were enucleated and processed for immunofluorescence microscopy. In the conventional outflow pathway, the eNOS-GFP fluorescence signal was restricted to the endothelial lining of the SC lumen, blood vessels of the ciliary body, collector channels and downstream episcleral vessels, with no staining detected in the TM (Figure 4.5). The eNOS-GFP signal colocalized with the endothelial marker CD31, which has been previously identified in human SC[106], confirming the endothelial-specific expression of the eNOS-GFP transgene.

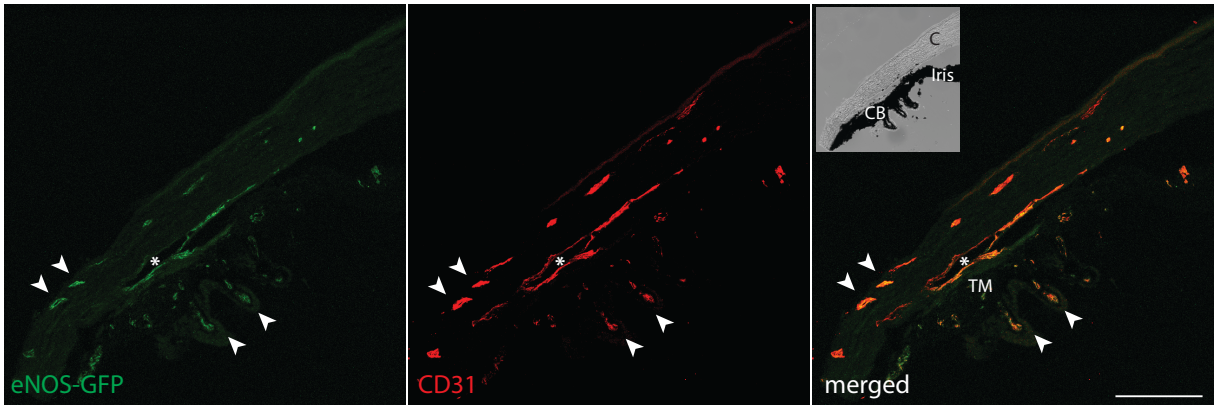


Figure 4.5: Localization of eNOS-GFP expression in the conventional outflow pathway of eNOS-GFP mice. **(Left)** Sagittal section through the trabecular meshwork (TM) and Schlemm's canal (asterisks) indicating that eNOS-GFP expression is labeling the SC endothelium as well as blood vessels (arrowheads) in the ciliary body (CB) and sclera. **(Middle)** Endothelial marker CD31 labeling the SC endothelium. **(Right)** Merged color image showing colocalisation of eNOS-GFP and CD31. (*Inset*) Bright field image of the conventional outflow pathway. *C: cornea, and CB: ciliary body*. Data are representative images from two eNOS-GFP mouse eyes. Scale bar, 100μm.

To visualize the spatial variations in eNOS-GFP expression in the conventional outflow pathway, typically *en face* imaging is carried out by removing the ciliary body and iris to expose the outer segments of TM and outflow pathway[165]. However, the ocular drainage structures in mouse eyes are delicate and easily damaged, thus the removal of the ciliary body and iris to expose the TM for *en face* imaging is technically challenging due to the close tethering between the TM and ciliary muscle (CM)[119,145,165] and could also disrupt the tracer filtration patterns. Therefore, we have adapted the flat-mount imaging procedure established by Kizhatil *et al.*[126] to visualize the tracer distribution pat-

terns along with the eNOS-GFP expression around the circumference of the eye, whilst preserving the structural integrity of the tissue. Flat-mount imaging of the eNOS-GFP expression was visualized by imaging through the corneoscleral shell, from this imaging method we were able to visualize the entirety of the conventional outflow pathway, which extended several hundred microns from the external ocular surface to the iris root, as illustrated by the Z-depth color coding (Figure 4.6). The superficial structures such as the perilimbal plexus and episcleral vessels were indicated by codes blue to cyan, whilst the inner structures of the outflow pathway such as the SC lumen was shown as codes pink to magenta (Figure 4.6B).

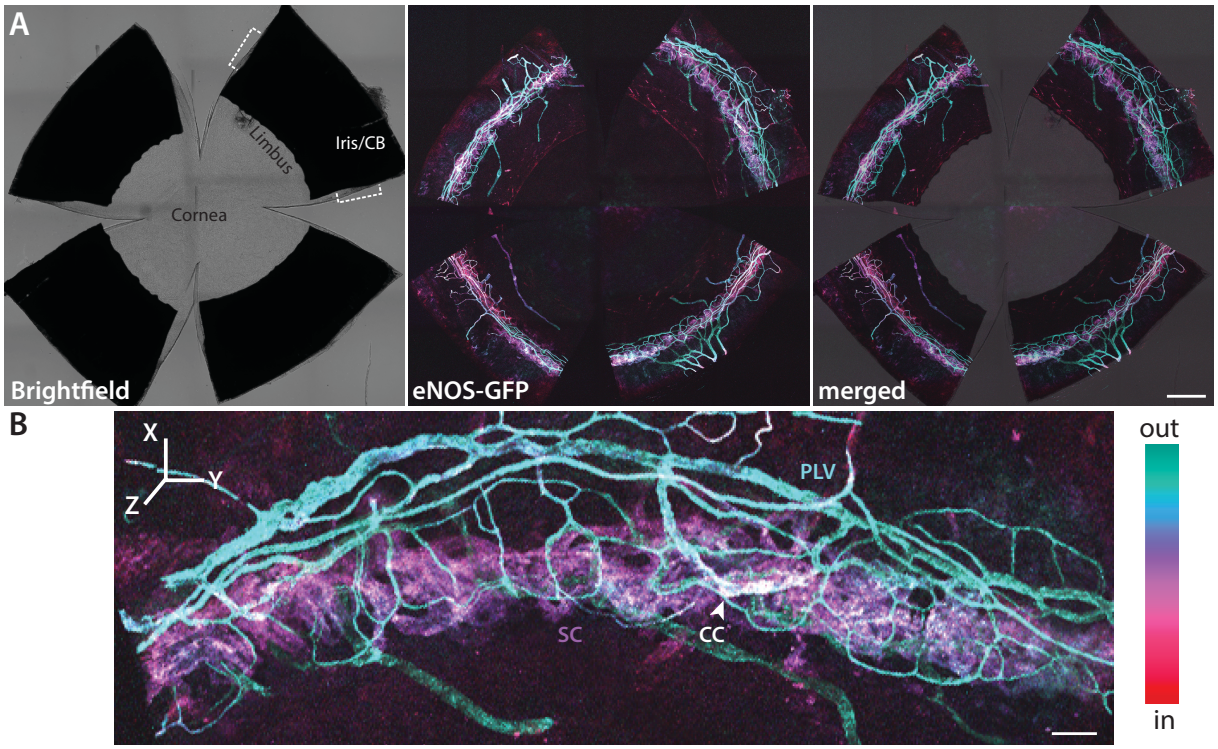


Figure 4.6: Schlemm's canal visualized via flat-mount imaging. **(A)** En face view of SC and limbal vessels. (Left) Brightfield image of a flat-mount eye. SC and limbal vessels are located in the region of the limbus. (Middle) Localization of the limbal vessels and the SC are visualized by the GFP fluorescence of the eNOS-GFP transgene in a Z-projection of confocal stacks encompassing the entire whole mount. The whole-mount stacks were Z-depth color-coded (ICE LUT). Color scale shows depth code colors of all structures expressing eNOS-GFP from inside the eye to the outer surface of the corneoscleral shell. (Right) Overlay of brightfield and eNOS-GFP fluorescence image. **(B)** Higher magnification showing the SC in relation to perilimbal vessels (PLV). The perilimbal vessels (cyan) are located closer to the external ocular surface than the SC (magenta). *CC: collector channel, CB: ciliary body.* Scale bar, (A) 500μm, and (B) 100μm

4.3.2 Relationship between eNOS-GFP expression and tracer intensity

To determine the relationship between eNOS-GFP and tracer intensity, we examined the spatial variations in eNOS-GFP expression in the SC in relation to the segmental outflow patterns in the TM via flat-mount confocal imaging. The GFP signal functions as a reporter for endogenous eNOS expression (Figure 4.7A), whilst the tracers (200 nm) were used to label the preferential drainage routes in the outflow tract. Confocal z-stack images were acquired to fully capture the tracer signal throughout the entire outflow pathway from the TM/JCT towards the SC lumen and onto the distal vasculature (Figure 4.7B). From these images, it was clear that aqueous humor outflow was segmental, as illustrated by regions of high vs. low tracer labeling in the outflow pathway where majority of the tracers were found enmeshed in the TM/JCT with little to no tracers observed downstream of the SC and in the distal vasculature. Hence, these tracer patterns can be considered as representative active filtration regions in the outflow pathway. Local regions of high tracer decoration varied in size from focal spots that were $\sim$100 μm wide to broader regions that extended several millimeters along the outflow pathway. Interestingly, the observed segmental filtration patterns in the JCT tend to coincide with the spatial variations in eNOS-GFP expression in the SC (Figure 4.7D-F), where regions of high eNOS-GFP expression reflected higher tracer decoration (*arrowheads*), and regions of low eNOS-GFP expression had lower tracer decoration (*asterisk*). Additionally, no obvious correlations were observed between the tracer distribution and the post-trabecular perilimbal plexus (Figure 4.7G-I).

To quantify the spatial relationship between eNOS-GFP expression within the SC and segmental tracer distribution in the TM/JCT, we measured the fluorescence intensities within each individual ROI for a given eye (16 ROIs per eye) subjected to either 8 or 16 mmHg. A linear regression analysis was then applied to the aggregate data which includes all 320 ROIs from 10 paired eyes, of which 160 ROIs were taken from eyes at each pressure condition. From the linear regression analysis, positive correlations were observed between GFP and tracer intensity when considering eyes perfused at both 8 and 16 mmHg, both achieving statistically significant correlations (R^2 = 0.272, p<10^{-6} and R^2 = 0.071, p<10^{-4}, respectively; Figure 4.8A). As the linear regression analysis assumes that all the data points are independent, statistical significance is inflated. The Spearman's rank correlation coefficient (ρ) for each individual eye were computed and averaged to obtain the relationship between GFP and tracer intensity for each pressure condition (N=10 for eyes perfused

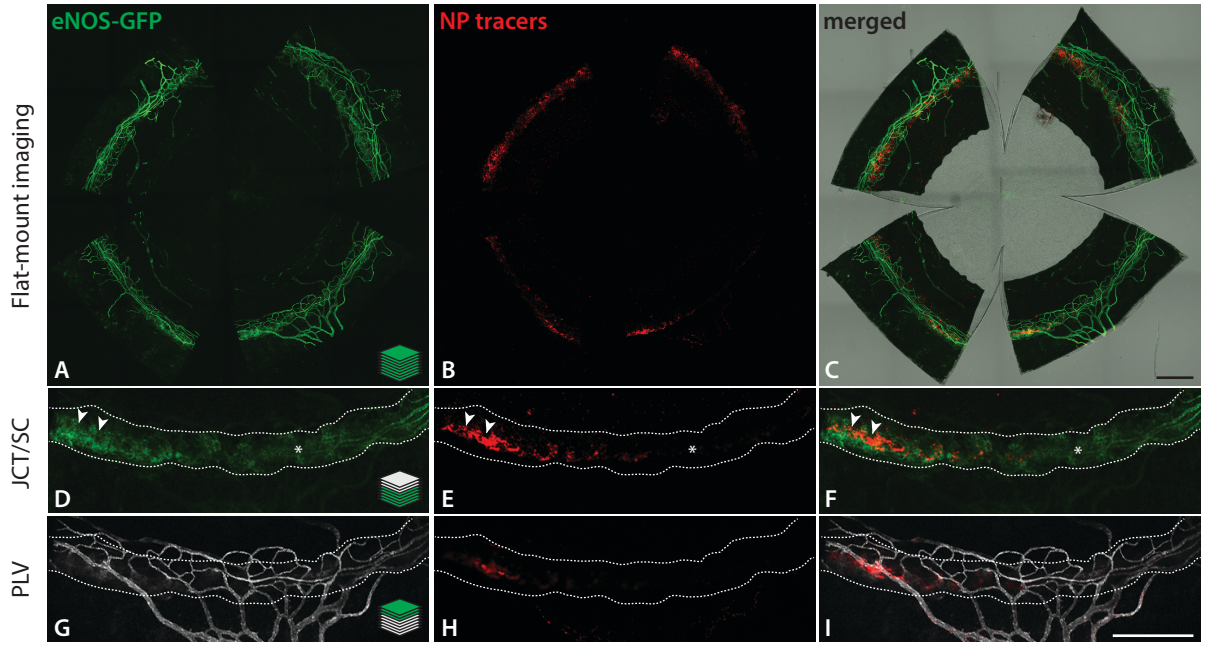


Figure 4.7: Representative whole mount confocal imaging of eye perfused at 8 mmHg to visualize the relationship between segmental tracer distribution in the TM and spatial variation of eNOS-GFP expression in the SC. **(A)** En face view of eNOS-GFP expression for the conventional outflow pathway. **(B)** En face view of segmental tracer distribution in the eye. **(C)** Merged color image showing the relationship between segmental tracer distribution and eNOS-GFP expression in the conventional outflow pathway. **(D-F)** Regional variations of eNOS-GFP expression (D) and tracer distribution (E) in the JCT/SC region. (F) Overlay of eNOS-GFP expression and tracer distribution in the JCT/SC region. Regions of high tracer accumulation in the TM/JCT (*arrowheads*) tend to colocalize with regions of higher eNOS-GFP expression in the SC, whilst low tracer accumulation tends to colocalize with regions of lower eNOS-GFP expression (*asterisks*). **(G-I)** Isolated superificial perilimbal plexus and episcleral veins (G) in relation to segmental tracer distribution (H). (I) Overlay of perilimbal vessels with segmental tracer distribution. Dotted lines outline the area occupied by the SC lumen. Scale bar, 500μm.

at 8 and 16 mmHg). These results also showed a positive correlation between GFP and tracer intensity for eyes perfused at 8 or 16 mmHg, both of which achieved statistically significant correlations (ρ = 0.451, p=0.003 and ρ = 0.299, p=0.049, respectively; Table 4.1).

To determine whether elevated pressure has an effect on GFP intensity and tracer intensity, we averaged the fluorescence intensities per eye and carried out a Student's *t*-test on the paired eye data. When considering the effect of pressure on tracer intensity for all the eyes, the averaged tracer intensity at 16 mmHg (2.906 $\pm$ 0.413; mean $\pm$ SD; N=10) was greater than the averaged tracer intensity at 8 mmHg (2.092 $\pm$ 0.448; N=10), resulting in a statistically significant increase in tracer accumulation at the higher pressure (p = 0.003; Figure 4.8B). However, when considering the effect of pressure on GFP intensity for all the eyes, no statistical significance was detected between 8 and 16 mmHg (31.492 $\pm$ 6.480 vs. 30.658 $\pm$ 7.800; N=10; p = 0.559). Taken together, these results show that increased GFP intensity correlates with increased tracer intensity in the TM, suggesting that regions of higher eNOS expression within the SC lumen coincides with regions of higher outflow

in the TM. However, the correlation between GFP intensity and tracer intensity was not affected by changes in IOP. The lack of a detectable increase in GFP intensity in response to increased IOP, may be due to time dependent effects of maturation and accumulation of GFP and may not reflect the true changes in eNOS expression. Furthermore, it still remains to be determined whether higher eNOS expression in the SC is an effect of increased shear stress within the SC lumen or increased outflow is caused by regional variations of eNOS activity and NO production, as the two factors are interlinked and is difficult to discern.

However, Increased IOP led to higher local tracer accumulation within the TM, suggesting a pressure-dependent mechanism that may be responsible for increased aqueous humor outflow. The increased outflow could potentially be attributed to an increase in hydrodynamic shear stress, as a result of the collapse of SC lumen at elevated IOP. SC endothelial cells have previously been shown to produce NO, presumably through the up-regulation of eNOS expression and activity, in response to elevated shear stress *in vitro*[11,135], which could potentially lead to increased local hydraulic conductivity in the outflow pathway. Therefore, to confirm the increased eNOS activity within the outflow pathway in response to increased IOP, we went on to quantify spatial changes in NO production with NO-sensitive peptide-sensors coupled to the surface of the tracers.

Table 4.1: Summary of the correlations between GFP intensity and tracer intensity.

Pressure (mmHg)	**Aggregate data (All ROIs)**			**Individual eye data (n=10)**		**Paired eye data (n=10)**	
	Linear Regression Analysis			*Correlation Analysis*			
	p-value	R^2	Slope	*p*-value	Avg. Spearman's rank (ρ)	Avg. Tracer Intensity	Avg. GFP Intensity
8	$< 10^{-6}$	0.272	+	0.003	0.451	2.092 $\pm$ 0.448	31.492 $\pm$ 6.480
16	$< 10^{-4}$	0.071	+	0.049	0.299	2.906 $\pm$ 0.413	30.658 $\pm$ 7.800
						$p = 0.003$	$p = 0.559$

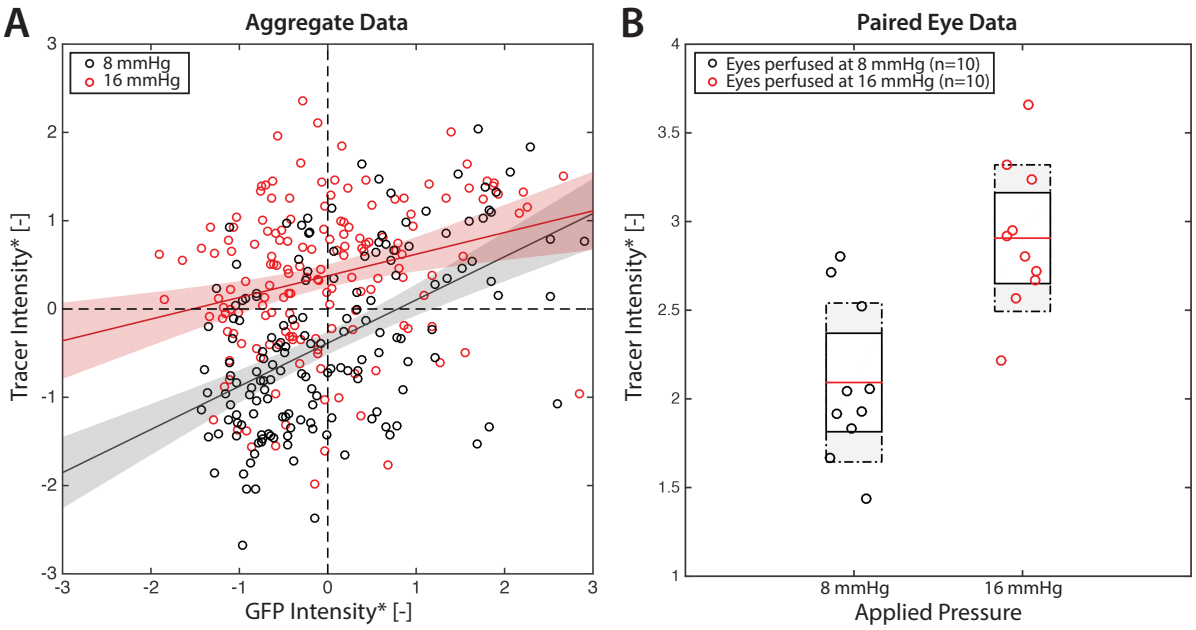


Figure 4.8: Relationship between eNOS-GFP expression and tracer intensity. Both GFP and tracer intensity have been normalized to allow for linear regression analysis. **(A)** Normalized tracer intensity plotted against normalized eNOS-GFP intensity for all 320 ROIs obtained from all the eyes separated by pressure conditions (*black circles = 8 mmHg; red circles = 16 mmHg*). Solid black line = linear regression for eyes perfused at 8 mmHg (160 ROIs). Solid red line = linear regression for eyes perfused at 16 mmHg (160 ROIs). Shaded region represents the 95% confidence bounds on the linear regression. (*) denotes normalized fluorescence intensities. **(B)** Modified boxplot of the averaged tracer intensity for each individual eye as a function of applied pressure. *Solid black line* indicates the 95% confidence interval of eyes perfused at each pressure. *Solid red line* represents the mean tracer intensity. *Dashed black lines* represents $\pm$ 1-standard deviation.

4.3.3 Effect of elevated IOP on NO production *in situ*

To examine local NO production in the conventional outflow tract we utilized a NO-sensitive peptide. When exposed to endogenous levels of NO-derived oxidants, tyrosine residues in the NO-sensitive peptide become nitrated thus forming a detectable end-product – 3-nitrotyrosine. These NO-sensitive peptide-sensors have previously been shown to detect shear-induced NO production in HUVECs in culture (as shown in *Chapter 3*). Here we utilize these probes to examine the effect of IOP on NO production in the conventional outflow tract.

In order to detect localized NO production *in situ*, perfused eyes were sagittally cryosectioned and then detected immunochemically with a monoclonal antibody that is selective for 3-nitrotyrosine, followed by incubation with a secondary fluorescently-labeled antibody. We then proceeded to determine if increased IOP results in elevated NO production by analyzing 3-nitrotyrosine levels in paired eyes perfused at 8 and 16 mmHg (physiological and elevated IOP, respectively). The fluorescence signals from the 3-nitrotyrosine staining and NP tracer channels were isolated from the flat-mount confocal z-stack images and processed to obtain a non-parametric fluorescence in-

tensity ratio for each individual eye (3-NT/tracer intensity ratio; as described in the Methods). The 3-NT/tracer intensity ratio provides a comparative measure of the level of NO detected *in situ* by the NO-biosensors in the conventional outflow pathway. This also allows for paired eye analysis of the dataset to determine whether elevated IOP results in the increased NO production, presumably through the up-regulation of eNOS expression and activity.

The majority of the peptide-NPs were found enmeshed in the TM/JCT region which is located adjacent to the inner wall endothelium of SC within the conventional outflow pathway correlating with the fluorescence from the NP tracers (Figure 4.9). Minimal non-specific α-3-nitrotyrosine signal was observed in the surrounding tissues of the conventional outflow pathway. This suggests that NO production was localized to the tissues residing in the JCT and inner wall of SC endothelium.

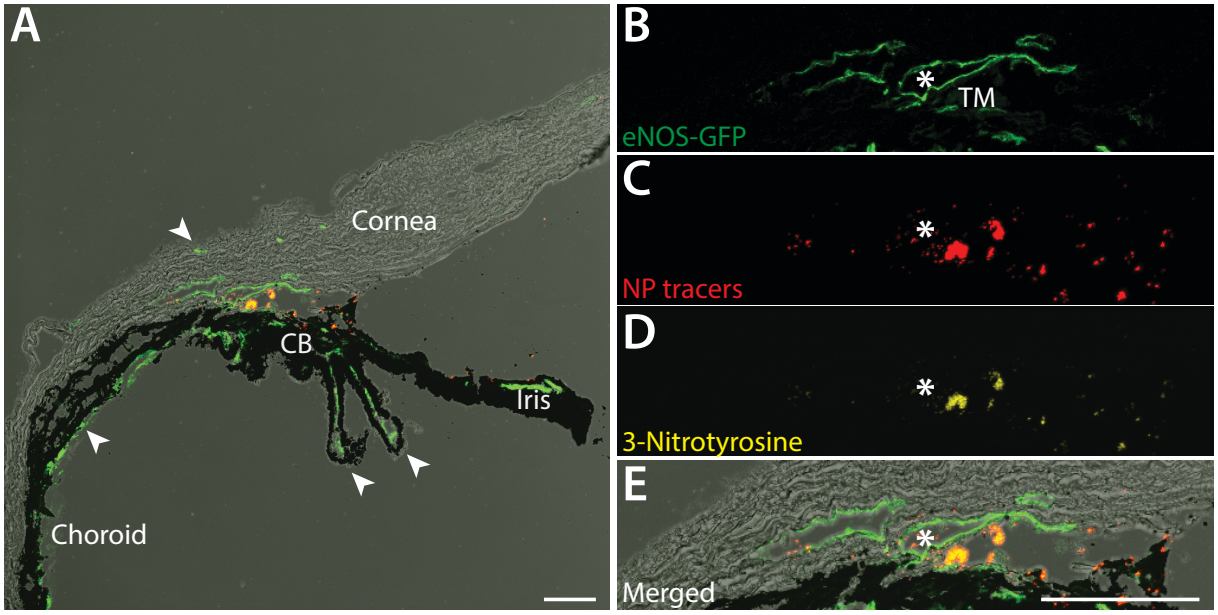


Figure 4.9: Localized detection of NO-mediated nitration in the conventional outflow pathway. **(A)** Sagittal section through the trabecular meshwork (TM) and Schlemm's canal (asterisks) indicating that eNOS-GFP expression is labeling the SC endothelium as well as blood vessels (arrowheads) in the ciliary body (CB), iris, choroid and sclera. **(B)** Fluorescent tracers (NP tracers) enmeshed in the TM labeling filtration-active regions of the outflow pathway. **(C)** Localized detection of NO-mediated nitration of peptide-conjugated nanoparticles enmeshed in the outflow pathway. The nitration of the peptide-sensors results in the formation of 3-nitrotyrosine, which was detected with anti-nitrotyrosine IgGs and fluorescent secondary IgGs. **(D)** Merged color image showing colocalisation of 3-nitrotyrosine detection and tracers, indicating the antibody detection was specific for the nitrated peptide-sensor and is located only on the surface of the nanoparticles with minimal non-specific binding. Data are representative images from two eNOS-GFP mouse eyes. Scale bar, 50μm.

For each individual pair of eyes, we detected higher NO production at 16 mmHg compared to 8 mmHg. This relationship holds true for all pairs, despite the variability in levels of NO detected between individual animals (N=10; Figure 4.10A). When considering the averaged 3-NT/tracer intensity ratio between the pressure conditions, the averaged 3-NT/tracer intensity ratio at 16 mmHg

was ∼3-fold greater than the averaged 3-NT/tracer intensity ratio at 8 mmHg (0.173 ± 0.110 vs. 0.055 ± 0.044; N=10 each; P=0.006; Figure 4.10B). Furthermore, the distribution of the data was generated for each pressure condition, which considers all the 3-NT/tracer intensity ratios across all the eyes in the dataset. From the population distribution, we detected higher amounts of 3-NT/tracer intensity ratios at 16 mmHg compared to 8 mmHg, as shown by the shift in distribution of the data towards the higher values of 3-NT/tracer intensity ratios (*red tracing*; Figure 4.10C). Interestingly, when comparing the 3-NT/tracer intensity ratios between the two pressures, the data seem to follow a similar distribution for the lower values of 3-NT/tracer intensity ratios, but as the 3-NT/tracer intensity ratio increases the distribution of the 16 mmHg dramatically increases (dotted black line), resulting in more counts of 3-NT/tracer intensity ratios detected. Taken together, these results show that a basal NO tone is present at physiological IOP and that elevated IOP results increased NO production in the JCT/SC.

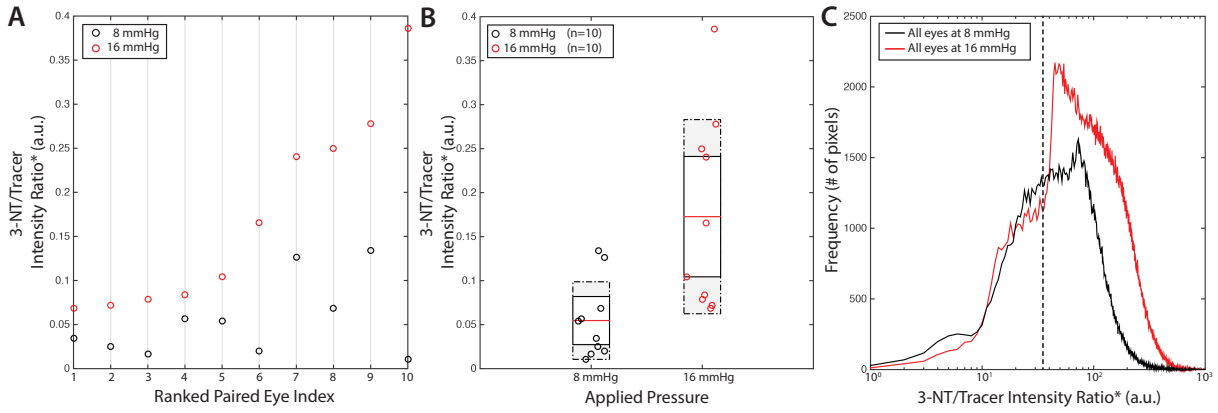


Figure 4.10: Comparison of 3-nitrotyrosine detection in the conventional outflow pathway as a function of IOP. **(A)** Paired eye comparison of 3-nitrotyrosine (3-NT) detection. The 3-nitrotyrosine signal was normalized by the tracer signal to obtain a non-parametric ratio of 3-NT/tracer intensity detected per eye. Each data point corresponds to an individual eye perfused at 8 or 16 mmHg (*black circles* and *red circles*, respectively). The 3-NT/tracer intensity ratio for each pair of eyes are compared and shown in ascending order from lowest to highest fluorescence intensity detected for eyes perfused at 16 mmHg. **(B)** Modified boxplot of the normalized 3-NT/tracer intensity ratio for each individual eye as a function of applied pressure. *Solid black line* indicates the 95% confidence interval of eyes perfused at each pressure. *Solid red line* represents the mean 3-nitrotyrosine/tracer ratio. *Dashed black lines* represents ± 1-standard deviation. **(C)** Distribution of the normalized 3-NT/tracer intensity ratios for all the eyes perfused at either 8 or 16 mmHg. For each given eye, the 3-NT/tracer intensity ratios were normalized by the area of the ROI to account for differences in ROI selection between eyes. Note that the 3-NT/tracer intensity ratios are presented on a log-scale.

4.4 Discussion

In this study, we demonstrated that in enucleated eNOS-GFP mouse eyes, perfused with fluorescent tracers, regions of higher tracer labeling in the TM coincided with regions of higher eNOS-GFP expression in the SC. This suggests that segmental tracer distribution may be partially regulated by the endogenous eNOS activity within the SC. Furthermore, the fluorescent tracers were functionalised with a NO-sensitive peptide that can detect local changes in NO production within the conventional outflow pathway *in situ*. We showed that these NO-biosensors were capable of detecting NO production at physiological IOP, suggesting a basal NO tone is present. We further showed that NO production within the conventional outflow pathway was pressure-dependent, resulting in a 3-fold increase in NO production at elevated IOP. To our knowledge this is the first demonstration that endogenous NO production increases in response to elevated IOP, where NO acts as a local mediator of outflow resistance within a mechano-regulatory system, which influences segmental outflow distribution within the conventional outflow pathway.

According to this pressure-dependent mechano-regulatory system, originally outlined by Stamer *et al.*[211], increases in IOP leads to the expansion of the JCT and pushes the inner wall endothelium into the SC lumen, leading to the collapse of SC lumen.[73,120,136] This effectively reduces the cross-sectional area and increases the circumferential flow rate within the canal, leading to increased shear stress experienced by the SC endothelial cells, as the same volumetric flow rate of AH must flow through a smaller SC lumen. Interestingly, these shear levels approaches theoretical wall shear stresses that are comparable to those experienced by the arterial system[73] that are known to up-regulate eNOS expression[51] and activity[58,91]. Increased eNOS activity consequently leads to an increase in NO production, which can act as an autocrine/paracrine signaling molecule to restore IOP homeostasis by modulating the local outflow resistance sites predominately involving mechanisms related to cellular contractility or endothelial permeability. NO is widely known to diffuse across cell membranes to affect the biological activity of several proteins and enzymes in the outflow tract. Most notably, the activation of sGC/cGMP/PKG signaling pathway, responsible for the relaxation of TM cells[61] and the decrease in TM[60] and SC[66] cell volume through activation of BK_{Ca} channels. Alternatively, NO could also mediate the endothelial permeability of the inner wall of SC by disrupting the adherens junctions[44,57] to potentially affect the dimensions of inner wall pores

and/or flow pathways in the JCT. Downstream of SC, NO may induce relaxation of smooth muscle cells that surround the collector channels[54] to increase intrascleral vessel diameter and therefore, may influence post-trabecular or distal outflow resistance downstream of SC[188].

Our results show that regions of higher eNOS-GFP expression in the SC lumen coincides with regions of higher tracer labeling in the TM, suggesting the spatial variations in eNOS-GFP expression may be partially responsible for the segmental tracer distribution within the outflow pathway. Furthermore, at elevated IOP, higher tracer labeling was detected in the TM compared to physiological IOP, showing a pressure-dependent increase in aqueous humour outflow. As elevated IOP causes the collapse of the SC lumen, the increased outflow is likely associated with NO-mediated effects resulting from the up-regulation of eNOS expression and activity in response to elevated shear within the SC lumen. However, the lack of a detectable increase in GFP intensity in response to elevated IOP could potentially be due to time dependent effects of maturation and accumulation of GFP. Previous studies have shown that the maturation time for GFP fluorescence can take up to $\sim$2-4 h post-protein expression[4,104,105], hence the GFP fluorescence may not be sensitive towards changes in IOP for the given experimental time ($\sim$4.5 and 2 h for eyes perfused at 8 and 16 mmHg, respectively; Supplementary Table 4.2). However, shear-induced eNOS mRNA expression has been shown to increase after 1 h of shear stress in bovine aortic endothelial cells (BAECs)[51]. Therefore, the lack of detectable changes in GFP intensity does not necessarily reflect the true endogenous eNOS expression and activity in response to pressure-induced shear stress within the SC lumen.

We proceeded to further investigate whether increases in IOP leads to increased eNOS activity through the detection of NO production within the conventional outflow pathway. NO-sensitive peptide sensors were utilized to detect local changes in NO production at the outflow resistance sites, through the NO-mediated nitration of the peptide sensors conjugated to the surface of fluorescent tracers. Previous studies have shown that human SC endothelial cells[11] and porcine angular aqueous plexus cells (the porcine equivalent of SC cells)[135] are shear-sensitive and secrete NO in response to increasing shear stress *in vitro*. Consistent with this notion, eyes perfused at 16 mmHg exhibited an average 3-fold increase in 3-NT/tracer intensity ratio compared to eyes perfused at 8 mmHg. Furthermore, majority of the tracers were found enmeshed in the TM/JCT region, located adjacent to the inner wall endothelium of SC. Therefore, this data strongly suggests that elevations in IOP results in the up-regulation of eNOS activity, which can be attributed to increased hydrody-

namic shear stress within the SC, leading to an increase in NO production. Secreted NO could then feed back into the mechano-regulatory system as an autocrine/paracrine signaling molecule by retrograde diffusion into the TM and/or advection along the circumference of the canal to modulate the outflow resistance sites to increase outflow facility in the eye. This endogenous feedback mechanism described here reaffirms previous studies[121,141,158,174] indicating that eNOS activity plays a crucial regulatory role in maintaining IOP homeostasis. One caveat to this study was that the perfusion studies were carried out using a pressure-controlled system held at constant-pressure, therefore we were unable to characterize the effect of NO release from the SC cells to restore IOP homeostasis, as we would expect from an endogenous regulatory mechanism *in vivo*.

While our data and others[43,158,191] strongly suggest that eNOS is the primary isoform in the conventional outflow pathway, studies have shown that both nNOS[149,165,195] and iNOS[192,239] are expressed in the TM region of the outflow pathway by nitrergic nerve fibers and resident macrophages, respectively. Therefore, endogenous NO production may not be limited to eNOS activity in the outflow tract. Further studies are required to help differentiate between the various NOS isoforms that may contribute towards this mechano-regulatory feedback mechanism. Previous data have shown that the selective inhibition of eNOS, with cavtratin, reduced outflow facility in WT mice compared to its contralateral control, suggesting a basal NO tone is involved in the regulation of outflow facility[43]. Consistent with this notion, our data also showed a basal NO tone in eyes perfused at physiological IOP, and increases in IOP leads to increased NO production in the SC. Therefore, by introducing the eNOS-selective inhibitor with the NO biosensor, we could potentially determine whether eNOS is the primary isoform responsible for this mechano-regulatory feedback loop, and in turn influence the segmental outflow distribution observed in the TM and NO secreted by the SC cells.

In conclusion, we have shown that segmental outflow in the TM is partially regulated by an endogenous NO-regulatory mechanism within the outflow tract, predominately through the up-regulation of eNOS expression and activity within the SC. Elevated IOP leads to increased NO production, and acts as the local mediator of outflow resistance in the TM and SC, by altering the local hydraulic conductivity, and thus the segmental outflow patterns in the outflow pathway to help restore IOP homeostasis. This homeostatic mechanism may become impaired in glaucomatous eyes, which leads to reduced NOS activity[157] and decreased NO production in SC cells[11], and thus resorts in increased outflow resistance and elevated IOP. Therefore, by targeting the NO-regulatory machinery

within the conventional outflow pathway may help restore the regulatory feedback mechanism and provide an sustained therapy for treating glaucoma.

4.5 Supplementary Information

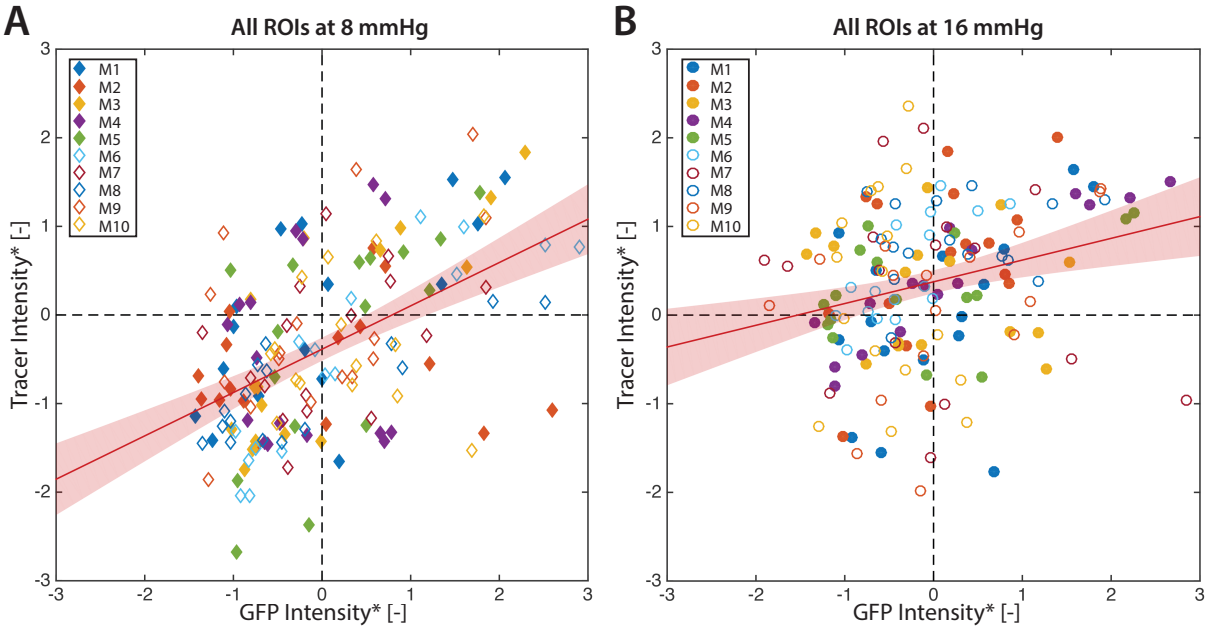


Figure 4.11: Relationship between eNOS-GFP expression and tracer intensity. Both GFP and tracer intensity have been normalized to allow for linear regression analysis. **(A)** Normalized tracer intensity plotted against normalized eNOS-GFP intensity for all 160 ROIs obtained from all the eyes pressurised at 8 mmHg (diamonds). Each mouse was separated into different colors to represent the distribution of ROIs for a given eye. **(B)** Normalized tracer intensity plotted against normalized eNOS-GFP intensity for all 160 ROIs obtained from all the eyes pressurised at 16 mmHg (circles). Each mouse was separated into different colors to represent the distribution of ROIs for a given eye. Solid red line = linear regression for eyes perfused either at 8 or 16 mmHg. Shaded region represents the 95% confidence bounds on the linear regression. (*) denotes normalized fluorescence intensities.

Table 4.2: Outflow facility data. "Baseline" facility was the average facility measured at *time = 30 mins* during the first bolus of perfused DBG. "Post-tracer" facility was the average facility measured at the end of the perfusion during the second bolus of perfused DBG. Average facility measurements were taken over 10 mins of stable data.

Eye			Sex	Age [wks]	Perfusion Time [hr:min]	Outflow Facility (nl/min/mmHg)	
ID	L/R	Perfusion Pressure [mmHg]				Baseline	Post-tracer
1	L	16	M	10	1:40	5.52	30.23
	R	8			1:49	23.77	35.20
3	L	8	F	10	4:01	5.99	15.32
	R	16			2:40	11.68	9.10
4	L	16	F	10	2:23	4.89	13.47
	R	8			3:15	6.24	22.92
6	L	8	M	10	2:35	9.62	25.59
	R	16			0:58	16.42	23.92
7	L	8	M	10	3:20	6.66	17.32
	R	16			2:22	6.70	12.24
8	L	16	F	15	1:56	11.61	10.69
	R	8			4:00	7.03	16.70
9	L	16	M	15	1:06	14.48	17.47
	R	8			5:48	2.68	12.02
12	L	16	F	15	1:26	11.17	15.24
	R	8			6.33	5.75	5.62
14	L	16	M	15	3:22	4.89	8.64
	R	8			6:58	4.98	7.16
15	L	8	M	15	5:54	2.48	14.59
	R	16			2:04	7.69	13.09
Mean ± SD (n=10)	Eyes perfused at 8 mmHg				**4:25**	**7.52±6.07**	**17.24±8.82**
	Eyes perfused at 16 mmHg				**1:59**	**9.51±4.14**	**15.41±6.86**

Chapter 5

Imaging of Segmental Outflow in *Ex Vivo* Mouse Eyes by Optical Projection Tomography

This chapter consists of a paper in preparation to be submitted to Experimental Eye Research: "Methods in Eye Research".

5.1 Introduction

The majority of aqueous humor outflow resistance is generated within close proximity to the inner wall endothelium of Schlemm's canal (SC), its underlying basement membrane and subsequent juxtacanalicular connective tissue (JCT) of the trabecular meshwork (TM)[117,166]. However, the hydrodynamic details of how aqueous humor filters through these tissues remain unclear. Aqueous humor outflow has been suggested to be non-uniform or "segmental" around the circumference of the TM[53,70]. This indicates that only a portion of the meshwork is considered filtration-active at any given time, and thus may influence the delivery of anti-glaucoma therapeutics that aim to lower IOP. Previous studies have shown that segmental outflow patterns are influenced by multiple factors occurring at both the macro- and micro-scale[42], therefore suggesting that aqueous humor outflow regulation should be considered as a multi-scale problem.

To study segmental outflow in the TM, researchers have often relied upon fluorescent tracers to identify and label preferential drainage routes in the outflow pathway[17,102,123,218,231]. The visualization of segmental outflow patterns are typically carried out with established imaging techniques such as epifluorescence and confocal microscopy. For these imaging techniques, typically the eye is dissected into smaller wedges for *en face* imaging, whereby the images are post-processed and merged together to re-create the segmental filtration patterns of the outflow pathway. However, by dissecting the eye it can potentially disrupt the flow patterns and introduce artifacts or result in the loss of information from processing the tissue for imaging. Hence, the ability to image segmental filtration patterns over the entire circumference of the eye without dissecting the tissue would be highly advantageous.

Optical projection tomography (OPT)[199] is a recently developed optical imaging technique that is capable of imaging small biological samples in three-dimensions (3D), typically for specimens that range between 1 to 10 mm[198]. This technology has already proven to be a valuable tool in developmental biology[179,198,199], being able to obtain high-resolution optical projections of fluorescent and non-fluorescent biological samples over 360° rotation. However, this technology has been limited to mainly embryonic studies, and has yet been adopted for wider applications such as the study of fluid dynamics in the eye. This is mainly due to two limiting factors: (i) the need to clarify biological samples to enable the transmission of light, and (ii) the quenching of fluorescent labels when

processed with tissue clarifying chemicals; both of which are essential for the 3D reconstruction of the optical projections.

In this study, we demonstrate for the first time, the use of fluorescence OPT combined with a novel embedding protocol to visualize the segmental outflow patterns in enucleated mouse eyes, without the need to dissect or optically clear the tissue with toxic chemicals, thus preserving both the anatomical structures of the eye and the fluorescence signals of interest. Furthermore, with this protocol, we have also illustrated that fluorescence OPT can potentially be used as a tool to correlate fluorescently labeled anatomical structures with segmental outflow patterns, to potentially understand the interconnectivity between the macro- and micro-scale components that may influence segmental outflow behavior in the eye.

5.2 Materials and Supplies

5.2.1 Animal Husbandry

All experiments were conducted in compliance with the Association for Research in Vision and Ophthalmology Statement for the Use of Animals in Ophthalmic and Vision Research under UK Home Office Project License approval for research at Imperial College London. This study used transgenic mice which express the human gene variant of the endothelial nitric oxide synthase (eNOS) promoter fused to green fluorescent protein (GFP) on a C57BL/6 background, as well as C57BL/6 wild-type (WT) mice. Perfusions were performed with enucleated (ex vivo) eyes from mice of either sex. eNOS-GFP mice were 8 – 15 wk of age (endogenous GFP labeled mice). WT mice were 8 – 12 wk of age (*in vivo* tracer injection experiments). Mice were housed in individually ventilated cages, fed ad libitum, and maintained at 21° C with a 12:12-h light-dark cycle, with lights on from 6 AM to 6 PM.

5.2.2 eNOS-GFP transgenic mice

Transgenic mice express the human gene variant of the eNOS promoter fused to green fluorescent protein (GFP; as a reporter) on a C57BL/6 background. The transgene contains the human eNOS promoter region only, such that transgene expression is regulated by endogenous transcriptional activity but there is no over-production of nitric oxide. In these animals, GFP expression has been shown to be specific to endothelial tissues, with no increase in endogenous NO-production. Transgenic mice were a kind gift from Prof. Rob Krams (Imperial College London, UK) and Prof. Rini de Crom (Erasmus MC, Rotterdam, The Netherlands). Genotyping of transgenic mice was performed to detect sequences of GFP and the human variant of eNOS promoter present in the genome of eNOS-GFP mice but are absent from the genome of WT mice. Genotyping was performed using ear tissue samples obtained at weaning, with tissue lysis and DNA purification performed according to manufacturer's instructions (Kapa Express Extract; Kapa- Biosystems, Cambridge, MA). Separate PCR reactions were performed using a hot-start mix (KAPA2G Robust HotStartReadyMix; Kapa- Biosystems, Cambridge, MA). For human eNOS promoter, 29 cycles were performed with an annealing temperature of 59.3℃ using the sense primer ACCAGGGCATCAAGCTCTTC and the antisense primer TCTGTGATGTGGCACCAGAC to yield a predicted product of 500 bp. These sequences are specific for the human eNOS promoter and are not predicted to react with C57BL/6 murine eNOS. For GFP, 29 cycles were performed with an annealing temperature of 59.9℃ using the sense primer AGCTGACCCTGAAGTTCATCTG and the antisense primer GACGTTGTGGCTGTTGTAGTTG to yield a predicted product of 327 bp. PCR products were resolved by gel electrophoresis (1% agarose) in the presence of DNA gel stain (SYBR Safe; Invitrogen, Carlsbad, CA). Bands were visualized on an imaging station (Biospectrum 500; UVP, Upland, CA).

5.2.3 Fluorescent Tracers for *Ex Vivo* Perfusions and *In Vivo* Injections

Fluorescent tracers (200 nm, carboxyl-coated nanoparticles) were purchased from Life Technologies (Austin, TX, USA). For *ex vivo* tracer perfusions, the perfusate consisted of a final concentration of 0.1% (v/v) red fluorescent tracers (580nm/605nm; 3.1×10^{11} particles/mL) resuspended in Dulbecco's phosphate buffered saline (PBS) including divalent cations and 5.5mM D-glucose (DBG) that was passed through a 0.2 μm filter. For *in vivo* tracer injections, yellow-green fluorescent trac-

ers (505nm/515 nm) were resuspended in Ultra^{TM} DNase/RNase free water (dH_2O; Invitrogen) and was delivered via 1.5μl bolus injections ($\sim$1x10^5 particles/eye) to decorate the segmental outflow patterns in living WT mice.

5.2.4 Anesthesia

The anesthetic solution consisting of ketamine (66.6 mg/kg, Fort Dodge Animal Health, Fort Dodge, IA) and medetomidine hydrochloride (Domitor® 0.66 mg/kg, Orion Pharma, Berkshire, UK) was diluted in sterile dH_2O (Hameln Pharmaceuticals, Gloucester, UK) and delivered to the mice via intraperitoneal injection. Antisedan® (atipamezole hydrochloride; 1.5 mg/kg, Orion Pharma, Berkshire, UK) was delivered via intraperitoneal injections after intracameral injections to assist with the recovery of mice from anesthesia.

5.2.5 Embedding of Mouse Eyes for OPT Imaging

Enucleated mouse eyes from each experiment were casted in a clear arcylic cylindrical container (25 mm x 8mm; RS Components Ltd, UK) with polydimethylsiloxane (PDMS; Sylgard 184, Dow Corning, Wiesbaden, Germany) or following established standard agarose embedding and tissue clearing protocol for OPT imaging[180]. For the standard OPT sample preparation, 1% agarose (low melting point) solution was used for the embedding of the tissue sample, followed by the dehydration of the tissue with 100% methanol and tissue clearing with BABB (2:1 mixture of benzyl alcohol and benzyl benzoate).

5.2.6 Glass Needles for *In Vivo* Injections

Custom-made glass needles were used for tracer injections. Needles were made out of borosilicate glass capillaries (BF100-50-10, Sutter Instruments, CA, US) with an inner diameter of 0.5 mm and outer diameter of 1 mm. Capillaries were pulled using a laser-based micropipette puller (P2000, Sutter Instruments, CA, US). Pulled capillaries were then further processed to obtain a nee-

dle tip diameter of $\sim$100 μm, by carefully pushing the needle tip against another needle positioned perpendicularly. Each needle was then inspected on an inverted microscope to control for the tip diameter. Prior to use, needles were autoclaved at 120° C and stored in 70% ethanol.

5.3 Detailed Methods

5.3.1 Experimental Design

The goal of this study was to develop a novel embedding protocol that can be used for OPT imaging of enucleated mouse eyes, in order to examine segmental outflow patterns globally and also be able to visualize the limbal vasculature of the outflow pathway in the same sample. Here, we propose two set of experiments to demonstrate a proof-of-concept that our embedding protocol is compatible with OPT imaging technique and presents an alternative to the standard agarose/BABB tissue clearing protocol commonly used for developmental biology[179,180,198]. For the first set of experiments, eyes obtained from eNOS-GFP mice were used to visualize the limbal vasculature, which expresses the transgene in vascular-derived endothelial cells that line the post-trabecular outflow pathway. These same set of mice were also perfused with fluorescent tracers to decorate the segmental outflow patterns in the TM. eNOS-GFP perfused eyes were then processed for OPT imaging with either the standard agarose/BABB protocol or the newly developed PDMS embedding protocol. The second set of experiments examined whether segmental outflow patterns in eyes obtained from living WT mice were comparable against *ex vivo* eyes. These experiments aim to validate the newly developed PDMS embedding protocol is compatible with OPT imaging, whilst preserving the fluorescence signals of interest from chemical quenching during sample preparation.

5.3.2 *Ex Vivo* Tracer Perfusions

Eyes obtained from eNOS-GFP mice were perfused with fluorescent tracers to decorate the segmental outflow patterns in the TM. Additionally, the GFP signal from the eNOS-GFP expression in the SC and downstream perilimbal vessels are used to identify the post-trabecular outflow path-

way and limbal vasculature in the mice. The eyes were enucleated within 10 minutes of death by cervical dislocation and stored in PBS at room temperature until perfusion, typically within 15 min. Experiments used paired contralateral eyes, which were perfused simultaneously on two identical iPerfusion systems[200] under identical experimental conditions.

Our perfusion method follows previously described techniques[25,27,43,134,211]. Briefly, the eye was affixed to a support using cyanoacrylate glue to stabilize the eye and submerged in PBS in a thermo-regulated bath at 35° C. A 33-gauge beveled needle (Nanofil; World Precision Instruments, Europe; Hitchin, UK) was used to cannulate the eye, with the tip of the needle positioned in the anterior chamber using a micro-manipulator. The pressure and flow rate inside the eye were measured using a wet-wet differential pressure transducer (PX409, Omegadyne, US) and a flow sensor (SLG64-0075, Sensirion, Switzerland), respectively. The enucleated eyes were perfused with DBG supplemented with red fluorescent tracers (0.1% concentration (v/v)) at 8 mmHg for 3 hours to decorate the segmental outflow patterns. After each perfusion the eyes were fixed in 4% paraformaldehyde (PFA) overnight at 4° C ready for further processing for OPT imaging.

5.3.3 *In Vivo* Tracer Injections

For this set of experiments WT mice were used to study the preferential drainage routes in the conventional outflow pathway of living WT mice, and whether the outflow patterns are consistent with the segmental outflow patterns observed in *ex vivo* eyes. WT mice were anesthetized with ketamine (66.6 mg/kg) and Dormitor® (0.66 mg/kg) via intraperitoneal injection. Dilation drops (phenylephrine hydrochloride (2.5% w/v) and tropicamide (1% w/v); Bausch & Lomb, Rochester, NY) were then applied to both eyes to minimize potential damage to the iris during cannulation of the glass needle. Each mouse was subcutaneously injected with 5 mg/kg enrofloxacin antimicrobial (Baytril; Bayer Healthcare, Leverkusen, Germany) and their eyes were kept moist with artificial tears (Vidisic® Bausch & Laumb, Rochester, NY) prior to intracameral injections. Once the mouse was fully sedated, it was secured in place with the assistance of a head-holder (Model 923-B; Kopf Instruments, CA, USA) and placed on a warm-water place mat. Liquid around the eye was removed using a Kimwipe (Fisher Scientific, Loughborough, UK) before cannulation. Eyes were cannulated with a pulled glass micro-needle (100 μm tip) positioned parallel to the iris and above the limbus

to remove a portion of the aqueous humor in the anterior chamber by capillary action. This helps reduce the amount of reflux during intracameral injections. Intracameral injections were then carried out with a pulled glass micro-needle (100 μm tip) filled with 1.5 μL of yellow-green tracers in dH_2O connected to a 10 μL glass syringe (Gastight; Hamilton, Reno, NV). The tracers filled glass micro-needle was then inserted into the same cannulation site with the assistance of a micro-manipulator, and the tracers were slowly delivered to the anterior chamber of the eye. Topical antibiotic ointment (1% w/w Fucithalmic; LEO Pharma, Denmark) was then applied to the cannulation site followed by removing the needle slowly from the eye to reduce reflux. After the procedures, the mice were given 1.5 mg/kg of Antisedan® via intraperitoneal injection and placed in a heated chamber (maintained at 28° C) to allow for faster recovery from anesthesia. To better distinguish the orientation of each eye, the right eye (OD) was cannulated in the inferior quadrant and the left eye (OS) was cannulated in the superior quadrant. The mice were allowed to recover for 48 hrs post-surgery for the cornea to fully heal then euthanized via an overdose of Pentobarbital (150 μL; Euthatal, Merial, UK). Once the mice have been euthanized, the eyes were enucleated and fixed in 4% PFA overnight at 4° C ready for further processing.

5.3.4 Embedding Protocol of Enucleated Mouse Eyes

Enucleated eyes obtained from eNOS-GFP and WT mice were washed in PBS several times to remove any fixative remaining on the eyes. Eyes were then cleaned of their surrounding extraocular muscles and the conjunctiva, to expose the limbal region of the eye for OPT imaging for both segmental tracer distribution and eNOS-GFP signal from the limbal vasculature. The sample was then processed for OPT imaging either via the standard agarose/BABB protocol established by Sharpe *et al.*[198,199] or by the newly developed PDMS embedding protocol (Figure 5.1).

For the standard agarose/BABB processing protocol (as shown in Figure 5.1A), the fixed tissue was first washed in distilled water several times to remove trace amounts of salts, which could crystalize during the dehydration and BABB clearing process. Followed by the embedding of the eye in a 1% solution of low-melting-point agarose in a 50-mm Petri dish, with the eye positioned horizontally in the middle of the dish at medium depth. The agarose gel was left to set at room temperature for 10 min or set overnight at 4° C. Once the agarose gel has completely set, the sample

was carefully removed from the Petri dish and trimmed to obtain an octagonal-shaped block, such that the long axis of the sample is aligned with the axis of rotation. The trimming of the specimen block minimizes the optical influence of 90° corners during image acquisition. The sample was then dehydrated for 24 h in a glass vial containing 100% methanol and covered with aluminum foil to protect the fluorescence signal from light. After dehydrating the sample, methanol was replaced with BABB solution to clear the agarose gel and the embedded tissue for an additional 24 h. After clearing the sample, the block was removed from the BABB solution and glued to a magnetic mount then attached to the rotating assembly of the OPT scanner. The sample was then immersed in a transparent cuvette filled with BABB solution to match the refractive index (n=1.55) for OPT imaging. For long-term storage, the samples were kept in BABB solution in an amber glass vial at room temperature.

For the PDMS embedding protocol (as shown in Figure 5.1B), PDMS was prepared by mixing the pre-polymer and cross-linker at a 10:1 ratio (w/w) and poured into an hollow acrylic cylinder of 25 mm x 8 mm (length and inner diameter, respectively) on a 50-mm Petri dish. The casting of the silicone elastomer in a cylindrical container eliminates the optical influence of corners, whilst also possessing good optical properties for OPT imaging. PDMS was then degassed in a desiccator to remove air bubbles, then semi-cured for 15 min at 65° C. During this time, the fixed sample was washed in PBS several times to remove residual PFA, and pre-incubated for 5 min in a 50-mm Petri dish filled with degassed PDMS to coat the surface of the sample to minimize the presence of an transition interface between the sample and the PDMS. After 15 min of curing the PDMS, the PDMS-incubated sample was carefully placed inside the semi-cured PDMS filled cylinder and positioned longitudinally, such that the long axis is aligned with the axis of rotation. The sample embedded in PDMS was then fully-cured for an additional 45 min at 65° C. After curing, the sample was left to cool at room temperature for 1 h then removed from the cylindrical mold and glued to a magnetic mount ready for OPT imaging. The sample was immersed in a transparent cuvette filled with 95% ethanol, which was used as an intermediate refractive index (n=1.36) between air and the sample. For long-term storage, the samples were kept in PBS solution in an amber glass vial and stored at 4° C and protected from light.

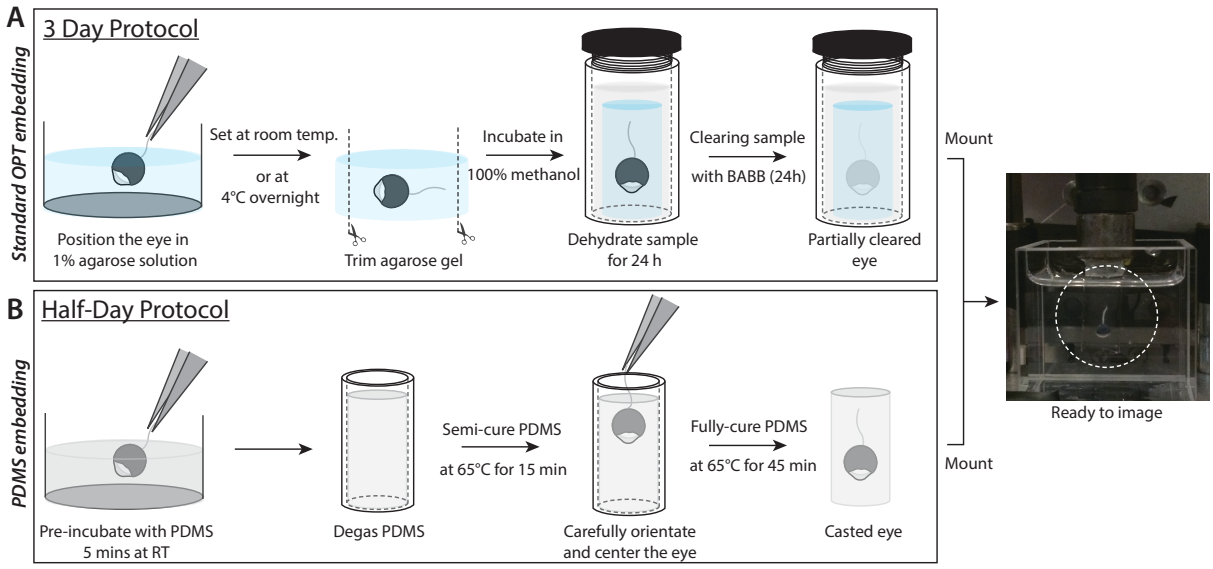


Figure 5.1: Schematic representation of tissue embedding protocol for OPT imaging. **(A)** Standard agarose embedding and clearing protocol for OPT imaging. The tissue sample was washed in distilled water several times to remove trace amounts of salts to prevent the formation of salt crystals during dehydration and clearing steps. The tissue sample was then embedded in 1% agarose gel and left to set at room temperature or 4 ° C overnight. The sample was then trimmed to an octagonal-shape and dehydrated in 100% methanol for 24 h. This was followed by clearing of the sample with BABB solution for an additional 24 h. The sample was then mounted onto a magnetic stub and attached to the rotating assembly of the OPT scanner. **(B)** PDMS embedding protocol for OPT imaging. The tissue sample was pre-incubated with PDMS for 5 min at room temperature. Cylindrical containers were used to cast the degassed PDMS, then semi-cured for 15 min at 65 ° C. The pre-incubated sample was then carefully placed and centered in the cylinder. The sample embedded in PDMS was then fully-cured for an additional 45 min at 65 ° C. The casted sample was allowed to cool for 1 h at room temperature before removing it from the cylinders and mounted for OPT imaging.

5.3.5 Image Acquisition with OPT

A custom-built OPT scanner was used to acquire both bright-field and fluorescent images from the tissue sample (Figure 5.2). For each sample, 400 projections were acquired with angular steps of 0.9° between projections over the full 360° rotation. For fluorescence imaging, the sample was illuminated with a xenon arc lamp (HPLS-30-04; Thorlabs Inc, UK) combined with an excitation filter to detect the fluorescence signal. The emitted light was then detected with a back illuminated CCD camera (sCMOS camera; Zyla, Andor, UK). The excitation filters used for this study consisted of the $GFP_{(470ex/525em)}$ and Texas $Red_{(560ex/630em)}$ channels, which acted as band-pass filters for fluorescence imaging and separation of fluorescence signals. The GFP channel was used to detect the GFP signal from the eNOS-GFP expression in the transgenic mice, in addition to the fluorescent tracers (yellow-green) injected into WT mice. The Texas Red channel was used to detect the fluorescent tracers in eNOS-GFP mice. Raw images were imported into FIJI (NIH, MD, USA) for further analysis and processing.

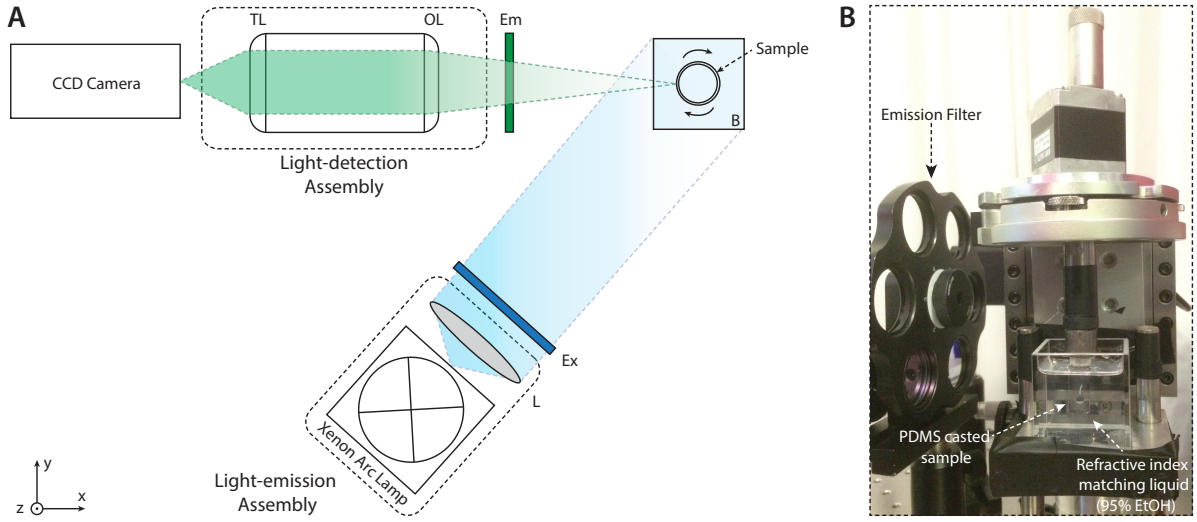


Figure 5.2: Schematic of the fluorescence OPT imaging setup. The sample is supported in a transparent material (such as agarose gel or PDMS) and rotated through a series of angular positions to acquire projections over 360°The sample is illuminated by a xenon arc lamp combined with an excitation filter (Ex) and detected with an emission filter (Em) connected to a CCD camera. *L: Lens, TL: Tube lens, OL: Objective lens.*

5.3.6 Segmental Tracer Distribution Analysis

To quantify whether segmental outflow patterns tend to preferentially drain towards certain quadrants of the eye, we measured the fluorescent tracer intensities along the entire circumference of the eye and examined the tracer patterns in relation to the quadrants of the eye. Additionally we examined whether the tracer patterns observed in *ex vivo* eyes are representative of the flow patterns in eyes obtained from a living WT mice. Here, we utilized the segmented line tool (FIJI, NIH), a piecewise linear ROI was drawn along the limbus of the eye, extending 150 μm above and below the limbus to capture the fluorescent tracers enmeshed in the TM (*dashed lines*; Figure 5.5A). The tracer intensity profiles was then measured along the ROI (averaged across the width of the segmented line) using the plot profile tool (FIJI). This returned an array of fluorescence intensity values for the tracers as a function of distance along the limbus.

Due to the technical challenges of *in vivo* anterior chamber injections, it is difficult to ensure the entire bolus of tracers remained in the eye once the glass needle was removed due to reflux of perfusate. Additionally, in *ex vivo* tracer perfused eyes, the amount of tracers delivered to each eye may vary depending on the outflow resistance. Therefore, to account for possible variations in tracer intensities that may arise between individual eyes, the fluorescence intensities of the tracers were normalized by dividing the averaged fluorescence intensity along the selected ROI by the maximum

intensity value to preserve the tracer patterns. The fundamental assumption here is that only the intensity was affected and not the spatial distribution of the tracer patterns, thus we only analyze the tracer patterns instead of the raw intensity values.

5.3.7 Image Processing of Limbal Vasculature

To improve the resolution of the acquired OPT images, image processing algorithms were implemented to enhance the anatomical structures of the limbal vascular network. Due to the similarities between OPT and single-photon emission computed tomography (SPECT/CT), image processing algorithms commonly used in SPECT/CT to improve image resolution may also be adopted for OPT images. Filtered back-projection algorithms are commonly used with ramp-based filters to emphasize the high spatial-frequencies[168], which typically coincides with the finer anatomical structures of the limbal vasculature, such as the corneal arcades and perilimbal vessels (Figure 5.4). However, in the spatial-frequency domain the highest frequencies are dominated by noise. Therefore, the ramp-based filter was combined with a low-pass window to de-emphasize the highest frequencies and reduce the noise but still preserve the signals of interest. For the OPT images acquired, we combined the ramp-based filter with a flat-top window to obtain the micro-vasculature in post-trabecular outflow pathway.

5.4 Results

5.4.1 Comparison of PDMS Protocol vs. Standard BABB Protocol

To determine whether the newly developed PDMS embedding protocol was compatible with fluorescence OPT imaging, eyes obtained from eNOS-GFP mice were processed either by (a) the standard agarose/BABB protocol or (b) the PDMS protocol, in order to compare the suitability of the protocols on preserving the fluorescence signals of interest in the tissue. Additionally, these eyes were also perfused with fluorescent tracers to label the segmental outflow pathways in the TM, whereby the tracers served as a secondary fluorescence signal of interest. The OPT imaging

showed that eyes processed with the standard agarose/BABB protocol, resulted in the quenching of both the endogenous GFP and fluorescent tracer signals after the BABB clearing step (Figure 5.3; *left panel*). After 24 h of incubation with BABB, the GFP signal was mostly quenched leaving only a faint band of fluorescence surrounding the limbus, but not clear enough to resolve any anatomical structures, such as the limbal vasculature. Furthermore, the perfused fluorescent tracers were completely quenched, rendering the agarose/BABB protocol unsuitable for most segmental outflow tracer studies used in eye research[42,102,123,143,231]. In contrast, eyes processed with the PDMS embedding protocol showed clear GFP fluorescence and tracer signals surrounding the limbus of the eye (Figure 5.3; *right panel*). With the PDMS embedding protocol, the fluorescence signals were preserved and eNOS-GFP labeled anatomical structures were clearly visualized with OPT imaging. Additionally, the PDMS embedding protocol was able to reduce the sample preparation time from a 3-day protocol to a half-day protocol. This indicates that the PDMS embedding protocol could be used as an alternative to the standard agarose/BABB protocol for fluorescence OPT imaging.

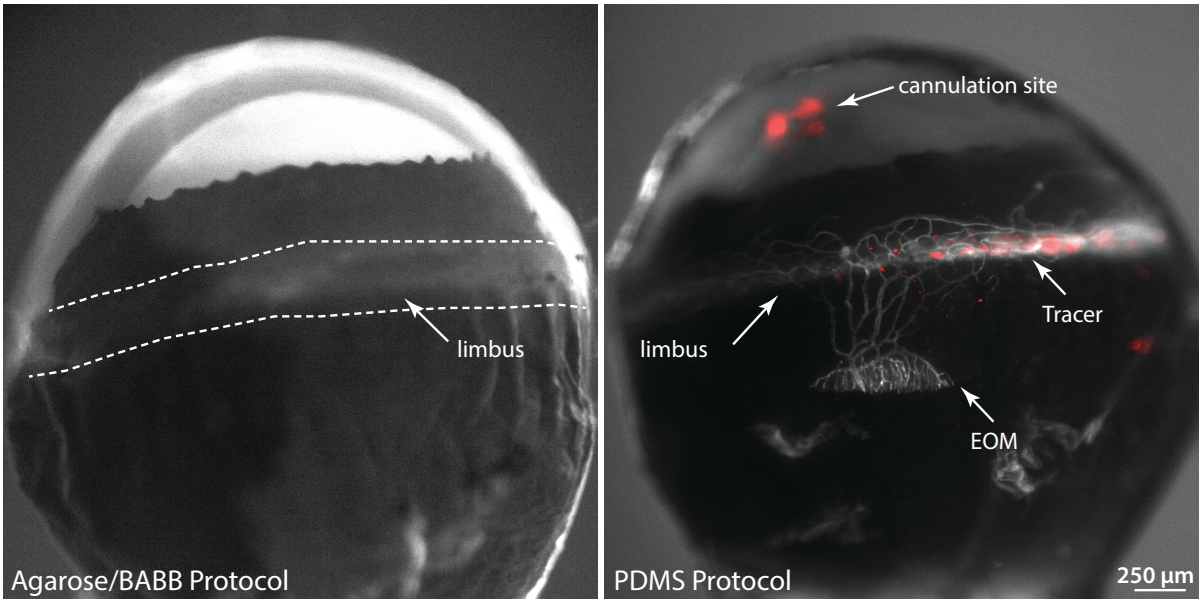


Figure 5.3: Comparison of sample preparation protocols used for fluorescence OPT imaging of eNOS-GFP mouse eyes. **(Left)** eNOS-GFP eye perfused with fluorescent tracers were processed for OPT imaging using the standard agarose embedding and BABB tissue clearing protocol. **(Right)** eNOS-GFP eye perfused with fluorescent tracers were processed for OPT imaging using the PDMS embedding protocol. *EOM: Extraocular muscles*.

5.4.2 Visualization of the Limbal Vasculature in eNOS-GFP Mice

Once the PDMS embedding protocol has been established to be compatible with fluorescence OPT imaging, we continued to acquire high resolution images of the limbal vascular network

of the eNOS-GFP mice. Figure 5.4 showed that the GFP signal was preserved with the newly developed PDMS embedding protocol, and the fluorescence signal is localized to the vascular-derived endothelial cells that line the limbal vasculature, which includes the SC endothelium, episcleral vessels (EV) and blood vessels in the extraocular muscles (EOM). At higher magnifications, we were able to resolve fine anatomical structures such as corneal arcades (CA) and perilimbal vessels (PLV), which are on the order of several microns wide ($\sim 10 - 20$ μm) surrounding the limbus of the eye. The perilimbal vessels was the most prominent vascular structure visualized in the superficial limbus, and often revolved around the whole circumference of the eye which connects to the downstream episcleral veins (Figure 5.4B-C). The episcleral veins extends posteriorly, often towards regions where the extraocular muscles were located which reconnects to the circulatory system for aqueous humor drainage (Figure 5.4D). In addition to the superficial vascular network along the limbus, we were also able to visualize the SC as shown by a "band of fluorescence" underlying the superficial limbal vasculature (Figure 5.4B-C). The Schlemm's canal was presented as a "hazy canal-like" structure, which is likely due to the limited depth of focus of the OPT imaging modality. These micro-anatomical features of the post-trabecular pathway have also been previously identified with confocal microscopy and confirms our observations[228].

5.4.3 360° View of Tracer Distribution

Fluorescence OPT imaging revealed a segmental tracer distribution in the TM/JCT of all the perfused mouse eyes (*n=3*), which was consistent with previous works carried out by epifluorescence and confocal microscopy in both human and animal models[42,102,123,143,231]. Segmental tracer distribution was observed over the entire circumference of the eye, as shown by four angular representative views separated by 90° rotation (Figure 5.5). The use of multichannel fluorescence OPT has provided a non-invasive imaging modality that can map the segmental tracer distribution, in relation to the limbal vasculature of the post-trabecular outflow pathway over the entire circumference of the eye. The perfused fluorescent tracers (*red*) were co-visualized with the endogenous GFP signal (*grey*) from the eNOS-GFP mice, which allows for potential colocalization analysis of the two fluorescent labels. Regions of higher tracer labeling (*arrowheads*) tends to coincide with regions of the limbal vascular network that are closely situated to downstream episcleral veins, which tend to feed into nearby extraocular muscles (Figure 5.5B,C,D). Whilst regions of lower tracer label-

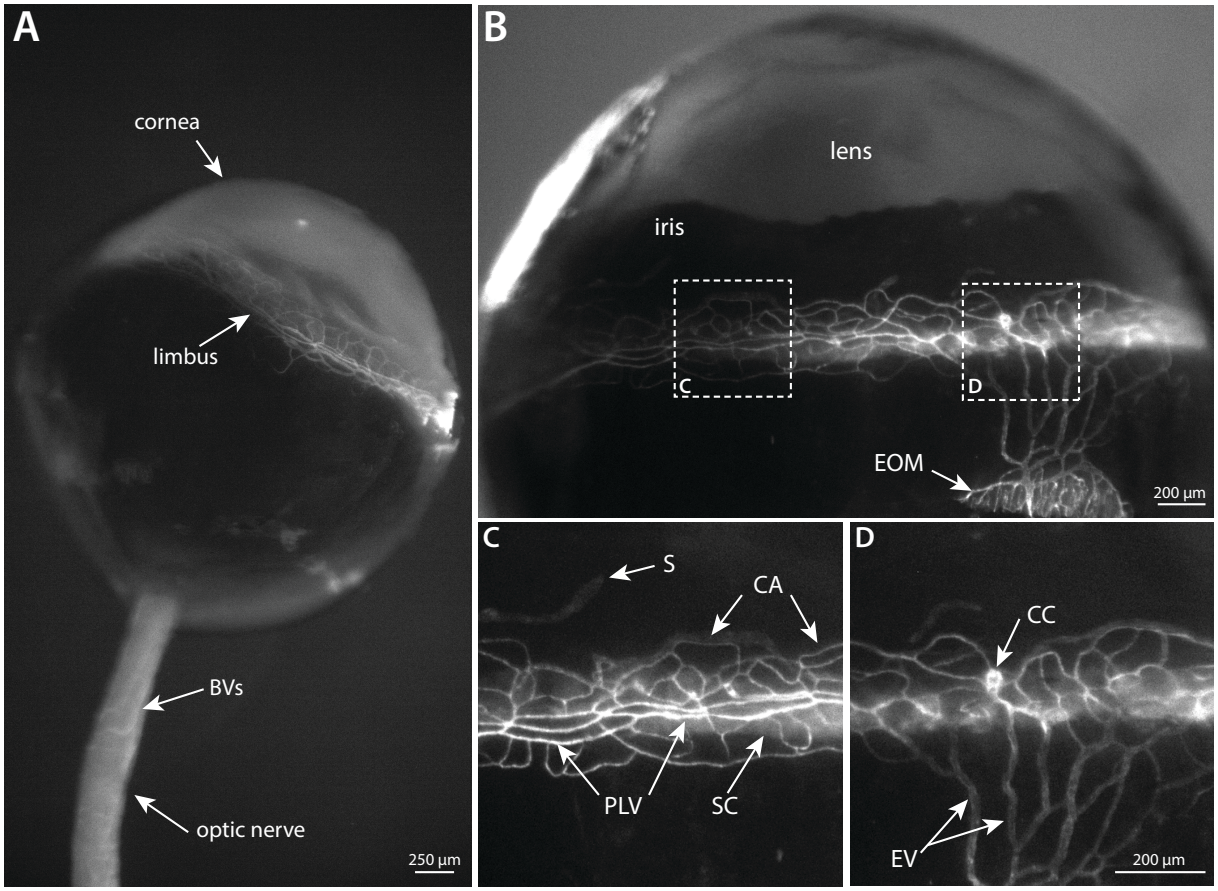


Figure 5.4: Visualization of the limbal vascular network of eNOS-GFP mouse eyes imaged with fluorescence OPT. **(A)** Fluorescence OPT image of the entire mouse eye, which also includes the optic nerve and it's surrounding blood vessels (BV). GFP fluorescence was also detected surrounding the limbal region, where the Schlemm's canal (SC), perilimbal vessels (PLV) and downstream episcleral vessels (EV) reside. **(B)** GFP fluorescence images of the anterior segment of the eNOS-GFP mice. Clear visualization of anatomical structures from the post-trabecular outflow pathway. **(C)** Higher magnification of region of interest showing the GFP signal in the Schlemm's canal (SC), which is defined as a "band of fluorescence" running along the limbus of the eye. **(D)** Higher magnification of region of interest showing the GFP signal in the Schlemm's canal connecting to the episcleral veins that drains the aqueous humor back to the vascular circulation. Collector channels (CC) could also be visualized with fluorescence OPT as "ring-like" structures. *S: Blind-ending lymphatic sprouts, CA: Corneal arcades, EOM: Extraocular muscles.*

ing (*asterisks*) tends to be located in the midway point between downstream episcleral veins that extend into the extraocular muscles (Figure 5.5E). Additionally, from the 360° tracer intensity profile along the entire circumference of the eye, more tracer labeling was found to be located in the nasal-superior quadrants (Figure 5.5F), which is consistent with previous findings in human eyes[42]. These findings were consistent across all three samples obtained from separate experiments. Interestingly, when analyzing the segmental outflow patterns in living mice, we observed a similar trend in tracer distribution over the circumference of the eye. Here, we typically found more tracer labeling in the nasal-superior quadrants compared to other quadrants of the eye (Figure 5.6). This suggests that tracer patterns observed in *ex vivo* eyes are comparable to the tracer patterns observed in living WT mice, and additionally, aqueous humor outflow tends to preferentially drain towards the

nasal-superior quadrants of the eye.

By processing the enucleated eyes with the newly developed PDMS embedding protocol, it allows for researchers to visualize the segmental outflow patterns in a global context and identify regions of high and low flow, which can later be isolated for further analysis. Hence, OPT imaging can add another dimension to tracer flow studies that compliments existing imaging techniques such as confocal microscopy and electron microscopy.

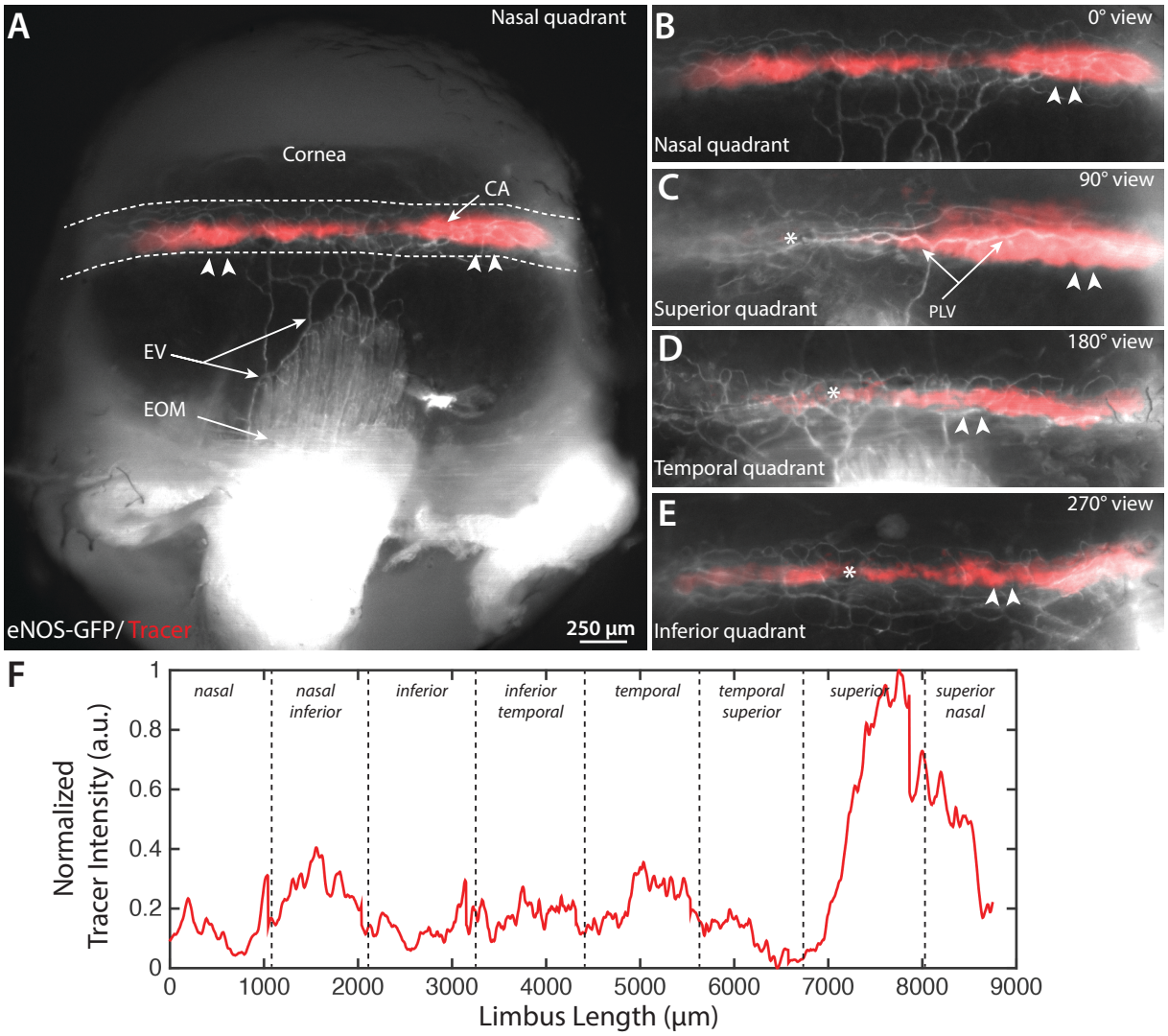


Figure 5.5: 360° view of tracer distribution in *ex vivo* mouse eyes. **(A)** Representative fluorescence OPT image of eNOS-GFP mouse eye visualized with the GFP channel, whilst the perfused fluorescent tracers were visualized with the Texas red channel (n=3). The tracer distribution in the conventional outflow pathway shows non-uniform labeling or segmental outflow. **(B-E)** Regions of high tracer labeling *(arrowheads)* and low tracer labeling *(asterisks)* are shown in relation to the anatomical structures of the post-trabecular outflow pathway as the whole eye is rotated over 360°. **(F)** Normalized tracer intensity profile over the entire circumference of the eye plotted as a function of length along the limbus to illustrate changes in segmental tracer distribution. *CA: Corneal arcades, EV: Episcleral vessels, EOM: Extraocular muscles, PLV: Perilimbal vessels.*

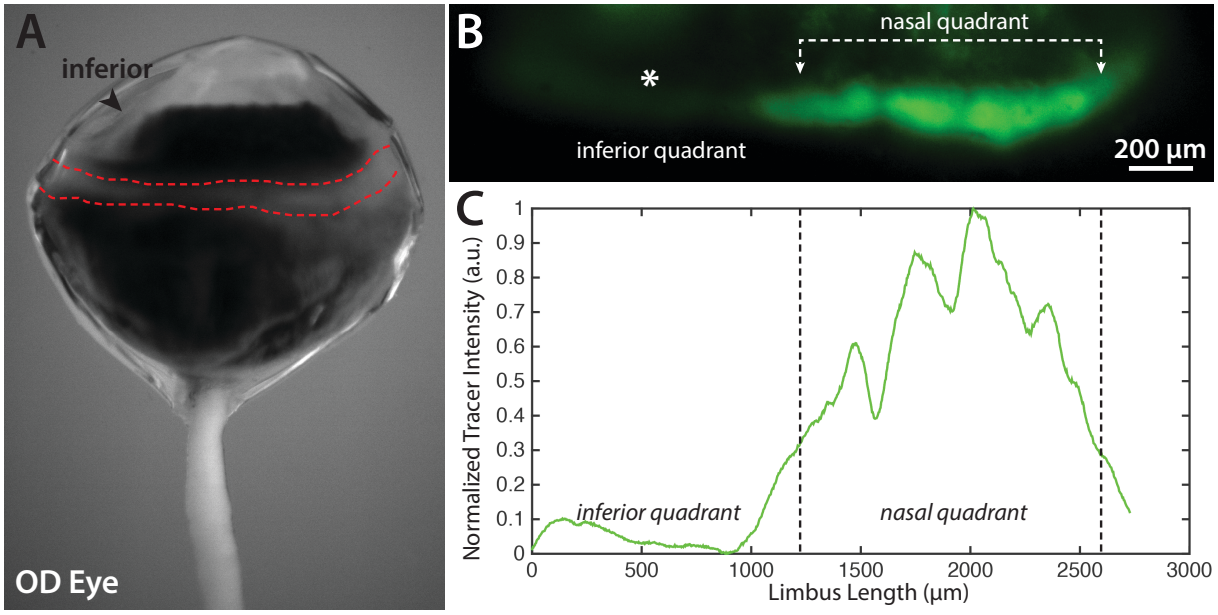


Figure 5.6: Segmental outflow patterns of living WT mice. **(A)** Representative mouse eye (OD) injected with a bolus of fluorescent tracers (1.5 μl; $\sim$1x10^5 particles/eye) to label the segmental outflow patterns imaged with bright-field OPT. Region of interest along the limbus of the eye where the TM/JCT resides is indicated by the *red dashed lines*. Tracer injection (yellow-green) was cannulated in the inferior quadrant of the eye indicated by the *arrowhead*. **(B)** Representative fluorescence OPT images obtained from tracer injection into the anterior chamber of the eye. **(C)** Normalized tracer intensity profile of each tracer (averaged across the ROI thickness; 300 μm) plotted as a function of length along the limbus to illustrate the segmental tracer distribution. *Asterisks = regions of low tracer labeling.*

5.4.4 Image Processed Limbal Vasculature

To obtain better resolution of the limbal vascular network, OPT acquired images were image processed with a ramp-based filter combined with a low-pass window to de-emphasise the highest spatial-frequencies, typically dominated by noise. Hence, we applied a flat-top window to enhance the visualisation of the micro-vasculature surrounding the limbus of the eye and reduce the noise of the raw OPT image. Figure 5.7 shows a side-by-side comparison of the raw fluorescence OPT image (*left panel*) against the flat-top filtered OPT image (*right panel*). The flat-top filtered image clearly enhances the micro-vascular network along the limbus, especially the finer anatomical structures such as the corneal arcades and perilimbal vessels when compared against the raw fluorescence OPT image. Although by applying the flat-top filter to the OPT image, other anatomical structures such as the SC becomes de-emphasized. Thus, depending on the anatomical features of interest, different low-pass windows combined with the ramp-based filter can be applied to the images.

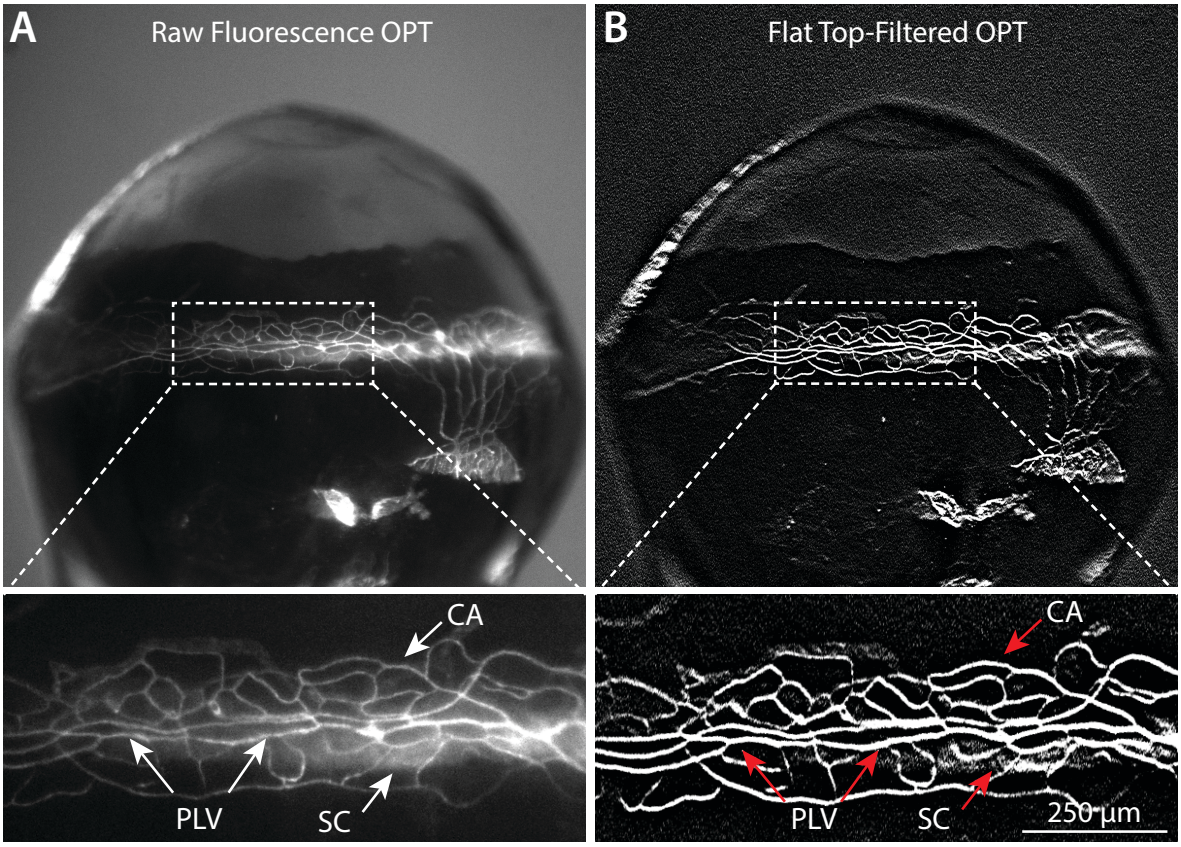


Figure 5.7: Enhancement of fluorescence OPT acquired images of the limbal vasculature. **(A)** Raw fluorescence OPT image of the limbal vasculature. *(Inset)* Higher magnification of the limbal vasculature before image processing enhancement. **(B)** Flat top-filtered fluorescence OPT image of the limbal vasculature. *(Inset)* Higher magnification of the limbal vasculature post-image processing enhancement. Flat top-filtering of OPT image has enhanced anatomical structures such as the corneal arcades (CA) and perilimbal vessels (PLV), but has reduced the GFP signal in the Schlemm's canal (SC).

5.5 Potential Pitfalls and Trouble Shooting

5.5.1 *In Vivo* Tracer Injections

During intracameral injections in living WT mice, in some eyes the cornea and lens started to exhibit acute reversible opacity under anesthesia. To reduce eye opacity we employed several methods: 1) eyes were kept moist with periodic drops of artificial tears, 2) the body temperature was maintained by using a custom-made water heating pad, and 3) the cannulation time was typically limited to $\sim$ 5 min per eye.

To minimize the amount of reflux during the delivery of tracers, the following steps were carried out: 1) use a glass micro-needle to initially cannulate the cornea to remove some aqueous

humor via capillary action, 2) use a micro-manipulator for the insertion of the tracer-loaded glass micro-needle and maintain it in the anterior chamber for ∼15 seconds to allow for the eye to slightly acclimatize, and 3) place a topical antibiotic ointment drop over the cannulation site followed by the slow removal of the needle. Note: the topical ointment has a higher viscosity than the perfusate, thus helps "partially" seal the insertion site.

5.5.2 PDMS Embedding and Positioning of Eyes

Several potential pitfalls may arise from embedding the eyes in PDMS, such as 1) the presence of micro-bubbles which interferes with the OPT imaging, 2) the formation of an "interface" between the surface of the eye and the PDMS (referred to as "halo effect"), and 3) off-centered positioning of the eye. To reduce the formation of micro-bubbles the PDMS was first poured into the casting cylinders then degassed in a dessicator for ∼15 min. This eliminates micro-bubble formation introduced from pouring the PDMS into the cylinders. Prior to positioning and embedding the eyes in the casting cylinders, the eyes should be transferred to a piece of Kimwipe to absorb any moisture on the surface of the eye, followed by pre-incubating the eye in a Petri dish filled with degassed PDMS for 5 min. Removing the residual PBS from the surface of the eye and pre-incubating in PDMS solution helps reduce the halo effect. The degassed PDMS-filled cylinders should be partially casted to increase the viscosity of the solution. This typically took ∼15 min in the oven at 65℃, although this pre-casting time needs to be refined by the user. To position the eye use a pair of fine forceps to hold the optic nerve and slowly lower the eye into the PDMS-filled cylinder. Make sure that the optic nerve is centered along the axis of rotation to ensure good OPT projections. Cure the eyes for another 45 min at 65℃. Note: check that the eye maintains in the middle of the casting cylinder, if the eye has moved, this indicates the pre-casting time needs to be extended. To remove the casted PDMS from the cylindrical molds, 70% ethanol was used to dislodge the sample.

5.6 Conclusion and Potential Applications

In this study, we developed a novel embedding protocol for imaging segmental outflow patterns in enucleated mouse eyes that is compatible with fluorescence OPT. This protocol enables researchers to visualize segmental outflow patterns in relation to the post-trabecular limbal vasculature, in particular, the aqueous veins and episcleral veins which play an important role in determining the distal resistances of the outflow pathway[188,203,245]. Tissues can now be imaged without being physically dissected into smaller wedges then reconstructed, therefore preserving the anatomical structures of the eye allowing for a global visualization of the interconnectivity of the outflow pathway with minimal disruption to the flow patterns. Additionally, with the PDMS embedding protocol, we can now bypass the tissue clarification step with toxic chemicals such as BABB, that often resulted in the quenching of fluorescent labels and thus the loss of tracer distribution information. By changing the embedding and tissue processing protocol, we have effectively reduced both the processing time from 72h to 6h preparation for OPT imaging, and the imaging time from 2-3h to less than 15 min per sample when compared against confocal microscopy. Furthermore, after OPT image acquisition, the tissue can be extracted from the PDMS cast and processed for other analytical or morphometric studies.

From this study, with the newly developed protocol, we were able to visualize the segmental outflow patterns in a global context and identify regions of high and low flow in relation to the post-trabecular limbal vasculature and extraocular muscles. Interestingly, regions of high tracer labeling tends to coincide with regions of the limbal vascular network that are closely situated with downstream aqueous veins and episcleral veins. Moreover, regions of higher tracer labeling tends to coincide with the nasal and superior quadrants of the eye (Figure 5.5). Previous studies have shown that in both bovine[17] and human[42,102] eyes, tracer patterns tend to coincide with the distribution of collector channel ostias, which coincidentally are also found more abundant in the nasal and superior quadrants of the eye[90,101]. These results suggest that segmental outflow is a multi-scale problem influenced by multiple aspects: from the distal resistance sites and the distribution of collector channels[17,42,102] at the tissue level; to the regional variations in extracellular matrix (ECM) proteins[123,218] and non-uniform distribution of pores along the inner wall of SC[29] at the cellular level; to the regional variations in ECM gene expression[231] at the molecular level.

Alternatively, with the PDMS embedding protocol, we can also potentially examine the effects of outflow enhancing drugs such as pilocarpine on segmental outflow patterns. Previous studies have shown that only a fraction of the TM is considered filtration-active at any given time[42,231]. Therefore, with our PDMS embedding protocol in conjunction with previously established two-color tracer technique[42], we can potentially visualize and compare the efficacy of drugs that target the filtration-inactive regions of the meshwork by comparing changes in filtration patterns. The use of OPT in conjunction with the two-color tracer technique can provide an visual assessment on whether drugs are targeting the filtration-inactive regions of the TM. With OPT imaging, along with other functional studies that can be carried out in *ex vivo* perfusions, this could lead to the development of better targeted anti-glaucoma therapeutics that aim to lower IOP. In conclusion, we have shown that fluorescence OPT to be a valuable imaging tool that compliments established imaging techniques, by providing a global view of how segmental outflow is distributed over the circumference of the eye in relation to the downstream resistance sites situated in the post-trabecular limbal vasculature.

Chapter 6

Targeted Delivery of Nitric Oxide to the Trabecular Outflow Pathway via Enzyme Loaded Nanoparticles

This chapter consists of a paper in preparation to be submitted to Proceedings of the National Academy of Science.

6.1 Introduction

Aqueous humor outflow is regulated by the resistance generated within the conventional or trabecular outflow pathway, which comprises of the trabecular meshwork (TM), juxtacanalicular connective tissue (JCT) and the inner wall endothelium of the Schlemm's canal (SC)[117,166]. Increased outflow resistance is responsible for elevated intraocular pressure (IOP) – a characteristic feature and primary risk factor associated with the development of glaucoma[210]. Reducing IOP is the only means to prevent further vision loss[3]. However the mechanism(s) responsible for modulating these resistance sites still remain largely unknown. Nitric oxide (NO), a key signaling molecule responsible for mediating various physiological functions, has been shown to regulate aqueous humor outflow by relaxing the TM cells[61,236,237], and modulating endothelial permeability of the inner wall of SC[44,57,65]. Both of these mechanisms have previously been shown to decrease outflow resistance and IOP in various animal and human models[24,43,62,65,111,191,233]. Recent efforts have resulted in the development of several NO-donating compounds[24,113,130], including latanoprostene bunod (LBN), a NO-donating prostaglandin F2α receptor agonist that has been shown to be more efficacious than latanoprost at reducing elevated IOP in ocular hypertensive patients[233]. Thus, suggesting that the improved IOP reduction is likely attributed to the effects of the NO-donating moiety targeting the TM/SC cells to enhance aqueous humor outflow.

However, NO has been shown to play a multifaceted role within the trabecular outflow pathway. Therefore, depending on the site at which NO is delivered, the physiological response elicited may in fact be counterproductive and result in an increase in IOP, rather than the desired IOP-lowering effect. For instance, NO can affect the contractility of the ciliary muscle[18,84,89,236], which can regulate the outflow resistance through the tendinous connections to the JCT and inner wall of SC[165,186,187,222]. Furthermore, NO can also lead to an increase in episcleral venous pressure[245], which can also result in an increase in IOP. Hence, the use of NO as a potential therapeutic treatment for ocular hypertension requires NO to be delivered on-site to the trabecular meshwork where the bulk of outflow resistance is generated to achieve the optimal therapeutic effect.

Here, we developed a targeted NO delivery platform that liberates NO within the trabecular meshwork to modulate the outflow resistance sites to increase aqueous humor outflow[43,62,65,158,191,211]. We demonstrate a proof-of-concept for localized NO synthesis within the outflow pathway through

the use of an enzyme prodrug therapy (EPT), whereby, β-galactosidase (enzyme; catalyst) catalyzes β-gal-NONOate (substrate; NO donor) to liberate NO on-site to potentially enhance aqueous humor outflow (Figure 6.1). To ensure on-site NO synthesis, the enzyme is encapsulated in micron-sized poly(methacrylic acid) (PMA) capsules that get enmeshed within the TM, which "localizes" the catalyst within the tissue. The NO donor, is then encapsulated in liposomes that can be delivered to the outflow pathway to elicit the NO-mediated response when the substrate is slowly released at the outflow resistance sites, thus achieving a targeted on-site NO delivery platform.

This chapter provides preliminary data to support our hypothesis that targeted and localized NO synthesis in the TM will provide enhanced therapeutic effect of NO-mediated increases in aqueous humor outflow in the eye, compared to non-targeted delivery of NO.

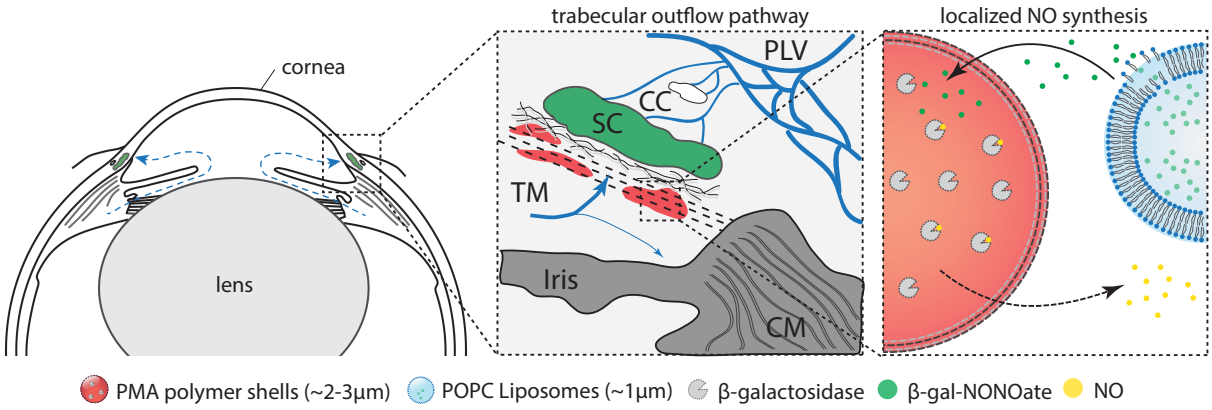


Figure 6.1: Schematic representation of targeted delivery of NO via enzymatic biocatalysis. **(Left)** Anterior segment of the mouse eye showing the direction of aqueous humor outflow in blue. **(Center)** Enlargement of the iridocorneal angle (boxed region in left panel) showing the trabecular outflow pathway. **(Right)** Schematic of localized NO synthesis within the juxtacanalicular connective tissue (JCT) region and inner wall of Schlemm's canal endothelium (SC). *TM: trabecular meshwork, CM: ciliary muscle, CC: collector channels, PLV: perilimbal vessels*

6.2 Materials and Methods

6.2.1 Materials

Poly(*N*-vinyl pyrrolidone) (PVP, Mw 10,000 Da), β-galactosidase, sodium acetate (NaOAc), and 2,2'-dithiopyridine were purchased from Sigma-Aldrich. β-Gal-NONOate was obtained from Cayman Chemical. Poly(methacrylic acid) (PMA, Mw 15,000 Da) was obtained from Polysciences (Eppelheim, Germany). 1-palmitoyl-2-oleoyl-*sn*-glycero-3-phosphocholine (POPC) was purchased

from Avanti Polar Lipids. Amine-functionalized SiO_2 particles (1 μm diameter) were obtained from Microparticles GmbH (Berlin, Germany). Alexa Fluor 488 succinimidyl ester was purchased from Invitrogen.

6.2.2 Experimental Design

This study consists of a two-step experimental protocol: (1) the delivery of the enzyme-encapsulated in crosslinked PMA capsules via intracameral injections in living mice, and (2) the delivery of the substrate-encapsulated in liposomes via *ex vivo* perfusions 48 h post-intracameral injections. All experiments were performed in wild-type (WT) mice using paired eyes, where the experimental eye received both enzyme-encapsulated PMA capsules and substrate-encapsulated liposomes, whilst the contralateral control eye received empty PMA capsules and substrate-encapsulated liposomes.

6.2.3 PMA Capsule Assembly

Firstly, PMA_{SH} capsules were synthesized and functionalized with 14 mol% of thiol groups as previously reported[246]. This was followed by the PMA capsule assembly procedure and encapsulation of the enzyme. SiO_2 particles (5 wt%) were washed with three centrifugation/redispersion cycles (1,200 g, 30 s) in Tris-EDTA buffer (10 mM, pH 7.5). β-galactosidase (1 mg/ml in Tris-EDTA buffer) was added to the particle solution and adsorption was allowed to proceed for 1 hour with constant shaking. The resulting particles were washed twice with Tris-EDTA buffer and twice with NaOAc buffer (20 mM, pH 4). Assembly of polymer multilayers was achieved by alternately incubating the particles with PMA_{SH} (1 mg/ml, 15 min) and PVP (1 mg/ml, 15 min) in NaOAc buffer with constant shaking. The particles were washed with three centrifugation/redispersion cycles in NaOAc buffer between layers and the process was repeated until four bilayers of PMA_{SH}/PVP were assembled. The thiols within the polymer layers were crosslinked with 2,2'-dithiopyridine (0.5 mg/ml, 15 h) in NaOAc buffer. Hollow capsules were obtained by dissolving the silica core using a 2 M hydrofluoric acid (HF)/8 M ammonium fluoride (NH_4F) solution for 2 min, followed by multiple centrifugation/washing cycles (4500 g, 3 min). **Caution! HF and NH_4F are highly toxic. Care should**

be taken when handling HF and NH_4F solutions and only small quantities should be prepared.

6.2.4 Preparation of Alexa Fluor 488-labeled β-galactosidase

A solution of 10 mg/ml β-galactosidase (5 mg) in carbonate buffer (100 mM, pH 8.3) was incubated with 100 μl of Alexa Fluor 488 succinimidyl ester (1 mg/ml in DMSO). The reaction was allowed to proceed overnight, followed by purification via size-exclusion chromatography (SEC).

6.2.5 Liposome Formation

POPC (5 mg) was dissolved in chloroform and dried by evaporation of the chloroform under nitrogen for 1 h. The dry lipid film was hydrated with 1 ml of 500 μM β-gal-NONOate in DBG solution (Dulbecco's PBS including divalent cations and 5.5 mM D-glucose). Liposomes were obtained by extruding the lipid solution through 1 μm filters (31 times). Non-encapsulated β-gal-NONOate was removed from the liposome suspension by SEC.

6.2.6 Characterization of β-galactosidase Mediated Release of NO

NO release kinetics from both non-encapsulated and encapsulated β-galactosidase/β-gal-NONOate enzymatic hydrolysis was determined with a NO-sensitive electrode (ISO-NOS II, WPI, Hertfordshire, UK) following previously described protocol[43]. Briefly, the NO-electrode was placed in a solution containing 0.1 M H_2SO_4 and 0.1 M KI to polarize the sensor and obtain a baseline current. To determine the standard curve, changes in current were measured in response to incremental volumes of 50 μM $NaNO_2$ added to the H_2SO_4/KI solution within a glass vial. Conversion of $NaNO_2$ to NO occurs rapidly and follows 1:1 stoichiometry, such that the NO concentration is dictated by the added concentration of $NaNO_2$.

Once the standard curve was generated, we first examined NO synthesis from non-encapsulated β-galactosidase and β-gal-NONOate enzymatic reaction. The NO-sensitive electrode was first equi-

librated in a 5 ml DBG solution supplemented with β-galactosidase (0.1 mg/ml) in a glass vial and left to stabilize for 2 hr at 37℃. To determine the standard curve for the NO synthesis from the enzymatic reaction, incremental volumes of β-gal-NONOate (25–150 μl, at 50 μM) was added to the glass vial and changes in current were measured. Secondly, we examined the NO release from β-galactosidase encapsulated PMA capsules and β-gal-NONOate encapsulated liposomes. The NO-sensitive electrode was again immersed in a 5 ml DBG solution supplemented with β-galactosidase encapsulated PMA capsules (400 μl; at 1 mg/ml) and left to stabilize for 2 hr at 37℃. NO release kinetics were determined for three different concentrations of β-gal-NONOate encapsulated liposomes (25, 50 and 75 μM). All NO measurements were performed in mock-aqueous humor solution typically used for *ex vivo* perfusions (DBG solution) at 37℃ with continuous mixing from a magnetic stir bar.

6.2.7 Animal Husbandry

All experiments were conducted in compliance with the Association for Research in Vision and Ophthalmology Statement for the Use of Animals in Ophthalmic and Vision Research under UK Home Office Project License approval for research at Imperial College London. This study used C57BL/6 male wild-type (WT) mice subjected to *in vivo* intracameral injections followed by *ex vivo* eye perfusions. WT mice were 10 – 12 wk of age. Mice were housed in individually ventilated cages, fed *ad libitum*, and maintained at 21℃ with a 12:12-h light-dark cycle, with lights on from 6 AM to 6 PM.

6.2.8 *In Vivo* Delivery of β-galactosidase Encapsulated PMA Capsules

For this portion of the experiment, WT mice were delivered with a bolus of β-galactosidase encapsulated PMA capsules into the anterior chamber of the eye via intracameral injections; this allows for the PMA capsules to be enmeshed within the JCT region of the TM via the preferential drainage routes in the trabecular outflow pathway. Before the delivery of the PMA capsules, WT mice were first anesthetized with ketamine (66.6 mg/kg, Fort Dodge Animal Health, Fort Dodge, IA) and Dormitor® (medetomidine hydrochloride; 0.66 mg/kg, Orion Pharma) via intraperitoneal

(i.p.) injection. Each mouse received dilation drops (phenylephrine hydrochloride (2.5% w/v) and tropicamide (1% w/v); Bausch & Lomb, Rochester, NY) to both eyes to minimize potential damage to the iris during cannulation of the glass needle. This was followed by a subcutaneous injection with enrofloxacin antimicrobial (5 mg/kg, Baytril; Bayer Healthcare, Leverkusen, Germany), additionally their eyes were kept moist with artificial tears (Vidisic®; Bausch & Laumb, Rochester, NY) prior to intracameral injections.

For the intracameral injections, the mouse was secured in place with the assistance of a head-holder (Model 923-B; Kopf Instruments, CA, USA) and placed on a warm-water place mat. Eyes were cannulated with a pulled glass micro-needle (100 μm tip) positioned parallel to the iris and above the limbus to remove a portion of the aqueous humor in the anterior chamber by capillary action. Intracameral injections were then carried out with a pulled glass micro-needle (100 μm tip) filled with 1.5 μL of either empty PMA capsules (vehicle-control eyes; $\sim 10^6$ particles/μl) or β-galactosidase encapsulated PMA capsules (treated eyes; $\sim 10^6$ particles/μl) suspended in dH_2O (Ultra^{TM} DNase/RNase free water; Invitrogen) connected to a 10 μL glass syringe (Gastight; Hamilton, Reno, NV) then inserted into the same cannulation site with the assistance of a micro-manipulator, and delivered to the anterior chamber of the eye. Topical antibiotic ointment (1% w/w Fucithalmic; LEO Pharma, Denmark) was then applied to the cannulation site followed by removing the needle slowly from the eye to reduce reflux. After the procedures, the mice were given 1.5 mg/kg of Antisedan® (atipamezole hydrochloride; 1.5 mg/kg, Orion Pharma, Berkshire, UK) via i.p. injection and placed in a heated chamber (maintained at 28° C) to allow for faster recovery from anesthesia. The mice were allowed to recover for 48 hrs post-intracameral injections before the mice were euthanized by overdose of Pentobarbital (150 μL; Euthatal, Merial, UK) and the eyes were enucleated for *ex vivo* perfusions.

6.2.9 *Ex Vivo* Delivery of β-gal-NONOate Encapsulated Liposomes via Mouse Eye Perfusions

Eyes obtained from WT mice (post-intracameral delivery of PMA capsules) were perfused with β-gal-NONOate encapsulated liposomes to determine the effect of localized synthesis of NO within the JCT region of the outflow tract. Eyes were enucleated within 10 minutes of death by

cervical dislocation and stored in PBS at room temperature until perfusion, typically within 15 min. Experiments used paired contralateral eyes, which were perfused simultaneously on two identical iPerfusion systems[200] under identical experimental conditions.

Our perfusion method follows previously described techniques[25,27,43,134,211]. Briefly, the eye was affixed to a support using cyanoacrylate glue to stabilize the eye and submerged in PBS in a thermo-regulated bath at 35° C. A 33-gauge beveled needle (Nanofil; World Precision Instruments, Europe; Hitchin, UK) was used to cannulate the eye, with the tip of the needle positioned in the anterior chamber using a micro-manipulator. The pressure and flow rate inside the eye were measured using a wet-wet differential pressure transducer (PX409, Omegadyne, US) and a flow sensor (SLG64-0075, Sensirion, Switzerland), respectively. The enucleated eyes were perfused with DBG supplemented with β-gal-NONOate encapsulated liposomes ($\sim 10^9$ particles/μl). Both the experimental and control eyes were pressurized from a reservoir at 9 mmHg for 45 mins to allow the eyes to acclimatize to the pressure and temperature environment. During this acclimatisation period, the anterior chamber is filled with liposomes which flows toward the filtration-active regions of the JCT, where the PMA capsules are enmeshed. After the acclimatisation period, eyes were perfused at sequential pressure steps, which consisted of the following applied pressures: 6, 7.5, 9, 10.5, 12, 13.5 and 15 mmHg. For each pressure step, steady state was reached when the rate of change in facility was less than 0.1 nl/min/mmHg over a 6 minute time period. Data points that did not reach stable facility for a given pressure step were not included in the analysis. Perfusions that had less than 4 pressure steps were excluded from the study. After each perfusion the eyes were fixed in 4% paraformaldehyde (PFA) overnight at 4° C ready for further processing.

For each eye, the last 4 minutes of steady state pressure-flow data was plotted. The steady flow rate into the eye (Q) exhibits a power-law dependence on perfusion pressure (P), consistent with a pressure-dependent outflow facility. As the standard linear fitting does not capture this non-linear Q–P relationship, we therefore defined C as Q/P at 8 mmHg, corresponding to the effective total facility at a physiological pressure drop across the outflow pathway, and we used a power-law fitting to obtain the best estimate and confidence intervals on C at 8 mmHg. Moreover, according to Sherwood *et al.*[200], in enucleated eyes there is negligible flow at zero pressure, therefore the power-law fitting was forced through a zero-zero intercept. Additionally, based upon the population distribution of the measured outflow facility, data was more accurately represented by a lognormal

distribution, therefore outflow facility values are expressed as C */ 95% confidence intervals.

6.3 Results

6.3.1 *In Vitro* Release of NO via Enzymatic Catalysis

To characterize the NO release kinetics from the enzymatic reaction between non-encapsulated β-galactosidase and β-gal-NONOate, we used a NO-sensitive electrode to measure changes in current in response to increasing volumes of β-gal-NONOate (50 μM) when added to a glass vial of well-mixed DBG solution supplemented with β-galactosidase (400 μl; at 1 mg/ml) (Figure 6.2). NO synthesis from the β-gal-NONOate after being hydrolyzed by β-galactosidase responded in a dose-dependent manner with increasing concentrations of substrate (Figure 6.2A). The release kinetics show a sharp rise in NO release followed by a decline back to the original baseline signal. The average half-life ($t_{1/2}$) of the NO-donor was $\sim$5 mins at physiological pH (7.4) and 37℃. Interestingly, with increasing volumes of β-gal-NONOate added to the solution in the presence of β-galactosidase, the peak NO concentration followed the predicted 1:2 stoichiometry, suggesting that the substrate was instantaneously metabolized by the enzyme and exhibited a linear relationship (Figure 6.2B).

6.3.2 Enzyme-Mediated NO Release from Encapsulated β-gal-NONOate *In Vitro*

In order to extend the NO release kinetics, we proceeded to encapsulate the enzyme and substrate in separate carrier vehicles (PMA capsules and liposomes, respectively) to allow for the gradual release of the NO donor to be hydrolyzed by the enzyme, resulting in an extended NO half-life. Firstly, to demonstrate successful enzyme encapsulation within the PMA capsules, we fluorescently-labeled the enzyme with Alexa Fluor 488, followed by visualization with fluorescence microscopy (Olympus IX73). The fluorescent images showed an uniform fluorescence signal from each PMA capsule, indicating that the enzymes were evenly encapsulated across the PMA capsules (Figure 6.3A), whilst unloaded PMA capsules had negligible fluorescence.

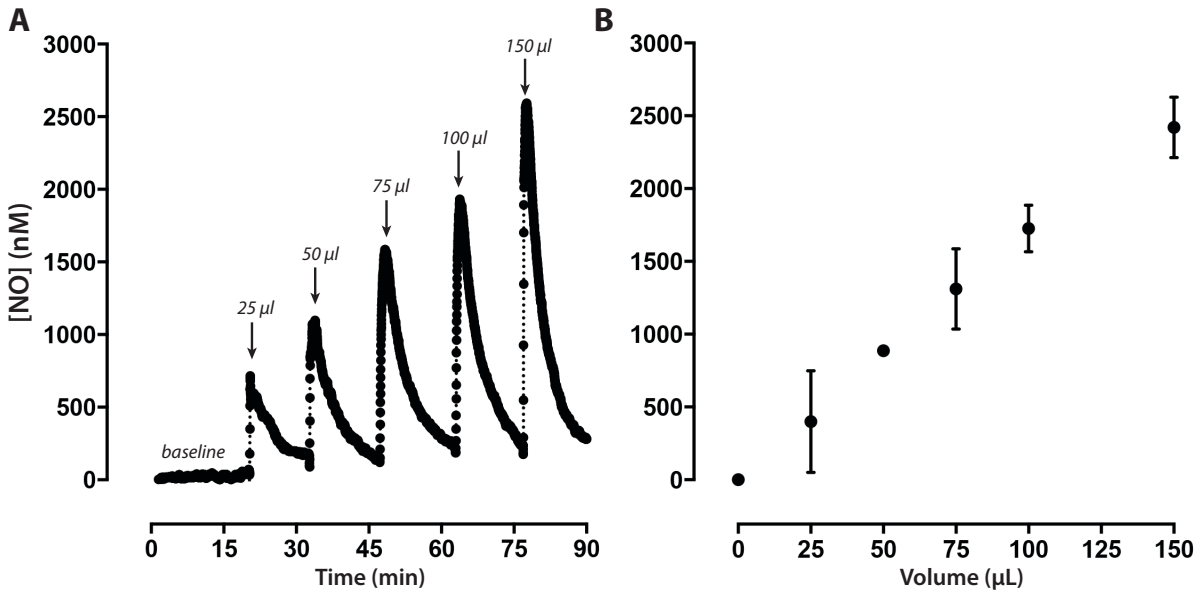


Figure 6.2: Characterization of NO synthesis resulting from β-galactosidase-mediated hydrolysis of β-gal-NONOate. **(A)** Representative dose response curve of NO release from enzymatic hydrolysis between β-galactosidase (0.1 mg/ml) and increasing boluses of β-gal-NONOate (50 μM) in DBG solution [Dulbecco's PBS including divalent cations and 5.5 mM D-glucose]. NO release was measured using a NO-sensitive probe (ISO-NOS II). **(B)** Relationship between NO release and increasing volume of non-encapsulated β-gal-NONOate when hydrolyzed by β-galactosidase (n=3; bars are SD).

We then proceeded to characterize the NO release kinetics for the encapsulated enzyme and substrate, using the same detection setup as the non-encapsulated enzymatic reaction described previously. The β-galactosidase enzymes were encapsulated in hollow PMA capsules, whilst β-gal-NONOate were encapsulated in liposomes to allow for the gradual release of the NO donor to be hydrolyzed by the enzyme. Here, we measured the change in current in response to β-gal-NONOate loaded liposomes (200 μl; at 50 μM) when added to a glass vial of well-mixed DBG solution supplemented with β-galactosidase encapsulated PMA capsules (400 μl; at 1mg/ml). After the liposomes were introduced to the solution, we saw an initial increase in NO release followed by a gradual decay over 6h, returning back to the initial baseline signal (Figure 6.3A). We further tested two additional β-gal-NONOate concentrations encapsulated in liposomes (25 and 75 μM; Figure 6.3B). These results showed a dose-dependent increase in NO release as a function of increasing concentration of β-gal-NONOate encapsulated inside the liposomes. Interestingly, by encapsulating the enzyme and substrate in separate carriers the duration of NO release were increased significantly, extending the $t_{1/2}$ from $\sim$5 min for the non-encapsulated enzyme and substrate to $t_{1/2}$ $\sim$2.15 h.

In addition to the prolonged and continuous delivery of NO *in vitro*, we went on to investigate the possibility of re-dosing the β-galactosidase encapsulated PMA capsules with β-gal-NONOate

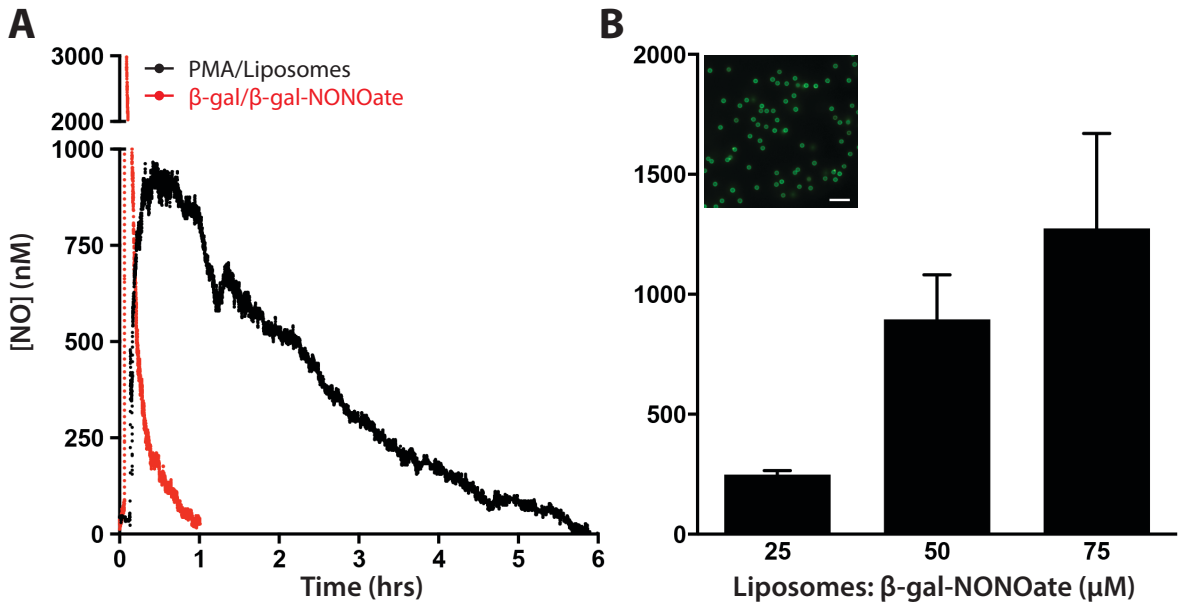


Figure 6.3: NO synthesis from β-galactosidase encapsulated PMA capsules and β-gal-NONOate encapsulated liposomes. **(A)** Representative NO decay curve from encapsulated and non-encapsulated β-galactosidase and β-gal-NONOate. The enzymatic hydrolysis between β-galactosidase encapsulated PMA capsules (1 mg/ml; $\sim 10^6$ particles/μl) and β-gal-NONOate encapsulated liposomes (50 μM; $\sim 10^9$ particles/μl) are shown by the *black tracing*. Non-encapsulated β-galactosidase (0.1 mg/ml) and β-gal-NONOate (200 μl; at 50 μM) are shown by the *red tracing*. **(B)** NO release as a function of increasing loading concentration of β-gal-NONOate encapsulated inside the liposomes (n=3 for each concentration; bars are SD). (*Inset*) Fluorescence microscopy images of PMA capsules loaded with Alexa Fluor 488 labeled β-galactosidase to illustrate the successful encapsulation of the enzyme. Scale bar,10μm.

containing liposomes to provide additional doses of NO treatment over extended periods of time. Figure 6.4 shows that the encapsulated enzyme can be reused to hydrolyze the β-gal-NONOate to release NO over a $\sim$42 h period, indicating that the enzymes remain active and the therapeutic treatment can be achieved over long periods of time.

6.3.3 Targeted Delivery of NO Synthesis to the Trabecular Meshwork

To simulate the effects of this targeted delivery of NO synthesis *in vivo*, WT mice were anesthetized and subjected to intracameral injections to deliver the PMA capsules. Paired eyes were used for all experiments, where the experimental eye received β-galactosidase encapsulated PMA capsules ($\sim 10^6$ particles/μl), whilst the contralateral control eye received empty PMA capsules ($\sim 10^6$ particles/μl). The PMA capsules were delivered 48h prior to *ex vivo* mouse eye perfusions, to allow for sufficient recovery time and for the PMA capsules to be enmeshed within the outflow pathway. Eyes were enucleated for *ex vivo* mouse eye perfusions, where the perfusate consisted of DBG solution supplemented with liposomes containing β-gal-NONOate (50 μM), to determine the

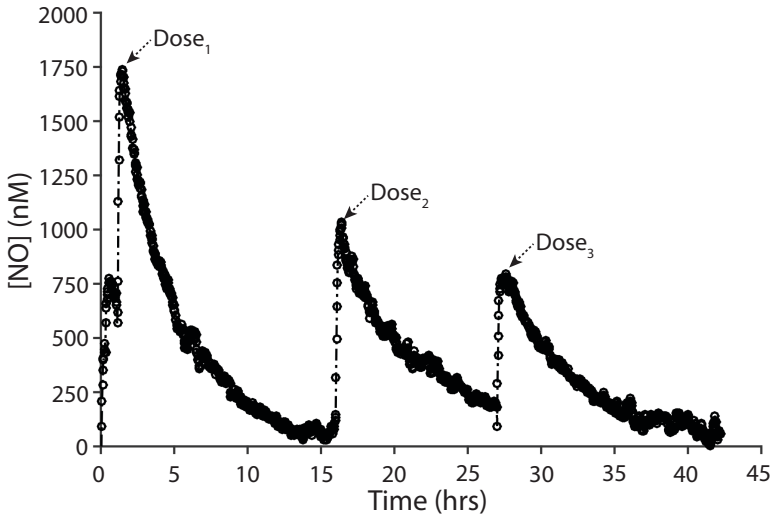


Figure 6.4: Cyclic NO synthesis from β-galactosidase encapsulated PMA capsules and β-gal-NONOate encapsulated liposomes. Representative NO release from cyclic additions of liposomes containing β-gal-NONOate (75 μM) over $\sim$42 h period. Each dose consisted of 200 μl of liposomes added to the DBG solution supplemented with PMA capsules containing β-galactosidase (1 mg/ml).

effect of localized NO synthesis on outflow facility.

Our preliminary data showed that the delivery of liposomes to the eye, resulted in an increase in trabecular outflow facility relative to the contralateral vehicle controls (Figure 6.5). Two independent experiments were carried out, the first pair showed a $\sim$3-fold increase in outflow facility between the experimental and control eye (8.6 */ 1.1 nl/min/mmHg vs. 2.6 */ 1.1 nl/min/mmHg, respectively), whilst the second pair showed a $\sim$1.5-fold increase in outflow facility between the experimental and control eye (5.8 */ 1.3 nl/min/mmHg vs. 4.0 */ 1.1 nl/min/mmHg, respectively). These results are consistent with previous studies, showing that exogenous delivery of NO-donors increases conventional outflow facility in various animal and human models[24,43,62,65,111,191]. In particular, when compared against the non-targeted delivery of NO-donor, S-nitroso-N-acetylpenicillamine (SNAP), outflow facility in *ex vivo* mouse perfusions only increased by 62% when compared against vehicle-control from a previous study[43]. Taken together, from our preliminary data, we show that the targeted and localized NO synthesis in the TM, proves to be a more efficacious treatment for decreasing outflow resistance and increasing outflow facility compared to non-targeted NO release in mice.

Currently, we are planning on obtaining more paired eye data to ensure the localized NO synthesis in the TM and outflow facility effect is reproducible and consistent across a larger cohort of mice.

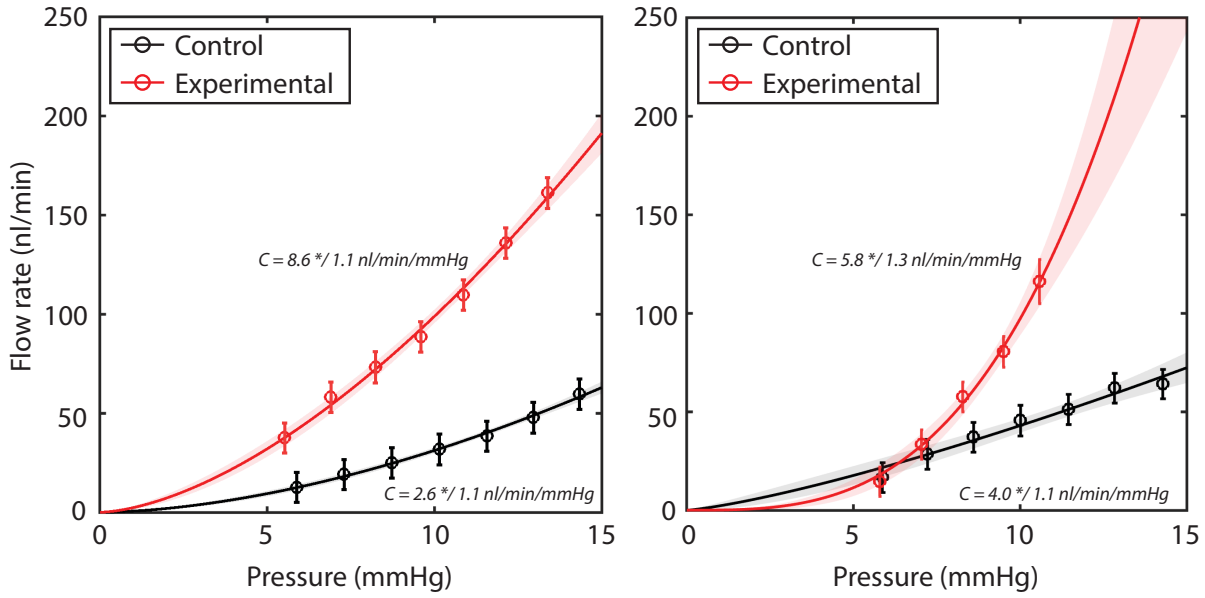


Figure 6.5: Effects of targeted delivery of NO synthesis on conventional outflow facility in eyes obtained from wild-type (WT) mice. Paired eyes were injected with either β-galactosidase containing PMA capsules (*red circles; experimental*) or empty PMA capsules (*black circles; control*) 48 h prior to *ex vivo* mouse eye perfusions. Enucleated eyes were perfused with β-gal-NONOate encapsulated liposomes to determine the pressure-flow relationships for paired eyes. Pressure-flow relationships are shown for two pairs of eyes. *Solid line* represents the power law fitting of the data set. *Shaded region* represents the 95% confidence bounds on the fitting. *Error bars* represents the 95% confidence bounds for the flow values at each pressure step.

6.4 Discussion

Exogenously delivered NO typically leads to an increase in outflow facility and a reduction in IOP. The precise mechanism(s) that NO mediates its physiological effects within the trabecular outflow pathway remains unclear, but most likely involves the modulation of cellular contractility of TM cells[61,236,237] and/or endothelial permeability of the SC cells[44,57] to enhance aqueous humor outflow. However, NO has also been shown to induce relaxation of the ciliary muscle[18,84,89,236], which tends to oppose the effects of TM relaxation through the extensive tendinous connections that exist between these two tissue structures[165,186,187,222]. Alternatively, NO may also affect aqueous humor dynamics by decreasing aqueous humor inflow[197], increasing episcleral venous pressure[245], or affecting choroidal blood volume[125]. Therefore, depending on the site of NO release within the anterior chamber, the physiological response may be counterproductive and result in increased IOP, rather than the desired IOP lowering effect. Furthermore, the reactive nature of NO and its typically short half-life (order of seconds[154,155,167]) makes the on-site delivery of NO to the outflow resistance sites challenging, which could result in limited efficacy on lowering IOP. Hence, the targeted delivery of NO to the outflow resistance sites would potentially achieve the optimal therapeutic benefit,

resulting in decreased outflow resistance and increased outflow facility.

Targeted delivery of β-galactosidase encapsulated PMA and β-gal-NONOate encapsulated liposomes to the site of outflow resistance within the TM, results in a 1.5–3-fold increase in outflow facility compared to control treated eyes, presumably through the localized synthesis of NO targeting the cellular mechanisms in the TM/SC cells. NO is capable of freely diffusing across cell membranes and between cells to trigger various signaling cascades and affect the biological activity of several proteins and enzymes. Most notably, the activation of sGC/cGMP/PKG signaling pathway, responsible for inducing smooth muscle relaxation by regulating intracellular Ca^{2+} levels, myosin light chain phosphorylation and BK_{Ca} channels[81]. Interestingly, in the trabecular outflow pathway, the ciliary muscle, TM and downstream collector channels all possess similar contractile properties to vascular smooth muscle cells, expressing common contractile proteins such as α-smooth muscle actin and smooth muscle myosin[54,79,236]. In human TM cells, NO has also been shown to not only induce relaxation of TM cells[61], but also decrease TM cell volume through the activation of BK_{Ca} channel[60]. Alternatively, NO can also mediate endothelial permeability of the inner wall of SC by disrupting the adherens junctions[44,57] or by altering the SC cell volume by activating the BK_{Ca} channel[65]. These results suggest that NO can mediate the cellular contractility of TM cells and the permeability of the SC endothelium, which in part regulate the outflow resistance by affecting the dimensions of inner wall pores or flow pathways to increase outflow facility.

Our preliminary data shows that the targeted delivery of NO to the trabecular outflow pathway, leads to increased outflow facility, consistent with previous studies conducted with non-targeted delivery of NO donors[24,43,62,65,111,191]. Here, we have developed a potential platform for delivering NO to the targeted outflow resistance sites within the JCT/SC region, utilizing the strategy of on-site NO synthesis to enhance aqueous humor outflow and potentially help compensate for the impaired NO-regulatory machinery[121,141,174] within the trabecular outflow pathway that contributes towards the pathogenesis of glaucoma.

Chapter 7

Conclusions

In this thesis, we examined the hypothesis that the conventional outflow pathway functions as a **dynamic mechano-regulatory feedback system** that regulates the outflow resistance sites through NO production to maintain IOP homeostasis. Within the outflow tract, the resistance sites consists of the TM/JCT, basement membrane and inner wall endothelium of SC, which work together synergistically as "controller(s)" of the endogenous feedback system. The inner wall experiences a basal-to-apical directed flow (Q_T) as aqueous humor crosses the outflow pathway. Increases in outflow resistance leads to elevated IOP, which in turn increases the mechanical load on the tissues of the outflow pathway, leading to morphological changes to the JCT and inner wall of SC. As IOP increases, the JCT expands and pushes the inner wall into the lumen. The collapse of SC lumen increases the hydrodynamic shear stress acting on the SC endothelial cells exerted from the circumferential flow (Q_C) along the canal (Figure 7.1A). The SC cells function as a "barostat" or "mechano-sensors" within this endogenous feedback loop by detecting IOP-induced changes in shear stress. In the presence of elevated shear stress, SC cells secrete NO[11,135], similar to vascular endothelial cells[44,45] through the up-regulation of eNOS expression and activity. NO acts as a key signaling molecule within this endogenous feedback loop to modulate the outflow resistance sites to enhance aqueous humor outflow and restore physiological IOP.

Firstly, in Chapter 2, we demonstrated that NO plays a crucial physiological role in regulating aqueous humor outflow in mice, whereby the exogenous delivery of NO, via SNAP (NO-donor), results in an increase in outflow facility by mediating the outflow resistance sites within the conventional outflow pathway. More importantly, we demonstrated that the inhibition of endogenous NOS activity leads to a reduction in outflow facility, suggesting a basal tone of endogenous NO is involved in the regulation of outflow facility. In particular, the selective inhibition of eNOS accounted for the majority of reduction in outflow facility, thus suggesting that eNOS is the primary isoform involved in the regulation of aqueous humor outflow. Therefore, impaired eNOS activity and NO signaling could potentially "short-circuit" this endogenous regulatory feedback mechanism and lead to elevated IOP – characteristic of primary open angle glaucoma. Interestingly, these results are consistent with prior studies indicating that reduced NOS activity[157] in the outflow pathway and polymorphisms in the *NOS3* gene (that encodes eNOS) are linked to the pathogenesis of glaucoma[121,141,174].

In Chapters 3 and 4, we examined the central hypothesis of the mechano-regulatory feedback mechanism that resides in the conventional outflow pathway. Here, we investigated whether

local eNOS expression and activity within the SC leads to local increase in hydraulic conductivity, which in turn may affect the segmental outflow patterns in the TM. Additionally, we also tested whether increases in IOP results in up-regulation of eNOS activity and NO production, lead presumably through increased hydrodynamic shear stress acting on SC cells. Firstly, we developed a NO-sensitive biosensor that can detect local changes in NO production in both *in vitro* and *in situ* models. This NO-biosensor exploits the peroxynitrite-mediated nitration process of tyrosine residues derived from nitration-prone proteins, a selective oxidation process that results in a post-translational modification of tyrosine residues to form 3-nitrotyrosine[19,184]. The conversion of tyrosine into 3-nitrotyrosine serves as a biological footprint for local changes in NO levels. We then validated our NO-biosensor in an *in vitro* shear stress model lined with HUVECs exposed to different levels of shear stress, showing that the biosensor was capable of detecting and distinguishing between low and high shear-induced NO production by living cells. The NO-biosensor achieved greater sensitivity over the standard Griess assay, commonly used for detection of nitrite from biological solutions. Furthermore, we showed that in enucleated eNOS-GFP mouse eyes, segmental outflow patterns in the TM correlates with the spatial distribution of eNOS-GFP expression within the SC, suggesting that regions of higher eNOS expression and activity colocalizes with regions of higher outflow. Additionally, with the newly developed NO-biosensors, we detected higher NO production at elevated IOP compared to physiological IOP. Here we demonstrated for the first time that increases in IOP lead to increased shear-induced NO production by the SC cells, which can then feed back into the outflow pathway as an autocrine/paracrine signaling molecule to modulate local outflow resistance sites to enhance outflow facility (as shown in Figure 7.1).

In Chapter 5, we examined the relationship between the post-trabecular outflow pathway and segmental filtration patterns in the TM of eNOS-GFP mice. Here, we developed a novel embedding protocol (with PDMS) for imaging segmental outflow patterns in enucleated mouse eyes with the use of fluorescence OPT. With this new protocol, we have overcome several technical challenges that have previously limited the use of OPT for imaging mouse eyes, such as the use of tissue clarifying chemicals (i.e. BABB) which are toxic and often result in the quenching of fluorophores. With OPT imaging, we now have the ability to visualize and map segmental outflow patterns in a "global" context, relating post-trabecular limbal vasculature and extraocular muscles to regions of high and low flow in the TM. Moreover, by embedding the tissue in PDMS it allows for a multi-scale analysis, whereby the tissue can be retrieved post-OPT imaging and be processed for further analysis, such

as examining morphological changes with electron microscopy or changes in gene expression in low and high flow regions in the outflow pathway.

Finally, in Chapter 6, we developed a targeted NO-based therapeutic that liberates NO within the trabecular meshwork, where the majority of the outflow resistance is generated within the conventional outflow pathway. Previous studies have shown that non-targeted delivery of NO donors has resulted in varied success in decreasing IOP and enhancing outflow facility[24,43,62,65,111,191,193,197,236,245]. Depending on the site of NO release within the anterior chamber, the physiological response may be counterproductive and result in increased IOP, rather than the desired IOP lowering effect. Here, we encapsulated β-galactosidase (enzyme; catalyst) in micron-sized PMA capsules which are delivered intracamerally to localize the polymers within the TM. This was followed by the delivery of β-gal-NONOate (substrate; NO donor) encapsulated in liposomes that gets delivered via *ex vivo* perfusions. Once the substrate is released from the liposomes, the NO donor gets catalyzed by the enzyme resulting in localized release of NO at the site of outflow resistance. Therefore, our targeted approach of localized NO synthesis within the TM/JCT through the use of an enzyme prodrug therapy (EPT) proves to be a more promising therapeutic approach for treating ocular hypertension and potentially glaucoma, where the endogenous NO-machinery has been suggested to be impaired[157].

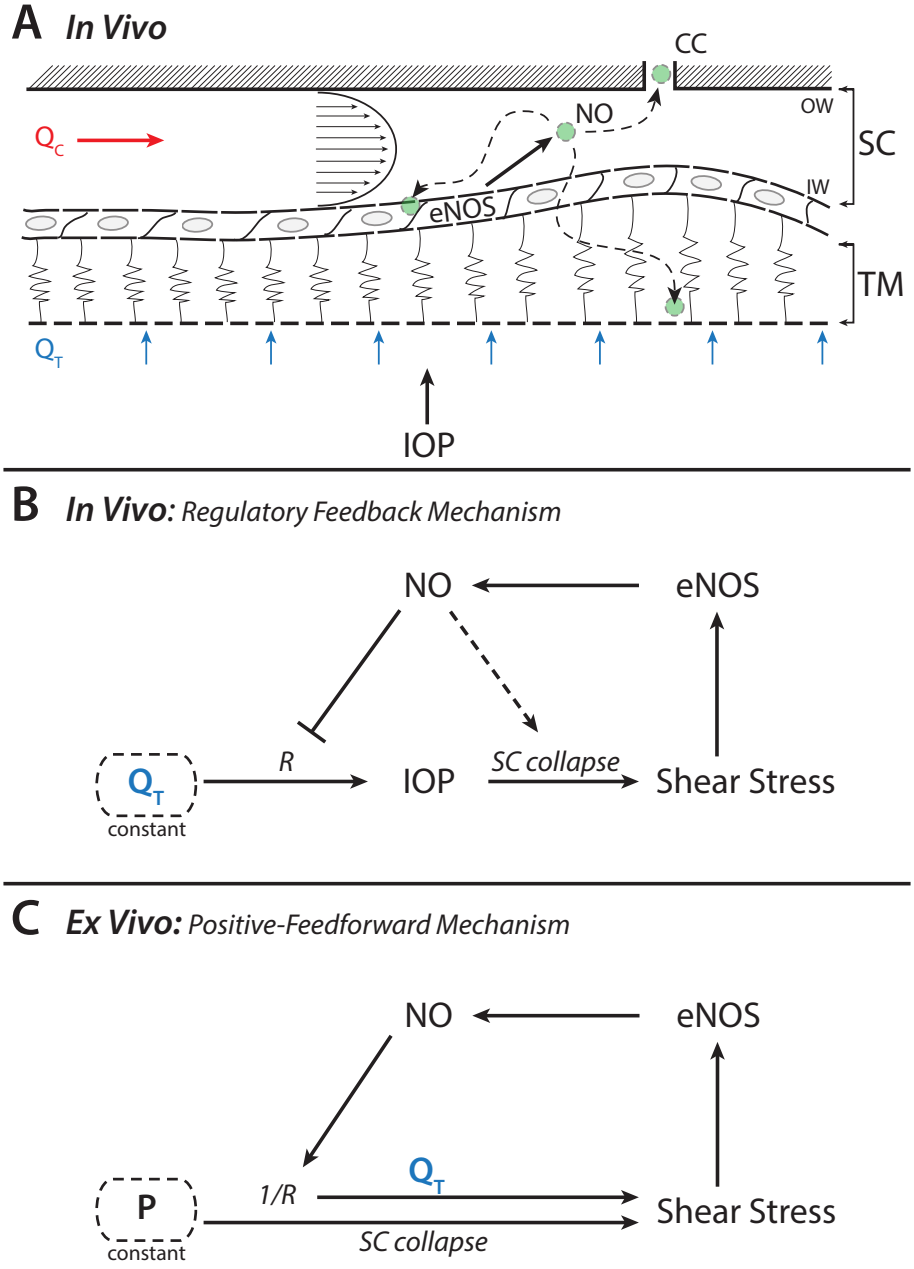


Figure 7.1: Mechano-regulatory feedback system via shear-induced eNOS activity and NO production. **(A)** Schematic representation of mechano-regulatory feedback system. As IOP increases, the TM/JCT expands and pushes the inner wall into the SC, partially collapsing the SC lumen. The collapse of SC effectively reduces the cross-sectional area of the lumen, and leads to an increase in shear stress acting on the SC endothelial cells exerted from the circumferential flow (Q_C) along the canal. Increased shear stress up-regulates eNOS expression and activity, resulting in increased NO production. NO acts as an autocrine/paracrine signaling molecule to modulate the various outflow resistance sites within the outflow pathway via retrograde diffusion and/or advection along the canal. **(B)** *In vivo* representation of regulatory feedback mechanism. Here, the regulatory feedback mechanism is driven by a constant-flow source, aqueous humor secreted by the ciliary processes resulting in transendothelial flow (Q_T) through the meshwork. Increases in IOP leads to increased shear stress and NO production. NO secreted by the SC cells feeds back into the outflow pathway to regulate outflow resistance sites to restore IOP homeostasis. **(C)** *Ex vivo* representation of positive feedforward mechanism. Here, in the *ex vivo* model, we use a constant-pressure system (P) as aqueous humor production is not present in the enucleated eye. Increases in IOP leads to increased shear stress and NO production. NO feeds back into the outflow pathway to decrease outflow resistance. As pressure is kept constant, the SC remains collapsed leading to sustained shear stress and NO production. This creates a "feedforward" mechanism resulting in increased outflow.

7.1 Future Work

This thesis has developed our understanding of the role of NO in the regulation of conventional outflow physiology. We have gained insights on the endogenous regulatory feedback mechanism that helps regulate the outflow resistance sites and maintain IOP homeostasis *in vivo*. In this section, we highlight several areas that would benefit from further investigation to build upon the results obtained thus far in this thesis.

7.1.1 Effect of Selective-Inhibition of eNOS on Segmental Outflow Distribution

In Chapter 4, we showed that segmental outflow in the TM is partially regulated by the endogenous NO-regulatory mechanism within the outflow tract. Our data strongly suggests that eNOS is the primary isoform involved in the regulation of aqueous humor outflow, although several studies have also indicated that both nNOS and iNOS are expressed in the TM region. Thus endogenous NO production may not be limited to eNOS activity. Here, we propose to use an eNOS-selective inhibitor, such as cavtratin (50 μM), in these eNOS-GFP mice to examine whether the disruption of endogenous NO signaling leads to altered segmental outflow patterns in the TM. These studies will shed light on whether eNOS is in fact the primary isoform responsible for regulating aqueous humor outflow, especially at elevated IOP where increased shear stress has been shown to trigger the NO signaling cascade. Hence, by disrupting the endogenous NOS activity, we can directly test the causality effect of eNOS within the endogenous mechano-regulatory feedback loop.

7.1.2 Targeted NO Synthesis within the Conventional Outflow Pathway

In Chapter 6, we have provided preliminary data suggesting that targeted and localized synthesis of NO within the trabecular meshwork, would lead to increased outflow facility with greater efficacy over non-targeted delivery of NO. Here, we propose to carry out more replicates to increase our statistical power and to show that the data we observed is in fact representative and repeatable. Moreover, we want to confirm that the PMA capsules loaded with β-galactosidase are in fact

enmeshed in the TM and that the enzymes are active, compared to the empty PMA. This would be done with standard β-gal staining on cryosectioned eyes co-stained with CD31 to identify where the SC lumen is located. Positive β-gal staining would confirm that the catalysis of the NO donor (β-gal-NONOate) is in fact due to the active enzyme encapsulated in the PMA capsules. Additionally, the enzymes activity should also be characterized to help understand the feasibility of utilizing these enzymes over extended periods of timescales. To fully validate the therapeutic potential of this enzyme prodrug therapy on lowering IOP, these PMA capsules and liposomes should also be tested *in vivo* in ocular hypertensive mice. Long-term IOP monitoring in these ocular hypertensive mice, would allow us to understand whether this NO-based therapeutic is a viable treatment option for lowering IOP.

Appendix A

Permission Documents for Reprint

Copyright Clearance Center RightsLink®

Home | Account Info | Help | Live Chat



Title: The trabecular meshwork outflow pathways: Structural and functional aspects
Author: Ernst R. Tamm
Publication: Experimental Eye Research
Publisher: Elsevier
Date: 30 April 2009
Copyright © 2009 Elsevier Ltd. All rights reserved.

Logged in as:
Jason Chang
LOGOUT

Order Completed

Thank you very much for your order.

This is a License Agreement between Jason Chang ("You") and Elsevier ("Elsevier"). The license consists of your order details, the terms and conditions provided by Elsevier, and the payment terms and conditions.

Get the printable license.

License Number	3770840480478
License date	Dec 16, 2015
Licensed content publisher	Elsevier
Licensed content publication	Experimental Eye Research
Licensed content title	The trabecular meshwork outflow pathways: Structural and functional aspects
Licensed content author	Ernst R. Tamm
Licensed content date	30 April 2009
Licensed content volume number	88
Licensed content issue number	4
Number of pages	8
Type of Use	reuse in a thesis/dissertation
Portion	figures/tables/illustrations
Number of figures/tables/illustrations	1
Format	both print and electronic
Are you the author of this Elsevier article?	No
Will you be translating?	No
Original figure numbers	Figure 1
Title of your thesis/dissertation	Mechano-regulation of intraocular pressure through eNOS
Expected completion date	Dec 2015
Estimated size (number of pages)	180
Elsevier VAT number	GB 494 6272 12
Permissions price	0.00 GBP
VAT/Local Sales Tax	0.00 GBP / 0.00 GBP
Total	0.00 GBP

ORDER MORE... CLOSE WINDOW

Copyright © 2015 Copyright Clearance Center, Inc. All Rights Reserved. Privacy statement. Terms and Conditions.
Comments? We would like to hear from you. E-mail us at customercare@copyright.com

Figure A.1: Permission for reprint of Figure 1.3.

Copyright Clearance Center RightsLink®

Home | Account Info | Help | Live Chat



Title: The changing paradigm of outflow resistance generation: Towards synergistic models of the JCT and inner wall endothelium

Author: Darryl R. Overby,W. Daniel Stamer,Mark Johnson

Publication: Experimental Eye Research

Publisher: Elsevier

Date: 30 April 2009

Copyright © 2008 Elsevier Ltd. All rights reserved.

Logged in as:
Jason Chang
LOGOUT

Order Completed

Thank you very much for your order.

This is a License Agreement between Jason Chang ("You") and Elsevier ("Elsevier"). The license consists of your order details, the terms and conditions provided by Elsevier, and the payment terms and conditions.

Get the printable license.

License Number	3770840795930
License date	Dec 16, 2015
Licensed content publisher	Elsevier
Licensed content publication	Experimental Eye Research
Licensed content title	The changing paradigm of outflow resistance generation: Towards synergistic models of the JCT and inner wall endothelium
Licensed content author	Darryl R. Overby,W. Daniel Stamer,Mark Johnson
Licensed content date	30 April 2009
Licensed content volume number	88
Licensed content issue number	4
Number of pages	15
Type of Use	reuse in a thesis/dissertation
Portion	figures/tables/illustrations
Number of figures/tables/illustrations	1
Format	both print and electronic
Are you the author of this Elsevier article?	No
Will you be translating?	No
Original figure numbers	3
Title of your thesis/dissertation	Mechano-regulation of intraocular pressure through eNOS
Expected completion date	Dec 2015
Estimated size (number of pages)	180
Elsevier VAT number	GB 494 6272 12
Permissions price	0.00 GBP
VAT/Local Sales Tax	0.00 GBP / 0.00 GBP
Total	0.00 GBP

ORDER MORE... CLOSE WINDOW

Copyright © 2015 Copyright Clearance Center, Inc. All Rights Reserved. Privacy statement. Terms and Conditions.
Comments? We would like to hear from you. E-mail us at customercare@copyright.com

Figure A.2: Permission for reprint of Figure 1.4a.

Copyright Clearance Center RightsLink®

Home | Account Info | Help | Live Chat



Title: A model of giant vacuole dynamics in human Schlemm's canal endothelial cells

Author: Ryan M. Pedrigi,David Simon,Ashley Reed,W. Daniel Stamer,Darryl R. Overby

Publication: Experimental Eye Research

Publisher: Elsevier

Date: January 2011

Copyright © 2010 Elsevier Ltd. All rights reserved.

Logged in as:
Jason Chang
LOGOUT

Order Completed

Thank you very much for your order.

This is a License Agreement between Jason Chang ("You") and Elsevier ("Elsevier"). The license consists of your order details, the terms and conditions provided by Elsevier, and the payment terms and conditions.

Get the printable license.

License Number	3770840960615
License date	Dec 16, 2015
Licensed content publisher	Elsevier
Licensed content publication	Experimental Eye Research
Licensed content title	A model of giant vacuole dynamics in human Schlemm's canal endothelial cells
Licensed content author	Ryan M. Pedrigi,David Simon,Ashley Reed,W. Daniel Stamer,Darryl R. Overby
Licensed content date	January 2011
Licensed content volume number	92
Licensed content issue number	1
Number of pages	10
Type of Use	reuse in a thesis/dissertation
Portion	figures/tables/illustrations
Number of figures/tables/illustrations	1
Format	both print and electronic
Are you the author of this Elsevier article?	No
Will you be translating?	No
Original figure numbers	1
Title of your thesis/dissertation	Mechano-regulation of intraocular pressure through eNOS
Expected completion date	Dec 2015
Estimated size (number of pages)	180
Elsevier VAT number	GB 494 6272 12
Permissions price	0.00 GBP
VAT/Local Sales Tax	0.00 GBP / 0.00 GBP
Total	0.00 GBP

ORDER MORE... CLOSE WINDOW

Copyright © 2015 Copyright Clearance Center, Inc. All Rights Reserved. Privacy statement. Terms and Conditions.
Comments? We would like to hear from you. E-mail us at customercare@copyright.com

Figure A.3: Permission for reprint of Figure 1.4b.

Copyright Clearance Center RightsLink®

Home | Account Info | Help | Live Chat



Title: The three-dimensional organisation of the post-trabecular aqueous outflow pathway and limbal vasculature in the mouse

Author: Elizabeth L. van der Merwe,Susan H. Kidson

Publication: Experimental Eye Research

Publisher: Elsevier

Date: August 2014

Copyright © 2014 Elsevier Ltd. All rights reserved.

Logged in as:
Jason Chang
LOGOUT

Order Completed

Thank you very much for your order.

This is a License Agreement between Jason Chang ("You") and Elsevier ("Elsevier"). The license consists of your order details, the terms and conditions provided by Elsevier, and the payment terms and conditions.

Get the printable license.

License Number	3770841116253
License date	Dec 16, 2015
Licensed content publisher	Elsevier
Licensed content publication	Experimental Eye Research
Licensed content title	The three-dimensional organisation of the post-trabecular aqueous outflow pathway and limbal vasculature in the mouse
Licensed content author	Elizabeth L. van der Merwe,Susan H. Kidson
Licensed content date	August 2014
Licensed content volume number	125
Licensed content issue number	n/a
Number of pages	10
Type of Use	reuse in a thesis/dissertation
Portion	figures/tables/illustrations
Number of figures/tables/illustrations	1
Format	both print and electronic
Are you the author of this Elsevier article?	No
Will you be translating?	No
Original figure numbers	3
Title of your thesis/dissertation	Mechano-regulation of intraocular pressure through eNOS
Expected completion date	Dec 2015
Estimated size (number of pages)	180
Elsevier VAT number	GB 494 6272 12
Permissions price	0.00 GBP
VAT/Local Sales Tax	0.00 GBP / 0.00 GBP
Total	0.00 GBP

ORDER MORE... CLOSE WINDOW

Copyright © 2015 Copyright Clearance Center, Inc. All Rights Reserved. Privacy statement. Terms and Conditions.
Comments? We would like to hear from you. E-mail us at customercare@copyright.com

Figure A.4: Permission for reprint of Figure 1.5b.

Bibliography

[1] Abello, N., Kerstjens, H. a. M., Postma, D. S. and Bischoff, R. [2009], 'Protein tyrosine nitration: Selectivity, physicochemical and biological consequences, denitration, and proteomics methods for the identification of tyrosine-nitrated proteins', *Journal of Proteome Research* **8**, 3222–3238.

[2] Acott, T. S. and Kelley, M. J. [2008], 'Extracellular matrix in the trabecular meshwork', *Experimental Eye Research* **86**, 543–561.

[3] AGIS, I. [2010], 'The advanced glaucoma intervention study (AGIS): 7. the relationship between control of intraocular pressure and visual field deterioration', *American Journal of Ophthalmology* **130**, 429–440.

[4] Albano, C., Randers-Eichhon, L., Chang, Q., Bentley, W. and Rao, G. [1996], 'Quantitative measurement of green fluorescent protein expression', *Biotechnology Techniques* **10**(12), 953–958.

[5] Alderton, W. K., Cooper, C. E. and Knowles, R. G. [2001], 'Nitric oxide synthases: structure, function and inhibition.', *The Biochemical Journal* **357**, 593–615.

[6] Alm, A. and Nilsson, S. F. E. [2009], 'Uveoscleral outflow - A review', *Experimental Eye Research* **88**(4), 760–768.

[7] Alvarado, J. a., Katz, L. J., Trivedi, S. and Shifera, A. S. [2010], 'Monocyte modulation of aqueous outflow and recruitment to the trabecular meshwork following selective laser trabeculoplasty.', *Archives of Ophthalmology* **128**(6), 731–737.

[8] Alvarado, J., Murphy, C., Polansky, J. and Juster, R. [1981], 'Age-related changes in trabecular meshwork cellularity', *Investigative Ophthalmology and Visual Science* **21**(5), 714–727.

[9] Alvarez, B. and Radi, R. [2003], 'Peroxynitrite reactivity with amino acids and proteins', *Amino Acids* **25**, 295–311.

[10] Ara, J., Przedborski, S., Naini, a. B., Jackson-Lewis, V., Trifiletti, R. R., Horwitz, J. and Ischiropoulos, H. [1998], 'Inactivation of tyrosine hydroxylase by nitration following exposure to peroxynitrite and 1-methyl-4-phenyl-1,2,3,6-tetrahydropyridine (MPTP).', *Proceedings of the National Academy of Sciences of the United States of America* **95**(13), 7659–7663.

[11] Ashpole, N. E., Overby, D. R., Ethier, C. R. and Stamer, W. D. [2014], 'Shear Stress-Triggered Nitric Oxide Release From Schlemm's Canal Cells', *Investigative Ophthalmology & Visual Science* **55**, 8067–8076.

[12] Aspelund, A., Tammela, T., Antila, S., Nurmi, H., Leppänen, V.-M., Zarkada, G., Stanczuk, L., Francois, M., Mäkinen, T., Saharinen, P., Immonen, I. and Alitalo, K. [2014], 'The Schlemm's canal is a VEGF-C/VEGFR-3-responsive lymphatic-like vessel.', *Journal of Clinical Investigation* **124**(22), 1–3.

[13] Bachmann, B., Birke, M., Kook, D., Eichhorn, M. and Lütjen-Drecoll, E. [2006], 'Ultrastructural and biochemical evaluation of the porcine anterior chamber perfusion model', *Investigative Ophthalmology and Visual Science* **47**(5), 2011–2020.

[14] Bárány, E. H. [1962], 'The mode of action of pilocarpine on outflow resistance in the eye of a primate (Cercopithecus ethiops).', *Investigative Ophthalmology* **1**, 712–727.

[15] Bartesaghi, S., Ferrer-Sueta, G., Peluffo, G., Valez, V., Zhang, H., Kalyanaraman, B. and Radi, R. [2007], 'Protein tyrosine nitration in hydrophilic and hydrophobic environments', *Amino Acids* **32**, 501–515.

[16] Bartesaghi, S., Valez, V., Trujillo, M., Peluffo, G., Romero, N., Zhang, H., Kalyanaraman, B. and Radi, R. [2006], 'Mechanistic studies of peroxynitrite-mediated tyrosine nitration in membranes using the hydrophobic probe N-t-BOC-L-tyrosine tert-butyl ester', *Biochemistry* **45**, 6813–6825.

[17] Battista, S. a., Lu, Z., Hofmann, S., Freddo, T., Overby, D. R. and Gong, H. [2008], 'Reduction of the available area for aqueous humor outflow and increase in meshwork herniations into collector channels following acute IOP elevation in bovine eyes', *Investigative Ophthalmology and Visual Science* **49**(12), 5346–5352.

[18] Beauregard, C., Liu, Q. and Chiou, G. C. [2001], 'Effects of nitric oxide donors and nitric oxide synthase substrates on ciliary muscle contracted by carbachol and endothelin for possible use in myopia prevention.', *Journal of Ocular Pharmacology and Therapeutics* **17**(1), 1–9.

[19] Beckman, J. S. and Koppenol, W. H. [1996], 'Nitric oxide, superoxide, and peroxynitrite: the good, the bad, and ugly.', *The American Journal of Physiology* **271**(73), C1424–C1437.

[20] Behar-Cohen, F. F., Goureau, O., D'Hermies, F. and Courtois, Y. [1996], 'Decreased intraocular pressure induced by nitric oxide donors is correlated to nitrite production in the rabbit eye', *Investigative Ophthalmology and Visual Science* **37**, 1711–1712.

[21] Bill, A. [1965], 'The aqueous humor drainage mechanism in the cynomolgus monkey (Macaca irus) with evidence for unconventional routes.', *Investigative ophthalmology* **4**(5), 911–919.

[22] Bill, A. and Phillips, C. I. [1971], 'Uveoscleral drainage of aqueous humour in human eyes', *Experimental Eye Research* **12**, 275–281.

[23] Bill, A. and Svedbergh, B. [1972], 'Scanning electron microscopic studies of the trabecular meshwork and the canal of Schlemm–an attempt to localize the main resistance to outflow of aqueous humor in man.', *Acta Ophthalmologica* **50**, 295–320.

[24] Borghi, V., Bastia, E., Guzzetta, M., Chiroli, V., Toris, C. B., Batugo, M. R., Carreiro, S. T., Chong, W. K. M., Gale, D. C., Kucera, D. J., Jia, L., Prasanna, G., Ongini, E., Krauss, A. H. P. and Impagnatiello, F. [2010], 'A novel nitric oxide releasing prostaglandin analog, NCX 125, reduces intraocular pressure in rabbit, dog, and primate models of glaucoma.', *Journal of Ocular Pharmacology and Therapeutics* **26**(2), 125–132.

[25] Boussommier-Calleja, A., Bertrand, J., Woodward, D. F., Ethier, C. R., Stamer, W. D. and Overby, D. R. [2012], 'Pharmacologic manipulation of conventional outflow facility in ex vivo mouse eyes', *Investigative Ophthalmology & Visual Science* **53**(9), 5838–5845.

[26] Boussommier-Calleja, A., Li, G., Wilson, A., Ziskind, T., Scinteie, O. E., Ashpole, N. E., Sherwood, J. M., Farsiu, S., Challa, P., Gonzalez, P., Downs, J. C., Ethier, C. R., Stamer, W. D. and Overby, D. R. [2015], 'Physical Factors Affecting Outflow Facility Measurements in Mice', *Investigative Opthalmology & Visual Science* **56**(13), 8331.
URL: *http://iovs.arvojournals.org/article.aspx?doi=10.1167/iovs.15-17106*

[27] Boussommier-Calleja, A. and Overby, D. R. [2013], 'The influence of genetic background on conventional outflow facility in mice.', *Investigative Ophthalmology & Visual Science* **54**, 8251–8258.

[28] Braakman, S. T., Pedrigi, R. M., Read, A. T., Smith, J. A. E., Stamer, W. D., Ethier, C. R. and Overby, D. R. [2014], 'Biomechanical strain as a trigger for Pore formation in Schlemm's canal endothelial cells.', *Experimental Eye Research* **127**, 224–235.

[29] Braakman, S. T., Read, A. T., Chan, D. W., Ethier, C. R. and Overby, D. R. [2015], 'Colocalization of out fl ow segmentation and pores along the inner wall of Schlemm ' s canal', *Experimental Eye Research* **130**, 87–96.

[30] Bradley, J. M. B., Vranka, J., Colvis, C. M., Conger, D. M., Alexander, J. P., Fisk, A. S., Samples, J. R. and Acott, T. S. [1998], 'Effect of matrix metalloproteinases activity on outflow in perfused human organ culture', *Investigative Ophthalmology & Visual Science* **39**, 2649–2658.

[31] Bredt, D. S. and Snyder, S. H. [1992], 'Nitric oxide, a novel neuronal messenger.', *Neuron* **8**, 3–11.

[32] Bron, A., Tripathi, R. and Tripathi, B. [1998], *Wolff's Anatomy of the Eye and Orbit, 8Ed*, CRC Press.

[33] Brubaker, R. F. [2004], 'Goldmann's equation and clinical measures of aqueous dynamics', *Experimental Eye Research* **78**, 633–637.

[34] Bucci, M., Gratton, J. P., Rudic, R. D., Acevedo, L., Roviezzo, F., Cirino, G. and Sessa, W. C. [2000], 'In vivo delivery of the caveolin-1 scaffolding domain inhibits nitric oxide synthesis and reduces inflammation.', *Nature medicine* **6**(12), 1362–1367.

[35] Buckley, C., Hadoke, P. W. F., Henry, E. and O'Brien, C. [2002], 'Systemic vascular endothelial cell dysfunction in normal pressure glaucoma.', *The British journal of ophthalmology* **86**(2), 227–32.

[36] Buxton, I. L., Cheek, D. J., Eckman, D., Westfall, D. P., Sanders, K. M. and Keef, K. D. [1993], 'NG-nitro L-arginine methyl ester and other alkyl esters of arginine are muscarinic receptor antagonists.', *Circulation research* **72**, 387–395.

[37] Buys, E. S., Ko, Y.-C., Alt, C., Hayton, S. R., Jones, A., Tainsh, L. T., Ren, R., Giani, A., Clerté, M., Abernathy, E., Tainsh, R. E. T., Oh, D.-J., Malhotra, R., Arora, P., de Waard, N., Yu, B., Turcotte, R., Nathan, D., Scherrer-Crosbie, M., Loomis, S. J., Kang, J. H., Lin, C. P., Gong, H., Rhee, D. J., Brouckaert, P., Wiggs, J. L., Gregory, M. S., Pasquale, L. R., Bloch, K. D. and Ksander, B. R. [2013], 'Soluble guanylate cyclase α1-deficient mice: a novel murine model for primary open angle glaucoma.', *PLoS ONE* **8**(3), e60156.

[38] Cai, H. and Harrison, D. G. [2000], 'Endothelial dysfunction in cardiovascular diseases: the role of oxidant stress.', *Circulation research* **87**, 840–844.

[39] Camras, L. J., Stamer, W. D., Epstein, D., Gonzalez, P. and Yuan, F. [2012], 'Differential effects of trabecular meshwork stiffness on outflow facility in normal human and porcine eyes', *Investigative Ophthalmology and Visual Science* **53**(9), 5242–5250.

[40] Camras, L. J., Stamer, W. D., Epstein, D., Gonzalez, P. and Yuan, F. [2014], 'Circumferential tensile stiffness of glaucomatous trabecular meshwork.', *Investigative ophthalmology & visual science* **55**(2), 814–23.

[41] Carreiro, S., Anderson, S., Gukasyan, H. J., Krauss, A. and Prasanna, G. [2009], 'Correlation of in vitro and in vivo kinetics of nitric oxide donors in ocular tissues.', *Journal of ocular pharmacology and therapeutics : the official journal of the Association for Ocular Pharmacology and Therapeutics* **25**(2), 105–112.

[42] Chang, J. Y. H., Folz, S. J., Laryea, S. N. and Overby, D. R. [2014], 'Multi-Scale Analysis of Segmental Outflow Patterns in Human Trabecular Meshwork with Changing Intraocular Pressure.', *Journal of Ocular Pharmacology and Therapeutics* **00**(00), 1–11.

[43] Chang, J. Y. H., Stamer, W. D., Bertrand, J., Read, a. T., Marando, C. M., Ethier, C. R. and Overby, D. R. [2015], 'Role of nitric oxide in murine conventional outflow physiology', *American Journal of Physiology - Cell Physiology* **309**(4), C205–C214.

[44] Chang, Y. S., Yaccino, J. a., Lakshminarayanan, S., Frangos, J. a. and Tarbell, J. M. [2000], 'Shear-induced increase in hydraulic conductivity in endothelial cells is mediated by a nitric oxide-dependent mechanism.', *Arteriosclerosis, Thrombosis, and Vascular Biology* **20**(1), 35–42.

[45] Cheng, C., Van Haperen, R., De Waard, M., Van Damme, L. C. a., Tempel, D., Hanemaaijer, L., Van Cappellen, G. W. a., Bos, J., Slager, C. J., Duncker, D. J., Van Der Steen, A. F. W., De Crom, R. and Krams, R. [2005], 'Shear stress affects the intracellular distribution of eNOS: Direct demonstration by a novel in vivo technique', *Blood* **106**, 3691–3698.

[46] Condorelli, P. and George, S. C. [2001], 'In vivo control of soluble guanylate cyclase activation by nitric oxide: a kinetic analysis.', *Biophysical journal* **80**(5), 2110–2119.

[47] Coneski, P. N. and Schoenfisch, M. H. [2012], 'Nitric oxide release: Part III. Measurement and reporting', *Chemical Society Reviews* **41**, 3753.

[48] Crow, J. and Beckman, J. [1995], 'Quantitation of Protein Tyrosine, 3-Nitrotyrosine, and 3-Aminotyrosine Utilizing HPLC and Intrinsic Ultraviolet Absorbance', *Methods* **7**(1), 116–120.

[49] Crow, J. P. and Ischiropoulos, H. [1996], 'Detection and quantitation of nitrotyrosine residues in proteins: in vivo marker of peroxynitrite.', *Methods in enzymology* **269**(4), 185–194.

[50] David, R., Zangwill, L., Stone, D. and Yassur, Y. [1987], 'Epidemiology of intraocular pressure in a population screened for glaucoma.', *The British journal of ophthalmology* **71**, 766–771.

[51] Davis, M. E., Cai, H., Drummond, G. R. and Harrison, D. G. [2001], 'Shear stress regulates endothelial nitric oxide synthase expression through c-Src by divergent signaling pathways.', *Circulation research* **89**, 1073–1080.

[52] Dawson, T. M., Bredt, D. S., Fotuhi, M., Hwang, P. M. and Snyder, S. H. [1991], 'Nitric oxide synthase and neuronal NADPH', *Neurobiology* **88**(September), 7797–7801.

[53] de Kater, A. W., Melamed, S. and Epstein, D. L. [1989], 'Patterns of aqueous humor outflow in glaucomatous and nonglaucomatous human eyes. A tracer study using cationized ferritin.', *Archives of ophthalmology* **107**(4), 572–576.

[54] De Kater, A. W., Spurr-Michaud, S. J. and Gipson, I. K. [1990], 'Localization of smooth muscle myosin-containing cells in the aqueous outflow pathway', *Investigative Ophthalmology and Visual Science* **31**(2), 347–353.

[55] Denninger, J. W. and Marletta, M. a. [1999], 'Guanylate cyclase and the .NO/cGMP signaling pathway', *Biochimica et Biophysica Acta - Bioenergetics* **1411**(3), 334–350.

[56] Derbyshire, E. R. and Marletta, M. a. [2012], 'Structure and Regulation of Soluble Guanylate Cyclase', *Annual Review of Biochemistry* **81**, 533–559.

[57] Di Lorenzo, A., Lin, M. I., Murata, T., Landskroner-Eiger, S., Schleicher, M., Kothiya, M., Iwakiri, Y., Yu, J., Huang, P. L. and Sessa, W. C. [2013], 'eNOS-derived nitric oxide regulates endothelial barrier function through VE-cadherin and Rho GTPases.', *Journal of Cell Science* **126**, 5541–52.

[58] Dimmeler, S., Assmus, B., Hermann, C., Haendeler, J. and Zeiher, A. M. [1998], 'Fluid shear stress stimulates phosphorylation of Akt in human endothelial cells: involvement in suppression of apoptosis.', *Circulation research* **83**(3), 334–41.

[59] Dimmeler, S., Fleming, I., Fisslthaler, B., Hermann, C., Busse, R. and Zeiher, a. M. [1999], 'Activation of nitric oxide synthase in endothelial cells by Akt-dependent phosphorylation.', *Nature* **399**(June), 601–605.

[60] Dismuke, W. M. and Ellis, D. Z. [2009], 'Activation of the BK(Ca) channel increases outflow facility and decreases trabecular meshwork cell volume.', *Journal of Ocular Pharmacology and Therapeutics* **25**(4), 309–314.

[61] Dismuke, W. M., Liang, J., Overby, D. R. and Stamer, W. D. [2014], 'Concentration-related effects of nitric oxide and endothelin-1 on human trabecular meshwork cell contractility', *Experimental Eye Research* **120**, 28–35.

[62] Dismuke, W. M., Mbadugha, C. C. and Ellis, D. Z. [2008], 'NO-induced regulation of human trabecular meshwork cell volume and aqueous humor outflow facility involve the BKCa ion channel.', *AJP: Cell Physiology* **294**(6), C1378–C1386.

[63] Dragusanu, M., Petre, B.-A. and Przybylski, M. [2011], 'Epitope motif of an anti-nitrotyrosine antibody specific for tyrosine-nitrated peptides revealed by a combination of affinity approaches and mass spectrometry', *Journal of Peptide Science* **17**(3), 184–191.

[64] Elfering, S. L., Haynes, V. L., Traaseth, N. J., Ettl, A. and Giulivi, C. [2004], 'Aspects, mechanism, and biological relevance of mitochondrial protein nitration sustained by mitochondrial nitric oxide synthase.', *American journal of physiology. Heart and circulatory physiology* **286**(1), H22–9.

[65] Ellis, D. Z., Dismuke, W. M. and Chokshi, B. M. [2009], 'Characterization of soluble guanylate cyclase in NO-induced increases in aqueous humor outflow facility and in the trabecular meshwork', *Investigative Ophthalmology and Visual Science* **50**(4), 1808–1813.

[66] Ellis, D. Z., Sharif, N. a. and Dismuke, W. M. [2010], 'Endogenous regulation of human schlemm's canal cell volume by nitric oxide signaling', *Investigative Ophthalmology and Visual Science* **51**(11), 5817–5824.

[67] Emre, M., Orgül, S., Haufschild, T., Shaw, S. G. and Flammer, J. [2005], 'Increased plasma endothelin-1 levels in patients with progressive open angle glaucoma.', *The British journal of ophthalmology* **89**(1), 60–3.

[68] Epstein, D. L. and Rohen, J. W. [1991], 'Morphology of the trabecular meshwork and inner-wall endothelium after cationized ferritin perfusion in the monkey eye', *Investigative Ophthalmology and Visual Science* **32**(1), 160–171.

[69] Ethier, C. R. [2002], 'The inner wall of Schlemm's canal.', *Experimental eye research* **74**, 161–172.

[70] Ethier, C. R. and Chan, D. W. H. [2001], 'Cationic ferritin changes outflow facility in human eyes whereas anionic ferritin does not', *Investigative Ophthalmology and Visual Science* **42**(8), 1795–1802.

[71] Ethier, C. R., Coloma, F. M., Sit, A. J. and Johnson, M. [1998], 'Two pore types in the inner-wall endothelium of Schlemm's canal', *Investigative Ophthalmology and Visual Science* **39**(11), 2041–2048.

[72] Ethier, C. R., Kamm, R. D., Palaszewski, B. a., Johnson, M. C. and Richardson, T. M. [1986], 'Calculations of flow resistance in the juxtacanalicular meshwork', *Investigative Ophthalmology and Visual Science* **27**, 1741–1750.

[73] Ethier, C. R., Read, a. T. and Chan, D. [2004], 'Biomechanics of Schlemm's canal endothelial cells: influence on F-actin architecture.', *Biophysical journal* **87**(October), 2828–2837.

[74] Fang, F. C. [1997], 'Mechanisms of nitric oxide-related antimicrobial activity', *Journal of Clinical Investigation* **99**, 2818–2825.

[75] Feelisch, M. [1998], 'The use of nitric oxide donors in pharmacological studies.', *Naunyn-Schmiedeberg's archives of pharmacology* **358**, 113–122.

[76] Ferrer-Sueta, G. and Radi, R. [2009], 'Chemical biology of peroxynitrite: Kinetics, diffusion, and radicals', *ACS Chemical Biology* **4**(3), 161–177.

[77] Fisher, R. A. [1915], 'Frequency Distribution of the Values of the Correlation Coefficient in Samples from an Indefinitely Large Population', *Biometrika* **10**(4), 507.
URL: *http://www.jstor.org/stable/2331838?origin=crossref*

[78] Fleming, I. [2010], 'Molecular mechanisms underlying the activation of eNOS', *Pflugers Archiv European Journal of Physiology* **459**(6), 793–806.

[79] Flügel, C., Tamm, E. R. and Lutjen-Drecoll, E. [1992], 'Age-Related Loss of [alpha]-Smooth Muscle Actin in Normal and Glaucomatous Human Trabecular Mesh work of Different Age Groups', *Journal of Glaucoma* .

[80] Förstermann, U. and Sessa, W. C. [2012], 'Nitric oxide synthases: Regulation and function', *European Heart Journal* **33**(7), 829–837.

[81] Francis, S. H., Busch, J. L., Corbin, J. D. and Sibley, D. [2010], 'cGMP-dependent protein kinases and cGMP phosphodiesterases in nitric oxide and cGMP action.', *Pharmacological reviews* **62**(3), 525–563.

[82] Fulton, D., Gratton, J. P., McCabe, T. J., Fontana, J., Fujio, Y., Walsh, K., Franke, T. F., Papapetropoulos, a. and Sessa, W. C. [1999], 'Regulation of endothelium-derived nitric oxide production by the protein kinase Akt.', *Nature* **399**(June), 597–601.

[83] Funk, R. H., Mayer, B. and Wörl, J. [1994], 'Nitrergic innervation and nitrergic cells in arteriovenous anastomoses.', *Cell and tissue research* **277**, 477–484.

[84] Gabelt, B. T., Kaufman, P. L. and Rasmussen, C. a. [2011], 'Effect of nitric oxide compounds on monkey ciliary muscle in vitro', *Experimental Eye Research* **93**(3), 321–327.

[85] García-Cardeña, G., Fan, R., Shah, V., Sorrentino, R., Cirino, G., Papapetropoulos, a. and Sessa, W. C. [1998], 'Dynamic activation of endothelial nitric oxide synthase by Hsp90.', *Nature* **392**(6678), 821–824.

[86] Giasson, B. I., Duda, J. E., Murray, I. V., Chen, Q., Souza, J. M., Hurtig, H. I., Ischiropoulos, H., Trojanowski, J. Q. and Lee, V. M. [2000], 'Oxidative damage linked to neurodegeneration by selective alpha-synuclein nitration in synucleinopathy lesions.', *Science (New York, N.Y.)* **290**(2000), 985–989.

[87] Gil, D. W., Krauss, H. a., Bogardus, A. M. and WoldeMussie, E. [1997], 'Muscarinic receptor subtypes in human iris-ciliary body measured by immunoprecipitation', *Investigative Ophthalmology and Visual Science* **38**(7), 1434–1442.

[88] Gloe, T., Sohn, H. Y., Meininger, G. a. and Pohl, U. [2002], 'Shear stress-induced release of basic fibroblast growth factor from endothelial cells is mediated by matrix interaction via integrin alpha(v)beta3.', *The Journal of biological chemistry* **277**(26), 23453–8.
URL: *http://www.ncbi.nlm.nih.gov/pubmed/11976347*

[89] Goh, Y., Hotehama, Y. and Mishima, H. K. [1995], 'Characterization of ciliary muscle relaxation induced by various agents in cats', *Investigative Ophthalmology and Visual Science* **36**(6), 1188–1192.

[90] Gong, H., Tripathi, R. C. and Tripathi, B. J. [1996], 'Morphology of the aqueous outflow pathway', *Microscopy Research and Technique* **33**, 336–367.

[91] Govers, R. and Rabelink, T. J. [2001], 'Cellular regulation of endothelial nitric oxide synthase.', *American journal of physiology. Renal physiology* **280**, F193–206.
URL: *http://www.ncbi.nlm.nih.gov/pubmed/11208594*

[92] Grant, W. M. [1951], 'Clinical measurements of aqueous outflow.', *American Journal of Ophthalmology* **34**, 1603–1605.

[93] Grant, W. M. [1963], 'Experimental aqueous perfusion in enucleated human eyes.', *Archives of ophthalmology* **69**, 783–801.

[94] Gratton, J. P., Fontana, J., O'Connor, D. S., Garcia-Cardena, G., McCabe, T. J. and Sessa, W. C. [2000], 'Reconstitution of an endothelial nitric-oxide synthase (eNOS), hsp90, and caveolin-1 complex in vitro. Evidence that hsp90 facilitates calmodulin stimulated displacement of eNOS from caveolin-1.', *The Journal of biological chemistry* **275**(29), 22268–72.

[95] Gratton, J. P., Lin, M. I., Yu, J., Weiss, E. D., Jiang, Z. L., Fairchild, T. a., Iwakiri, Y., Groszmann, R., Claffey, K. P., Cheng, Y. C. and Sessa, W. C. [2003], 'Selective inhibition of tumor microvascular permeability by cavtratin blocks tumor progression in mice', *Cancer Cell* **4**(July), 31–39.

[96] Guzik, T. J., West, N. E. J., Pillai, R., Taggart, D. P. and Channon, K. M. [2002], 'Nitric oxide modulates superoxide release and peroxynitrite formation in human blood vessels.', *Hypertension* **39**(icl), 1088–1094.

[97] Hamanaka, T. and Bill, A. [1987], 'Morphological and functional effects of Na2EDTA on the outflow routes for aqueous humor in monkeys.', *Experimental eye research* **44**(2), 171–190.

[98] Hamanaka, T. and Bill, A. [1988], 'Effects of alpha-chymotrypsin on the outflow routes for aqueous humor.', *Experimental eye research* **46**(3), 323–341.

[99] Hamanaka, T., Bill, A., Ichinohasama, R. and Ishida, T. [1992], 'Aspects of the development of Schlemm's canal.', *Experimental eye research* **55**, 479–488.

[100] Hann, C. R., Bahler, C. K. and Johnson, D. H. [2005], 'Cationic ferritin and segmental flow through the trabecular meshwork', *Investigative Ophthalmology and Visual Science* **46**, 1–7.

[101] Hann, C. R., Bentley, M. D., Vercnocke, A., Ritman, E. L. and Fautsch, M. P. [2011], 'Imaging the aqueous humor outflow pathway in human eyes by three-dimensional micro-computed tomography (3D micro-CT)', *Experimental Eye Research* **92**(2), 104–111.

[102] Hann, C. R. and Fautsch, M. P. [2009], 'Preferential fluid flow in the human trabecular meshwork near collector channels', *Investigative Ophthalmology and Visual Science* **50**(4), 1692–1697.

[103] Hann, C. R., Vercnocke, a. J., Bentley, M. D., Jorgensen, S. M. and Fautsch, M. P. [2014], 'Anatomic Changes in Schlemm's Canal and Collector Channels in Normal and Primary Open-Angle Glaucoma Eyes Using Low and High Perfusion Pressures', *Investigative Ophthalmology & Visual Science* **55**, 5834–5841.

[104] Heim, R., Cubitt, A. B. and Tsien, R. Y. [1995], 'Improved green fluorescence.', *Nature* **373**(6516), 663–4.

[105] Heim, R., Prasher, D. C. and Tsien, R. Y. [1994], 'Wavelength mutations and posttranslational autoxidation of green fluorescent protein', *Proc Natl Acad Sci U S A* **91**(26), 12501–12504.

[106] Heimark, R. L., Kaochar, S. and Stamer, W. D. [2002], 'Human Schlemm's canal cells express the endothelial adherens proteins, VE-cadherin and PECAM-1.', *Current eye research* **25**(5), 299–308.

[107] Henry, E., Newby, D. E., Webb, D. J. and O'Brien, C. [1999], 'Peripheral endothelial dysfunction in normal pressure glaucoma.', *Investigative ophthalmology & visual science* **40**(8), 1710–4.

[108] Herrnberger, L., Ebner, K., Junglas, B. and Tamm, E. R. [2012], 'The role of plasmalemma vesicle-associated protein (PLVAP) in endothelial cells of Schlemm's canal and ocular capillaries', *Experimental Eye Research* **105**, 27–33.
URL: *http://dx.doi.org/10.1016/j.exer.2012.09.011*

[109] Hess, D. T., Matsumoto, A., Kim, S.-O., Marshall, H. E. and Stamler, J. S. [2005], 'Protein S-nitrosylation: purview and parameters', *Nature Reviews Molecular Cell Biology* **6**(2), 150–166.

[110] Hetrick, E. M. and Schoenfisch, M. H. [2009], 'Analytical chemistry of nitric oxide.', *Annual review of analytical chemistry (Palo Alto, Calif.)* **2**, 409–433.

[111] Heyne, G. W., Kiland, J. a., Kaufman, P. L. and Gabelt, B. T. [2013], 'Effect of nitric oxide on anterior segment physiology in monkeys', *Investigative Ophthalmology and Visual Science* **54**, 5103–5110.

[112] Hunter, R. A., Storm, W. L., Coneski, P. N. and Schoenfisch, M. H. [2013], 'Inaccuracies of nitric oxide measurement methods in biological media', *Analytical Chemistry* **85**, 1957–1963.

[113] Impagnatiello, F., Borghi, V., Gale, D. C., Batugo, M., Guzzetta, M., Brambilla, S., Carreiro, S. T., Chong, W. K. M., Prasanna, G., Chiroli, V., Ongini, E. and Krauss, a. H. P. [2011], 'A dual acting compound with latanoprost amide and nitric oxide releasing properties, shows ocular hypotensive effects in rabbits and dogs', *Experimental Eye Research* **93**(3), 243–249.
URL: *http://dx.doi.org/10.1016/j.exer.2011.02.006*

[114] Ischiropoulos, H. [1998], 'Biological tyrosine nitration: a pathophysiological function of nitric oxide and reactive oxygen species.', *Archives of biochemistry and biophysics* **356**(1), 1–11.

[115] Ischiropoulos, H. [2003], 'Biological selectivity and functional aspects of protein tyrosine nitration', *Biochemical and Biophysical Research Communications* **305**, 776–783.

[116] Johnson, M. [2006], 'What controls aqueous humour outflow resistance?', *Experimental Eye Research* **82**, 545–557.

[117] Johnson, M. C. and Kamm, R. D. [1983], 'The role of Schlemm's canal in aqueous outflow from the human eye', *Investigative Ophthalmology and Visual Science* **24**, 320–325.

[118] Johnson, M., Shapiro, a., Ethier, C. R. and Kamm, R. D. [1992], 'Modulation of outflow resistance by the pores of the inner wall endothelium', *Investigative Ophthalmology and Visual Science* **33**(5), 1670–1675.

[119] Johnstone, M. A. [1979], 'Pressure-dependent changes in nuclei and the process origins of the endothelial cells lining Schlemm's canal', *Investigative Ophthalmology and Visual Science* **18**(1), 44–51.

[120] Johnstone, M. a. and Grant, W. G. [1973], 'Pressure-dependent changes in structures of the aqueous outflow system of human and monkey eyes.', *American Journal of ophthalmology* **75**(3), 365–383.

[121] Kang, J. H., Wiggs, J. L., Rosner, B. a., Hankinson, S. E., Abdrabou, W., Fan, B. J., Haines, J. and Pasquale, L. R. [2010], 'Endothelial nitric oxide synthase gene variants and primary open-angle glaucoma: interactions with sex and postmenopausal hormone use.', *Investigative ophthalmology & visual science* **51**(2), 971–979.

[122] Keller, K. E., Bradley, J. M., Kelley, M. J. and Acott, T. S. [2008], 'Effects of modifiers of glycosaminoglycan biosynthesis on outflow facility in perfusion culture', *Investigative Ophthalmology and Visual Science* **49**(6), 2495–2505.

[123] Keller, K. E., Bradley, J. M., Vranka, J. a. and Acott, T. S. [2011], 'Segmental versican expression in the trabecular meshwork and involvement in outflow facility', *Investigative Ophthalmology and Visual Science* **52**(8), 5049–5057.

[124] Kerr, J., Nelson, P. and O'Brien, C. [2003], 'Pulsatile ocular blood flow in primary open-angle glaucoma and ocular hypertension', *American Journal of Ophthalmology* **136**(6), 1106–1113.

[125] Kiel, J. W. [1999], 'Modulation of choroidal autoregulation in the rabbit.', *Experimental eye research* **69**, 413–429.

[126] Kizhatil, K., Ryan, M., Marchant, J. K., Henrich, S. and John, S. W. M. [2014], 'Schlemm's Canal Is a Unique Vessel with a Combination of Blood Vascular and Lymphatic Phenotypes that Forms by a Novel Developmental Process', *PLoS Biology* **12**(7), 1–22.

[127] Klein, B. E., Klein, R. and Linton, K. L. [1992], 'Intraocular pressure in an American community. The Beaver Dam Eye Study.', *Investigative ophthalmology & visual science* **33**(7), 2224–2228.

[128] Knyushko, T. V., Sharov, V. S., Williams, T. D., Schöneich, C. and Bigelow, D. J. [2005], '3-Nitrotyrosine modification of SERCA2a in the aging heart: A distinct signature of the cellular redox environment', *Biochemistry* **44**, 13071–13081.

[129] Kotikoski, H., Vapaatalo, H. and Oksala, O. [2003], 'Nitric oxide and cyclic GMP enhance aqueous humor outflow facility in rabbits.', *Current eye research* **26**(2), 119–123.

[130] Krauss, A. H. P., Impagnatiello, F., Toris, C. B., Gale, D. C., Prasanna, G., Borghi, V., Chiroli, V., Chong, W. K. M., Carreiro, S. T. and Ongini, E. [2011], 'Ocular hypotensive activity of BOL-303259-X, a nitric oxide donating Prostaglandin F2α agonist, in preclinical models', *Experimental Eye Research* **93**(3), 250–255.

[131] Krupin, T., Weiss, A., Becker, B., Holmberg, N. and Fritz, C. [1977], 'Increased intraocular pressure following topical azide or nitroprusside', *Investigative Ophthalmology and Visual Science* **16**, 1002–1007.

[132] Kubes, P. and Granger, D. N. [1992], 'Nitric oxide modulates microvascular permeability.', *The American journal of physiology* **262**(2 Pt 2), H611–5.
URL: *http://classic.ajpheart.physiology.org/content/262/2/H611.abstract*

[133] Last, J. a., Pan, T., Ding, Y., Reilly, C. M., Keller, K., Acott, T. S., Fautsch, M. P., Murphy, C. J. and Russell, P. [2011], 'Elastic modulus determination of normal and glaucomatous human trabecular meshwork', *Investigative Ophthalmology and Visual Science* **52**(5), 2147–2152.

[134] Lei, Y., Overby, D. R., Boussommier-Calleja, A., Daniel Stamer, W. and Ross Ethier, C. [2011], 'Outflow physiology of the mouse eye: Pressure dependence and washout', *Investigative Ophthalmology and Visual Science* **52**(3), 1865–1871.

[135] Lei, Y., Stamer, W. D., Wu, J. and Sun, X. [2014], 'Endothelial Nitric Oxide Synthase-Related Mechanotransduction Changes in Aged Porcine Angular Aqueous Plexus Cells', *Investigative Ophthalmology & Visual Science* **55**, 8402–8408.

[136] Li, G., Farsiu, S., Chiu, S. J., Gonzalez, P., Lütjen-Drecoll, E., Overby, D. R. and Daniel Stamer, W. [2014], 'Pilocarpine-induced dilation of Schlemm's canal and prevention of lumen collapse at elevated intraocular pressures in living mice visualized by OCT', *Investigative Ophthalmology and Visual Science* **55**, 3737–3746.

[137] Lin, M. I., Yu, J., Murata, T. and Sessa, W. C. [2007], 'Caveolin-1 - Deficient mice have increased tumor microvascular permeability, angiogenesis, and growth', *Cancer Research* **67**, 2849–2856.

[138] Liu, J. H. K., Gokhale, P. a., Loving, R. T., Kripke, D. F. and Weinreb, R. N. [2003], 'Laboratory assessment of diurnal and nocturnal ocular perfusion pressures in humans.', *Journal of ocular pharmacology and therapeutics : the official journal of the Association for Ocular Pharmacology and Therapeutics* **19**(4), 291–297.

[139] Liu, J. H. K., Zhang, X., Kripke, D. F. and Weinreb, R. N. [2003], 'Twenty-four-hour intraocular pressure pattern associated with early glaucomatous changes', *Investigative Ophthalmology and Visual Science* **44**(4), 1586–1590.

[140] Llobet, A., Gasull, X. and Gual, A. [2003], 'Understanding trabecular meshwork physiology: a key to the control of intraocular pressure?', *News in physiological sciences : an international journal of physiology produced jointly by the International Union of Physiological Sciences and the American Physiological Society* **18**, 205–209.

[141] Logan, J. F. J., Chakravarthy, U., Hughes, A. E., Patterson, C. C., Jackson, J. a. and Rankin, S. J. a. [2005], 'Evidence for association of endothelial nitric oxide synthase gene in subjects with glaucoma and a history of migraine', *Investigative Ophthalmology and Visual Science* **46**(9), 3221–3226.

[142] Lowe, S. B., Dick, J. A. G., Cohen, B. E. and Stevens, M. M. [2012], 'Multiplex sensing of protease and kinase enzyme activity via orthogonal coupling of quantum dot-peptide conjugates.', *ACS nano* **6**(1), 851–7.
URL: *http://www.ncbi.nlm.nih.gov/pubmed/22148227*

[143] Lu, Z., Overby, D. R., Scott, P. a., Freddo, T. F. and Gong, H. [2008], 'The mechanism of increasing outflow facility by rho-kinase inhibition with Y-27632 in bovine eyes', *Experimental Eye Research* **86**, 271–281.

[144] Lu, Z., Zhang, Y., Freddo, T. F. and Gong, H. [2011], 'Similar hydrodynamic and morphological changes in the aqueous humor outflow pathway after washout and Y27632 treatment in monkey eyes', *Experimental Eye Research* **93**(4), 397–404.

[145] Lütjen-Drecoll, E., Wiendl, H. and Kaufman, P. L. [1998], 'Acute and chronic structural effects of pilocarpine on monkey outflow tissues.', *Transactions of the American Ophthalmological Society* **96**(10-12), 171–191; discussion 192–195.

[146] Mäepea, O. and Bill, a. [1989], 'The pressures in the episcleral veins, Schlemm's canal and the trabecular meshwork in monkeys: effects of changes in intraocular pressure.', *Experimental eye research* **49**(4), 645–663.

[147] Maepea, O. and Bill, A. [1992], 'Pressures in the juxtacanalicular tissue and Schlemm's canal in monkeys', *Experimental Eye Research* **54**, 879–883.

[148] Martínez-Ruiz, A. and Lamas, S. [2004], 'S-nitrosylation: A potential new paradigm in signal transduction', *Cardiovascular Research* **62**, 43–52.

[149] May, C. A., Fuchs, A. V., Scheib, M. and Lütjen-Drecoll, E. [2002], 'Characterization of nitrergic neurons in the porcine and human ciliary nerves', *Investigative Ophthalmology and Visual Science* **43**(3), 581–586.

[150] May, C. A., Skorski, L. M. and Lütjen-Drecoll, E. [2005], 'Innervation of the porcine ciliary muscle and outflow region', *Journal of Anatomy* **206**, 231–236.

[151] Millar, J. C., Clark, A. F. and Pang, I. H. [2011], 'Assessment of aqueous humor dynamics in the mouse by a novel method of constant-flow infusion', *Investigative Ophthalmology and Visual Science* **52**, 685–694.

[152] Millard, L. H., Woodward, D. F. and Stamer, W. D. [2011], 'The role of the prostaglandin EP4 receptor in the regulation of human outflow facility.', *Investigative ophthalmology & visual science* **52**(6), 3506–3513.

[153] Moncada, S. [1997], 'Nitric oxide in the vasculature: Physiology and pathophysiology', *Annals of the New York Academy of Sciences* **811**, 60–69.

[154] Moncada, S. and Higgs, A. [1993], 'The L-arginine-nitric oxide pathway.', *The New England journal of medicine* **329**, 2002–2012.

[155] Moncada, S., Palmer, R. M. and Higgs, E. A. [1991], 'Nitric oxide: physiology, pathophysiology, and pharmacology.', *Pharmacological reviews* **43**, 109–142.

[156] Nathanson, J. a. [1992], 'Nitrovasodilators as a new class of ocular hypotensive agents.', *The Journal of pharmacology and experimental therapeutics* **260**(3), 956–65.
URL: *http://www.ncbi.nlm.nih.gov/pubmed/1532035*

[157] Nathanson, J. a. and McKee, M. [1995*a*], 'Alterations of ocular nitric oxide synthase in human glaucoma', *Investigative Ophthalmology and Visual Science* **36**(1774), 1774–1784.

[158] Nathanson, J. a. and McKee, M. [1995*b*], 'Identification of an extensive system of nitric oxide-producing cells in the ciliary muscle and outflow pathway of the human eye', *Investigative Ophthalmology and Visual Science* **36**(9), 1765–1773.

[159] Nie, H., Wu, J. L., Zhang, M., Xu, J. and Zou, M. H. [2006], 'Endothelial nitric oxide synthase-dependent tyrosine nitration of prostacyclin synthase in diabetes in vivo', *Diabetes* **55**(November), 3133–3141.

[160] Nilsson, S. F. [1997], 'The uveoscleral outflow routes.', *Eye (London, England)* **11 (Pt 2)**, 149–154.

[161] Noske, W. [1997], 'Endothelin-like immunoreactivity in aqueous humor of patients with primary open-angle glaucoma and cataract', *Graefe's Archive for Clinical and Experimental Ophthalmology* **235**(9), 551–552.

[162] O'Brien, R. F., Robbins, R. J. and McMurtry, I. F. [1987], 'Endothelial cells in culture produce a vasoconstrictor substance', *J Cell Physiol* **132**(2), 263–270.
URL: *http://www.ncbi.nlm.nih.gov/entrez/query.fcgi?cmd=Retrieve&db=PubMed&dopt=Citation&list_uids=3114270*

[163] Orsenigo, F., Giampietro, C., Ferrari, A., Corada, M., Galaup, A., Sigismund, S., Ristagno, G., Maddaluno, L., Koh, G. Y., Franco, D., Kurtcuoglu, V., Poulikakos, D., Baluk, P., McDonald, D., Grazia Lampugnani, M. and Dejana, E. [2012], 'Phosphorylation of VE-cadherin is modulated by haemodynamic forces and contributes to the regulation of vascular permeability in vivo.', *Nature communications* **3**(2041-1723 (Electronic)), 1208.

[164] Overby, D., Gong, H., Qiu, G., Freddo, T. F. and Johnson, M. [2002], 'The mechanism of increasing outflow facility during washout in the bovine eye', *Investigative Ophthalmology and Visual Science* **43**(11), 3455–3464.

[165] Overby, D. R., Bertrand, J., Schicht, M., Paulsen, F., Daniel Stamer, W. and Lütjen-Drecoll, E. [2014], 'The structure of the trabecular meshwork, its connections to the ciliary muscle, and the effect of pilocarpine on outflow facility in mice', *Investigative Ophthalmology and Visual Science* **55**, 3727–3736.

[166] Overby, D. R., Stamer, W. D. and Johnson, M. [2009], 'The changing paradigm of outflow resistance generation: Towards synergistic models of the JCT and inner wall endothelium', *Experimental Eye Research* **88**(4), 656–670.

[167] Pacher, P., Beckman, J. S. and Liaudet, L. [2007], 'Nitric oxide and peroxynitrite in health and disease.', *Physiological reviews* **87**, 315–424.

[168] Pan, X., Sidky, E. Y. and Vannier, M. [2009], 'Why do commercial CT scanners still employ traditional, filtered back-projection for image reconstruction?', *Inverse Problems* **25**(12), 123009.

[169] Park, D.-Y., Lee, J., Park, I., Choi, D., Lee, S., Song, S., Hwang, Y., Hong, K. Y., Nakaoka, Y., Makinen, T., Kim, P., Alitalo, K., Hong, Y.-K. and Koh, G. Y. [2014], 'Lymphatic regulator PROX1 determines Schlemm canal integrity and identity.', *Journal of Clinical Investigation* pp. 1–3.

[170] Pedrigi, R. M., Simon, D., Reed, A., Stamer, W. D. and Overby, D. R. [2011], 'A model of giant vacuole dynamics in human Schlemm's canal endothelial cells', *Experimental Eye Research* **92**(1), 57–66.

[171] Peluffo, G. and Radi, R. [2007], 'Biochemistry of protein tyrosine nitration in cardiovascular pathology', *Cardiovascular Research* **75**, 291–302.

[172] Perkumas, K. M. and Stamer, W. D. [2012], 'Protein markers and differentiation in culture for Schlemm's canal endothelial cells', *Experimental Eye Research* **96**(1), 82–87.

[173] Pfeiffer, S., Leopold, E., Schmidt, K., Brunner, F. and Mayer, B. [1996], 'Inhibition of nitric oxide synthesis by NG-nitro-L-arginine methyl ester (L-NAME): requirement for bioactivation to the free acid, NG-nitro-L-arginine.', *British journal of pharmacology* **118**, 1433–1440.

[174] Polak, K., Luksch, A., Berisha, F., Fuchsjaeger-Mayrl, G., Dallinger, S. and Schmetterer, L. [2007], 'Altered nitric oxide system in patients with open-angle glaucoma.', *Archives of ophthalmology* **125**, 494–498.

[175] Predescu, D., Predescu, S., Shimizu, J., Miyawaki-Shimizu, K. and Malik, A. B. [2005], 'Constitutive eNOS-derived nitric oxide is a determinant of endothelial junctional integrity.', *AJP: Lung Cellular and Molecular Physiology* **289**, L371–L381.

[176] Quigley, H. a. [2011], Glaucoma, *in* 'The Lancet', Vol. 377, pp. 1367–1377.

[177] Quigley, H. a. and Broman, a. T. [2006], 'The number of people with glaucoma worldwide in 2010 and 2020.', *The British journal of ophthalmology* **90**, 262–267.

[178] Quijano, C., Hernandez-Saavedra, D., Castro, L., McCord, J. M., Freeman, B. a. and Radi, R. [2001], 'Reaction of peroxynitrite with Mn-Superoxide dismutase. Role of the metal center in decomposition kinetics and nitration', *Journal of Biological Chemistry* **276**(15), 11631–11638.

[179] Quintana, L. and Sharpe, J. [2011*a*], 'Optical projection tomography of vertebrate embryo development', *Cold Spring Harbor Protocols* **6**(6), 586–594.

[180] Quintana, L. and Sharpe, J. [2011*b*], 'Preparation of mouse embryos for optical projection tomography imaging', *Cold Spring Harbor Protocols* **6**(6), 664–669.

[181] Radi, R. [2004], 'Nitric oxide, oxidants, and protein tyrosine nitration.', *Proceedings of the National Academy of Sciences* **101**(12), 4003–4008.

[182] Radi, R. [2013*a*], 'Peroxynitrite, a stealthy biological oxidant', *Journal of Biological Chemistry* **288**(37), 26464–26472.

[183] Radi, R. [2013*b*], 'Protein tyrosine nitration: Biochemical mechanisms and structural basis of functional effects', *Accounts of Chemical Research* **46**(2), 550–559.

[184] Radi, R., Peluffo, G., Alvarez, M. N., Naviliat, M. and Cayota, A. [2001], 'Unraveling peroxynitrite formation in biological systems', *Free Radical Biology and Medicine* **30**(5), 463–488.

[185] Ramos, R. F., Hoying, J. B., Witte, M. H. and Daniel Stamer, W. [2007], 'Schlemm's canal endothelia, lymphatic, or blood vasculature?', *Journal of glaucoma* **16**(4), 391–405.

[186] Rohen, J. W., Futa, R. and Lutjen-Drecoll, E. [1981], 'The fine structure of the cribriform meshwork in normal and glaucomatous eyes as seen in tangential sections', *Investigative Ophthalmology & Visual Science* **21**, 574–585.

[187] Rohen, J. W., Lütjen, E. and Bárány, E. [1967], 'The relation between the ciliary muscle and the trabecular meshwork and its importance for the effect of miotics on aqueous outflow resistance - A study in two contrasting monkey species, Macaca irus and Cercopithecus aethiops', *Albrecht von Graefes Archiv für Klinische und Experimentelle Ophthalmologie* **172**(1), 23–47.

[188] Rosenquist, R., Epstein, D., Melamed, S., Johnson, M. and Grant, W. M. [1989], 'Outflow resistance of enucleated human eyes at two different perfusion pressures and different extents of trabeculotomy.', *Current Eye Research* **8**(12), 1233–1240.

[189] Schmidt, P., Youhnovski, N., Daiber, A., Balan, A., Arsic, M., Bachschmid, M., Przybylski, M. and Ullrich, V. [2003], 'Specific nitration at tyrosine 430 revealed by high resolution mass spectrometry as basis for redox regulation of bovine prostacyclin synthase', *Journal of Biological Chemistry* **278**(15), 12813–12819.

[190] Schmitz, M., Zerr, I. and Althaus, H. H. [2011], 'Effect of Cavtratin, a Caveolin-1 Scaffolding Domain Peptide, on Oligodendroglial Signaling Cascades', *Cellular and Molecular Neurobiology* pp. 1–7.

[191] Schneemann, A., Dijkstra, B. G., van den Berg, T. J., Kamphuis, W. and Hoyng, P. F. J. [2002], 'Nitric oxide/guanylate cyclase pathways and flow in anterior segment perfusion.', *Graefe's archive for clinical and experimental ophthalmology = Albrecht von Graefes Archiv fur klinische und experimentelle Ophthalmologie* **240**, 936–941.

[192] Schneemann, A., Leusink-Muis, A., van den Berg, T., Hoyng, P. F. J. and Kamphuis, W. [2003], 'Elevation of nitric oxide production in human trabecular meshwork by increased pressure', *Graefe's Archive for Clinical and Experimental Ophthalmology* **241**, 321–326.

[193] Schuman, J. S., Erickson, K. and Nathanson, J. a. [1994], 'Nitrovasodilator effects on intraocular pressure and outflow facility in monkeys.'.

[194] Seeley, K. W. and Stevens, S. M. [2012], 'Investigation of local primary structure effects on peroxynitrite-mediated tyrosine nitration using targeted mass spectrometry', *Journal of Proteomics* **75**(6), 1691–1700.

[195] Selbach, J. M., Gottanka, J., Wittmann, M. and Lütjen-Drecoll, E. [2000], 'Efferent and afferent innervation of primate trabecular meshwork and scleral spur', *Investigative Ophthalmology and Visual Science* **41**(8), 2184–2191.

[196] Sellers, S. L., Trane, A. E. and Bernatchez, P. N. [2012], 'Caveolin as a potential drug target for cardiovascular protection', *Frontiers in Physiology* **3 JUL**(July), 1–10.

[197] Shahidullah, M., Yap, M. and To, C.-H. [2005], 'Cyclic GMP, sodium nitroprusside and sodium azide reduce aqueous humour formation in the isolated arterially perfused pig eye.', *British journal of pharmacology* **145**(February), 84–92.

[198] Sharpe, J. [2004], 'Optical Projection Tomography', *Annual Review of Biomedical Engineering* **6**(1), 209–228.

[199] Sharpe, J., Ahlgren, U., Perry, P., Hill, B., Ross, A., Hecksher-Sørensen, J., Baldock, R. and Davidson, D. [2002], 'Optical projection tomography as a tool for 3D microscopy and gene expression studies.', *Science (New York, N.Y.)* **296**(5567), 541–545.

[200] Sherwood, J. M., Reina-Torres, E., Bertrand, J. A., Rowe, B. and Overby, D. R. [2016], 'Measurements of outflow facility using iPerfusion', *PLoS ONE* **11**(3), e0150694.
URL: *http://dx.plos.org/10.1371/journal.pone.0150694*

[201] Shyy, J. Y. J. and Chien, S. [2002], 'Role of integrins in endothelial mechanosensing of shear stress', *Circulation Research* **91**(icl), 769–775.

[202] Sigal, I. A. and Ethier, C. R. [2009], 'Biomechanics of the optic nerve head', *Experimental Eye Research* **88**(4), 799–807.

[203] Sit, A. J. and McLaren, J. W. [2011], 'Measurement of episcleral venous pressure', *Experimental Eye Research* **93**(3), 291–298.

[204] Smith, R., John, S., Nishina, P. and Sundberg, J. [2001], *Systematic evaluation of the mouse eye: anatomy, pathology, and biomethods*, CRC Press.

[205] Smith, R. S., Zabaleta, A., Savinova, O. V. and John, S. W. [2001], 'The mouse anterior chamber angle and trabecular meshwork develop without cell death.', *BMC developmental biology* **1**(1), 3.
URL: *http://www.biomedcentral.com/1471-213X/1/3*

[206] Souza, J. M., Daikhin, E., Yudkoff, M., Raman, C. S. and Ischiropoulos, H. [1999], 'Factors determining the selectivity of protein tyrosine nitration.', *Archives of biochemistry and biophysics* **371**(2), 169–178.

[207] Souza, J. M., Giasson, B. I., Chen, Q., Lee, V. M. Y. and Ischiropoulos, H. [2000], 'Dityrosine cross-linking promotes formation of stable α-synuclein polymers: Implication of nitrative and oxidative stress in the pathogenesis of neurodegenerative synucleinopathies', *Journal of Biological Chemistry* **275**, 18344–18349.

[208] Souza, J. M., Peluffo, G. and Radi, R. [2008], 'Protein tyrosine nitration-Functional alteration or just a biomarker?', *Free Radical Biology and Medicine* **45**, 357–366.

[209] Sowa, G., Pypaert, M. and Sessa, W. C. [2001], 'Distinction between signaling mechanisms in lipid rafts vs. caveolae.', *Proceedings of the National Academy of Sciences of the United States of America* **98**, 14072–14077.

[210] Stamer, W. D. and Acott, T. S. [2012], 'Current understanding of conventional outflow dysfunction in glaucoma', *Current Opinion in Ophthalmology* **23**, 135–143.

[211] Stamer, W. D., Lei, Y., Boussommier-Calleja, A., Overby, D. R. and Ethier, C. R. [2011], 'eNOS, a pressure-dependent regulator of intraocular pressure', *Investigative Ophthalmology and Visual Science* **52**, 9438–9444.

[212] Stamer, W. D., Perkumas, K. M., Hoffman, E. a., Roberts, B. C., Epstein, D. L. and McKay, B. S. [2006], 'Coiled-coil targeting of myocilin to intracellular membranes', *Experimental Eye Research* **83**, 1386–1395.

[213] Stone, J. R. and Marletta, M. a. [1996], 'Spectral and kinetic studies on the activation of soluble guanylate cyclase by nitric oxide', *Biochemistry* **35**(4), 1093–1099.

[214] Su, W.-W., Cheng, S.-T., Ho, W.-J., Tsay, P.-K., Wu, S.-C. and Chang, S. H. L. [2008], 'Glaucoma is associated with peripheral vascular endothelial dysfunction.', *Ophthalmology* **115**(7), 1173–1178.e1.

[215] Su, W.-W., Cheng, S.-T., Hsu, T.-S. and Ho, W.-J. [2006], 'Abnormal flow-mediated vasodilation in normal-tension glaucoma using a noninvasive determination for peripheral endothelial dysfunction.', *Investigative ophthalmology & visual science* **47**(8), 3390–4.

[216] Sumida, G. M. and Stamer, W. D. [2011], 'S1PâĆĆ receptor regulation of sphingosine-1-phosphate effects on conventional outflow physiology.', *American journal of physiology. Cell physiology* **300**(5), C1164–71.

[217] Sun, J., Zhang, X., Broderick, M. and Fein, H. [2003], 'Measurement of Nitric Oxide Production in Biological Systems by Using Griess Reaction Assay', *Sensors* **3**, 276–284.

[218] Swaminathan, S. S., Oh, D. J., Kang, M. H., Ren, R., Jin, R., Gong, H. and Rhee, D. J. [2013], 'Secreted protein acidic and rich in cysteine (SPARC)-null mice exhibit more uniform outflow', *Investigative Ophthalmology and Visual Science* **54**(3), 2035–2047.

[219] Szabó, C., Ischiropoulos, H. and Radi, R. [2007], 'Peroxynitrite: biochemistry, pathophysiology and development of therapeutics.', *Nature reviews. Drug discovery* **6**(2), 662–680.

[220] Tamm, E. R. [2009], 'The trabecular meshwork outflow pathways: Structural and functional aspects', *Experimental Eye Research* **88**(4), 648–655.

[221] Tarbell, J. M. [2010], 'Shear stress and the endothelial transport barrier', *Cardiovascular Research* **87**, 320–330.

[222] Tektas, O. Y. and Lütjen-Drecoll, E. [2009], 'Structural changes of the trabecular meshwork in different kinds of glaucoma', *Experimental Eye Research* **88**, 769–775.

[223] Thorleifsson, G., Walters, G. B., Hewitt, A. W., Masson, G., Helgason, A., DeWan, A., Sigurdsson, A., Jonasdottir, A., Gudjonsson, S. a., Magnusson, K. P., Stefansson, H., Lam, D. S. C., Tam, P. O. S., Gudmundsdottir, G. J., Southgate, L., Burdon, K. P., Gottfredsdottir, M. S., Aldred, M. a., Mitchell, P., St Clair, D., Collier, D. a., Tang, N., Sveinsson, O., Macgregor, S., Martin, N. G., Cree, A. J., Gibson, J., Macleod, A., Jacob, A., Ennis, S., Young, T. L., Chan, J. C. N., Karwatowski, W. S. S., Hammond, C. J., Thordarson, K., Zhang, M., Wadelius, C., Lotery, A. J., Trembath, R. C., Pang, C. P., Hoh, J., Craig, J. E., Kong, A., Mackey, D. a., Jonasson, F., Thorsteinsdottir, U. and Stefansson, K. [2010], 'Common variants near CAV1 and CAV2 are associated with primary open-angle glaucoma.', *Nature genetics* **42**(10), 906–9.

[224] Tinker, A. C., Beaton, H. G., Boughton-smith, N., Cook, T. R., Cooper, S. L., Fraser-rae, L., Hallam, K., Hamley, P., Mcinally, T., Nicholls, D. J., Pimm, A. D. and Wallace, A. V. [2003], 'Highly Selective Inhibitors of Inducible Nitric Oxide Synthase Which Show Antiinflammatory Activity in Vivo', *J. Med. Chem.* **46**, 913–916.

[225] Tripathi, R. C. [1971], 'Mechanism of the aqueous outflow across the trabecular wall of Schlemm's canal.', *Experimental eye research* **11**, 116–121.

[226] Truong, T. N., Li, H., Hong, Y. K. and Chen, L. [2014], 'Novel characterization and live imaging of Schlemm's canal expressing Prox-1', *PLoS ONE* **9**(5), 1–8.

[227] van der Merwe, E. L. and Kidson, S. H. [2010], 'Advances in imaging the blood and aqueous vessels of the ocular limbus', *Experimental Eye Research* **91**(2), 118–126.

[228] van der Merwe, E. L. and Kidson, S. H. [2014], 'The three-dimensional organisation of the post-trabecular aqueous outflow pathway and limbal vasculature in the mouse', *Experimental Eye Research* **125**, 226–235.

[229] van Haperen, R., Cheng, C., Mees, B. M. E., van Deel, E., de Waard, M., van Damme, L. C. a., van Gent, T., van Aken, T., Krams, R., Duncker, D. J. and de Crom, R. [2003], 'Functional expression of endothelial nitric oxide synthase fused to green fluorescent protein in transgenic mice.', *The American journal of pathology* **163**(4), 1677–1686.

[230] VanderWyst, S. S., Perkumas, K. M., Read, a. T., Overby, D. R. and Stamer, W. D. [2011], 'Structural basement membrane components and corresponding integrins in Schlemm's canal endothelia.', *Molecular vision* **17**(January), 199–209.

[231] Vranka, J. a., Bradley, J. M., Yang, Y.-F., Keller, K. E. and Acott, T. S. [2015], 'Mapping Molecular Differences and Extracellular Matrix Gene Expression in Segmental Outflow Pathways of the Human Ocular Trabecular Meshwork', *Plos One* **10**(3), e0122483.

[232] Walford, G. and Loscalzo, J. [2003], 'Nitric oxide in vascular biology', *Journal of Thrombosis and Haemostasis* **1**, 2112–2118.

[233] Weinreb, R. N., Ong, T., Scassellati Sforzolini, B., Vittitow, J. L., Singh, K. and Kaufman, P. L. [2015], 'A randomised, controlled comparison of latanoprostene bunod and latanoprost 0.005% in the treatment of ocular hypertension and open angle glaucoma: the VOYAGER study', *British Journal of Ophthalmology* **99**(6), 738–745.

[234] Weinreb, R. N., Scassellati Sforzolini, B., Vittitow, J. and Liebmann, J. [2016], 'Latanoprostene Bunod 0.024% versus Timolol Maleate 0.5% in Subjects with Open-Angle Glaucoma or Ocular Hypertension', *Ophthalmology* pp. 1–9.
URL: *http://linkinghub.elsevier.com/retrieve/pii/S0161642016000646*

[235] Weinreb, R. N. and Tee Khaw, P. [2004], 'Primary open-angle glaucoma', *Lancet* **363**, 1711–1720.

[236] Wiederholt, M., Sturm, a. and Lepple-Wienhues, a. [1994], 'Relaxation of trabecular meshwork and ciliary muscle by release of nitric oxide', *Investigative Ophthalmology and Visual Science* **35**(5), 2515–2520.

[237] Wiederholt, M., Thieme, H. and Stumpff, F. [2000], 'The regulation of trabecular meshwork and ciliary muscle contractility', *Progress in Retinal and Eye Research* **19**(99), 271–295.

[238] Wiggs, J. L., Kang, J. H., Yaspan, B. L., Mirel, D. B., Laurie, C., Crenshaw, A., Brodeur, W., Gogarten, S., Olson, L. M., Abdrabou, W., DelBono, E., Loomis, S., Haines, J. L., Pasquale, L. R. and GENEVA Consortium [2011], 'Common variants near CAV1 and CAV2 are associated with primary open-angle glaucoma in Caucasians from the USA.', *Human molecular genetics* **20**(23), 4707–13.

[239] Xie, Q. W., Cho, H. J., Calaycay, J., Mumford, R. a., Swiderek, K. M., Lee, T. D., Ding, a., Troso, T. and Nathan, C. [1992], 'Cloning and characterization of inducible nitric oxide synthase from mouse macrophages.', *Science (New York, N.Y.)* **256**, 225–228.

[240] Xu, S., Ying, J., Jiang, B., Guo, W., Adachi, T., Sharov, V., Lazar, H., Menzoian, J., Knyushko, T. V., Bigelow, D., Schöneich, C. and Cohen, R. a. [2006], 'Detection of sequence-specific tyrosine nitration of manganese SOD and SERCA in cardiovascular disease and aging.', *American journal of physiology. Heart and circulatory physiology* **290**(January 2006), H2220–H2227.

[241] Yanagisawa, M., Kurihara, H., Kimura, S., Tomobe, Y., Kobayashi, M., Mitsui, Y., Yazaki, Y., Goto, K. and Masaki, T. [1988], 'A novel potent vasoconstrictor peptide produced by vascular endothelial cells.'.

[242] Yang, C. Y. C., Liu, Y., Lu, Z., Ren, R. and Gong, H. [2013], 'Effects of Y27632 on aqueous humor outflow facility with changes in hydrodynamic pattern and morphology in human eyes', *Investigative Ophthalmology and Visual Science* **54**(8), 5859–5870.

[243] Ye, Y., Quijano, C., Robinson, K. M., Ricart, K. C., Strayer, A. L., Sahawneh, M. A., Shacka, J. J., Kirk, M., Barnes, S., Accavitti-Loper, M. A., Radi, R., Beckman, J. S. and Estévez, A. G. [2007], 'Prevention of peroxynitrite-induced apoptosis of motor neurons and PC12 Cells by tyrosine-containing peptides', *Journal of Biological Chemistry* **282**, 6324–6337.

[244] Yücel, Y. H., Johnston, M. G., Ly, T., Patel, M., Drake, B., GümüÅ§, E., Fraenkl, S. a., Moore, S., Tobbia, D., Armstrong, D., Horvath, E. and Gupta, N. [2009], 'Identification of lymphatics in the ciliary body of the human eye: A novel "uveolymphatic" outflow pathway', *Experimental Eye Research* **89**(5), 810–819.

[245] Zamora, D. O. and Kiel, J. W. [2010], 'Episcleral venous pressure responses to topical nitroprusside and N-nitro-L-arginine methyl ester', *Investigative Ophthalmology and Visual Science* **51**(3), 1614–1620.

[246] Zelikin, A. N., Quinn, J. F. and Caruso, F. [2006], 'Disulfide cross-linked polymer capsules: En route to biodeconstructible systems', *Biomacromolecules* **7**(1), 27–30.